Université Pierre et Marie Curie

Sciences mécaniques, acoustique, électronique et robotique

Onera / Département d'Aérodynamique Appliquée

Development of Moderate-Cost Methodologies for the Aerodynamic Simulation of Contra-Rotating Open Rotors

Par Ignacio Gonzalez-Martino

Thèse de doctorat de Mécanique des Fluides Numérique

Dirigée par Michel Costes et Philippe Devinant

Présentée et soutenue publiquement le February 14, 2014

Devant le jury composé de :

Serge Huberson	ENSAM (Paris)	*Rapporteur*
Elie Rivoalen	INSA de Rouen	*Rapporteur*
Georges Gerolymos	UPMC (Paris)	*Président*
Michel Costes	Onera (Meudon)	*Examinateur*
Philippe Devinant	Institut PRISME (Orléans)	*Examinateur*
Florian Blanc	Airbus Operations S.A.S. (Toulouse)	*Examinateur*
Ricardo Martinez-Botas	Imperial College (London)	*Examinateur*
Benoit Rodriguez	Onera (Meudon)	*Invité*

Except where otherwise noted, this work is licensed under
http://creativecommons.org/licenses/by-nc-nd/3.0/

A la meva família.

Acknowledgments

Je tiens à remercier toutes les personnes qui m'ont accompagné – de près ou de loin – dans cette aventure de trois ans, la rendant ainsi possible.

Tout d'abord, mes encadrants à l'Onera, Michel Costes et Benoit Rodriguez. Votre support au quotidien, votre confiance et vos encouragements m'ont permis de mener à bien cette thèse ! Encore merci pour toutes vos relectures qui ont permis à ce mémoire de prendre forme. Je n'oublie pas Philippe Devinant mon co-directeur pour son suivi et pour ses conseils au cours de mes recherches.

Je tiens également à remercier très chaleureusement les membres du jury qui ont eu la gentillesse d'accepter de juger ce travail. En particulier Serge Huberson et Elie Rivoalen pour avoir accordé de leur temps à la lecture de ce mémoire en tant que rapporteurs.

Je remercie aussi Frédéric Barrois et Fabien Magaud, mes encadrants à Airbus, pour leur accueil au sein de l'équipe des Méthodes pour l'Aérodynamique, pour l'intérêt porté sur mes travaux de recherche et pour leur soutien.

Je voudrais remercier toutes les personnes qui ont suivi cette thèse, qui se sont intéressées à ces travaux ou qui simplement par leur jovialité ont rendu le quotidien agréable en tant que collègue. Un grand merci tout particulier à toute l'équipe H2T et, bien évidemment, à tous les doctorants de l'Onera à Meudon.

Enfin, je remercie ma famille et mes amis pour leur soutien indéfectible. Votre inestimable soutien, parfois à distance, m'a permis de tenir bon jusqu'au bout. Merci !

I amunt puja i més amunt,
com aucells de branca en branca;
d'aqueixa cova damunt
una altra veu de més blanca.

Mes, com puja de grat,
troba curta tota escala;
per un cor enamorat
cada pas és un cop d'ala.

Mn. Jacint Verdaguer, *Canigó*, Cant VI

Contents

Nomenclature **ix**

Introduction **1**

Literature Review **5**

Propeller and Open Rotor assets & challenges 5

Research on Propellers and Open Rotors 5

Key Assets and Challenges of Open Rotors 11

In-Plane Loads on Propellers and Open Rotors 15

Impact of 1P Loads on Aircraft 15

Physical Mechanisms behind 1P Loads 17

Methods for the Prediction of Aerodynamic Performance 21

Analytical Models for Propellers 22

Numerical Singularity Methods 25

Potential, Euler and RANS Methods 26

Eulerian/Lagrangian Coupling 28

The Lifting-Line Theory 31

The Onset of the Lifting-Line Theory 40

Developing the Lifting-Line Theory 44

The Unified Lifting-Line Theory 45

Numerical Application of the UCLL Theory 47

Methods and Tools **49**

Available Methods for Single Propellers and CROR 49

Selected Methods for the Preliminary Design of Open Rotors 54

HOST. A Comprehensive Code for Aeromechanical Simulations 55

An Helicopter Overall Simulation Tool 56

The Blade Module for Aero-Mechanical Simulations 57

Vortex Wake Models in HOST: METAR and MESIR 57

MINT Wake Model 59

Installation Effects in HOST 64

Main Hypothesis of the Lifting-Line in HOST 65

Computational Fluid Dynamics Solver: *elsA* 66

HOST/MESIR-elsA Coupling: RVA Module 67

APIAN Single-Rotating Propeller 68

AI-PX7 Contra-Rotating Open Rotor 70

1 HOST Assessment on APIAN Single Propeller Case 73
1.1 Parametric Study and Best Practices . . . 73
1.2 High-Speed Simulations Assessment with Wind Tunnel Data and CFD computations . . . 78
1.2.1 Wind Tunnel Data . . . 78
1.2.2 *elsA* CFD Computations . . . 78
1.2.3 HOST-MINT Simulations . . . 80
1.2.4 Incidence Effect . . . 83
1.2.5 Advance Ratio Effect . . . 88
1.3 Way Forward in HOST Simulations . . . 91

2 A Physical Insight into Propeller 1P loads 93
2.1 Theodorsen's Theory: A Two-Dimensional Analogy . . . 93
2.2 Quantifying the Impact of Aerodynamic Mechanisms on 1P Loads . 95
2.2.1 Main Contributors on 1P Load Phase Lag . . . 98

I Unsteady Airfoil Model 99

3 Analyzing an Unsteady Curved Lifting-Line Method (UCLL) 101
3.1 An Unsteady Curved Lifting-Line Theory . . . 101
3.1.1 Theoretical Basis . . . 101
3.1.2 A Numerical Implementation of the UCLLT . . . 105
3.2 Outer Domain. The Singular Panel . . . 105
3.2.1 The Doublet Formulation . . . 106
3.2.2 The Vortex Formulation . . . 111
3.2.3 Hess' Equivalence for Singular Panels . . . 112
3.2.4 Current Implementation in the AILE Code . . . 115
3.3 Inner Domain. Two-Dimensional Wake in Lifting-Line Formulation . 116
3.4 Theoretical Analysis of the Model . . . 116
3.4.1 Inner Domain. Airfoil Model . . . 116
3.4.2 Outer Domain. The Singular Panel . . . 118
3.4.3 Remarks on the Model . . . 118

4 Developing and Implementing an UCLL Method in HOST without Finite Part Integrals 121
4.1 The Complete Unsteady Curved Theory . . . 121
4.2 Implementation in HOST . . . 124
4.3 Concluding remarks . . . 125

5 UCLL Method Assessment on APIAN Single Propeller Case 127
5.1 Impact of Incidence on High-Speed HOST-MINT Simulations . . . 128
5.2 Impact of Advance Ratio on High-Speed HOST-MINT Simulations . 131
5.3 Concluding Remarks . . . 134

6 UCLL Method Assessment on AI-PX7 Counter-Rotating Open Rotor Case 135
6.1 Test Case Description . . . 135
6.2 Code-to-Code Assessment. elsA vs. HOST-MINT . . . 137
6.3 Aerodynamic Mechanisms behind 1P Loads. . . . 143
6.4 Concluding Remarks . . . 147

II Code Coupling 151

7 Development of a Coupling Strategy between HOST-MINT and elsA Codes 153
7.1 Current Coupling between HOST/MESIR and elsA . . . 154
7.1.1 HOST/MESIR-elsA Coupling Strategy . . . 154
7.1.2 Main Advantages and Shortcomings of the Strategy . . . 155
7.2 Implementation of a One-Way Coupling between elsA and HOST-MINT codes . . . 156
7.3 Assessment of MESIR and MINT Coupling Strategies for Single Propellers . . . 157
7.3.1 Induced velocity fields . . . 159
7.3.2 Induced Velocities Interpolation Time Step . . . 165
7.4 Coupling Strategy Assessment on APIAN Single Propeller Case . . . 168
7.4.1 Test Case Description. . . . 168
7.4.2 Blade Loading . . . 169
7.4.3 Propeller Performance . . . 169
7.4.4 Blade Load Distribution . . . 170
7.4.5 Pressure on Blade Skin . . . 171
7.4.6 Flow Analysis . . . 173
7.5 Induced Velocity Fields . . . 174
7.6 Concluding Remarks . . . 177

A Finite Part Integrals 183
A.1 Principal Value of a Singular Integral . . . 183
A.2 Hadamard's Finite Part Integrals . . . 183

B Sweep Effect 187

C Alternative Form of the Singular Panel Integration 189
C.1 Development of the Singular Panel Integration . . . 189
C.1.1 The Complete Parabolic Wake . . . 189
C.1.2 The Regular Part of the Parabolic Wake . . . 192
C.1.3 The Complete Expression . . . 193

D Résumé en français **195**
D.1 Introduction 195
D.2 Un aperçu des mécanismes à l'origine des efforts 1P 196
D.2.1 Les mécanismes physiques à l'origine des efforts 1P 196
D.2.2 Une méthode pour quantifier les mécanismes sur les efforts 1P 197
D.3 Développement et implémentation d'une méthode de ligne portante courbe et instationnaire 199
D.4 Évaluation de la méthode de ligne portante courbe et instationnaire dans le cas d'hélice simple APIAN 201
D.5 Évaluation de la méthode de ligne portante courbe et instationnaire dans le cas de l'Open Rotor AI-PX7 202
D.5.1 Évaluation de HOST-MINT dans un cas d'open rotor 202
D.5.2 Un aperçu dans les mécanismes des efforts 1P 204
D.6 Développement d'une méthodologie de couplage entre les codes HOST et elsA 206
D.7 Conclusions 208

Bibliography **209**

List of Figures **227**

List of Tables **233**

Nomenclature

α	Propeller incidence (deg)
α_∞	Freestream angle of attack (deg)
α_{ind}	Induced angle of attack (deg)
δx	Panel length (m)
η_P	Propulsive Efficiency, $\eta = V_\infty \dfrac{T}{P}$
Γ	Circulation on the blade (m^2/s)
κ	Local radius of curvature (m), $\dfrac{(1+l'(y)^2)^{3/2}}{l''(y)}$
Ω	Rotational speed (rpm)
$\partial\tau/\partial\xi$	Spanwise gradient of the thrust coefficient, $\dfrac{\partial T}{\partial r}\dfrac{R}{\rho_\infty N^2(2R)^4}$
Φ	Velocity potential ($\text{m}^2.\text{s}^{-1}$)
ψ	Azimuthal position (deg)
Ψ_{1P}	1P load phase lag (deg), $\arctan(F_Y/F_Z)$
Ψ_{M1P}	1P moment phase lag (deg), $\arctan(M_Y/M_Z)$
ρ_∞	Freestream density (kg.m^{-3})
$\vec{v}$	Freestream velocity vector in the body-fixed reference frame (m.s^{-1})
$\vec{v}_{\text{ind}}$	Induced velocity (m/s)
ξ	Relative propeller radius, r/R
C	Theodorsen's function, depends on reduced frequency k
c_0	Maximum chord (m)
C_{L}	Airfoil lift coefficient
C_{1P}	1P load coefficient, $\sqrt{F_Y^2+F_Z^2}/(\rho N^2 D^4)$
C_{M1P}	1P moment coefficient, $\sqrt{M_Y^2+M_Z^2}/(\rho N^2 D^5)$
C_{PW}	Power coefficient, $P/(\rho N^3 D^5)$

C_{TH} Thrust coefficient, $T/(\rho N^2 D^4)$

D Propeller diameter (m)

f Oscillation frequency of an airfoil (s^{-1})

F_Y Side force (N)

F_Z Vertical Force (N)

J Propeller advance ratio, $V_\infty/(N.D)$

k Reduced frequency in Theodorsen's theory, $2\pi fc/(2V_\infty)$

$l(y)$ Quarter-chord line equation (m)

M_∞ Freestream Mach number

N Rotational speed (s^{-1})

n Normal unit vector

P Power ($\mathrm{N.m.s}^{-1}$)

R Propeller radius (m)

r Radius (m)

T Thrust (N)

U_∞ Freestream velocity ($\mathrm{m.s}^{-1}$)

V_θ^{ind} Circumferential induced velocity ($\mathrm{m.s}^{-1}$)

$V_{\mathrm{X}}^{\mathrm{ind}}$ Axial induced velocity ($\mathrm{m.s}^{-1}$)

$V_\perp$ In-plane velocity ($\mathrm{m.s}^{-1}$)

$V_{X\infty}$ Axial freestream velocity ($\mathrm{m.s}^{-1}$)

w Induced velocity in the airfoil plane and normal to the chord ($\mathrm{m.s}^{-1}$)

BPF Blade passing frequency (s^{-1})

CFD Computational Fluid Dynamics

CROR Contra-rotating open rotor

RANS Reynolds-averaged Navier-Stokes equations

UCLL Unsteady-curved lifting-line

uRANS Unsteady Reynolds-averaged Navier-Stokes equations

Introduction

In a context of oil crisis, the U.S. Senate in 1975 directed NASA to look at every potential fuel-saving concept that aviation technology could produce. Within all identified concepts, contra-rotating open rotors (CROR) promised the highest potential fuel saving for high-speed subsonic aircraft [Hager 1988]. Even if the open rotor was the most challenging concept, the significant potential payoff that could be obtained forced the other partners to adhere to the project until the end of the 1980s. By that time, mainly because of the decrease in oil prices and the complexity of such systems, the interest on this engine technology diminished.

Today, the world of commercial aircraft is facing a similar context. To the rise of oil prices, more prevalent environmental and noise concerns have been added in the last years. Thus, aircraft and engine manufacturers, as well as research laboratories and academia, are doing an important effort to push forward again the contra-rotating open rotor concept, still promising a much better propulsive efficiency than future turbofans. However, open rotor challenges regarding installation on aircraft, noise and certification remain.

The research on contra-rotating open rotors started at Airbus Operations around ten years ago. During the last years, in collaboration with a number of research centers, the company has launched a number of projects aiming at developing the numerical analysis capabilities adapted to each design phase of the engine and its integration on the aircraft. In order to identify the best numerical methodology among all the different possibilities, it has been necessary to identify the main requirements at each of the design phases and at each application case. This requirement identification has been done progressively, leading to the development of a number of tools which, in the end, where not completely adapted for the problem to be addressed.

In particular, the analysis tools for preliminary design phases have been clearly identified during these years. First, they should be able to provide an insight into the global design space in a relatively short elapse of time, and with low CPU and memory costs. Second, this type of tools should be adaptable to easily address an important number of topics that should be studied from the beginning of the design. Third, in the case of propellers and open rotors, tools should also be able to predict with enough accuracy the main critical propeller parameters in order to point out the optimal engine designs, that can be used in the next design steps. The critical parameters in propeller design are the performance (thrust and power) and the so-called in-plane loads. These in-plane loads appear as a consequence of a blade load disymmetry due to the effects of the engine installation on the aircraft. The importance of these loads on the global aircraft design imposes that preliminary design tools should correctly account for these effects of installation. In addition, the mean propeller moments and load distribution on the blade are precious data for the structural design of the blade and the pitch change mechanism. Moreover, the unsteadiness in these loads and moments are also important to predict fatigue

issues and to estimate vibrations. Finally, the accuracy of the predictions must be sufficient to establish the main tendencies or sensitivity of these critical parameters on a given modification on an engine design.

This Ph.D. thesis starts with an extended *Literature Review* chapter. First, a review of the research on propellers and open rotors and an explanation of their main assets and challenges of these engine technologies are presented. Second, the aerodynamic mechanisms at the origin of in-plane loads are identified, and its impact on aircraft design is evoked. Third, an historical review of the simulation methodologies is presented. Last, a special attention is paid to the lifting-line theory, from its onset to the last developments in the 90's.
After, in the *Methods and Tools* chapter, the main available methodologies are critically analyzed to help the reader better understand the current context of numerical methodologies for the simulation of open rotors. Here, in this introduction, only a rapid overview of the most representative ones is provided.

Among the different methodologies developed specifically for the aerodynamic simulation of open rotors, the first and more simple ones were the steady singularity methods. These classical approaches, like the lifting-line or the the lifting-surface methods, solve only the inviscid problem and, in general, they simplify the geometry of the blade. However, they have proven to predict open rotor performances with a relatively fair accuracy and at very low computational costs, of the order of the seconds. Moreover, as the solution of the problem is obtained by superposing a series of singularities distributed in the space, these methods provide a precious tool to obtain a better insight into the mechanisms behind a certain aerodynamic phenomenon.
Unfortunately, the steady or quasi-steady approaches in the majority of these codes prevent them from predicting the open rotor in-plane loads with enough accuracy.

During the last decades, due to the increase in the computational capabilities, numerous CFD codes solving the Reynolds-Averaged Navier-Stokes (RANS) equations have been developed. Their success to reproduce the main key aerodynamic phenomena of interest for the companies have lead to its hegemony in the world of numerical simulations for aeronautics.

A number of methods exists to apply these RANS solvers to the case of contra-rotating open-rotors. The first and more simple methodology is called the *mixing-plane*. It solves the steady RANS equations in a one-blade-per-row domain and the information between the rows is averaged azimuthally so as to be able to reach a converged steady state.
This steady approach has the advantage to account for viscosity and compressibility effects and it is a powerful tool for the prediction of open rotor performance. However, due to its steady approach, the mixing-plane cannot take into account the effects of installation of the engine on the aircraft, and therefore it cannot predict the in-plane loads.

The more complex RANS methodology consists of considering the full computational domain and of solving the unsteady RANS equations. This approach enables to take rigorously into account the open rotor performance, the unsteady blade load-

ing and hence the in-plane loads. Unfortunately, current computational capabilities are not adapted to use this approach in preliminary design phases.

In the last years, a number of *frequency-based CFD methods* have been applied to the simulation of contra-rotating open rotors. Originally developed for turbomachinery, these methods take the advantage of seeking for a periodically-dominated solution, which is the case for the major part of considered open rotor cases. The periodicity hypothesis avoids the computation of long transitive solutions, hence reducing the global computational costs. Though theoretically very interesting approaches, these methods are still not mature and first results on open rotors have shown significant convergence problems to be addressed.

Within the Airbus group, other business units have developed their simulation tools for the aerodynamic design of their products. In particular, Airbus Helicopters France[1], has developed a comprehensive code for the aeromechanical simulation of rotorcraft. The structure of the code is highly modular, enabling the integration of very different models into a single computation. In particular, the aerodynamic model couples a module based on the blade-element method, and an unsteady wake model based on the lifting-line theory. This allow for unsteady time-marched simulations. Besides, the effects of installation can be taken into account in HOST, and therefore in-plane loads may be correctly predicted.

After a detailed study of the different simulation tools for open rotors, presented in this introduction as a rapid overview, it has been highlighted that none of the available tools fulfill the main requirements for preliminary design phases. On the contrary, an external comprehensive code, HOST, has been identified as a possible candidate to fill this gap in the available methodologies.

Therefore, the main motivation of the present Ph.D. thesis is the need to develop and assess reliable moderate-cost methodologies for the aerodynamic simulation of open rotors that are adapted to the needs of Airbus' designers.

To do so, a first assessment of the HOST code on the APIAN propeller case, an advanced single-propeller geometry, has been performed in Chapter 1. The propeller performance, the in-plane loads, and the blade load distribution have been analyzed and compared to experimental data and CFD unsteady RANS computations when possible. A particular attention has been paid to the effects of the rotating-speed and the propeller incidence. Moreover, based on a series of parametric studies, a number of best practices in propeller simulations could be established.

In a second step, an original method to analyze the impact of a number of aerodynamic mechanisms on the in-plane loads has been proposed in Chapter 2. This method uses the linearity hypothesis on which all singularity methods are based to decompose the different contributions to the unsteady aerodynamic loads of the blade. With this, the major contributors to the propeller in-plane loads could be identified, together with the main limits of the present modeling of the problem.

Based on these two main results, the contribution of each term and the limits of the models, the next two chapters have been devoted to the improvement of one of

[1] Eurocopter France until 2013.

these models, contributing to the in-plane loads: the unsteady airfoil model. First, in Chapter 3 the numerical implementation of Guermond and Sellier's unsteady curved lifting-line theory [Guermond 1991] proposed by Muller [Muller 2007] has been critically analyzed. A special attention has been paid to the integration of the singular integrals by Finite Parts in the calculation of induced velocities [Hadamard 1932]. The main shortcomings of this numerical approach have been put forward.

From the limits of the model studied in the previous chapter, a new numerical implementation of Guermond and Sellier's theory has been developed and implemented in the HOST code. Hence, Chapter 4 has been devoted to the development, the theoretical analysis, and the implementation of an unsteady airfoil model that enables, on one side, to correct the quasi-steady airfoil data to include the loads due to airflow unsteadiness and, on the other side, to account for the local blade sweep and curvature. Again, the main assets and shortcomings of the implemented model have been put forward.

Chapter 5 focuses on the assessment of this new unsteady airfoil model in HOST when applied to the APIAN case, a single-rotating propeller. The same computation conditions and comparisons performed in Chapter 1 are here used to assess the new implemented model.

The assessment of the HOST code done in Chapters 1 and 5 for the case of a single-rotating propeller has been extended in Chapter 6 to the AI-PX7 case, an Airbus' generic contra-rotating open rotor geometry. The models to account for the effects of installation and the unsteadiness in the airfoil inflow have been assessed by comparing HOST simulation results to more complex and accurate CFD uRANS simulations. The open rotor performance, the in-plane loads, and the blade unsteady loadings have been again analyzed and compared.
Finally, the method to analyze 1P loads developed in Chapter 2 has been adapted and applied to the case of a contra-rotating open rotor. This method has been developed to provide a better insight into the aerodynamic mechanisms controlling propeller and open rotor in-plane loads.

Therefore, this first part of the Thesis aims at validating a comprehensive tool for the aerodynamic design of propellers and open rotors. Moreover, this tool opens the door to tackle multiple propeller and open rotor simulations of industrial interest: whirl flutter simulations, blade pitch default studies, aeroelastic simulations, aeroacoustic preliminary studies, etc.

Based on the limits in the hypothesis of the lifting-line methodology, an exploratory study has been performed to assess a possible future methodology in order to better capture the blade-vortex interaction phenomenon, and the three-dimensional compressibility and viscous effects close to the blade wall. Hence, Chapter 7 exposes the partial implementation and a preliminary assessment of an innovative Eulerian/Lagrangian coupling between HOST and a CFD uRANS simulation using the *elsA* code.

The thesis finishes with a conclusion and a number of future works that might be interesting to explore as a way to continue with the development of these moderate-cost methodologies.

Literature Review

Propeller and Open Rotor Assets & Challenges

Research on Propellers and Open Rotors

On December the 17th 1903 the first manned, sustained and self-controlled flight became reality when the Wright brothers' aircraft took off at Kitty Hawk for a 12 seconds flight. Although being rudimentary, Wright's aircraft was propelled by a wooden propeller with a surprising peak efficiency around 70%. Wilbur Wright was the first person to recognize that a propeller is nothing more than a rotating twisted wing, that converts shaft power into propulsive thrust [Anderson 2001]. Since that moment and for the next 45 years, propellers remained the sole available propulsion system for aircraft.

During the first decades of the 20th century, the aviation developed at an astonishing rate mainly in Europe and the US. As a natural consequence, the research on wing aerodynamics and propulsive systems flourished during those years.

Propeller Research at NASA. From its inception aviation has been driven by the consistent desire to fly faster, farther, and higher. This natural evolution brought early to light the loss in efficiency of propellers when increasing the speed of flight [Sullivan 1977]. As a consequence of higher advancing and rotational velocities, the relative velocity near blade tips came close to Mach 1. This increased significantly the propeller wave drag and led to an important efficiency losses. As a way to overcome these limits, different blade geometries were tested between 1927 and the mid-1950's at NACA (the NASA predecessor). Variable pitch-angle systems in the 1930's, highly loaded and swept blade tips in the 1940's, and thin airfoils in the 1950's were the three main tested innovations. First, the blade pitch-angle is modified in order to adapt to each flight condition, determined by a flight speed and a required thrust. Second, swept blade tips modify the aerodynamic behavior of the blade and reduce the intensity of shock waves. Finally, thin airfoils are better adapted for high subsonic conditions.

The propeller technology advanced steadily until the 1950's. By that time, important progresses on turbojet technology were achieved, presenting tremendous speed advantages with respect to propellers. Moreover, propellers at that time were unable to overcome compressibility losses at high subsonic conditions with adequate structural reliability. Thus, by end of the 1950's, the interest on propellers waned and the aviation industry plunged into the development of turbojet engines. By that time, even if it was known that propellers had a much more important propulsive efficiency than turbojet engines even for relatively high Mach numbers ($M \sim 0.6$), fuel costs were not an important element in the airline budget.

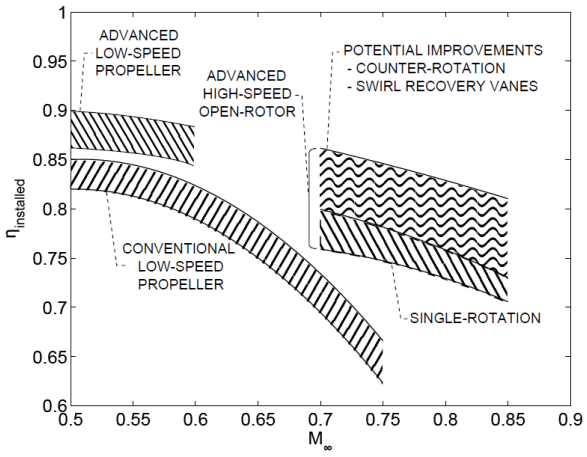


Figure 1: Propeller and open rotor efficiency as estimated by Jeracki [Jeracki 1981]

The Advanced Turboprop Program in the U.S. The Middle East oil embargo in 1973 made perspectives change again. Fuel prices tripled and disrupted airline service. Fuel costs, which so far had been a small portion of operating costs, started to account for almost half of an airline's budget. This pushed industries and governements to put fuel efficiency as one of the main research priorities and to look for all possible fuel-efficient solutions for aircraft and engines. Six main technological projects were launched in the United States in 1976: three were airframe related (composite materials, practical active controls, and laminar flow control) and the other three were propulsion related. While the two first aimed at improving existing turbojet engines, the latter and most challenging project was to develop advanced turboprops.

Similar to turbofans, a gas-turbine core is used in turboprop and open rotor engines. The energy of fuel combustion in the inner core is used to drive one or two large-diameter fans which propel an important amount of cool air. The ratio between the cool airflow and the airflow passing through the engine core is commonly known as the Bypass Ratio (BPR). As the cool air is not confined by the nacelle, turboprops and open rotors present a much higher BPR than turbofans. Therefore, it increases considerably the propulsive efficiency η_P of this kind of engines, which is the main asset of propeller-driven engines (see Fig. 1) compared to turbofans ($\eta_P \simeq 0.6$).

The Advanced Turboprop (ATP) program was officially launched in 1978 [Hager 1988]. Since the beginning of the program, two types of configurations were tested: the single-rotating propellers, consisting of one row of blades; and the contra-rotating propellers, consisting of two rows of blades rotating in opposite directions. Although the advanced turboprop concept promised the highest potential fuel savings, at least 30%, it presented several challenging points coming from the available technologies and the market. The technical ones were the cruise performance, the airframe and environmental noise, the installation effects, and the maintenance costs.

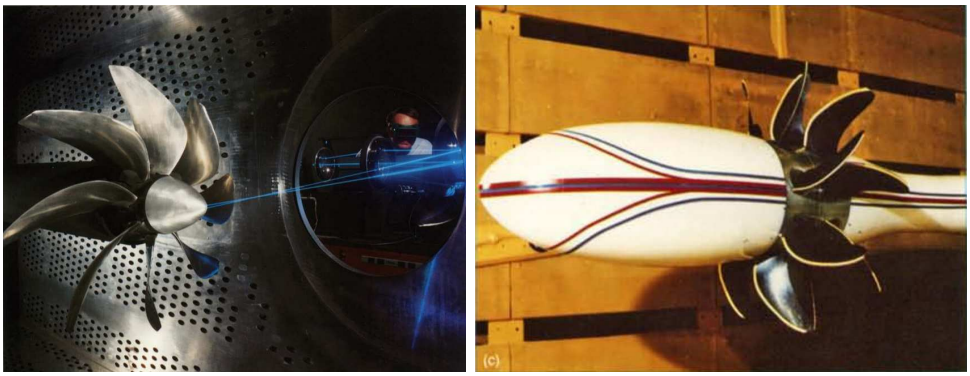


Figure 2: Wind tunnel tests during the ATP program [Hager 1988]

The main market issue was the customers' acceptance of propellers, that may be seen as a step backwards compared to turbojet engines.
The ATP project was structured to solve technical problems through code development and scale-model tests before ground and flight testing of large-scale systems. Until 1986, several wind tunnel tests were conducted on single-rotating propellers. Meanwhile, in 1986, the first contra-rotating propeller test rig was finished and tested. Finally, ground and flight tests were conducted by NASA and several companies (General Electric, Pratt & Whitney-Allison, Hamilton Standard, etc.) between 1986 and 1988 [Harris 1987].

The ATP program ended in 1987. As the energy crisis passed in the 1980's and the fuel prices decreased, there was no longer a favorable ratio of cost to implement turboprop technology versus savings in fuel efficiency. Therefore, instead of developing an all new aircraft with high-speed contra-rotating propellers, industries focused again on traditional and cheaper turbofan-powered aircraft.

The Propeller and Open Rotor research at Onera. The research on advanced propellers started at Onera, the French research center in aerospace, by end-1978, after a request from Aérospatiale company and the French Government. The CHARME research program on high-speed propellers was officially launched more than three years later, in the beginning of 1982. This program was carried out by the collaboration of Aérospatiale and Ratier-Figeac companies, and Onera research center. Several calculation methods with different levels of accuracy were implemented and wind tunnel campaigns were conducted (see Fig. 3), leading to the definition of a series of advanced single-rotating propellers (HT1, HT2 & HT3 propellers) [Bousquet 1985, Bousquet 1986].

Moreover, numerical studies were performed to define HTC5 contra-rotating propeller blades. This was the result of a collaboration between Aérospatiale company and Onera in the CHARME advanced propeller integration program. The main goal was to develop the AS100 aircraft, a 100-seat short- to medium-haul aircraft project conducted by Aérospatiale in the 1980's. The CHARME program was however stopped at the end of its first phase, in 1991, for almost the same reasons as

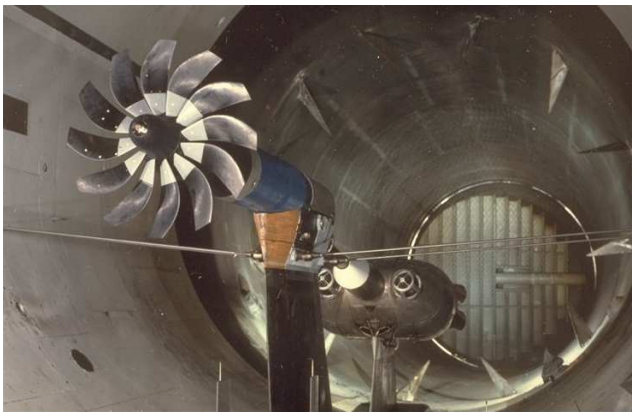


Figure 3: HT3 minimum-body configuration in Onera S1MA transonic wind tunnel facility

the ATP NASA program: fuel prices decreased and the development of a high-speed propeller-powered aircraft was no longer economically interesting.

In parallel and within a more transnational context, airframe manufacturers in collaboration with research centers and academia launched in the late 1980's four successive European-funded research programs on high-speed propellers: GEMINI, GEMINI II, SNAAP, and APIAN.
These four programs were devoted to the numerical and experimental investigation of the acoustic and the aerodynamic effects of installation on a high-speed propeller for a representative regional aircraft architecture.
The GEMINI pilot program (1990-1992) focused on designing and proving the feasibility of a given regional aircraft configuration for the rest of the programs. Between 1993 and 1996, two programs were launched in parallel: GEMINI II, devoted to the analysis of propeller aerodynamics when installed on the aircraft (see Fig. 4), and SNAAP, devoted to the isolated propeller aeroacoustics. Between 1996 and 2000, the APIAN program, based on the experience and tools developed previously, analyzed the aeroacoustics of the installed propeller.
The APIAN program included several wind tunnel campaigns, first on a minimum-body propeller configuration and then installed on an aircraft representative geometry (see Fig. 5). A particular effort was done to better understand the incidence and installation effects on propeller performance, as well as the prediction of the propeller acoustic footprint.

The knowledge on high-speed propellers acquired during these projects has helped in the design and production of propeller-powered aircraft in Europe in the last years, like for example the Airbus Generic Transport Aircraft A400M [Malard 2005].

The Open Rotor Renaissance. Today, the world of commercial aircraft is facing a context similar to the 1970's. To the rise of oil prices, more prevalent environmental and noise concerns have been added in the last years. Thus, aircraft and engine



Figure 4: Gemini II full-aircraft model at Onera S1MA transonic wind tunnel facility



Figure 5: APIAN Full-aircraft model in the low-speed DNW-LLF wind tunnel facility

manufacturers, as well as research laboratories, are doing an important effort to push forward again the Contra-Rotating Open Rotor concept, still promising a much better propulsive efficiency than future turbofans.

In 2000 a group of personalities from the key aeronautical stakeholders in Europe published a report with their vision for 2020 of commercial aviation in Europe. This group of personalities established also the Advisory Council for Aeronautical Research in Europe (ACARE), to develop and maintain the Strategic Research Agenda to achieve the Vision 2020. In its first document, the ACARE proposed the following environmental goals for 2020 to the aeronautical industry in Europe: *"(1) Total engagement by the industry in the task of studying and minimising the industry's impact on the global environment. (2) A reduction in perceived noise to one half of current average levels. (3) Eliminate noise nuisance outside the airport boundary by day and night by quieter aircraft, better land planning and use around airports and systematic use of noise reduction procedures. (4) A 50% cut in CO2 emissions per passenger kilometre (which means a 50% cut in fuel consumption in the new aircraft of 2020) and an 80% cut in nitrogen oxide emissions."* [Adv 2001] These goals have been assumed by stakeholders in three main points included in the ACARE Strategic Research and Innovation Agenda (SRA) [Adv 2004]:

- Reducing fuel consumption and CO_2 by 50% with 20% reduction coming from the engine alone,
- Reducing the perceived external noise by 50%, with 6dB per operation for the engine alone,
- Reducing NO_X by 80%, with 60 to 80% coming from the engine alone.

The SRA has provided a roadmap outlining the strategic orientations to be taken if Europe wants to develop a more sustainable aviation sector. As a consequence, important research programs at European and national levels have appeared in the last years: EU collaborative research in Aeronautics and Air Transport, the Clean Sky Joint Technology Initiative (JTI), the SESAR Joint Undertaking, and many national research projects coming from public or private establishements.
In 2012, the ACARE members have reconsidered the Vision 2020 and extended it to a new horizon towards 2050.

The Clean Sky JTI research program, launched for the 2008-2017 period, is devoted to the development of breakthrough technologies to significantly increase the environmental performance of air transport. The program aims at delivering demonstrators in all segments of civil air transport grouped into six Integrated Technological Demonstrators or technological areas: the SMART Fixed Wing Aircraft (SFWA), the Green Regional Aircraft (GRA), the Green Rotorcraft (GRC), the Sustainable and Green Engines (SAGE), the Systems for Green Operation (SGO), and the Eco-Design (ECO).

The research on open rotors has been significantly encouraged within the Clean Sky SFWA area. Airframe and engine manufacturers, as well as research laboratories

and universities are working together to deliver the first European CROR-powered flight test demonstrator by 2020. During last years, industries and research laboratories have used several existing analysis capabilities and developed new ones that are specific for open rotors. It is worth mentioning that different wind tunnel tests have been conducted by the European manufacturers Rolls-Roys, Snecma, and Airbus.

In parallel, similar programs have been launched by NASA in the US: the Subsonic Fixed Wing (SFW) program and the Environmentally Responsible Aircraft (ERA) project [Suder 2012]. With the collaboration of aeronautical manufacturers and universities, NASA focuses on developing and demonstrating integrated system technologies up to mature readiness levels by 2020. Similar to European ACARE goals, the ERA project aims at simultaneously reduce fuel burn (by 50%), emissions (-75% NO_X in landing and take-off cycle, and -55% at cruise), and noise (-42dB relative to FAA Stage 4 reference) in future aircraft.
With the large amount of experience that NASA acquired during the 1980's and the ATP program, several analysis capabilities have been reused in the last years to update the research on open rotors. Aerodynamic and aeroacoustic performance of isolated and installed open rotors have been measured at low- and high-speed conditions. Moreover, a number of blade geometries have been developed and tested to optimize the acoustic signature of open rotors [Van Zante 2012]. Recently, different conventional and unconventional airframe architectures have been tested for acoustic shielding [Czech 2013].

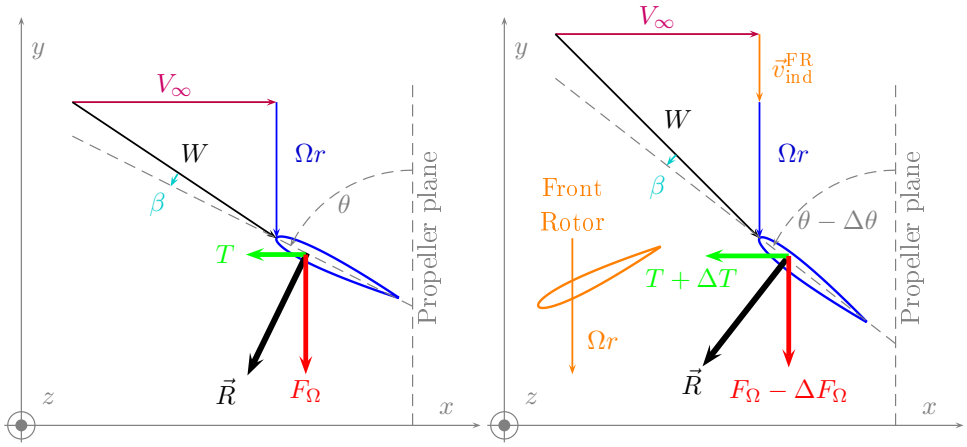
Key Assets and Challenges of Open Rotors

Main Assets. Three main assets of contra-rotating propellers with respect to turbofan engines have been identified:

- *Higher bypass ratio*: increasing the ratio between the propelled cool air (uncombusted air) over the air going into the engine core (air involved in combustion) increases significantly the engine propulsive efficiency. Open rotors are likely to offer bypass ratios above 30, whereas turbofans are expected to reach bypass ratios of 14 to 18. Thus, open rotors have better propulsive efficiencies even at Mach numbers around 0.8 and are expected to offer significant fuel savings with respect to turbofans.
  Compared to a 1998-reference, aircraft powered with Ultra High Bypass ratio (UHB) turbofan are likely to give a 27% fuel gain, whereas open rotor-powered aircraft promise a 36% fuel gain [Van Zante 2013].

- *Swirl recovery*: the highly loaded, single-rotating propellers have an efficiency loss of 6 to 8% due to residual swirl [Hager 1988]. Most of this loss can be recovered with a well-designed contra-rotating propeller. Moreover, as the rear rotor faces a swirled airflow from the front rotor, its efficiency is greater. Indeed, under a contra-rotating swirl, a smaller blade pitch is needed for the same blade incidence and loading (see Fig. 6). For a given blade loading, a smaller pitch implies a more important thrust component and a less important

off-axis component, which is linked to the torque. Increasing the thrust and reducing the torque implies increasing the propulsive efficiency η_P^{RR} of the rear rotor.



(a) Without FR swirl $\vec{v}_{ind}^{FR}$ (b) With FR swirl $\vec{v}_{ind}^{FR}$

Figure 6: Effect of the front rotor induced swirl on rear rotor efficiency

- *Reduced tip diameter*: contra-rotating propellers can offer around twice the thrust of a single-rotating propeller for a given diameter. This is particularly interesting for the integration on large aircraft.

At the end of the ATP program, fuel gains of 25 to 30% compared to turbofans of that time were estimated by NASA engineers. Today, although these benefits would not be so drastic due to the constant progress on turbofans, the open rotor technology is still the most radical step-change in commercial airplane propulsion with the sufficient readiness level for an entry in service in 2020 or 2025.

Open Rotor Challenges. However, contra-rotating propellers still present several competitive market and technological challenges that should be addressed in the years to come [Butterworth-Hayes 2010].

- *Competitive technologies.* The efficiency of current engines improves at an average of 1% a year, which means that classical turbofan engines available in 2025 are likely to be 11% more efficient than today's production without any major technology risk. Meanwhile, the Pratt & Whitney geared turbofan PW1000G could provide around $17 - 19\%$ fuel efficiency gain by 2020 [Norris 2007], whereas the CFM International direct drive LEAP could provide around 15% gain by 2015-2017 [Dron 2008]. In parallel with open rotors, UHB turbofans are being studied. They provide a very efficient and quieter solution, but they present some major drawbacks: the weight and drag penalties, and the issues linked to installation on aircraft due to the size of the nacelle.

- *Increased flight times.* An open rotor powered aircraft is likely to have a cruising speed 5 to 10% slower than a turbofan powered aircraft. This limit in cruise velocity comes from the important losses of efficiency and aerodynamic instabilities occur when the blade tips reach supersonic velocities. Even if this limit in cruise speed can be an important drawback for medium- and long-haul aircraft, it becomes negligible for short-haul flights, where the cruise phase is shorter, i.e. an increase of 5 to 10min.

- *Regulatory issues.* The engine layout and the blade containment are two issues to be investigated for the airworthiness certification of open rotor powered aircraft.
  For the certification of a turbofan engine, it must be demonstrated that one released fan blade can be safely contained in within the engine's fan case. In the case of an open rotor, where the nacelle and the fan case are absent, rules for conventional propellers are applied and designers must prove that the probability of blade release is "extremely remote", i.e. under 1×10^{-8} flying hours. For light weighted highly-loaded open rotor blades, this requirement is a real challenge.
  Aircraft manufacturers must also ensure that critical aircraft systems and passengers are sufficiently protected in the case of blade release. To fulfill this requirement, it may be necessary to reposition certain aircraft systems or the use of shielding.

- *Accessibility and maintenance costs.* Mounting the engines under the wing offers a easy access for on-wing checks and maintenance. However, what was possible until now for turbofan engines, it is not likely to be with the open rotor, mainly due to the more important engine diameter. New engine positioning could have a significant impact on maintenance times and cost. Moreover, the reliability of some complex components such as the gearbox or the blade pitch control systems must be assessed to make open rotors a desirable choice for airlines.

- *Public perception.* In the 1980's passengers considered propeller powered aircraft as outmoded, noisy and slow. Today, the environmental concerns of the traveling public would make the open rotor easier to be accepted.

- *Effects of installation.* The airframe-engine interaction is more important in an open rotor powered aircraft than in a turbofan powered aircraft, as in the first case the engine is not isolated from the aircraft effect by a nacelle. Thus, the pylon, the fuselage and the wing can impact significantly the performance of the open rotor by introducing a non-homogeneous inflow in its propeller planes [Borst 1981, Block 1984]. Some engine manufacturers believe that the installation impact and extra weight of open rotors will offset their fuel burn benefit [Barrie 2007].

- *Pitch change mechanism.* As open rotor blades see large changes in inlet flow

depending on the flight point, reliable pitch change mechanisms should be developed in order to ensure acceptable propulsive efficiencies. This mechanism should enable the blade to sweep all the pitch angles to cover reverse, ground idle, taxi, take-off, climb, cruise, approach, and feather.

- *Structural design and vibrations.* In order to be efficient, advanced propeller blades must be light, highly-loaded and present very complex geometries in terms of sweep, twist, and airfoil thickness. This makes the blade structural design an important challenge. The structure must fulfill three main requirements: withstand with foreign object damage, be free of high-speed and static stall flutter, and cope with fatigue issues due to forced vibrations in all the flight domain.
  Moreover, the vibrations transmitted by the open rotor engine on the airframe can be important and lead to structural fatigue. These aspects were studied by Donelson *et al.* [Donelson 1988] in test campaigns. In order to avoid resonance minor modifications and specific materials were used in the airframe structure. They demonstrated that in that case vibration levels were equivalent to those of a turbofan powered aircraft. However, those modifications led to a penalty in the airframe mass, which cannot be neglected in future studies.

- *Integration in the airframe.* The integration of the engine within the airframe becomes a critical issue because of the propeller diameter. Several different aircraft layouts are still under investigation, as all of them present important advantages but also drawbacks. Due to the installation effects, a non-homogeneous airflow is induced in the planes of rotation of the propellers, and thus the direction of the resultant forces and moments is modified. Consequently, together with the thrust and the torque, in-plane forces and moments appear. These components can reach important values and cannot be neglected in the prediction of the aircraft stability and handling qualities. For example, these loads and moments are a dimensioning factor of the vertical and the horizontal tail planes of the aircraft for the pusher configuration.
  Flight tests, wind tunnel tests and numerical simulations conducted in the 1980's [Vernon 1987, Donelson 1988] bring to light the impact of the open rotor engine at low- and high-speeds for a pusher configuration. These campaigns showed how the engine installation systems, the forces they developed and their flutter limits, played an important role in the overall aircraft performance and operability.

- *Acoustics.* Probably, acoustics is the major issue to be addressed to obtain a sufficiently mature open rotor technology [Peake 2012]. An important amount of acoustic data was collected during the different flight tests in the 1980's. Analysis put forward that the noise generated by an isolated open rotor could be very sensitive to an important number of parameters: the number of blades, the distance between rotors, the speed of rotation, the propeller diameters, etc. [Nichols 1988, Donelson 1988, Hager 1988, Simpson 1989].

Moreover, the noise generated by an open rotor has shown to be very sensitive to its installation on the aircraft [Block 1984]. A number numerical simulations have been conducted recently aiming at studying the main acoustic sources both of isolated and installed open rotors [Stuermer 2009, Peters 2010, Boisard 2012]: the blade tip noise due to transonic speeds, the interaction between the wake and vortex from the front rotor and the rear rotor blade, the pylon-rotor interaction in the case of a pusher configuration, and the propeller-wing interaction in the case of a puller configuration. All these phenomena induce a certain noise level both in the passengers' cabin and on the far field. Absorbent materials such as liners may reduce this noise, but imply an increase in weight of the fuselage and the engine. Community noise levels are more important in open rotor engines than in turbofan because the nacelle confines an important part of the propagated noise.
Several key design parameters have been studied for the noise reduction of installed open rotors –namely: the disk loading, the aft rotor clipping, the inter-rotor spacing [Khalid 2013], the leading-edge vortex control, or pylon blowing [Czech 2013], etc. Recent full-aircraft noise models based on open rotor wind tunnel data predict acceptable levels of noise to accomplish the FAR 36 Stage IV noise regulations with a 12.6EPNdB margin [Hendricks 2013]. However, it is also noted that to achieve these levels of noise unconventional architectures may be necessary, like for example a blended wing-body architecture with open rotors mounted on the rear part of the fuselage [Suder 2012, Czech 2013].

In-Plane Loads on Propellers and Open Rotors

The forces and moments developed by an open rotor can impact in a significant way the aerodynamic behavior of the whole aircraft during flight. Thus, it is important to understand their physical mechanisms and predict them accurately from the first design steps. This section is devoted to the comprehension of in-plane loads generated by single-rotating and contra-rotating propellers. As it will be detailed hereafter, these loads appear as a consequence of non-homogeneous inflows, produced by the aircraft incidence or the influence of the airframe elements on the engine, i.e. pylon, fuselage, wing, etc.

Impact of 1P Loads on Aircraft

The balance of forces and moments in an open rotor powered aircraft depend significantly on the thrust, torque, 1P loads and 1P moments generated by the engine (see Fig. 7). Moreover, the slipstream effect due to the propellers can also have an impact on the aerodynamic behavior of the aircraft. *Thrust and 1P loads* impact directly the drag balance. Depending on the aircraft attitude with respect to the freestream, the contribution of 1P loads can be positive or negative. The *vertical 1P load and the side 1P moment* impact the longitudinal stability of the aircraft and thus they modify the trim drag of the aircraft. The *1P moments derivatives with*

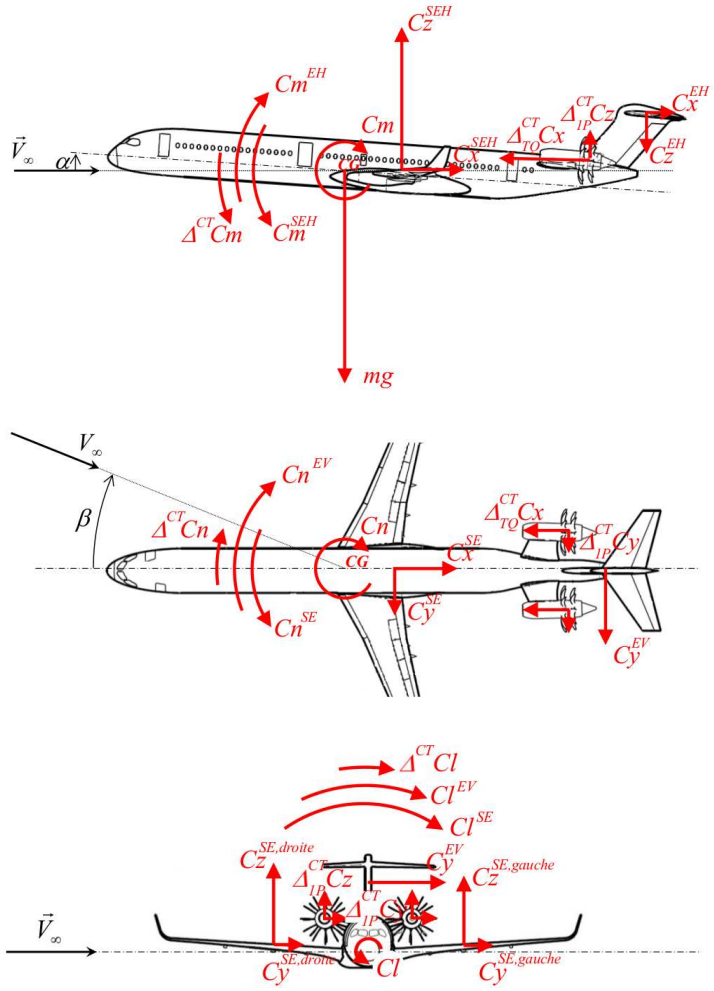


Figure 7: Longitudinal and lateral stability of an open rotor powered aircraft [Barth 2012]

respect to the angle of attack and the angle of yaw impact the longitudinal and side stability; they contribute to the dimensioning of the vertical and the horizontal tail planes; and thus they have an impact on the mass and on the friction drag of the aircraft. Finally, the *slipstream effect* impacts the behavior of the different surfaces. In the case of reverse thrust, for example, the important flow perturbation can lead to a partial or total loss of the effectiveness of the vertical tail plane. The slipstream forces and moments can modify the required dimension of different aircraft elements and thus their mass and their resulting friction drag.

Barth [Barth 2012] conducted a number of numerical studies on an open rotor powered aircraft in pusher configuration. It was shown that in this configuration the engines have a positive impact on the static and the dynamic stability of the aircraft. This stabilizing effect comes mainly from 1P loads and moments and has a positive

effect on the overall drag. In this configuration, Barth estimated a significant drag reduction, that would lead to an interesting reduction of the block fuel burn.

Physical Mechanisms behind 1P Loads

In the general case of a non-axisymmetric inflow, each blade experiences unsteady loads along a rotation. As a result, when adding the contribution of each blade, the net force may be no longer normal to the propeller plane. Therefore, the resulting force can be decomposed into a load normal to the propeller plane, the thrust, and an in-plane load. These in-plane loads are usually called "1P loads", as they appear as a consequence of a 1/rev oscillation of the inflow conditions in the blade frame. As it has been noted before, they constitute a dimensioning factor in terms of stiffness and damping of the engine installation systems and in the aircraft handling qualities. Thus, it is important to understand their aerodynamic mechanisms and predict them accurately in simulations.

1P Load Modulus or Vertical Force. A very common case of non-homogeneous inflow is the propeller in incidence. Very early it was realized that a propeller in that conditions develops significant in-plane loads [Clark 1913, Lanchester 1917].

For the simple case of an isolated propeller, the incidence implies a periodic variation of the inflow angle and relative velocity seen by each blade. As the velocity and angle of attack of the downward moving blade are more important than for the upward moving blade, the first generates more lift and drag. Projecting these loads for all blades on the propeller plane results in a net force in the direction of the incidence, i.e. a vertical positive force if the angle of incidence of the propeller is positive (see Fig. 8).

This local incidence seen by the propeller can appear due to the freestream velocity, but also to the installation effects. For example, even for the so-called "minimum-body" propeller configuration, the spinner and the wind tunnel rig can have a non-negligible effect on the propeller aerodynamics when it is placed in incidence.

However, this purely "geometrical" explanation of 1P loads accounts only for the presence of a vertical load, but cannot explain the measured and predicted side component. Indeed, in wind-tunnel test measurements, as well as in several sorts of simulations, a non-zero side force appears.

1P Load Phase Lag or Side Force. To give an insight on the side force aerodynamic mechanisms, a rotating reference frame is considered, following one blade along a cycle. As an example, we consider a single propeller CFD simulation using the *elsA* CFD code [Cambier 2008]. It can then be noticed that the maximum and minimum aerodynamic loads of the blades are not respectively placed at 90° and 270°, but shifted by a certain azimuth angle, as shown in Fig. 9(a).

Figure 9(b) shows the blade loads in the rotating frame projected on the propeller plane. For each blade, a sinusoidal evolution of frequency 1/rev can be noticed, with

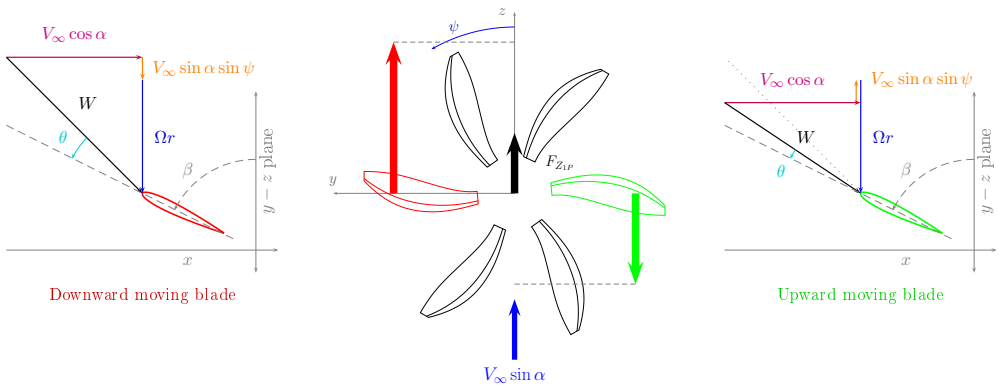
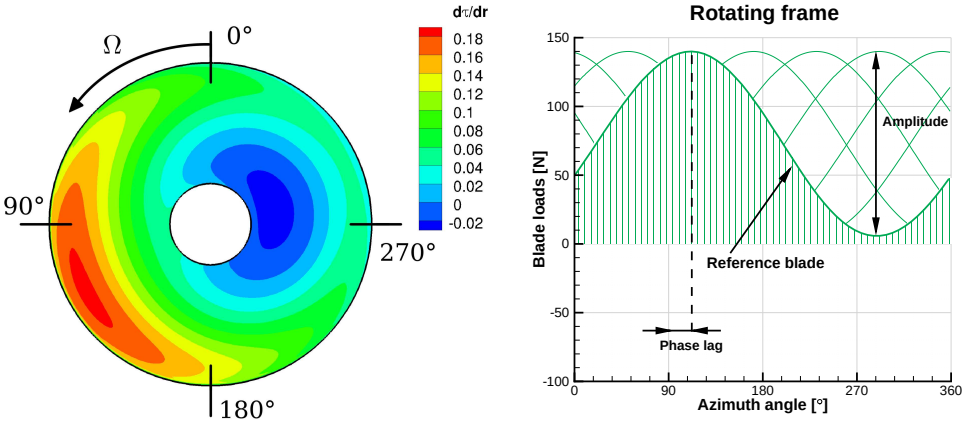


Figure 8: Geometrical explanation of 1P loads of a propeller under incidence α



(a) Blade sectional loads and coordinates. (b) In-plane blade loads in the rotating frame.

Figure 9: Blade circulation and in-plane loads along a cycle for a propeller in incidence. *elsA* simulation.

a certain amplitude and phase lag. Adding these forces in the fixed reference frame we obtain the propeller 1P loads. Thus, a link can be established between blade loads' amplitude and phase lag, and propeller 1P loads' amplitude and phase lag, respectively.

Therefore, to understand the physics behind 1P loads, the analysis is going to be done, not by the classical decomposition into a vertical and a side force, but by decomposing 1P loads into *modulus* and *phase lag* with respect to the 0° azimuth.

While 1P load modulus can be explained by the simple geometrical approach described before, 1P load phase lag is a more complex phenomenon. Several possible explanations have been put forward in literature, taking as starting point this phase lag between geometrical incidence and aerodynamic incidence:

1. *Distance between current blade and neighbor wakes.* Downward moving blades shed wakes with more vorticity than wakes shed from upward moving blades.

Due to the inclination of the wake, the blade at $\psi = 0°$ is closer to the wake shed by the downward moving blade than the blade at $\psi = 180°$. By the Biot-Savart's law, we can deduce that velocities induced on the first will be greater than on the latter, and so the blade at $\psi = 0°$ will generate less lift and drag than the one at $\psi = 180°$. Integrating all blades, it can be concluded that a net side force will appear in the direction of the downward moving blade [Ortun 2012].

2. *Unsteady blade motion and near wake effect.* As it has been explained before, when the propeller is placed at a given incidence, the airflow velocity seen by the blade and its geometrical angle of attack change during a cycle at 1/rev. The aerodynamic behavior of a lifting surface is not the same whether it is under steady or unsteady conditions: a hysteresis cycle appears for periodic movements of this kind (Fig. 10). These differences between steady and unsteady aerodynamic behaviors come from two sides: first, the relative velocity variations on the blade and, second, the effect of the unsteady vorticity shed in the wake.
   By analogy, we can extend this explanation to the case of rotating blades. Regardless of the induced velocities, each point of the blade will experience a different velocity vector, not only due to rotation, but also due to the fact that they are not placed at the same azimuth, because of pitch, sweep and dihedral angles. This fact is equivalent to the pitching motion of an airfoil, where the incident velocity varies along the chord.
   As the downward moving blade is put in incidence, the wake becomes more loaded in circulation. This circulation induces a velocity on the blade which tends to diminish the effective (or aerodynamic) incidence. This increase in induced velocities delays the maximum loading of the blade. For the upward moving blade, the same explanation is valid to explain the phase lag in the minimum blade loading.

3. *Dynamic stall.* It is a well-known but difficult to predict phenomenon in helicopter aerodynamics [Leishman 1989]. The dynamic stall appears commonly at high-speed forward flight conditions. In these cases, while the advancing blade might be under transonic speeds at low angles of attack, the retreating blade sees very low velocities at high angles of attack. This can induce the stall of important parts of the rotor blade.
   Propellers are more likely to experience another type of dynamic stall, more similar to the one experienced in delta wings [Jarrah 1989] (see Fig. 11). In the case of a propeller, the off-axis inflow is always relatively small compared with the axial component. This means that relative velocity variations along a cycle are not very important. However, as blades are swept for high-speed conditions and highly loaded, the stall can appear for the downward moving blade at high angles of attack. This stall, which takes the form of a leading edge vortex, can shift the maximum load and thus induce a certain phase lag in the propeller in-plane loads.

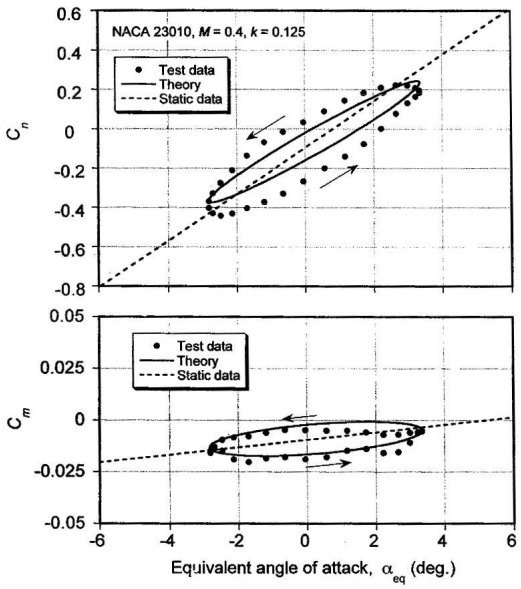


Figure 10: Comparison of theory and experiment for the lift and pitching moment coefficients in fully attached flow under oscillatory plunge forcing conditions at $M = 0.4$ (in [Leishman 2006])

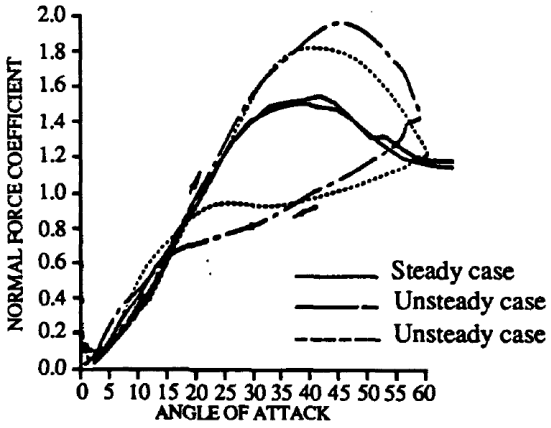


Figure 11: Unsteady lift of a delta wing (in [Jarrah 1989])

4. *Compressibility and evolution of shock wave effect.* Experimental and numerical studies on helicopter rotors in forward flight [Caradonna 1978, Chattot 1980] can explain this phenomenon. Analogously to what happens on the advancing blade of the rotor, where the development of shock waves is shifted with respect to relative Mach number, a propeller in high-speed conditions might develop also this kind of hysteresis cycle.

5. *Blade aeroelasticity* [Srivastava 1990]. There are two main contributions to blade deformations: the inertial effects and the airloads. These two phenomena tend mainly to untwist the blade. However, while inertial effects are constant along a cycle, airloads on a propeller in incidence are unsteady. Thus, as the deformation of the blade is not instantaneous with respect to the loads, a certain phase lag is susceptible to appear between the maximum load and the maximum blade deformation. This might have an impact on the phase lag of the propeller loads.

Other possible mechanisms may exist, such as laminar-turbulent transition, but to the author's knowledge, they have not been investigated and they are far beyond the objectives of the present study.

Methods for the Prediction of Aerodynamic Performance

An important number of methods have been developed during more than a hundred years for the prediction of propeller performance and 1P loads, presenting a wide dispersion in terms of type of approach, calculation costs, accuracy, and domain of application.
The research on propellers being directly linked to its use in industrial contexts, we can distinguish two main periods in the development of propeller prediction tools. The first period goes from the beginning of aviation to the 1950's, with the onset of turbojet technology and the decrease in interest on propellers. The second period of time goes from the 1970's, with the Middle-East oil crisis and the increase in fuel costs, to today.

During the first half of the century, propeller technologies developed steadily based mainly on numerous experimental tests. Numerical tools played a secondary role, giving some orders of magnitude for design phases or preparing experimental campaigns. A number of methods were developed for each specific application, yielding to a wide scope of approaches. Two main topics are of interest here: on one side, the prediction of propeller performance, and on the other side, the aircraft stability and aeroelastic issues due to propellers.
The first group of tools, focused on establishing the optimum blade load distribution for the ideal case of an isolated propeller under homogeneous air flows. On that cases, only the steady part of the problem was considered.
On the other hand, the research on handling qualities and aeroelasticity of propeller-driven aircraft tried to better understand the behavior of propellers in off-design

conditions. Empirical models or simulations of the unsteady blade loads were needed, which were limited by the available calculation capabilities.

The renaissance of propellers in the 1970's was mainly motivated by fuel costs. If the research in the first 50 years was pushed forward mainly by experimental capabilities, in this second period it has evolved rapidly to an equilibrium and even an hegemony of numerical tools over experimental data. Comprehensive multi-disciplinary tools are more and more common enabling to treat all the different domains of study in a single problem. Still, it is compulsory that researchers and engineers in the 21st century decide which of the multiple available methods will present the optimal accuracy-cost ratio in the considered problem.

Analytical Models for Propellers

Propeller performance prediction. First methods were mainly based on experimental data collected from marine or aeronautical propellers. Thanks to these data, semi-empirical expressions could be formulated very early in the 20th century. These expressions often gave a theoretical optimum that helped in the design of more efficient propellers.

In the marine propeller domain, the first and simplest method is the axial momentum theory proposed by Rankine [Rankine 1865]. This theory models the propeller by a disk of pressure discontinuity in an incompressible inviscid flow. The propeller induces only an axial velocity (i.e. no swirl), and it is calculated by application of the mass conservation law. Finally, the propeller performance is obtained from the momentum conservation law in the axial direction.
A first improvement to Rankine's theory was introduced by Froude [Froude 1878]: the general momentum theory, taking the effects of slipstream rotation into account. Only in recent studies, the momentum theory has been extended to consider compressibility effects [Vogeley 1951], arbitrary radial load distribution [Conway 1995] and highly-loaded conditions [Conway 1998].
These simple approaches are good enough to predict the overall performance of single propellers, but they fail at predicting the details of the airflow around the propeller. This comes from the fact that these theories do not consider essential elements in the problem, such as the finite number of blades or the viscous effects.

A second group of methods started with the blade element theory, also proposed by Froude [Froude 1889]. This theory decomposes the blade into finite-span sections along the pitch axis. Each section is modeled by its local airfoil data at a certain incidence and velocity. Thus, the propeller performance is obtained from the integration of the loads at each blade station.
The major drawback of this method was identified by Glauert, as it does not consider the slipstream effect on the incident velocity. Thus, Glauert proposed a theory coupling the blade element and the momentum theories [Glauert 1922]. The wake model introduces the global effect of the wake, but does not consider radial velocities due to the slipstream contraction. Moreover, they are always limited to lightly loaded propellers.

From a design standpoint, the research on propellers focused during those years on the analytical determination of the optimal circulation distribution along the blade, as it is the case for fixed wings with elliptic distribution of circulation. In the case of propellers, Betz [Betz 1927] proved that the optimal circulation distribution is such that the induced velocities on the wake far behind the propeller is independent of the radius, and thus the trailing vortex sheet may be considered as a rigid surface moving parallel to the propeller axis. Goldstein [Goldstein 1929] proposed an exact solution for these optimum propellers with a finite number of blades which would be later used by many other researchers until the development of the strip theory method [Lock 1945].
Theodorsen extended the optimum circulation distribution to the case of contra-rotating propellers, noting that only the mean value of interference velocities was considered [Theodorsen 1944].

Methods for predicting propeller 1P loads. Apart from performance prediction, the integration of propellers in the airframe has led very early to the development of a number of analysis tools to assess the propeller-airframe interference. With the increase in engine shaft power and propeller solidity, researches focused on the effect of propellers on the stability and control of aircraft. An important part of this effect is due to the aerodynamic forces and moments developed by the propeller under any deviation from uniform flight parallel to the thrust axis. The remaining part of the effect is due to the interference between the propeller slipstream and the airframe. Lanchester noticed very early that a propeller in yaw (or in incidence) develops an important side force (or vertical force) in the propeller plane [Lanchester 1917].

Investigations led rapidly to the development of the first theories in the 1920's and 1930's. They established semi-empirical models to predict the 1P load magnitude as a function of the performance of the propeller without incidence [Harris 1918, Glauert 1935]. Glauert proposed a widely used analytical expression of the in-plane force, by analogy with a fin, as a function of the incidence, the advance ratio, the power coefficient, and the thrust distribution along the blade. Meanwhile, a series of methods were proposed to take into account the wake induction effects [Pistolesi 1928, Misztal 1933] or the blade shape in the prediction of in-plane loads [Bairstow 1939]. In 1945, Ribner [Ribner 1945] established an expression of the in-plane force that accounted both for the blade shape and the induction velocities and applied this method to single- and dual-rotating propellers.

Propeller flutter has been pointed out very early as a series of unstable aeroelastic phenomena on aircraft that could have catastrophic consequences. First investigations on propeller aeroelastic instabilities revealed that isolated propellers present three types of propeller flutter [Theodorsen 1945]:

1. *Classical flutter*: Coupling between bending and torsion modes occurs when the cross-sectional angles of attack along the blade are smaller than stall angles. It is equivalent to fixed-wing flutter.

2. *Stall flutter*: Occurs when the cross-sectional angles of attack along significant parts of the blades are in the vicinity of the airfoil stall angle. The blade vibrations include mainly torsion components.

3. *Wake flutter*: Involves mainly torsional vibrations and occurs at small pitch angles and low advance ratios. The cascade effect of the returning wakes is important because of the low advance ratios.

Moreover, a fourth type of flutter can occur for the coupled airframe-propeller aeroelasticity, the so-called *whirl flutter*.
Several experimental campaigns were conducted in the 1950's on classical propellers and the 1970's on advanced turboprops to better understand flutter limits. In parallel, analytical and numerical tools were developed to reproduce these experimental limits and estimate them on future propeller installations. A famous method was developed by Reed [Reed 1966] for the prediction of whirl flutter. The mean value of the propeller loads is estimated by applying Ribner's model [Ribner 1945]. For the blade load flutter, a two-dimensional model for an oscillating rotary wing airfoil developed by Loewy [Loewy 1957] is also included. This wake modeling includes the cascade effect, i.e. the effect of vorticity shed by previous blades and/or previous revolutions. The harmonic approach in Loewy's model leads to a formulation identical in form to that of classical fixed-wing flutter (Theodorsen's theory [Theodorsen 1935]) but with a modified lift deficiency function ($C'(k)$) due to the cascade effect.

A number of other two-dimensional analytical wake models have been developed along the years for rotary wings under unsteady airflows. Similar to Loewy's model, Whitehead [Whitehead 1960] presented a model that was better adapted for propellers at high advance ratios. Smith [Smith 1985] included the compressibility effects to this model, and Jones and Moore [Jones 1976] replaced the wake vortex by a series of doublets for the compressible case.
The first analytical wake model including three-dimensional effects was developed by Miller [Miller 1964], but presented numerous limiting simplifications. Iosilevskii [Iosilevskii 1999] proposed a more detailed model, under the hypothesis of rigid wake and constant radial distribution of circulation but varying in time. Yoshpe [Yoshpe 1996] extended Iosilevskii's model to arbitrary circulation distributions. Finally, while previous models could only predict classical and wake flutter, Delamore *et al.* [Delamore-Sutcliffe 2006] studied the case of a blade that develops stall flutter. For that, nonlinear unsteady aerodynamic loads were modeled at blade cross-sections at incidences near stall.
Analytical models present the advantage of being efficient in modeling unsteady aerodynamic loads along oscillating blades. They also offer an insight into the complex phenomena and understanding of the influence of various parameters. Yet these models include simplifying assumptions that reduce their accuracy in many cases. On the other side, comprehensive numerical models offer a detailed description of the flow field.

Numerical Singularity Methods

At the demand of the US National Advisory Committee for Aeronautics, Prandtl published a paper in 1923 giving "a detailed treatise on the present condition of those applications of hydrodynamics which lead to the calculation of the forces acting on airplane wings and airship bodies" [Prandtl 1923]. The last section of that paper presented the application of the *lifting-line theory* to screw propellers. Here, the blade is modeled by a single bound vortex line of circulation Γ located at the quarter-chord line and shedding the vorticity to the wake at both tips, forming the well-known horseshoe vortex. Circulation is determined by the Biot-Savart law and by stating a tangency condition (no flow normal to the blade surface) at the control points on the blade. Once the circulation is known, the induced velocities and the lift are deduced from the Kutta-Joukowski theorem.
As it will be described hereafter (see *The Lifting-Line Theory* section), a number of studies have extended this theory to consider (1) a radial variation of the load, (2) two-dimensional and compressibility effects, (3) the curvature of the lifting-line, and (4) the unsteady lifting-line theory.

A widespread extension to the lifting-line theory is the *Vortex-Lattice method* (VLM), developed by Falkner in 1943 [Falkner 1943] for the lift prediction of wings of arbitrary shapes. Instead of using only one horseshoe vortex or a line of vortices, the VLM models the wing by a lattice of vortices located at different spanwise and chordwise positions. To calculate the circulation of N vortices, the tangency condition is again applied on N control points distributed on the blade. This approach implies the inversion of a filled $N \times N$ coefficient matrix, which is the main drawback of this type of methods.
Extensions to the original VLM exist to include compressibility, viscous losses, the thickness of the blades, and the effect of the spinner [Schulten 1996].

Rigorously, the lifting-line theory and the vortex-lattice method, based on the thin-airfoil theory, apply only to thin airfoils at small angles of attack. When considering thick airfoils it is more coherent to consider the *Vortex Panel method* (see for example [Hess 1990]). In this method, the blade is divided in quadrilateral facets with a certain vorticity. Moreover, the effect of the wake is modeled by a lattice of horseshoe vortices. Again, the solution is found by applying the Biot-Savart law and stating a tangency condition at the control points.

The three methods described before (lifting-line, vortex-lattice, and vortex panel methods) have been behind the majority of aerodynamic calculation tools for many decades, and are still useful for first design and optimization phases. During this work, the aerodynamic part of the comprehensive code that has been chosen for propeller and open rotor simulations lies on the lifting-line theory. Therefore, a special attention will be paid hereafter to the different formulations of the lifting-line theory.

Potential, Euler and RANS Methods

From the 1950's to the 1970's, very few studies about propellers appeared, due to the decreasing interest in propellers and the emergence of turbofan technology. In the mid-1970's NASA launched the Advanced Turboprop (ATP) project as one component of the Aircraft Energy Efficiency Program. In parallel with wind tunnel and flight test campaigns [Groeneweg 1988], the ATP project developed a wide variety of simulation codes for single-rotating and counter-rotating propellers –namely: steady lifting-line codes [Egolf 1979, Lesieutre 1985], steady transonic potential methods [Jou 1982], steady and unsteady solvers for compressible Euler equations [Denton 1980, Yamamoto 1986, Celestina 1986, Whitfield 1987], and steady and unsteady solvers for Navier-Stokes equations (still under development at the end of ATP program).

Potential flow solutions about a single-rotating propeller were obtained for the first time by Jou [Jou 1982]. In order to account for three-dimensional compressibility effects, the full-potential equation in the rotating frame was solved in a body-fitted grid for a single-blade passage computational domain. Two years later, a similar methodology was developed by Collercandy and Luu [Collercandy 1984, Luu 1984].

First three-dimensional steady Euler computations were computed by Bober *et al.* for an isolated propeller under high-speed conditions [Bober 1983]. The computational domain could be reduced to a single blade passage channel using periodicity boundary conditions, as it considered the case of a propeller without incidence. The unsteady Euler equations in cylindrical coordinate system were marched in time until the steady state was obtained. Although numerical results for power coefficient and swirl were higher than experimental results, their variation with blade angle matched very well with data. These offsets in power coefficient and swirl were attributed to viscous effects. Subsequent studies were conducted by Barton and Yoon [Barton 1986] and Yamamoto *et al.* [Yamamoto 1986]. None of these studies considered the propeller under an angle of attack.
First attempts of considering incidence effects were conducted by Heidelberg and Clark [Heidelberg 1986] using Denton's three-dimensional Euler code [Denton 1980] in a quasi-steady fashion by including inflow swirl. However, these simulations did not handle a variation in inflow angle across a blade passage.

Euler methods were extended to contra-rotating propellers by Celestina *et al.* [Celestina 1986] by using Adamczyk's average condition used in multistage turbomachinery problems [Adamczyk 1986] and called the *mixing-plane* condition. Applied to the matching grid between both propellers, this condition simulates the inviscid time-averaged flow from one rotor to another, allowing to perform steady Euler computations at a reduced computational time. Similar simulations were conducted by Wong [Wong 1988] and Nicoud [Nicoud 1989], also using the mixing-plane boundary condition.
Whitfield was the first to perform three-dimensional time-dependent Euler simulations on dynamic blocked grids using a finite-volume, flux-split, upwind, implicit

scheme with the specific application being to single-rotating and counter-rotating propellers in transonic flow [Whitfield 1987]. The computational domain includes only one blade passage for the front rotor and one for the aft rotor and periodicity conditions are used in the side boundaries. In the block interface located between the blade rows, the grid is constructed so that grid lines are uniformly distributed in the circumferential direction. Therefore, at each time-step, each block is moved such that the grid lines which cross the interface join. Hence, the method is only valid for contra-rotating propellers with the same front and aft blade counts.

First unsteady Euler simulations on an advanced propeller (SR7L) in incidence were performed by Nallasamy [Nallasamy 1994]. In this case, all the blades must be included in the computational domain as no blade-to-blade periodicity exists. Moreover, a time-marched simulation is necessary to account for the unsteady inflow variation in the relative frame due to the propeller angle of attack. The paper focuses on compressibility effects on blade pressures and compares Euler simulations to flight test data. Acceptable mismatches in unsteady pressure on the blade skin are obtained. A relative phase lag in the waveforms is observed at all Mach numbers, and is attributed to the effects of propeller installation on the aircraft (in flight tests). Moreover, some nonlinear variations in waveforms are not captured by this inviscid method.

Unsteady Euler simulations on an installed propeller have been performed by Bousquet *et al.* [Bousquet 2003] some years later. It has shown the impact of unsteady installation effects on blade loading by comparing isolated and installed experimental data with the respective unsteady simulations.

Meanwhile, improvements in computational capabilities have enabled the use of solvers using the Reynolds-Averaged Navier-Stokes equations in the study of propeller and open rotor aerodynamics. The main assets of these methods are the viscosity simulation and the turbulence models.

Comparisons of simulations with experimental data of in-plane loads have been performed [Bousquet 2000, Bousquet 2003, Ortun 2012]. These studies have assessed different methodologies for the prediction of in-plane loads and moments: steady lifting-line codes, time-marching lifting-line codes, CFD Euler solvers, and CFD uRANS solvers. They have brought to light, on one hand, the difficulty to precisely analyze the physics behind these 1P loads, and in particular behind their direction and, on the other hand, the possibility to predict with a certain degree of accuracy the 1P load magnitude even with simple lifting-line methods. However, the direction of these in-plane loads can only be predicted with a certain degree of accuracy using time-marched simulations [Bousquet 2003].

Recently, Stuermer *et al.* have analyzed 1P loads on isolated contra-rotating propellers at low and high-speed conditions using uRANS computations [Stuermer 2008]. An interesting code-to-code assessment and analysis of 1P load mechanisms has been conducted by François *et al.* [François 2013b]. Moreover, numerical simulations to study installation effects on open rotors have been conducted by Laban *et al.* [Laban 2010] and Stuermer *et al.* [Stuermer 2011].

Several comparisons between uRANS simulations and wind tunnel tests have been

performed during last years [Zachariadis 2011, Stuermer 2012, Boisard 2012]. However, these comparisons focused on numerical parameters in mesh and boundary conditions, on flow field around propellers, and on near and far field acoustics, respectively. The next step would be a systematic comparison of the 1P loads between experimental data and simulations.

Eulerian/Lagrangian Coupling

The interactions between front rotor wakes and rear rotor blades can play a vital role in open rotor performance and noise predictions. As no moderate-cost methodologies exist to simulate these interactions, studies should be conducted to discover new methodologies and assess their capability to capture the interaction between wakes and blades. This blade-vortex interaction is a largely-studied problem in modern rotorcraft simulations. The approaches that are typically used to capture this phenomenon can be divided in two families: the Eulerian methods, where a spatial distribution of the flow variables is provided in a fixed reference frame, and the Lagrangian methods, where the reference frame follows the streamlines of the particles.

On one side, Eulerian methods are generally used to compute the unsteady flow field around the propellers with a particular ability to simulate the near-body field. They present however an important weakness: their dissipative behavior. Mesh refinement is the simplest solution to avoid dissipation but usually it implies unaffordable CPU costs to reach the industrial accuracy requirements. Different approaches can be used in the simulation of the Blade-Vortex Interactions to capture the vortex flow within reasonable CPU costs: adaptive mesh refinement [Dietz 2007], high-order schemes [Boyd 2009, Renaud 2008] or vorticity confinement strategies [Wenren 2001, Murayama 2001, Costes 2012].

On the other side, Lagrangian methods have the ability to preserve the vorticity source terms in the flow field either by solving the vorticity transport equation [Zhao 2012] or by convecting the vorticity density itself in the case of potential wake models [Toulmay 1986, Michéa 1992b, Le Bouar-Coppens 2004]. Unfortunately, these methods are usually inaccurate in predicting three-dimensional, viscosity, and compressibility effects in the near-body field, mainly when using blade geometry simplifications such as the lifting-line method.

In order to handle with the complexity of the problem, rotorcraft comprehensive codes have classically used low-order aerodynamic models based on lifting-line theory and two-dimensional airfoil tables. Moreover, these codes often include a structure code (CSD solver) to account for the blade deformation. Indeed, for rotorcraft blades that are very flexible and with important aspect ratios, their deformations impact significantly the aerodynamic loads and moments.
Although, airload predictions using these fast low-fidelity aerodynamic methods often show significant shortcomings. Two main unsolved problems in rotor airloads prediction have been identified [Bousman 1999]: (1) the azimuthal phase lag of advancing blade negative lift in high-speed flight and (2) the underprediction of

blade pitching moments over the entire speed range.

These two deficiencies have motivated the development of a number of codes based on Eulerian/Lagrangian approaches in order to benefit from the advantages of each method: on one side, the Eulerian methods for the near-body flow field and, on the other side, the Lagrangian methods for the convection of the wake in the outer domain.
The coupling between CFD and comprehensive codes has been accomplished in two ways. In loose (weak) coupling methodology, the information between CFD and the comprehensive code is transferred on a per revolution, periodic basis. In the tight (strong) coupling strategy, both codes are coupled at every time step and integrated in parallel.

Weak coupling strategies. A well-known loose coupling strategy was developed by Tung *et al.* [Tung 1984] using a transonic small disturbance code. Other TSD [Kim 1991] and full-potential methods [Strawn 1989, Strawn 1991, Beaumier 1994] were later coupled with comprehensive codes. These methods require the inflow angles from the comprehensive codes in order to consider structural deformation and the influence of the wake outside the near-body CFD domain, usually limited to some chords away. Issues were encountered with convergence and complex boundary conditions.

With the increase in high-performance computation capabilities, it has become possible to use Euler [Altmikus 2002, Servera 2000] and Navier-Stokes solvers in CFD/CSD coupling. Solving the full domain in the Euler or Navier-Stokes solver avoids using a potential wake model in the prediction of the inflow angles. However, this implies an important increase in mesh size and complexity.

On the contrary, Berkman *et al.* [Berkman 1997] proposed a method coupling a Navier-Stokes domain near the blade and a full potential outer domain, including a Lagrangian wake model to avoid its diffusion. Using this strategy, Min *et al.* [Min 2010] showed an important sensitivity of the BVI prediction to the mesh refinement and the trailing tip-vortex release point. Similarly, Sitaraman *et al.* [Sitaraman 2003, Datta 2004] solved only the near-field of a single blade and used a free-wake model to compute the induced velocities at all the grid points.

Another approach proposed by Jobard *et al.* [Jobard 1996] consists of an interface between MESIR wake model and the full-potential code FP3D. In this case, the velocities induced by the free-wake model are considered as a perturbation on the blade surface.

Postdam *et al.* [Potsdam 2004] proposed a method that couples the OVERFLOW-D CFD code and the CAMRAD-II rotorcraft computational structural dynamics (CSD) code to calculate helicopter rotor airloads across a range of flight conditions. An iterative loose (weak) coupling methodology is used to couple the CFD and CSD codes on a per revolution, periodic basis. In this strategy, the whole aerodynamic problem is calculated by the RANS solver and thus no wake model is needed in the farfield. CFD/CSD coupled simulations gave very good pre-

dictions in terms of normal loads and pitching moments when compared to full-CFD simulations and experimental data for a complex rotor geometry. However, the rotor performance was still not an objective in the study.
Another similar method is used at DLR by Pahlke *et al.* [Pahlke 2005] which couples the FLOWer CFD solver with S4 comprehensive code. 4-bladed rotors are meshed by the chimera approach with a cartesian background mesh. A 10 to 15° advancing side phase lag is obtained, but normal force magnitudes are well predicted. However, pitching moment magnitudes and shapes are not satisfactory.

Recently, a Viscous Vortex Particle Model (VVPM) has been coupled with a CFD model in a CSD/CFD coupling context [Zhao 2012]. The comparisons between full-CFD computations and the coupled strategy have given encouraging results, but the gain in CPU costs is limited due to the cost of the VVPM model.

Rodriguez and Mayeur [Rodriguez 2012] present a weak coupling strategy between the *elsA* CFD solver and the HOST comprehensive code. Only one blade is considered in the CFD solver with a reduced near-body mesh, whereas all the wakes and the other blades are simulated in the potential wake model. A low-order, periodic, free-wake model (MESIR) is used to predict the velocities induced by the wakes and the other blades on the CFD problem. This hybrid methodology is compared to the full-CFD simulations and to experimental data for an isolated rotor in flight conditions presenting transonic phenomena and for a descending flight with BVI events. The hybrid method predictions are very close to full-CFD computations, but important shortcomings are observed with respect to experimental data, mainly in terms of pitching moment coefficients.

Strong/Tight coupling applied to rotorcraft. Two main drawbacks have arisen in the use of tight coupling procedures in helicopter rotor simulations: on one side, the increase in computational costs due to massive communication between codes and, on the other side, the difficulty to trim a rotor in non-periodic time-marching simulations. For example Pomin and Wagner used overset methods and deformable grids in a tight coupling procedure but avoided the trim issue by fixing control angles [Pomin 2001].

In the case of propeller simulations the trim is simpler than in helicopters. Only a constant blade pitch trim is considered in order to obtain the mean value of the thrust. Nevertheless, this remains a problem to be assessed in tight coupled simulations, where the mean value of the thrust is not easy to obtain or may not exist in more general unsteady simulations.

Although strong coupling is more rigorous, an efficient communication between codes is needed to avoid losses in computational performance. On the other hand, weak coupling allows a modular approach and communication through files. Nevertheless, weak coupling is limited to per revolution periodic problems.
A loose and a tight coupling methods were successfully applied within the German-French research project CHANCE (Complete Helicopter AdvaNced Computational Environment) [Pahlke 2000]. Altmikus *et al.* [Altmikus 2002] presented a compar-

ison between these two approaches in a coupling strategy between HOST and two CFD codes in Euler mode, FLOWer and WAVES. A 2.5 times increase in computational costs was indicated for the strong coupling computations, while yielding similar results to weak coupling computations for high-speed forward flight conditions. This study is an important benchmark in the comparison of both approaches using the same codes.

The Lifting-Line Theory

In this section, a general solution of the incompressible potential flow problem is detailed first, in order to introduce one of the derived theories, known as the *lifting-line*. The main milestones in the development of lifting-line theories during the 20th century are then described. Two main approaches are at the onset of this theory: first, the Prandtl's integro-differential equation and iterative solution approach, and then Van Dyke's approach based on the matched asymptotic expansions technique. From the presentation of these theories to today, many studies have been conducted to extend them to a larger scope of problems, mainly focused on considering general wing planforms and unsteady airflows.

Fundamentals of Inviscid, Incompressible Flow

Circulation definition. The *vorticity* of a fluid is defined as follows:

$$\vec{\zeta} = \nabla \wedge \vec{v} = \left(\frac{\partial v_z}{\partial y} - \frac{\partial v_y}{\partial z}, \frac{\partial v_x}{\partial z} - \frac{\partial v_z}{\partial x}, \frac{\partial v_y}{\partial x} - \frac{\partial v_x}{\partial y} \right) \tag{1}$$

where $\vec{v} = (v_x, v_y, v_z)$ is the airflow velocity, in this case in Cartesian coordinates.

Considering an open surface $\mathcal{S}$ with a curve C at its boundary, by the Stokes' theorem it can be found that:

$$\int_{\mathcal{S}} (\nabla \wedge \vec{v}).\vec{n} d\mathcal{S} = \int_{\mathcal{S}} \vec{\zeta}.\vec{n} d\mathcal{S} = \oint_{C} \vec{v}.d\vec{l} \equiv \Gamma \tag{2}$$

where the integral on the right-hand side is called the circulation and denoted by Γ. Hence the circulation is somehow tied to the rotation of the fluid.

Following Helmholtz's theorem of the circulation conservation, it can be stated for a tube of vorticity that:

$$\Gamma = \int_{\mathcal{S}_1} \vec{\zeta}.\vec{n}_v d\mathcal{S} = \int_{\mathcal{S}_2} \vec{\zeta}.\vec{n}_v d\mathcal{S} = \text{const.} \tag{3}$$

which expresses the spatial conservation of the vorticity along the tube (see Fig. 12).

The flowfield of a two-dimensional vortex is commonly modeled by assuming a rigid cylinder of radius R rotating in a viscous fluid at a constant angular velocity ω_y (see Fig. 13). It results in a flow with circular streamlines varying only in radial direction:

$$v_r = 0 \qquad \text{and} \qquad v_\theta = v_\theta(r) \tag{4}$$

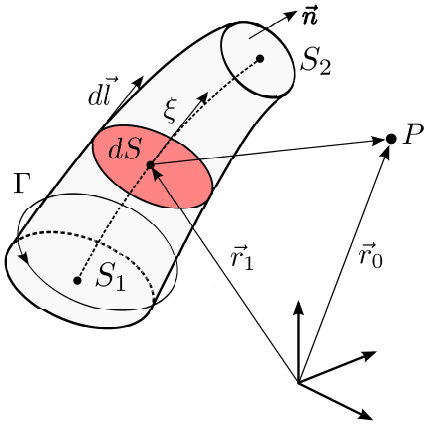


Figure 12: Vorticity conservation and velocity at point P induced by a vortex segment

From the density and momentum conservation equations it can be finally deduced:

$$v_\theta = -\frac{\omega_y R^2}{r} \tag{5}$$

Thus, for any circle of radius $r > R$, the circulation is constant and can be calculated as:

$$\Gamma = \int_{2\pi}^{0} v_\theta r d\theta = 2\omega_y \pi R^2 \tag{6}$$

and thus, the tangential velocity can be rewritten as:

$$v_\theta = -\frac{\Gamma}{2\pi r} \tag{7}$$

Biot-Savart's law. To calculate the velocity induced by a volume V containing a distribution of vorticity ζ on a point r_0 (see Fig. 12) Biot-Savart's law can be used as follows:

$$\vec{v} = \frac{1}{4\pi} \int_V \frac{\vec{\zeta} \wedge (\vec{r}_0 - \vec{r}_1)}{|\vec{r}_0 - \vec{r}_1|^3} dV \tag{8}$$

For the case of a vorticity filament of cross-sectional area dS, Biot-Savart's law takes the form:

$$\vec{v} = \frac{\Gamma}{4\pi} \int_{\mathcal{L}} \frac{d\vec{l} \wedge (\vec{r}_0 - \vec{r}_1)}{|\vec{r}_0 - \vec{r}_1|^3} \tag{9}$$

where the circulation Γ is considered to be constant along the filament $\mathcal{L}$. The *vortex filament* with constant circulation can be defined as the limiting case of a zero cross-sectional area vortex, with infinite concentrated vorticity.

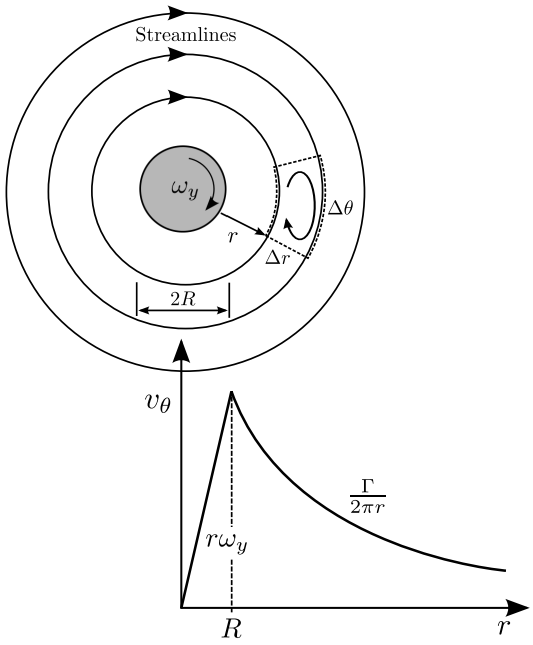


Figure 13: Vortex modeled as the flowfield around a cylindrical core rotating as a rigid body

General Solution of the Incompressible Potential Flow Equations

Statement of the potential flow problem. Most of engineering problems using aerodynamics require the solution in a fluid domain Ω containing a solid body and additional boundaries that define the outer flow boundary. If the flow is considered to be incompressible and irrotational, the continuity equation reduces to Laplace's equation:

$$\nabla^2\Phi = 0 \tag{10}$$

The solid surface of the body imposes that in the body-fixed reference frame the velocity component normal to the body's surface must be zero:

$$\nabla\Phi.\vec{n} = 0 \tag{11}$$

where $\vec{n}$ is the vector normal to the body's surface. Moreover, the disturbance created by the solid body must decay far from the body ($r \to \infty$):

$$\lim_{r\to\infty}(\nabla\Phi - \vec{v}) = 0 \tag{12}$$

where $\vec{r} = (x, y, z)$ and $\vec{v}$ is the velocity at infinity in the body-fixed reference frame.

The general solution, based on Green's identity. The scheme in Fig. 14 describes the considered mathematical problem. Laplace's equation for the velocity potential must be solved around an arbitrary volume in a body with boundary Σ_B in the volume Ω, with the outer boundary Σ_∞. The boundary conditions in Eqs. 11

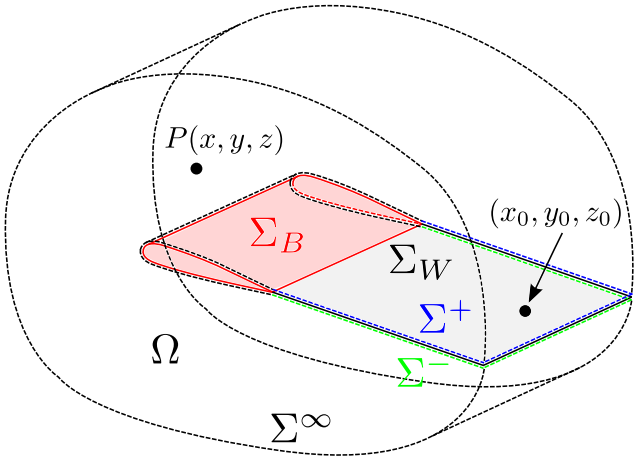


Figure 14: The wing and the domain of integration

and 12 apply to Σ_B and Σ_∞, respectively. The normal vector $\vec{n}$ always points outside the studied volume Ω.

One of Green's identity apply the divergence theorem to the vector $\Phi_1 \nabla \Phi_2 - \Phi_2 \nabla \Phi_1$, to obtain:

$$\int_\Sigma (\Phi_1 \nabla \Phi_2 - \Phi_2 \nabla \Phi_1).\vec{n} d\Sigma = \int_\Omega (\Phi_1 \nabla^2 \Phi_2 - \Phi_2 \nabla^2 \Phi_1) d\Omega \tag{13}$$

where the surface integral is taken over all the boundaries Σ, including a wake model Σ_W, that can account for a discontinuity in the velocity potential or the velocity. Thus, $\Sigma = \Sigma_B + \Sigma_W + \Sigma_\infty$.

Φ_1 and Φ_2 must be solution of Laplace's equation. Let us set: $\Phi_1 = 1/r$ and $\Phi_2 = \Phi$, where Φ is the velocity potential in the volume Ω and r is the distance from a point $P(x, y, z)$, as shown in Fig. 14.

In the case where the point P is outside the domain Ω both Φ_1 and Φ_2 satisfy Laplace's equation and Eq. 13 becomes:

$$\int_\Sigma \left(\frac{1}{r} \nabla \Phi - \Phi \nabla \frac{1}{r} \right) .\vec{n} d\Sigma = 0 \tag{14}$$

On the other hand, when the point P is inside the domain Ω, Φ_1 becomes singular when $r \to 0$. Thus, the point P must be excluded from the domain of integration and it is surrounded by a sphere Σ_ε of radius ε. Equation 13 becomes:

$$\int_{\Sigma + \Sigma_\varepsilon} \left(\frac{1}{r} \nabla \Phi - \Phi \nabla \frac{1}{r} \right) .\vec{n} d\Sigma = 0 \tag{15}$$

In the spherical coordinate system at P, $\vec{n} = -\vec{e}_r$, $\vec{n}.\nabla\Phi = \partial\Phi/\partial r$, and $\nabla(1/r) = -1/r^2 \vec{e}_r$. Thus yielding:

$$-\int_{\Sigma_\varepsilon} \left(\frac{1}{r} \frac{\partial \Phi}{\partial r} + \frac{\Phi}{r^2} \right) d\Sigma + \int_\Sigma \left(\frac{1}{r} \nabla \Phi - \Phi \nabla \frac{1}{r} \right) .\vec{n} d\Sigma = 0 \tag{16}$$

On the sphere surrounding P and for $\varepsilon \to 0$, it can be assumed that $(\partial\Phi/\partial r)_{\Sigma_\varepsilon} \to 0$. Thus, the first term in the first integral vanishes, while the second term yields:

$$-\int_{\Sigma_\varepsilon} \frac{\Phi}{r^2} d\Sigma = -4\pi\Phi(P) \tag{17}$$

and Eq. 16 becomes:

$$\Phi(P) = \frac{1}{4\pi}\int_{\Sigma}\left(\frac{1}{r}\nabla\Phi - \Phi\nabla\frac{1}{r}\right).\vec{n}d\Sigma \tag{18}$$

This equation gives the potential at any point P in the domain Ω as a function of Φ and $\partial\Phi/\partial n$ on the boundaries Σ.

The *internal potential* Φ_i is defined for describing the flow inside the body's volume Ω_B. As the point P in Ω is outside the domain Ω_B, the Eq. 14 yields:

$$\int_{\Sigma_B}\left(\frac{1}{r}\nabla\Phi_i - \Phi_i\nabla\frac{1}{r}\right).\vec{n}d\Sigma_B = 0 \tag{19}$$

This expression can be added to Eq. 18 in order to include the effect of the inner potential on the global solution:

$$\begin{aligned}\Phi(P) = & \frac{1}{4\pi}\int_{\Sigma_B}\left[\frac{1}{r}\nabla(\Phi-\Phi_i) - (\Phi-\Phi_i)\nabla\frac{1}{r}\right].\vec{n}d\Sigma \\ & -\frac{1}{4\pi}\int_{\Sigma_W+\Sigma_\infty}\left(\frac{1}{r}\nabla\Phi - \Phi\nabla\frac{1}{r}\right).\vec{n}d\Sigma\end{aligned} \tag{20}$$

Far from the solid body, the contribution of surface Σ_∞ on the potential can be defined as a constant $\Phi_\infty(P)$ in an inertial reference system of a body moving in a steady flow. Thus, the previous equation becomes:

$$\begin{aligned}\Phi(P) = & \frac{1}{4\pi}\int_{\Sigma_B}\left[\frac{1}{r}\nabla(\Phi-\Phi_i) - (\Phi-\Phi_i)\nabla\frac{1}{r}\right].\vec{n}d\Sigma \\ & -\frac{1}{4\pi}\int_{\Sigma_W}\Phi\vec{n}.\nabla\frac{1}{r}d\Sigma + \Phi_\infty(P)\end{aligned} \tag{21}$$

Again, an expression of $\Phi(P)$ as a function of Φ and $\partial\Phi/\partial n$ on the boundaries is obtained. The problem is reduced to determining the value of these quantities on the boundaries. For a segment on Σ_B, the *doublet* (μ) and the *source* (σ) elements can be defined as follows:

$$-\mu = \Phi - \Phi_i \qquad \text{and} \qquad -\sigma = \frac{\partial\Phi}{\partial n} - \frac{\partial\Phi_i}{\partial n} \tag{22}$$

Thus, Eq. 21 can be reformulated as:

$$\Phi(P) = \frac{1}{4\pi}\int_{\Sigma_B}\left[\frac{\sigma}{r} - \mu\frac{\partial}{\partial n}\left(\frac{1}{r}\right)\right]d\Sigma - \frac{1}{4\pi}\int_{\Sigma_W}\mu\frac{\partial}{\partial n}\left(\frac{1}{r}\right)d\Sigma + \Phi_\infty(P) \tag{23}$$

where μ in the integral over Σ_W is the potential difference between the upper and the lower surface of the wake surfaces. Notice also that $\vec{n}.\nabla$ has been replaced by $\partial/\partial n$, where $\vec{n}$ is the local normal to the surface and in the sense of the doublet.

Notice that the effect of doublets and sources decay far from the body and thus automatically satisfy the boundary condition at surface Σ_∞. The solution of the problem is to be found by determining the strength of the distribution of doublets and sources. Yet the choice of a particular combination of singularities is not imposed by Eq. 23. Thus, the choice of the doublet-source combination is made depending on the physics of the problem. Two types of extreme cases can be considered, were only one kind of singularity is considered:

- *Doublet distribution*: the source term vanishes on Σ_B if the following boundary condition is imposed: $\partial\Phi_i/\partial n = \partial\Phi/\partial n$. This is one of the formulations to solve lifting-surface problems.
- *Source distribution*: the doublet term vanishes on Σ_B if the following boundary condition is imposed: $\Phi_i = \Phi$. This is the formulation to solve volume or thickness effects.

A general approach to the solution of incompressible potential flow problems has been presented here. It has been shown that the solution of Laplace's equation ($\nabla^2\Phi = 0$) can be found by distributing elementary solutions (sources and doublets) on the boundaries Σ_B and Σ_W of the volume of interest Ω. However, when $r \to 0$, the velocity becomes singular, and therefore these basic elements are called *singular solutions* of Laplace's equation. These basic solutions are integrated over any surface Σ containing these singularities in order to obtain the general solution.

With this approach, the solution of the fluid dynamic problem can be reduced to finding the appropriate singularity distribution over some of the boundaries, in order to fullfil the boundary condition in Eq. 11. Two possible approaches exist to solve this boundary condition, whether the potential is specified in the boundary conditions (Dirichlet problem), or the zero normal flow is specified in the boundary conditions (Neumann problem).

Basic solution: Point doublet. The second basic solution introduced in Eq. 23 is the doublet. The velocity potential due to a doublet placed at (x_0, y_0, z_0) is:

$$\Phi(x,y,z) = \frac{\mu}{4\pi}\vec{n}.\nabla\left(\frac{1}{|\vec{r}-\vec{r}_0|}\right) = \frac{\mu}{4\pi}\frac{\partial}{\partial n}\left(\frac{1}{|\vec{r}-\vec{r}_0|}\right) \tag{24}$$

The dot product $\vec{n}.\nabla(1/r)$ shows the directional property of doublets. Thus, three elements can be defined in Cartesian coordinates, depending on the derivative direction. If a z-directional doublet is considered, the previous equation yields:

$$\Phi(x,y,z) = \frac{-\mu}{4\pi}\frac{z-z_0}{[(x-x_0)^2+(y-y_0)^2+(z-z_0)^2]^{3/2}} \tag{25}$$

Finally, the velocity potential generated by a distribution of z-directional doublets on a surface Σ is:

$$\Phi(x,y,z) = \frac{-1}{4\pi}\int_\Sigma \frac{\mu(x_0,y_0,z_0).(z-z_0)}{[(x-x_0)^2+(y-y_0)^2+(z-z_0)^2]^{3/2}}d\Sigma \tag{26}$$

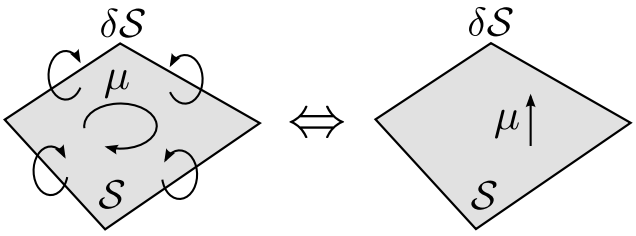


Figure 15: Hess equivalence between a surface doublet distribution (right), and a combination of surface vortex distribution and vortex filaments (left).

Basic solution: Vortex. The general solution of the Eq. 23 consists of source and doublet distributions only. However, other solutions to Laplace's equation exist, based on vortex singularity distributions.

Hess proved the equivalence between a surface distribution of doublets, and a surface distribution of vortex together with vortex filaments (see Fig. 15) [Hess 1972]. Therefore, the induced velocities in both formulations can be written as follows:

$$\begin{aligned}\vec{v} &= \frac{-1}{4\pi}\iint_{\mathcal{S}} \mu\nabla\left(\frac{\vec{n}.\vec{r}}{r^3}\right)d\mathcal{S} \\ &= \frac{1}{4\pi}\oint_{\partial\mathcal{S}} \mu\frac{d\vec{l}\wedge\vec{r}}{r^3} - \frac{1}{4\pi}\iint_{\mathcal{S}}\frac{(\vec{n}\wedge\nabla\mu)\wedge\vec{r}}{r^3}d\mathcal{S}\end{aligned} \tag{27}$$

Small Disturbance Flow over Three-Dimensional Wings

The study of the airflow around a simplified finite wing is presented and it is showed how thanks to the hypothesis of an incompressible, irrotational and perfect fluid the three-dimensional problem can be reduced to a system of equations to be solved only on the surface of the wing.

The formulation of the problem. The problem of a finite wing in an orthonormal coordinate system is considered. The wing surface is considered to be flat and contained in the $x-y$ plane. Each wing section is defined by a span position, y, by a chord, $c(y)$, and by a displacement of the quarter-chord line in x, $l(y)$ (see Fig. 16).

The freestream velocity is constant, $U_\infty\vec{i}$. Thus, the local airfoil incidence, $\alpha(y)$, is defined as the angle between the zero-lift incidence of the airfoil and the upstream velocity vector.

A vortex sheet is then formed downstream the wing as a consequence of the confluence of the suction and the pressure side boundary layers at the trailing edge. The problem to solve is to determine the velocity circulation at each wing section, Σ, as shown in Fig. 17. The velocity circulation on an airfoil is defined as follows:

$$\Gamma(y) = \oint_{\delta\Sigma}\vec{U}(P)\mathrm{d}\vec{l}_P \tag{28}$$

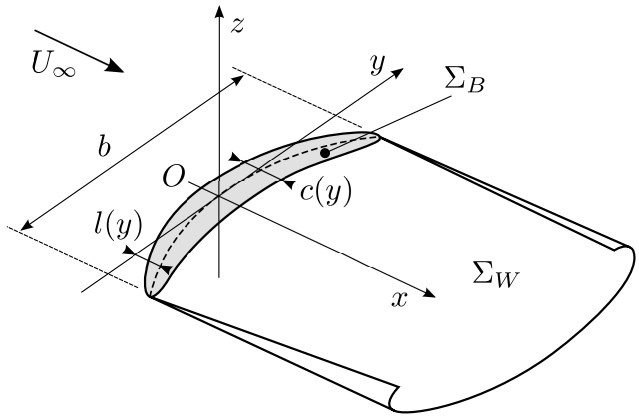


Figure 16: The wing and its wake.

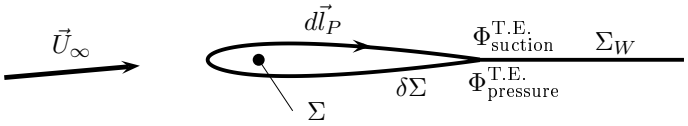


Figure 17: A blade cross-section Σ and its two-dimensional wake Σ_W.

Hypothesis and models. A perfect, incompressible and irrotational fluid is considered all over the three-dimensional domain, except in the wing and the wake. The wake is then modeled by a surface (Σ_W) of tangential velocity discontinuity, starting from the trailing edge and propagating downstream to infinity. It is supposed that the wake remains almost flat and in the vicinity of the $x-y$ plane. In this case, the circulation around the Σ section can be calculated as follows:

$$\Gamma(y) = \iint_{\Sigma} \vec{\nabla} \wedge \vec{U} \mathrm{d}\vec{l}_P \tag{29}$$

Then the circulation represents the rotation of the fluid due to the presence of the wing [Chassaing 2000]. For a potential airflow, a velocity potential Φ exists in the whole volume and is defined as $\vec{v} = \vec{\nabla}\Phi$. In the case of a potential airflow and following the notation introduced in Fig. 17, the circulation around the Σ section is:

$$\Gamma(y) = \Phi^{\text{TE}}_{\text{suction}} - \Phi^{\text{TE}}_{\text{pressure}} \tag{30}$$

where $\Phi^{\text{TE}}_{\text{suction}}$ and $\Phi^{\text{TE}}_{\text{pressure}}$ are the velocity potentials at the pressure and suction side of the airfoil trailing edge.

Once the circulation $\Gamma(y)$ on each wing section has been calculated, the Kutta-Joukowski theorem can be used to calculate the airfoil lift $L'(y)$, as follows:

$$L'(y) = -\rho_\infty U_\infty \Gamma(y) \tag{31}$$

where ρ_∞ is the freestream density and U_∞ is the freestream velocity.

Zero-thickness wing in incidence. Steady case. A zero-thickness flat wing and wake are now considered, and outer boundary conditions are considered to be far from the wing and the wake. In this case, only z-directional doublet singularities distributed along the wing and the wake are needed to satisfy boundary conditions (Eqs. 11 and 12). The intensity of the doublet distribution is given by: $-\mu = \Phi^+ - \Phi^-$, where Φ^+ and Φ^- are the velocity potentials in the upper surface Σ^+ and the lower surface Σ^- of the wake, respectively.

Thus, Eq. 26 can be written as:

$$\Phi(x,y,z) = \frac{-1}{4\pi}\int_{\Sigma_B+\Sigma_W} \frac{\mu(x_0,y_0,z_0).(z-z_0)}{|\vec{r}|^3} d\Sigma \tag{32}$$

where $\vec{r}$ is the vector from the doublet position $P(x_0,y_0,z_0)$ to the point of interest $M(x,y,z)$.
Considering that:

$$\frac{1}{|\vec{r}|^3} = \frac{\partial}{\partial x}\left[\frac{1}{(y-y_0)^2+(z-z_0)^2}\left(1+\frac{x-x_0}{|\vec{r}|}\right)\right] \tag{33}$$

the previous integral can be transformed as follows:

$$\Phi(x,y,z) = \frac{-1}{4\pi}\int_{\Sigma_B+\Sigma_W} \frac{\partial\mu}{\partial x}\frac{z-z_0}{(y-y_0)^2+(z-z_0)^2}\left(1+\frac{x-x_0}{|\vec{r}|}\right) d\Sigma \tag{34}$$

In the steady case, the intensity μ of the doublets in the wake is constant in the direction of the airflow and varies only spanwise. Therefore, $\partial\mu/\partial x = 0$ for all the points in the wake. On the contrary, doublet intensity on the wing may vary both spanwise and chordwise, in order to fulfill the boundary condition along the wall. Therefore, the velocity potential can be obtained by integrating the effect of doublets only over the solid body Σ_B:

$$\Phi(x,y,z) = \frac{-1}{4\pi}\int_{\Sigma_B} \frac{\partial\mu}{\partial x}\frac{z-z_0}{(y-y_0)^2+(z-z_0)^2}\left(1+\frac{x-x_0}{|\vec{r}|}\right) d\Sigma \tag{35}$$

Zero-thickness wing in incidence. Unsteady case. Velocity potential can also be computed in the unsteady case using Eq. 34. However, to remove the integration along the wake, in this case it is necessary to introduce the *acceleration potential* as follows:

$$\Psi(x,y,z) = \frac{\mathrm{D}\Phi}{\mathrm{D}t} = \frac{\partial\Phi}{\partial t} + \vec{v}.\nabla\Phi \simeq \frac{\partial\Phi}{\partial t} + U_\infty\frac{\partial\Phi}{\partial x} \tag{36}$$

which has been approximated to the case of a thin-wing case under small incidences and small motion amplitudes. In this equation, U_∞ is the freestream velocity in the x-axis. The interesting property of the acceleration potential Ψ is that it is continuous in all the domain except across the wing.

Again, the solution of Ψ must fulfill Laplace's equation:

$$\nabla^2\Psi = 0 \tag{37}$$

The zero-velocity normal to the solid surface boundary condition, in the body frame, imposes on Σ_B that:

$$\frac{\partial \Psi}{\partial z} = \frac{\mathrm{D}\alpha}{\mathrm{D}t} = \frac{\partial \alpha}{\partial t} + \vec{v}.\nabla\alpha \simeq \frac{\partial \alpha}{\partial t} + U_\infty \frac{\partial \alpha}{\partial x} \tag{38}$$

The acceleration potential is continuous in both sides Σ^+ and Σ^- of the wake:

$$\Psi^+ - \Psi^- = [[\Psi]] = 0 \tag{39}$$

Finally, the perturbation must decay far from the wing and the wake:

$$\lim_{r\to\infty} \nabla\Psi = 0 \tag{40}$$

By a procedure similar to the one used in the steady case, it is obtained:

$$\Psi(x,y,z) = \frac{1}{4\pi} \int_{\Sigma_B} \frac{\partial [[\Psi]]}{\partial x} \frac{z - z_0}{(y-y_0)^2 + (z-z_0)^2} \left(1 + \frac{x - x_0}{|\vec{r}|}\right) d\Sigma \tag{41}$$

Methods based on the unsteady lifting-surface theory can solve either Eq. 41 on the wing surface or, in a more common implementation, they can solve Eq. 34 on the wing and the wake surfaces. To do so, a discrete description of the wing and the wake is used. More details on these methods can be found in [Ashley 1985, Katz 2001].

The Onset of the Lifting-Line Theory

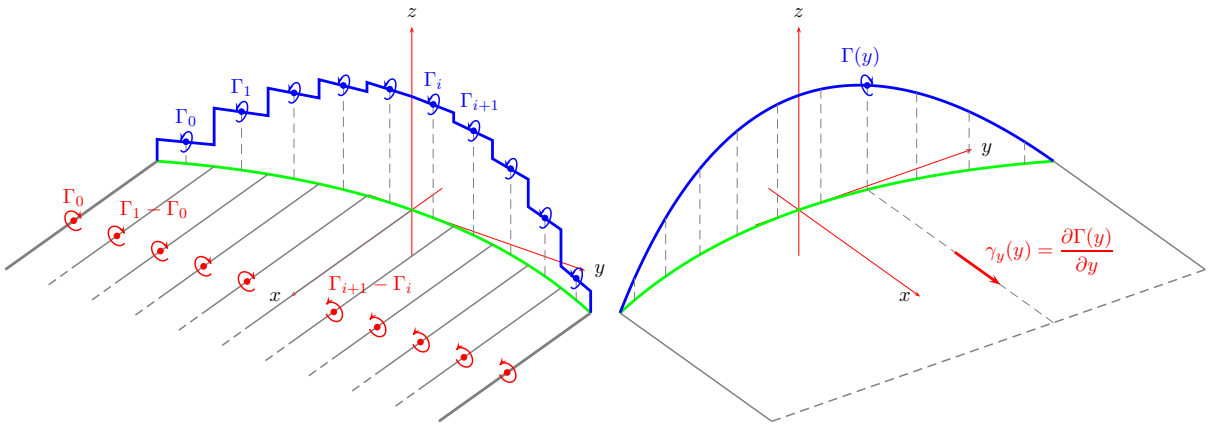
Prandtl's theory. The origin of the classical lifting-line theory is commonly attributed to the works done by Prandtl and his team at Gottingen during the World War I [Prandtl 1923]. This theory is the first and simpler way to represent the three-dimensional airflow around a finite wing. It considers an incompressible and inviscid fluid along a finite-span straight wing with high aspect ratio under steady conditions and small incidences. The theory has been detailed in several reference books [Katz 2001, Anderson 2001] and here only the main results, as well as the hypothesis and limits of the theory will be presented.

The problem is governed by the Laplace's equation for the velocity potential: $\nabla^2\Phi = 0$. The solutions of this equation can be found using the superposition of fundamental solutions, i.e. sources, sinks, doublets, vortices, etc. In particular, Prandtl's theory represents the wing and its vortical wake by a series of horseshoe vortices.

These vorticity structures are solution of Laplace's equation when they meet with the Helmholtz's theorems [Saffman 1992]: (a) The intensity of the vortex is constant all along its path, and (b) a vortex cannot be cut, it must finish at infinity or form a closed path.

Prandtl's theory uses the Biot-Savart law to calculate the velocity induced at a point M by a vorticity filament $\mathcal{L}$ of intensity Γ:

$$\vec{V}_{\mathrm{ind}} = -\frac{\Gamma}{4\pi} \int_{\mathcal{L}} \frac{\overrightarrow{PM} \wedge \mathrm{d}\vec{l}_{\mathrm{P}}}{PM^3} \tag{42}$$



(a) Step Γ distribution. Vortex filaments (b) Prandtl's continuous Γ distribution

Figure 18: Different orders in the lifting-line. Constant Γ in each blade section or continuous Γ distribution

In the beginning of the 20th century Lanchester modeled the wing by a single horseshoe vortex [Lanchester 1907]. The so-called *bound vortex* followed the span of the wing, while the *free vortices* represented the wingtip vortices. In that case, Helmholtz's condition imposed a constant intensity all along the wingspan, which does not correspond to the real wing behavior. Indeed, the constant vortex circulation can be linked to the lift developed by the wing at each span position, which shall not be constant in the general case.
On the contrary, if a series of horseshoe vortices of different intensity are considered along the wing (see Fig. 18(a)), a step distribution of the circulation can be obtained along the wingspan. Prandtl extended this idea and considered an infinite number of horseshoe vortices, hence obtaining a continuous distribution of circulation along the wing (see Fig. 18(b)).

For each point on the lifting-line, the velocity induced by a free vortex filament of this continuous wake is:

$$\mathrm{d}\vec{V}_{\mathrm{ind}} = \frac{\Gamma'(\eta)}{4\pi(y-\eta)}\mathrm{d}\eta.\vec{k} \tag{43}$$

where $\Gamma'(\eta) = \partial\Gamma/\partial y|_\eta$. Thus, the velocity induced by the whole wake is:

$$\vec{V}_{\mathrm{ind}}(y) = \frac{1}{4\pi}\mathrm{PV}\int_{-b/2}^{b/2}\frac{\Gamma'(\eta)}{y-\eta}\mathrm{d}\eta.\vec{k} \tag{44}$$

where b is the wingspan and PV indicates the *Principal Value* of the integral as defined in Appendix A.
The Kutta-Joukowski condition for two-dimensional airfoils is then modified to include the induced velocities from the three-dimensional wake, α_{ind}:

$$\Gamma(y) = \pi c(y) U_\infty(\alpha - \alpha_{\mathrm{ind}}) \tag{45}$$

For small incidence angles, it is supposed that:

$$\alpha_{\text{ind}} = \arctan(\vec{V}_{\text{ind}}.\vec{k}/U_\infty) \simeq \vec{V}_{\text{ind}}.\vec{k}/U_\infty \tag{46}$$

Which yields to the Prandtl's integro-differential equation:

$$\Gamma(y) = \pi c(y) U_\infty \left(\alpha - \frac{1}{4\pi U_\infty} \text{PV} \int_{-b/2}^{b/2} \frac{\Gamma'(\eta)}{y-\eta} \text{d}\eta \right) \tag{47}$$

For a two-dimensional, incompressible and irrotational airflow, the Kutta-Joukowski theorem links the airfoil lift to the velocity circulation around it. This condition can be extended to the lifting-line problem to obtain the sectional lift and the section induced drag:

$$L'(y) = \rho_\infty U_\infty \Gamma(y) \quad ; \quad D'(y) = \rho_\infty U_\infty \Gamma(y) \alpha_{\text{ind}}(y) \tag{48}$$

The wing loads can be obtained by spanwise integration of the sectional loads:

$$L = \rho_\infty U_\infty \int_{-b/2}^{b/2} \Gamma(y) \text{d}y \quad ; \quad D = \rho_\infty U_\infty \int_{-b/2}^{b/2} \Gamma(y) \alpha_{\text{ind}}(y) \text{d}y \tag{49}$$

Prandtl's lifting-line method presents a rather heuristic formulation, without a rigorous mathematical demonstration. Moreover, still today, the final integro-differential equation has no analytical solution and therefore it must be solved in an iterative process.

Van Dyke's Asymptotic Expansions. The theoretical justification of the lifting-line theory is attributed to Van Dyke [Van Dyke 1964]. In his works, he noticed that problems presenting singular perturbations, such as the wing model used in the lifting-line theory, can be solved by using the Matched Asymptotic Expansion technique (MAE).

When fluid dynamics equations are written in dimensionless form small parameters appear. For a problem with a unique exact solution, we can formulate an approximate problem by supposing that those small parameters are negligible ($\varepsilon \to 0$). This approached problem may be easier to solve and may give an approximate solution. However, nothing tells us whether the problem is still well-conditioned or whether the approached solution is close to the exact solution for all the fluid domain.

Matched Asymptotic Expansions method focuses on problems where the described perturbation becomes singular. In that case, there are some zones in the problem where the effect of the small parameters is no longer negligible. Thus, two approached problems must at least be formulated: the "outer domain", where the small parameter is neglected, and the "inner domain", where this parameter becomes important. Both solutions are matched by continuity conditions to obtain the approached solution of the problem for the entire fluid domain (see [Van Dyke 1964] for more details).

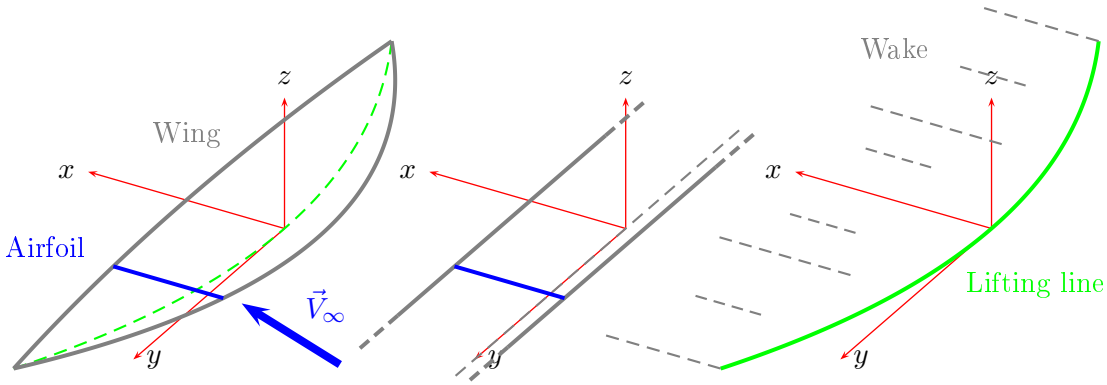


Figure 19: Finite wing problem (left) solved using the Matched Asymptotic Expansions method: infinite-span airfoil (center) and the lifting-line method(right)

The lifting-line model is based on two main assumptions: First, the aspect ratio, AR (ratio of the span lengthscale, b, of a lifting wing to its chord lengthscale, c_0) is much greater than one ($1 \ll b/c_0$); and second, the spanwise variation of the flow occurs on the long lengthscale b. While Prandtl's approach implies solving an integro-differential equation, Van Dyke realized that the problem could be considered as a singular perturbation and he introduced the matched asymptotic expansion technique (MAE) into the solution of the problem. He proposed an expansion of the solution with the small parameter $\varepsilon = \mathrm{AR}^{-1}$.
The global solution is obtained by matching an "inner solution", which considers only the airfoil aerodynamics and its two-dimensional wake, neglecting all spanwise variations, and an "outer solution", which neglects the chord dimension and considers the problem as a system of bound and free vortex, representing the blade and its wake, respectively (see Fig. 19).

The velocity potential and the circulation are developed asymptotically under the form:

$$\begin{aligned}\Phi(x,y,z)&=\Phi_0(x,y,z)+\varepsilon\Phi_1(x,y,z)+\varepsilon^2\ln\varepsilon\Phi_2(x,y,z)+\varepsilon^2\Phi_3(x,y,z)+o(\varepsilon^2)\\ \Gamma(x,y,z)&=\Gamma_0(x,y,z)+\varepsilon\Gamma_1(x,y,z)+\varepsilon^2\ln\varepsilon\Gamma_2(x,y,z)+\varepsilon^2\Gamma_3(x,y,z)+o(\varepsilon^2)\end{aligned} \tag{50}$$

While Prandtl's approach led to an integro-differential equation without analytical solution for an arbitrary wing geometry, Van Dyke's approach yields to the

following asymptotic solution:

$$
\begin{aligned}
\overline{\Gamma}_0(\overline{y}) &= \pi \overline{c} \alpha \\
\overline{\Gamma}_1(\overline{y}) &= \frac{\pi \overline{c} \alpha}{2} \int_{-1}^{1} \frac{\overline{c}'(\overline{\eta}) d\overline{\eta}}{\overline{y} - \overline{\eta}} \\
\overline{\Gamma}_2(\overline{y}) &= \frac{\pi \overline{c} \alpha}{4} (2\overline{c}'^2(\overline{y}) + 3\overline{c}(\overline{y})\overline{c}''(\overline{y})) \\
\overline{\Gamma}_3(\overline{y}) &= \frac{\pi \overline{c} \alpha}{4} \left[\left(2 \ln \frac{4}{\overline{c}(\overline{y})} - \frac{3}{2} \right) \overline{c}'^2(\overline{y}) + \left(3 \ln \frac{4}{\overline{c}(\overline{y})} + \frac{1}{2} \right) \overline{c}(\overline{y}) \overline{c}''(\overline{y}) \right. \\
&\quad + \frac{\partial}{\partial \overline{y}} \int_{-1}^{1} \left(\int_{-1}^{1} \frac{\overline{c}'(\overline{\sigma}) d\overline{\sigma}}{\overline{\eta} - \overline{\sigma}} \right) \frac{\overline{c}(\overline{\eta})}{\overline{y} - \overline{\eta}} d\overline{\eta} \\
&\quad \left. + \frac{1}{2} \frac{\partial^3}{\partial \overline{y}^3} \int_{-1}^{1} \overline{c}(\overline{\eta}) (\overline{c}(\overline{y}) + \overline{c}(\overline{\eta})) sgn(\overline{y} - \overline{\eta}) \ln |\overline{y} - \overline{\eta}| d\overline{\eta} \right]
\end{aligned}
\tag{51}
$$

where the non-dimensional variables are defined as follows: $\overline{y} = y/b$, $\overline{c} = c/c_0$, $\overline{c}' = \partial \overline{c}/\partial \overline{y}$, $\overline{c}'' = \partial^2 \overline{c}/\partial \overline{y}^2$, and $\overline{\Gamma} = \Gamma/(bU_\infty)$.

Developing the Lifting-Line Theory

The success of Van Dyke's approach boosted other researchers to find extensions of the original model which was restricted to unswept wings and steady flows. Hence successive studies focused on the extension of the lifting-line theory on one side to general blade forms and on the other side to unsteady airflow conditions.

General blade form. Thurber [Thurber 1965] was the first to apply the Van Dyke's asymptotic technique to curved wings of high aspect ratio. However, his formulation was too complicated and did not enable any physical interpretation of the different terms. Then, Cheng [Cheng 1978] proposed a clearer formulation of the MAE approach and applied it to straight swept wings. Some years later, Cheng and Murillo [Cheng 1984] developed an unsteady lifting-line theory for curved wings which was limited to very-low frequencies. Moreover, the formulation presented some difficulties from the use of the curvilinear coordinates in the "inner" domain in the MAE approach.

Unsteady airflow. The development of the unsteady lifting-line theory was done in several steps and focused mainly on harmonic airflows. First, Cheng [Cheng 1976] identified five frequency domains, depending on the ratio between the wavelength λ and the characteristic dimensions of the wing, i.e. the span b and the chord length c. The five frequency domains are: (a) Very-low frequencies, $b \ll \lambda$, (b) low frequencies, $b = O(\lambda)$, (c) intermediate frequencies, $c \ll \lambda \ll b$, (d) high frequencies, $c = O(\lambda)$, and (e) very-high frequencies, $\lambda \ll c$.
Regarding the shape of the induced velocity distribution, first works from James [James 1975] and Van Holten [Van Holten 1976] considered a constant distribution along the chord like in the steady lifting-line theory. On the contrary, Ahmadi and Widnall [Ahmadi 1985] showed that this assumption was asymptotically correct only

for very-low frequencies ($b \ll \lambda$), whereas for the low-frequency domain ($b = O(\lambda)$), induced velocities presented a sinusoidal dependence on the chordwise variable. Sclavounos [Sclavounos 1987] noticed a non-uniformity in the frequency domain that avoided previous work to obtain a unified formulation of the unsteady lifting-line theory. Indeed, previous theories covered a narrow range of frequencies because they tried to asymptotically relate the wavelength λ to either the span lengthscale or the chord lengthscale. Such a comparison restricted automatically the development to a small range of frequencies.

The Unified Lifting-Line Theory

Guermond and Sellier [Guermond 1990, Guermond 1991] developed what can be considered the most complete unified lifting-line theory, which rigorously solves the problem of a swept and curved wing under the full range of oscillation frequencies. Instead of solving the PDE, they generalized the approach proposed by Kida and Miyai [Kida 1978] to the case of a curved wing of high aspect ratio. This approach used the integral equation formulation of the problem; it solved asymptotically a Fredholm equation of the first kind which links the unknown pressure jump and the normal velocity imposed on the wing. An asymptotic expansion of the surface integral with respect to AR was found using the finite-part integral theory introduced by Hadamard [Hadamard 1932]. At each approximation order the problem reduced to a classical, two-dimensional, integral equation, whose unknown were the pressure jump, and whose right-hand side depended only on the previous approximation orders of the solution.

Steady formulation. In 1990, Guermond presented an asymptotic development of the lifting-surface equation (Eq. 41) as a function of the small parameter $\varepsilon = 1/AR = b/c$, the inverse of the wing aspect ratio [Guermond 1990]. The asymptotic development of the circulation Γ is written in non-dimensional variables as follows:

$$\Gamma(y) = \Gamma_0(y) + \varepsilon \ln \varepsilon \Gamma_1(y) + \varepsilon \Gamma_2(y) + o(\varepsilon) \tag{52}$$

where,

$$\begin{aligned}
\Gamma_0(y) &= \pi c(y) U_\infty \cos\Lambda \alpha \\
\Gamma_1(y) &= \pi c(y) U_\infty \cos\Lambda \left[\frac{\Gamma_0(y)}{4\pi\kappa(y)} + \sin\Lambda \frac{\dot{\Gamma}_0(y)}{2\pi} \right] \\
\Gamma_2(y) &= \pi c(y) U_\infty \cos\Lambda \left\{ \frac{1}{4\pi} \mathrm{PF} \int_{-b/2}^{b/2} \frac{\Gamma_0(\eta)}{(y-\eta)^2} \left(1 + \frac{l(y) - l(\eta)}{\sqrt{(l(y)-l(\eta))^2 + (y-\eta)^2}} \right) d\eta \right. \\
&\quad + \left[\frac{\Gamma_0(y)}{4\pi\kappa(y)} + \sin\Lambda \frac{\dot{\Gamma}_0}{2\pi} \right] \left(\ln \frac{c}{4} + \frac{1}{2} \right) + \frac{\Gamma_0(y)}{4\pi\kappa(y)} \left[1 - \tan^2\Lambda - \ln \frac{2}{\cos^2\Lambda} \right] \\
&\quad \left. + \frac{\dot{\Gamma}_0(y)}{2\pi} \left[\ln \left| \frac{1+\sin\Lambda}{\cos\Lambda} \right| - \sin\Lambda \ln \frac{2}{\cos^2\Lambda} \right] \right\}
\end{aligned} \tag{53}$$

Notice the addition of a term in $\varepsilon \ln \varepsilon$ which did not exist in Van Dyke's formulation. This term is indeed linked to the wing sweep and curvature.

In dimensional variables and writing the different terms under the form of induced velocities, it yields:

$$\Gamma(y) = \pi c(y) \cos \Lambda (U_\infty \alpha + w_0(y) + w_c(y)) \tag{54}$$

where the w_0 term comes from the outer domain and stands for the velocity induced by the wake. It can be calculated as follows:

$$w_0(y) = \frac{1}{4\pi} \mathrm{PF} \int_{-b/2}^{b/2} \frac{\Gamma_0(\eta)}{(y-\eta)^2} \left(1 + \frac{l(y) - l(\eta)}{\sqrt{(l(y) - l(\eta))^2 + (y-\eta)^2}} \right) d\eta \tag{55}$$

On the contrary, the w_c term does not appear in Van Dyke's expansions, and is linked to the effects of wing sweep and curvature. It can be written as follows:

$$w_c(y) = a_1 \Gamma(y) + a_2 \frac{\partial \Gamma}{\partial y}(y) \tag{56}$$

where:

$$a_1 = \frac{1}{4\pi\kappa(y)} (1 - \tan^2 \Lambda(y) + K) \; ; \quad a_2 = \frac{1}{2\pi} \left(K \sin \Lambda(y) + \ln \left| \frac{1 + \sin \Lambda(y)}{\cos \Lambda(y)} \right| \right) \tag{57}$$

$$K = \frac{1}{2} + \ln \frac{c(y) \cos^2 \Lambda(y)}{4b} \tag{58}$$

Unsteady formulation. One year later, Guermond and Sellier extended their unified theory to the unsteady case [Guermond 1991], thus leading to what is called here the Unsteady Curved Lifting-Line theory (UCLL). The asymptotic development of the circulation is done for the case of a wing under an harmonic motion of ω pulsation. Two reduced frequencies are of consideration in this case: the reduced frequency in the spanwise length $\nu = \dfrac{\omega b}{U_\infty}$ and the reduced frequency in chordwise length $k = \dfrac{\omega c_0}{U_\infty}$. Again, the asymptotic expansions use the small parameter $\varepsilon = 1/AR = c_0/b$, leading to the division of the problem into several *influence domains*. For each M point in the lifting-surface, three domains can be distinguished (see Fig. 20):

- The *inner domain* I: all points at a distance from M of the order of c_0.
- The *outer domain* O: all points at a distance from M of the order of b.
- The *outer domain* O_{wi}: all points of O placed in the wake of I domain.

Moreover, their study put forward the harmonic dependency of the induced velocities along a given wing section. Hence if M' is another point on the same wing section than M at a distance of x, then the induced velocities on that point follow: $w(M') = \exp^{-ikx} w(M)$.

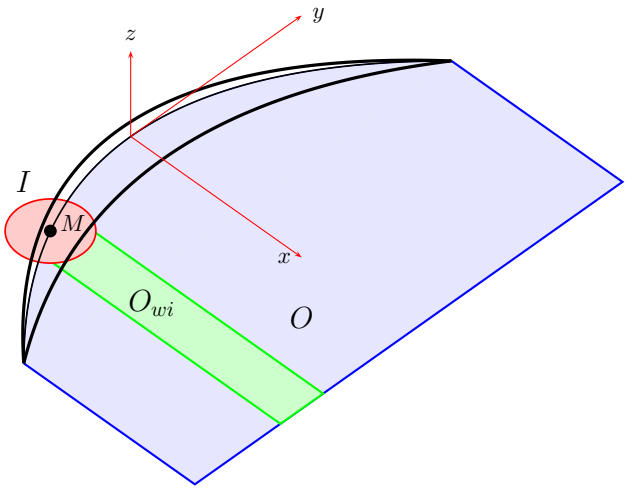


Figure 20: Influence domains in the unified theory [Guermond 1991]

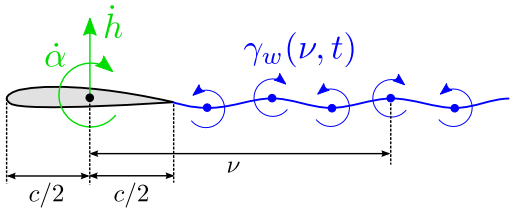
Numerical Application of the UCLL Theory

Devinant's hypothesis. The works of Guermond and Sellier put forward the harmonic dependence of the induced velocities along the chord. For low and very-low cases, Devinant [Devinant 1999] proposed to suppress this harmonic dependence. Similar to what was proposed by James and Van Holten, this assumption implies the same induced velocities on all the points for a given section. Thus, the circulation of a point M in the lifting-line up to order ε can be written as:

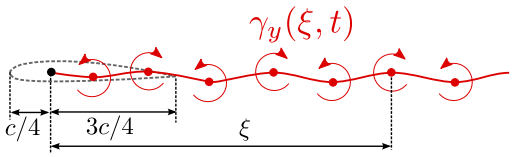
$$\Gamma(M) = \pi c(y) \cos\Lambda \left(w_{2D}(M) + w_c(M) + w_O(M) - w_{O_{\text{wi}}}(M) \right) \tag{59}$$

where: w_{2D} stands for the velocity induced by the unsteady two-dimensional wake $I \cup O_{\text{wi}}$, w_O is the velocity induced by the wake O, $w_{O_{\text{wi}}}$ is the velocity induced by the wake O_{wi}, and w_c is the complementary velocity induced by the local sweep and curvature.
Assuming constant induced velocities along the chordwise dimension allows also to overcome the periodicity hypothesis in the wing motion. Thus, general unsteady conditions can be studied, which is useful for time-marching simulations.

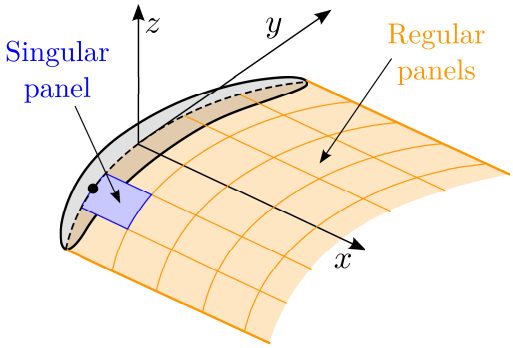
Previous numerical implementations of the UCLL theory. The theory developed by Guermond and Sellier has been implemented into a lifting-line code during two consecutive Ph.D. works [Gallois 2003, Muller 2007]. Following previous works of Devinant [Devinant 1998], the problem is divided in two influence domains (inner and outer) and linked by the MAE technique (see Fig. 21).
On one side, the outer domain considers the three-dimensional wing and its wake. It is modeled with a classical lifting-line method that reduces the wing to its quarter-chord line and discretizes the wake into surface elements of constant vorticity. The velocity induced by all the panels on the considered section is regular, and solved using the four-point Gaussian quadrature rule, except the panel in contact with the calculation point. The velocity induced by this panel is calculated using the



(a) Inner domain, $I \cup O_{\text{wi}}$



(b) Two-dimensional wake domain, O_{wi}



(c) Three-dimensional wake domain, O

Figure 21: Different $\vec{v}_{\text{ind}}$ terms in the unified lifting-line theory.

Hadamard's Finite Part integrals.
On the other side, the inner domain represents a two-dimensional airfoil and its wake. It is modeled by a classical linearized thin-airfoil theory in temporal formulation, which takes into account the motion of the airfoil together with the unsteady two-dimensional wake shed from its trailing edge. In order not to consider two times the wake behind the considered airfoil, the two-dimensional wake in the lifting-line formulation is removed. To calculate the term to be removed, Finite Part integrals are used again.

This numerical application will be detailed and analyzed in Chapter 3. It has already been implemented in the academic code AILE giving excellent results when compared to lifting-surface codes for the case of a swept and curved wing in general unsteady airflow conditions. Therefore, the purpose of the first part of the present study has been to adapt and implement it in an industrial code like HOST.

Methods and Tools

This chapter is divided in two main parts: the first one is devoted to the methodologies used during this Thesis, and the second one to the test cases used for validating the methodologies.

On one side, the chapter focuses on describing the main features, hypothesis, strengths and weaknesses of the available methods for single- and contra-rotating propeller simulations. The state-of-the-art of the available methods in an industrial context is exposed, in order to justify the selection of some methods among the others. Finally, the selected methods are described more in detail.

On the other side, this chapter describes the details of the two test cases that are used all along the study. First, a representative single-rotating advanced propeller (APIAN) and then an Airbus generic geometry of a contra-rotating open rotor used in a number of European projects (AI-PX7).

Available Methods for Propellers and CROR

From the preliminary design phases of propellers and open rotors, methodologies should be available to predict a number of key parameters with a relatively good accuracy. Most important parameters are related to the *propeller performance* at the main flight points: the thrust and the shaft power. Moreover, for off-design conditions, which are very common when propellers and open rotors are installed on aircraft, *1P loads* are of capital importance. Finally, for structural preliminary design, it is also important to predict accurately *unsteady load and moment distributions along the blade*. On one side, steady blade loads are important for the structure dimensioning and, on the other side, unsteady loads are taken into account to determine vibrations and the limit of flutter.
In the case of an open rotor, the *potential and wake interaction* between propellers impacts strongly the behavior of the propeller. Due to the fact that open rotors are unducted, their interaction with the airframe is much more important than in the case of a turbofan. Therefore, being able to predict correctly these *installation effects* becomes a must when predicting the behavior of an installed open rotor.

An important number of simulation methods are available for the simulation of single-rotating and contra-rotating propellers. This wide variety is necessary to respond to each design phase requirements, while maintaining an optimum ratio between computational time and accuracy over computational costs.
A short description of these methods is given hereafter, together with their main assets and drawbacks for their application to preliminary design phases of open rotor blades.

Quasi-steady Lifting-Line methods. Rapid aerodynamic simulations of isolated single-rotating and contra-rotating propellers are currently performed using

the LPC2 code, developed at Onera. This code is based on the blade-element theory where the aerodynamic coefficients (lift, drag and pitching moment) of each blade section are computed using two-dimensional airfoil data. A singularity method is used to compute the velocities induced by the propellers on each blade section. This singularity method describes the wake as a lattice of vortex filaments with a prescribed motion and the blade is described as a vortex filament along its quarter-chord line.
LPC2 has been extended to provide information for the prediction of aero-acoustic signal of single- and contra-rotating propellers. In order to extract the unsteady loadings of the blade, one blade passage is divided in several blade positions keeping a wake with constant circulation. With this approach, induced velocities are calculated at each azimuthal position and thus unsteady loads on the blade can be predicted.
Non-homogeneous inflows can be taken into account in LPC2 computations, but in a quasi-steady approach. These non-homogeneous inflows can be due to the propeller in incidence or to the installation effects. The quasi-steady approach performs a first simulation considering an isolated propeller without incidence is computed. Then, the induced velocities computed in this first simulation are corrected to include the different perturbation fields, i.e. incidence or installation effects. However, the velocities induced by the wake are not modified by these perturbation fields to account for the incidence or for the effects of installation.

LPC2 was conceived as a tool for very rapid propeller and open rotor performance predictions. During several years, the code has been developed to broaden its domains of application, yet keeping a rather simple approach. Apart from performance, LPC2 can compute in-plane loads in the case of non-homogeneous inflow conditions. Moreover, the code provides adequate outputs for aero-acoustic computations with the PARIS code, which solves the Ffowcs Williams and Hawkings integral equation for noise propagation. Finally, the extensive use of the code in an applied research and in an industrial context has also helped to develop interesting features such as targeted-thrust and power computations for open rotors by varying front and rear blades' pitch.

The simplicity of LPC2 is still an important asset of the code, which enables a fair prediction of open rotor performance within few minutes of computation.
Regarding the prediction of key aerodynamic parameters, LPC2 has shown on one side an acceptable accuracy in terms of thrust and power for high-speed computations. However, important mismatches have been observed in highly-loaded low-speed computations. These mismatches are commonly attributed to the important three-dimensional vortex structures that form on the blade and that cannot be predicted by two-dimensional blade-element methods.
Moreover, LPC2 has presented noticeable mismatches in the prediction of the 1P load magnitude. Besides, simulations are not able to predict any 1P load phase lag due to the steady approach in the wake emission.
In addition, unsteady load and moment distributions along the blade are fairly predicted around the blade mid-span. Nevertheless, important mismatches are observed

near the blade tip, due to the limits of a two-dimensional simulation of the airflow, and near root, due to the lack of wall effects.
Finally, the steady approach in LPC2 code avoids its use in all aeroelastic applications. For example, the blade pitch default or the whirl flutter of a propeller or a CROR cannot be taken into account.

Although the simplicity of the code and the large amount of best practices already acquired, the Aerodynamics Tools and Simulations Department at Airbus decided to study and propose other methodologies to fulfill all the key requirements of open rotor preliminary design processes. This is why, within this Ph.D. thesis, HOST a comprehensive code for aeromechanical simulations has been investigated on single- and contra-rotating propellers.

Unsteady lifting-line simulations. The lifting-line theory has been extended to general unsteady cases in a number of industrial solvers by using time-marched simulations. MINT [Le Bouar-Coppens 2004] and MESIR [Michéa 1992a] codes at Onera or CAMRAD-II code at NASA [Johnson 1998] are some examples of this kind of approach.

These solvers have an accuracy in terms of performance that is similar to the case of classical lifting-line solvers. Again, they are based on a quasi two-dimensional description of the blade, and the effect of propeller slipstream is taken into account by a potential wake model. Due to its time-marched scheme, more important computational times are required, but remain between several minutes and some hours. An important asset of the unsteady approach is that it enables to account for the history in the vorticity shed by the blades, and thus they are able to predict a certain 1P load phase lag.
Moreover, the quality of the blade-vortex interaction is directly linked to the simulation time step. A compromise must be established however between the accuracy of the interaction and the computational costs, that increase rapidly as the time step diminishes.
Finally, installation effects can be introduced as a perturbation of the velocity seen by the blade, depending on the azimuth, the radius, and the time. Although models of the wall effect may be implemented in these codes, these corrections can increase significantly the computational costs and must be used carefully.

Mixing-plane RANS simulations. This method considers a one-channel computational domain, both for the front rotor and the aft rotor (see Fig. 22). One computational domain is considered for each row and source terms are imposed to the walls of each rotor in order to account for their rotational velocities. Each domain is discretized and the steady RANS equations are solved for each mesh cell. The interface between front and aft domains is managed by a mixing-plane condition. This boundary condition computes the azimuthal average of the conservative variables' fluxes and transmits the information to the opposite domain by interpolation on its interface mesh. Therefore, the averaged interference effect between rotors

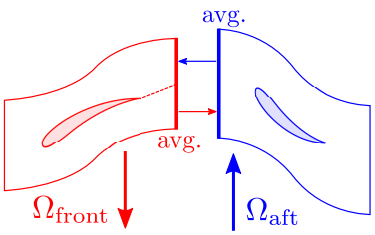


Figure 22: One channel per row domain with mixing-plane condition in the stage interface.

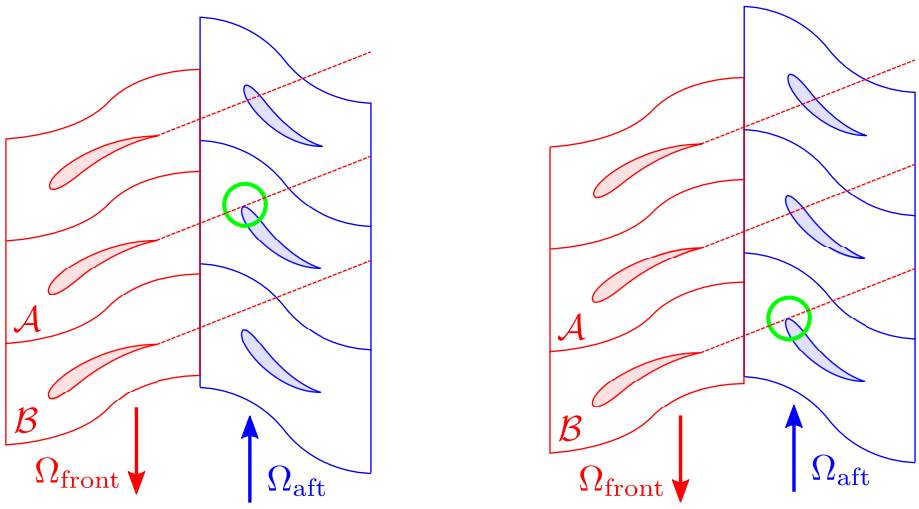
is taken into account while keeping a steady solution of the problem [Denton 1979].

Both, the one-channel computational domain and the steady approach used in the mixing-plane method lead to cheap simulations (some hours of meshing and computation), while accounting rigorously for the blade geometry, the compressibility, the viscosity, and the turbulence effects. Therefore, this method is particularly well adapted for the performance prediction of open rotors. However, as it considers only a steady solution, neither 1P loads nor blade-vortex interaction can be predicted. Moreover, these simulations can only account rigorously for the effects of the hub in the case of an isolated open rotor.

Chorochronic uRANS simulations. Introduced first by Erdos *et al.* [Erdos 1977] for turbomachinery simulations, the chorochronic approach relies on the natural space (choro) and time (chronic) periodicity of the flow and hence allows to perform unsteady simulations of stages' interaction considering only one channel per row. Therefore, the flow seen by a given channel $\mathcal{A}$ at the time t is the same as the flow seen by another channel $\mathcal{B}$ at a certain time $t+T_{\text{choro}}$, where T_{choro} is the chorochronic period (see Fig. 23).
It has to be noted that the chorochronic period has no sense for phenomena that are not correlated with the rotational velocities of the row, like for example the vortex shedding. These phenomena have their own frequency and, though captured in a given row domain, they cannot be transmitted to adjacent rows.

The unsteady approach of the chorochronic technique allows for a number of open rotor industrial applications: performance prediction, blade-vortex interactions, unsteady blade loadings, and aero-acoustics. Moreover, considering only one channel per row reduces significantly memory and computational costs (some days). On the contrary, the method is limited to a single stage interaction and cannot account for non-homogeneous inflow due to the effects of installation or the incidence.

Time-spectral method (TSM). Spectral methods in CFD simulations were first presented by He [He 1992] for the case of multi-stage turbomachinery. This method starts from the fact that uRANS simulations do not consider the periodic nature of the airflow and therefore an important part of the computational time is wasted to pass the unsteady transient of the solution [Sicot 2009]. A way to avoid this is to express the variables of the aerodynamic field in Fourier's series and perform $2N+1$



(a) Instant t (b) Instant $t + T_{\text{choro}}$

Figure 23: Chorochronic or time-space periodicity in two contra-rotating rows

coupled steady simulations. Each of the steady simulations represent particular instant in the period of the studied phenomena, and it is coupled to the other instants by adding source terms to RANS equations. Considering $2N + 1$ simulations, the highest harmonic in the solution that is expected to be captured is N. However, the number of computed instants $2N + 1$ should be chosen carefully in order to capture the phenomena of interest with enough accuracy, but without tremendously increasing memory and computational time.

The domains of application of TSM simulations are theoretically the same as chorochronic simulations: performance, blade-vortex interaction, unsteady blade loading and acoustics. Again, installation effects inducing non-homogeneous inflow cannot be considered. Moreover, first industrial applications of the method have shown unphysical oscillations due to the Fourier's series truncation, which might reduce the application of the method to aero-acoustic problems [Yabili 2010]. To reduce these oscillations, an important number of harmonics are needed and thus, computational costs might be no longer interesting compared to equivalent uRANS computations.

Multi-frequential methods. Both chorochronic and TSM methods have been extended to the case of multi-stage interactions: multi-chorochronic approach [Castillon 2012] and Harmonic Balance Technique [Hall 1987]. The method principles are the same as in mono-frequency approaches but considering multiple characteristic frequencies in each row. Yet the solution of the problem can be very sensitive to the arbitrary choice of the frequencies (or the instants) and their harmonics.

The first spectral method simulations applied to an isolated CROR case were conducted by Hoffer using the nonlinear harmonic method (NLH) of FINE/Turbo

software [Hoffer 2012]. Similar simulations have been recently conducted by François using the *elsA* code [François 2013a].
Theoretically, although considering only one channel per stage, these methods are able to account for general non-homogeneous inflow generated by the effects of installation. However, recent applications to the case of an installed open rotor with pylon have shown the limits of these methods in terms of convergence rate and computational costs.

Full-Annulus uRANS simulations. This method computes the whole engine geometry and can include also other elements around the engine, like the whole nacelle, the pylon, the fuselage, etc. Thus, the method can theoretically take into account all three-dimensional airflow structures on the blade and all kinds of effects of installation. Two similar techniques can be used in order to consider the rotation of both rotors with respect to the fixed-body reference frame: the sliding grid technique or the chimera grid technique. The *sliding mesh* technique is applied in the interface between two non-coincident meshes having different velocities. At each time step, the fluxes are interpolated between both meshes in contact. The *chimera mesh* technique allows an overlapping of different meshes to simplify the mesh generation. Donor and masked cells are declared in order to transmit the airflow information and reduce the number of redundant cells, respectively.

François *et al.* have compared these two techniques for the case of an open rotor [François 2011]. Although similar results were obtained, computational costs were slightly higher when using the Chimera mesh technique.

These methods can be used for performance prediction, but also for all the rest of aerodynamic applications: to rotor-rotor and pylon-rotor interaction prediction, aero-acoustic predictions, blade aero-elastic effects, whirl flutter, laminar-turbulent transition effects, etc.

These two methods can provide an excellent accuracy and installation effects can be taken into account in detail. However, due to important meshing and computational costs, it is not affordable to use them in open rotor preliminary design phases. Even for the isolated open rotor test case, several days of meshing and computing are required to obtain a converged solution.

Selected Methods for the Preliminary Design of Open Rotors

Figure 24 sums up the position of the different available methods for the aerodynamic simulation of Open Rotors with respect to three key parameters for preliminary design simulations: the computational time, the accuracy of computations, and the installation effects. The strengths of each method are marked in green, the major weaknesses in red and the relative weaknesses in yellow.

The objectives of the Ph.D. can be summarized in three points:

1. Develop moderate-costs methodologies for preliminary design phases. The assessment of these methodologies should focus on the prediction of key parameters such as performance and 1P loads. Installation effects and unsteady

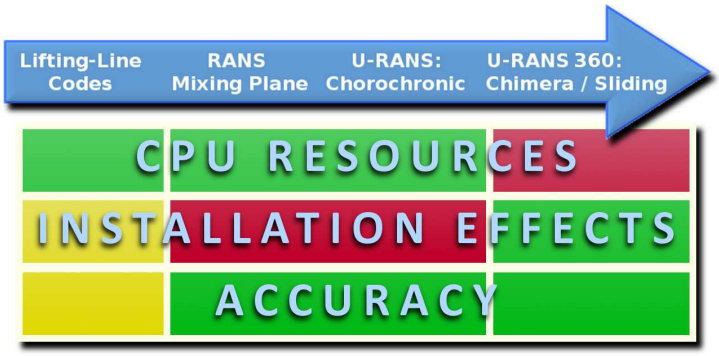


Figure 24: Assets and drawbacks of different available simulation tools.

aerodynamics on the blade being key factors in the prediction of 1P loads, they should also be studied in detail.

2. Provide a reliable and flexible tool for future whirl flutter simulations, aeroelastic simulations, and aeroacoustic preliminary studies.

3. Explore Eulerian/Lagrangian coupling strategies for a better simulation of the airflow around the blade and assess its impact on key parameters in open rotor design.

To fulfill these objectives, two codes have been used: On one side, HOST, a comprehensive code for aero-mechanical simulations of aircraft with rotatory wings; and, on the other side, *elsA*, a CFD code solving the unsteady Reynolds-Averaged Navier-Stokes equations. The state-of-the-art of these codes is described hereafter, together with a short description of the existing coupling strategy between them.

HOST. A Comprehensive Code for Aeromechanical Simulations

This section describes the main features of HOST, a comprehensive code for aeromechanical simulations of rotary-wing aircraft. A special attention is paid to the description of the code modules devoted to aerodynamic simulations, which are the blade module and a number of wake modules. Finally, the main hypothesis linked to the methodologies for aerodynamic simulations in HOST are described.

This code has shown satisfactory results in the simulation of conventional and unconventional helicopter rotors under general unsteady aerodynamic conditions [Rodriguez 2010]. However, it has not been tested before for advanced turboprop high- and low-speed cases.

An Helicopter Overall Simulation Tool

Several simulation codes existed in Aérospatiale Hélicoptères in the 1980s: *R85* for isolated rigid articulated rotor, *R85S* which added an elastic blade model, and a number of codes for flight mechanics (*S87*, *S89*,...). No common libraries existed and hence each development had to be implemented separately in each of the codes. Therefore, in 1991 the MNGH project was launched in order to develop (1) a code that merged all the existing capabilities; (2) could simulate all existing configurations and new ones; (3) fit requirements for flight mechanics, loads, dynamics, vibrations, and real-time simulations; (4) ease the implementation of new models; and (5) reduce maintenance costs.

The result was HOST, *Helicopter Overall Simulation Tool* [Benoit 2000], an aeromechanic calculation tool for helicopters. It was conceived in a modular way: the system is divided in several elements and each element is associated to a physical model, e.g. rotor aerodynamics, rotor structure, fuselage, engine, etc. This modularity enables a maximum number of system configurations, from an isolated rotor to a "complete" helicopter –including the rotor, the engine, the transmission system, the fuselage, the tail rotor, etc.– by adding or removing the different modules representing each of the helicopter elements. Three layers can be distinguished in HOST: the kernel, where all the generic routines are run independently from the overall configuration, the model routines, where each physical model in the problem is simulated, and the interface routines, to connect each model with the others and with HOST kernel.

Several types of calculations are available in HOST:

- *Equilibrium calculation*: predicts the global state of the rotor to maintain a given flight condition.
- *Simulation calculation*: a time-dependent solution that characterizes the helicopter response depending on the environment conditions and the control laws.
- *Linearized calculation*: predicts the helicopter stability by calculating its sensitivity around an equilibrium state.

This modular structure makes it easier to extend the use of HOST to other applications such as single and counter-rotating propellers. For these cases, the aerodynamic simulations use the following structure in HOST: on the top of it, the "rotor" module, to link the motion of all the blades; next, one or more "blade" modules, used to simulate the aerodynamic and elastic behavior of each blade; finally, a wake model, in order to provide the induced velocities on each of the blade sections. Furthermore, in Open Rotor cases a fuselage module is needed to link the motion of the two propellers. Figure 25 shows an example of an Open Rotor configuration.

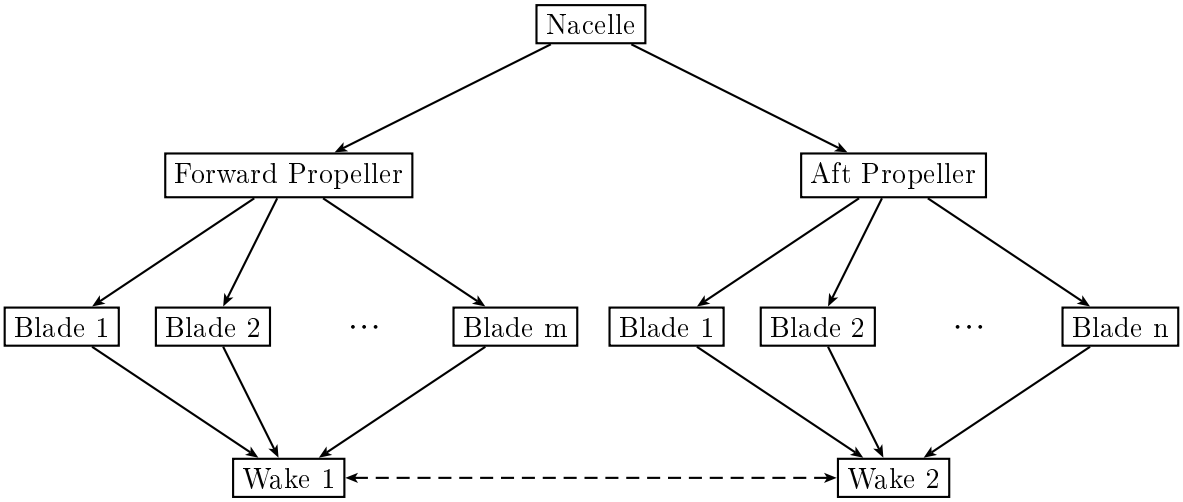


Figure 25: HOST modules for the simulation of an Open Rotor

The Blade Module for Aero-Mechanical Simulations

The method for predicting the aero-mechanical behavior of the blade in HOST is based on a non-linear lifting-line method, which couples a blade-element theory with a model of the wake. Hence this part of the code is divided in two coupled modules: a Blade Module and a Wake Module. The Blade Module describes the blade as a range of finite-span sections. The position, motion and acceleration of each section is determined by the addition of rigid blade motions and blade deformations. Moreover, it computes structural and aerodynamic forces and moments on each blade section. The aerodynamic loads and moments of each airfoil are determined by using non-linear steady airfoil data. This airfoil data is obtained from external simulations or experimental data and depends on the relative velocity, the airfoil incidence, and the local sweep angle.
The geometrical relative velocity and the incidence are modified by the Wake Module under the form of induced velocities along the quarter-chord line of the blade. Therefore, the Wake Module allows to take into account the three-dimensional airflow induced by the whole propeller slipstream. Finally, the Blade Module includes two-dimensional sweep corrections based on Jones' theory in order to consider the local sweep angle between the blade and the airflow [Jones 1945].

Vortex Wake Models in HOST: METAR and MESIR

Several wake models are available in HOST for the aerodynamic simulations, from simple analytical models, like Meijer-Drees [Meijer-Drees 1949], to high-order free-wake models like MINT. The development of these types of models is the result of a long process along the years and different codes. Only three of them will be described: METAR, a prescribed wake, MESIR, a periodic free-wake, and MINT, a

high-order free-wake model.

METAR (Modèle d'ÉTude de l'Aérodynamique du Rotor) was first an external code based on singularities. It was developed in the 1980s at Aérospatiale Hélicoptères by Toulmay [Toulmay 1986].
The flight conditions and the geometry of the rotor are the input data for the calculation. The blade is described as a lifting-line located at its quarter-chord line and the method uses a quasi-steady approach, which means that a steady problem is solved for each rotor position. The Laplace's equation of the velocity potential is solved by distributing a matrix of vortex filaments along the blade and the wake.
At each azimuthal position, the blade sheds a row of vortex filaments parallel and another series of vortex filaments normal to blade. At each time step, these filaments are convected at the freestream velocity plus the induced velocity normal to the rotor calculated by Meijer-Drees model. Moreover, in order to simplify the method, the problem is supposed to be periodic along a complete rotor rotation. The vortex intensity is constant along each filament. This vorticity is calculated at the emission of the filament, in order to meet with the Kelvin's circulation conservation theorem, and it is conserved during the convection of the vortex filaments.
The influence of the wake on the blades is taken into account by calculating the induced velocity of each vortex filament on each blade section. These induced velocities follow the Biot-Savart law.
In the lifting-line method, this approach is equivalent to an induced incidence on each blade airfoil. Then, experimental or calculated airfoil data is used to obtain its lift, drag and pitching moment coefficients. With this approach, the compressibility and viscosity effects are taken into account in a simplified way. The Kutta-Joukowski condition is used to calculate the circulation at each blade section: $\Gamma = 1/2VcC_L$.
Based on the periodicity hypothesis of the problem, an influence matrix can be established to converge iteratively the section circulation at all the azimuthal positions. The convergence criterion is based on the induced velocities on the blades.

In order to improve the description of the wake and to better predict Blade-Vortex Interaction (BVI) phenomena, Michéa [Michéa 1992a] developed the MESIR code (Mise en Équilibre du SIllage Rotor) based on METAR. The BVI is a usual phenomenon on helicopter rotors for low-forward advancing speeds or for low-angle descending flights. It stands for the interaction between the blade and the wake emitted by the previous blade, and it constitutes an major noise source in helicopters [Conlisk 2001, Johnson 1980].
Thus, in MESIR code, even if a periodic solution is considered, the form of the wake is no longer fixed, i.e. the wake is deformed until the equilibrium is reached. To do so, each node of the vortex filament matrix is convected at the freestream velocity plus the velocity induced by all the vortex filaments.
As it has been noticed by Coppens [Le Bouar-Coppens 1999] this wake model presents two important limits. On one side, it is limited to stabilized flights, as it considers only periodic solutions, and on the other side, it is not stable for time steps smaller than the equivalent to 10° of azimuth.

These two external codes described before were implemented in HOST as one of

the available wake models.

MINT Wake Model

As a way to overcome the two main limits presented by MESIR a new code was developed by Coppens [Le Bouar-Coppens 1999, Le Bouar-Coppens 2004]. Similarly to METAR and MESIR codes, MINT was initially developed as an external code and then implemented in HOST with some modifications. The main improvements in MINT with respect to MESIR code are two:

- A rigorous wake evolution and deformation, using the thin-wake theory developed by Mudry [Mudry 1982], to allow time-marched simulations.
- An unsteady lifting-line theory proposed by Guermond and Sellier [Guermond 1991], but limited to straight blades.

MINT uses a time-marching scheme to overcome the periodicity hypothesis and be able to address maneuver problems. The circulation is determined on the blades at each time step, and the loads are calculated in the end of the convergence process.

The wake modeling. The wake model formulation in MINT is based on the unsteady thin-wake theory proposed by Mudry [Mudry 1982]. The problem is governed by the Laplace's equations of the velocity potential and the wake is represented by a vorticity surface containing a series of surface doublets. This elementary singularities ensure the continuity of the velocity component normal to the wake surface and impose a discontinuity between both sides of the surface in the tangential component of the velocity.

Thus, the wake can be parametrized by ϖ, which gives the position in the absolute frame (x, y, z) of a point in the wake at instant t of the particle emitted at instant τ at the position q in the lifting-line. Moreover, this wake contains a certain local vorticity density γ in the parametrization frame. Thus, the vorticity density can be linked to the parametrization by:

$$\gamma(q,\tau,t) = \gamma^1 \frac{\partial \varpi}{\partial q}(q,\tau,t) + \gamma^2 \frac{\partial \varpi}{\partial \tau}(q,\tau,t) \tag{60}$$

An important characteristic of this formulation is the conservation of the two contravariant components γ^1 and γ^2 after the emission. As explained by Mudry, this conservation comes from the fact that, for an inviscid fluid, where singularities are very local, vortex do not diffuse and do not dissipate energy. Therefore, variations in vorticity are only due to the deformation of the wake. These contravariant components can be calculated as follows:

$$\gamma^1 = \frac{\partial \Gamma}{\partial q}(q,\tau) \quad ; \quad \gamma^2 = \frac{1}{U_\infty}\frac{\partial \Gamma}{\partial \tau}(q,\tau) \tag{61}$$

The velocity induced by the wake on a point P follows Biot-Savart's law:

$$\vec{V}_{\text{ind}} = \frac{1}{4\pi}\iint_{\Sigma} \frac{\vec{\gamma}(Q,t) \wedge \overrightarrow{QP}}{QP^3} dS_Q + \frac{1}{4\pi}\int_{\delta\Sigma} \Gamma(Q,t) \frac{\overrightarrow{QP} \wedge d\vec{l}_Q}{QP^3} \tag{62}$$

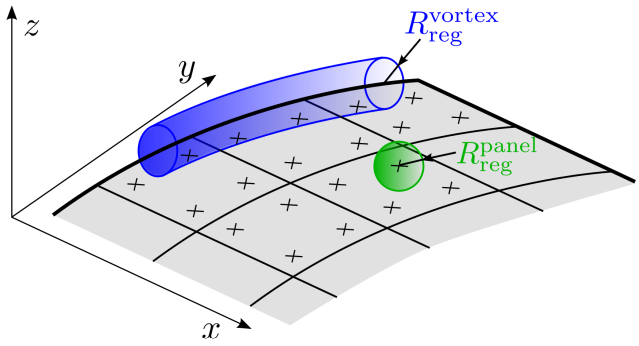


Figure 26: Vortex filament and panel regularization strategies in MINT wake model.

MINT code discretizes the wake in a series of vorticity panels and filaments. Each panel carries a vorticity density $\vec{\gamma}$ that is constant (also noted μ in the Eqn. (22) in the *Literature Review* chapter), whereas each filament carries a circulation Γ that varies linearly. The induced velocities of panels and segments are calculated by the Biot-Savart law (62) in its discrete form. The integrals in the expressions are numerically calculated by the Gauss-Legendre method [Euvrard 1984]. For the panels, a four-point quadrature is used to obtain an approximation of the surface integral, whereas a two-point quadrature is used for the vortex filaments. Coppens [Le Bouar-Coppens 1999] and Muller [Muller 2007] have shown that these induced velocities are singular when the calculation point and the integration points become closer. Actually, to avoid too important and unphysical induced velocities, a regularization is applied when the calculation point is too close to the integration point. Among all the regularization techniques that exist, a linear regularization is applied on vortex filaments in MINT, whereas a zero value is imposed for the Gauss points on the panels (see Fig. 26).

A particular attention must be paid to the velocities induced by the singular panel, i.e. the panel in contact with the calculation point. Coppens treated this panel as the rest of the wake, neglecting the fact that in this particular case Biot-Savart's integrals in (62) become singular. In this case, the four-point Gaussian quadrature rule, being a discrete integration method, may induce significant numerical errors. Of particular interest may be the study conducted by Muller [Muller 2007], where the numerical errors were assessed comparing the analytical integration and the four-point Gaussian quadrature rule for different distances to the panel and different panel forms.

The scheme in Fig. 27 shows the link between the vorticity contained in the wake panels and the circulation along the blade. Notice how the circulation at each blade section Γ_i is located at the center of the wake panels. These Γ_i are then used to interpolate the circulation at the borders of the panel wakes $\bar{\Gamma}_i$. At each time step, a new row of wake panels is shed from the lifting-line. Then, the variation of $\bar{\Gamma}$ at the panel borders is used to calculate the vorticity density γ_x and γ_y in the freshly-emitted panels.

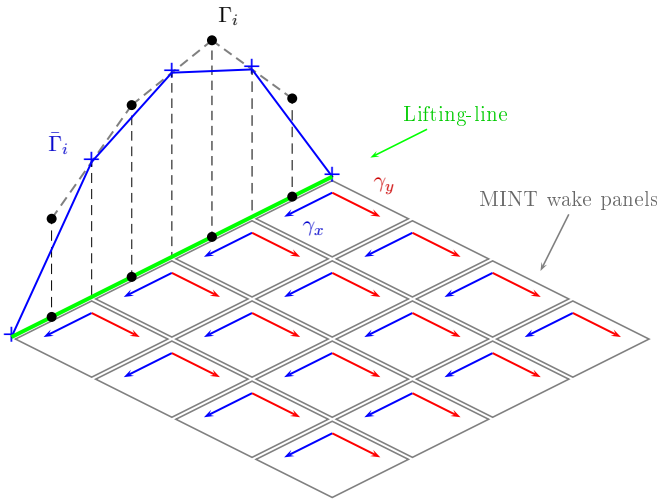


Figure 27: MINT wake panels, surface vorticity and lifting-line circulation

Circulation along the blade. The circulation along the blade is decomposed in four terms, based on the numerical approach proposed by Devinant [Devinant 1998] for straight wings:

$$\Gamma(y,t) = \Gamma_{1/4}(y,t) + d\Gamma(y,t) + \Gamma_{2D}(y,t) - \Gamma_{2D3D}(y,t) \tag{63}$$

where the different components are:

- *Quasi-steady component.* Lift coefficient is calculated in MINT by using two-dimensional airfoil data $C_L^T(M,\alpha)$ as a function of the local Mach number M and the incidence α. This airfoil data can be obtained from experiments or simulations, and can therefore account for viscosity and compressibility effects. The aerodynamic incidence is the difference between the geometric incidence and the incidence induced by the wake. This induced incidence results from the addition of the velocities induced by all the wake panels.

$$\Gamma_{1/4}(y,t) = \frac{c(y)}{2} U_\infty(y,t) C_L^T(y,t) \tag{64}$$

- *Pitching motion component.* This term appears to take into account the lift generated by the linear chordwise variation of the local velocity seen by the airfoil. This is modeled as a rotation at $\dot{\alpha}$ of a flat-plate around its half-chord axis.

$$d\Gamma(y,t) = \frac{\pi}{2} c^2(y) \dot{\alpha}(y,t) \tag{65}$$

- *Unsteady two-dimensional wake component.* This term represents the effect of unsteadiness in the two-dimensional wake on the airfoil incidence. Its expression can be found from the classical linearized thin-airfoil theory

[Von Karman 1938].

$$\Gamma_{2D}(y,t) = \pi c Q + \int_{c/2}^{\infty} \left(\sqrt{\frac{2\xi + c}{2\xi - d}} - 1 \right) \gamma_y^T(\xi, t) d\xi \tag{66}$$

where Q is a generalized velocity, $Q = U_\infty \alpha + \dot{h} + c\dot{\alpha}/2$.

- *MAE correction component.* This component appears to link the inner and the outer domains in the MAE approach. It is removed from the airfoil circulation in order not to take into account twice the effect of the airfoil wake, once in $\Gamma_{1/4}$ and once in Γ_{2D} components.

$$\Gamma_{2D3D} = \mathrm{FP} \int_0^{+\infty} \frac{\gamma_y(\xi, t)}{\xi} d\xi \tag{67}$$

where FP stands for Hadamard's Finite Part of the integral (see Appendix A).

The unsteady lifting-line implemented by Coppens in MINT presented convergence problems for small panel sizes which were attributed to Finite Part integrals. Coppens proposed to solve these Finite Part integrals by regularization, removing the singularity from the calculation domain in an arbitrary way. Similarly, the induced velocities from the singular panel were also regularized by the discrete integration method.

Aerodynamic loads on the blade. The HOST Blade Module applies the Kutta-Joukowski condition to link the circulation with the loads and moments in each blade section. Following this, the lift coefficient is divided in five terms:

$$C_L^{1/4} = C_L^T(\alpha^\star) \qquad \alpha^\star = \frac{Q - d\dot{\alpha}}{U_\infty} + \alpha_{\mathrm{ind}} \tag{68}$$

$$dC_L = \frac{\pi c \dot{\alpha}}{U_\infty} \tag{69}$$

$$C_L^{2D\mathrm{inst}} = \frac{1}{U_\infty} \int_d^{\infty} \frac{\gamma_y}{\nu} d\nu \tag{70}$$

$$C_L^{2D3D} = \frac{1}{U_\infty} P.f. \int_0^{\infty} \frac{\gamma_y}{\nu} d\nu \tag{71}$$

$$C_L^{NC} = \frac{\pi c}{2U_\infty^2} \left(\ddot{h} + U_\infty \dot{\alpha} + \frac{c}{4} \ddot{\alpha} \right) \tag{72}$$

Notice that, together with the four terms in the circulation, a term must be added to take into account the added mass in the airfoil motion. This term, generates unsteady loads, but no information is transmitted in form of wake vorticity.
Similarly, Coppens proposes a decomposition of the pitching moment coefficient.

Coppens' unsteady model implements rigorously the asymptotic approach that combines the lifting-line method and the unsteady thin-airfoil theory. When tested in realistic helicopter rotor cases, this development improved the prediction of unsteady loads on the blades (see [Le Bouar-Coppens 1999]). However, due to the

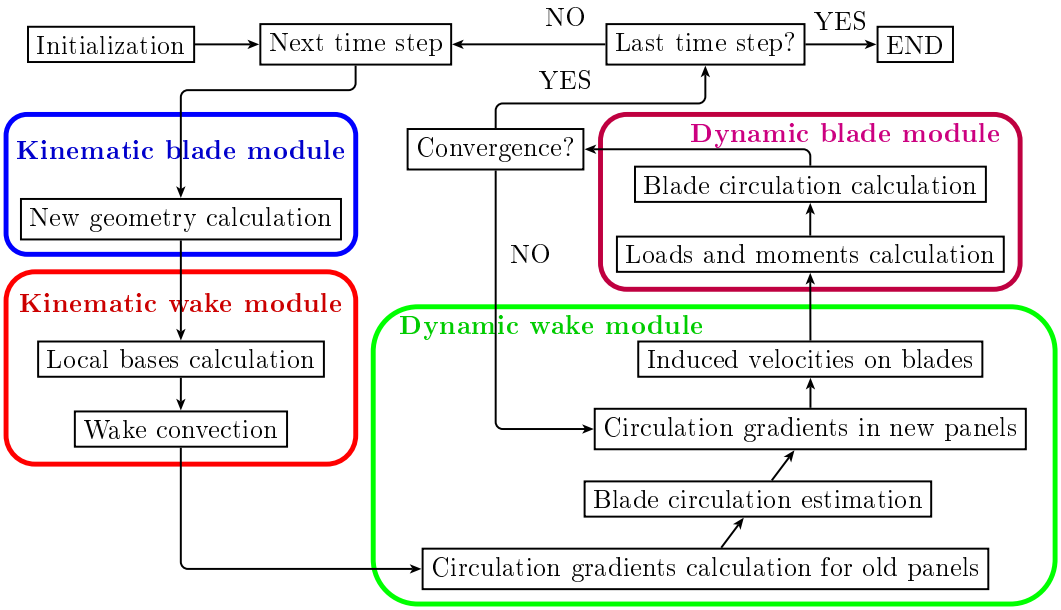


Figure 28: HOST-MINT code structure

generated instabilities in small time step computations, Coppens' unsteady model was not included when MINT wake module was implemented in HOST.

Instead of it, only the quasi-steady airfoil terms were implemented and assessed on helicopter rotor cases [Kruppa 2004]. The author identified that the predominant error came from neglecting the contribution from the vortex wake in the calculation of the derivative of the incidence. Indeed, the blade module receives the induced velocities from the wake model, without having access to the induced velocities derivatives or the wake history. Therefore, these derivatives are estimated based on the Meijer-Drees analytical inflow model.

Therefore, a number of studies were conducted by Onera and the Université d'Orléans in the following years in order to improve this unsteady model by implementing an unsteady lifting-line theory for general rotor blade shapes [Devinant 2002, Gallois 2003, Muller 2007]. Together with the derivatives of the induced velocities, these studies put forward another limiting hypothesis in the implemented approach: based on the asymptotic approach of the problem, it was shown that the effect of the unsteadiness on the wake vorticity were considered from the quarter-chord line, instead of considering them from the trailing-edge of the blade.

HOST-MINT code structure. Figure 28 shows a diagram of the HOST-MINT code structure for aerodynamic computations. First, two calculation paths can be identified: (1) an up-bottom *kinematic path*, where the motion of the elements is transmitted, and (2) a bottom-up dynamic path, where loads and moments are transmitted. In the case of MINT wake model, as it has been shown in Fig. 25, the Wake Model is linked under the Blade Model.

For each new time step, the position of the blade is modified to account for its rotation and deformation. This geometry is transmitted to the wake model as an array of points corresponding to the panel edges attached to the blade quarter-chord line. Each panel represents a blade section and its calculation point is at the half distance between these two edges.

With the new blade position, the Wake Module computes the local bases of the panels. The bases are two vectors indicating the position in space and the size of each panel. With this computation, MINT can account for the wake convection and deformation. Then, a row of new panels is emitted to link the convected wake panels with the edges of the blade sections.

Vorticity is conserved in MINT wake panels. However, due to the convection and deformation of the wake, the size of the panels may change. Therefore, circulation gradients must be recalculated to conserve constant vorticity in the panel surface. These circulation gradients are first computed in the old panels (all except the freshly-emitted panels).
Then, the circulation on the blade is estimated by a 2nd-order extrapolation of the circulation in the previous panels. As shown in Fig. 27, the circulation at the panel edges is estimated by interpolation. This interpolated circulation at edges is used then to determine the circulation gradients in the freshly-emitted panels. With this, the induced velocities can be computed on the calculation points.

These induced velocities are transmitted to the Blade Module in order to compute the aerodynamic incidence and Mach number of each blade section. These values are used as the input of two-dimensional airfoil data to obtain lift, drag, and pitching moment coefficients. The forces and moments at each section are then obtained by dimensioning the aerodynamic coefficients with the local density, velocity, and section span. Finally, the circulation of each blade section is linked to the lift by the Kutta-Joukowski condition.

The convergence is checked with respect to the initial estimation of the circulation or to the circulation in the previous sub-iteration. If convergence is not achieved, a relaxed new circulation value is calculated and used to re-compute the circulation gradients in the new panels. And thus, the loop is closed. When convergence is achieved, results are stored and the next time step can start.

Installation Effects in HOST

HOST-MINT simulations can take into account installation effects on propeller by a steady three-component velocity perturbation field depending on azimuthal and radial positions. The so-called "installed" simulations presented during this thesis consider the perturbation field induced by a spinner on the rotation plane of the propellers.
These case-dependent fields have been obtained by *elsA* CFD computations of a blade-off spinner configuration at a given incidence, depending on the test case. Velocities on the surface described by the rotation of the blade quarter-chord line have been extracted and stored in an ASCII input file before HOST simulations.

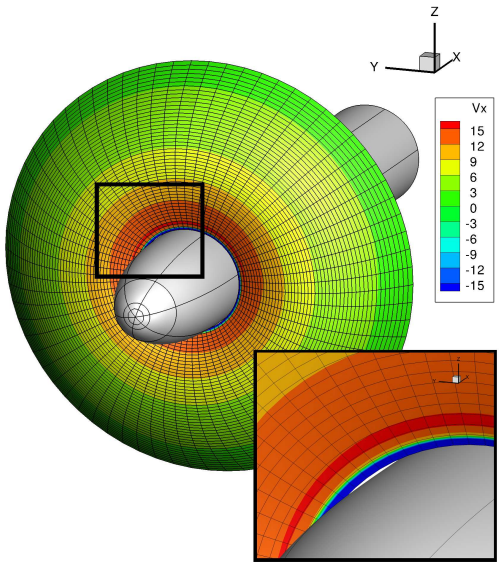


Figure 29: Absolute value of the perturbation velocity field for a propeller at high-speed conditions ($M_\infty = 0.7$) and at 3° of incidence

Figure 29 shows the magnitude of the velocity perturbation field for a high-speed test case at 3° of incidence.
Notice that three assumptions have been done in this process: (1) the perturbation field is not time-dependent in the fixed frame, (2) no wall effect near blade root is considered in the lifting-line formulation ($\Gamma = 0$ at root) and (3) the effect of the propeller on the spinner is neglected.

Main Hypothesis of the Lifting-Line in HOST

Compressibility and viscosity effects. The aerodynamic problem formulation in HOST combines a blade-element method for the near-wall problem and a wake model for the three-dimensional slipstream. On one side, the airfoil aerodynamic behavior is predicted from RANS simulations, and thus it takes into account two-dimensional viscosity and compressibility effects. On the other side, the three-dimensional slipstream is modeled by a wake of vorticity singularities in a potential uniform flow, thus neglecting compressibility and viscosity.

Chord effects. Both models are combined by considering, on one side, that the wake induces constant velocities along the chord of the blade section, represented by the quarter-chord line. On the other side, the vorticity shed at the freshly-emitted wake panels is obtained directly from the blade loading by the Kutta-Joukowski condition.
Considering constant induced velocities along the chord has the advantage to allow steady airfoil data to be used, including viscosity and compressibility. On the contrary, the approach neglects the effect of airflow unsteadiness along the chord.

Moreover, the wake is emitted at the quarter-chord line of the blade, instead of the trailing edge, which can induce some mismatches in the wake position for airfoils at large angles of attack.

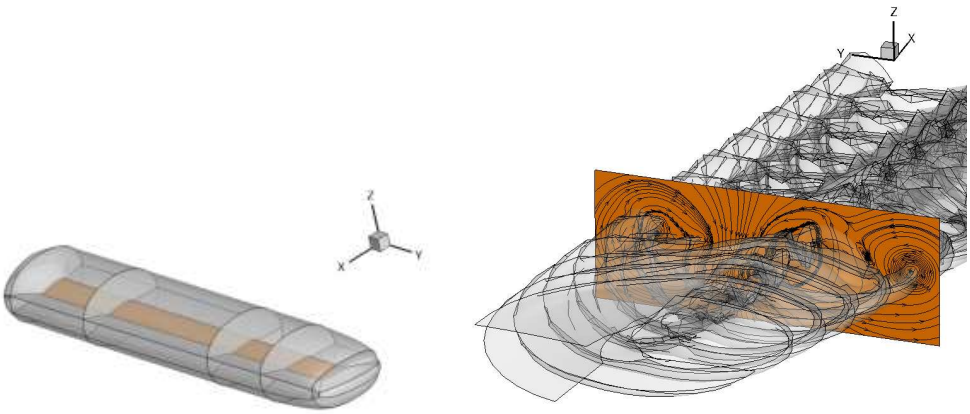
Three-dimensional flows. HOST simulations consider that each blade section behaves as a two-dimensional airfoil under a certain incidence and velocity. To account for three-dimensional effects, the local aerodynamic incidence is modified by the propeller slipstream and the relative velocity is modified by the local chord. Moreover, the airfoil normal to the quarter-chord line is considered.
However, these corrections cannot account for complex three-dimensional flow structures that form in highly-swept and low aspect ratio propeller blades. A clear example of this is the leading-edge vortex, a common structure that appears in highly-loaded swept blades [Nallasamy 1991], similar to the phenomenon observed on delta wings. This vortex decreases the pressure in the suction side of the blade and thus creates an important extra lift, which cannot be predicted by blade-element methods.

Computational Fluid Dynamics Solver: *elsA*

The simulation software used for aerodynamic analysis in the aeronautical industry is usually developed and maintained by Research Establishments or the companies themselves, instead of being provided by commercial software vendors. This is due to the fact that the high levels of accuracy and reliability required today in aerodynamic simulations can only be obtained through long-term expertise and innovative research in several domains: physical modeling, numerical methods, software efficiency and validation, and software validation by comparison with detailed experimental data.

elsA, *Ensemble Logiciel pour la Simulation Aérodynamique*, is the Onera software for complex external and internal flow aerodynamics and multidisciplinary applications. The *elsA* project started in 1997 at Onera as a way to create a multi-purpose aerodynamic solver that merged the main capabilities developed in previous Onera codes. *elsA* is based on a Object-Oriented design method and on an Object-Oriented implementation based on C++, Fortran and Python languages. The code covers a wide variety of applications, e.g. aircraft, helicopters, tilt-rotors, turbomachines, contra-rotating open rotors, missiles, launchers, etc. This capability to handle both internal and external aerodynamic problems is quite uncommon and it provides a key advantage: common CFD features can be shared between very different applications. The main goals of the project were to obtain:

- A co-operative support for research on physical and numerical modeling,
- A long-term easiness for capitalizing research results,
- A tool helping to investigate and understand flow physics,



(a) Multiblock topology of the near-wall blade grid

(b) MESIR wake geometry and induced velocity streamlines in a plane. 7A rotor in advancing flight

Figure 30: Two coupled computations: uRANS computation in *elsA* (left) and a lifting-line computation in HOST (right).

- A powerful multi-purpose tool for applied CFD and multi-physics,
- A communication path between research and industry,
- And a tool open to co-operative work

HOST/MESIR-elsA Coupling: RVA Module

A hybrid methodology to couple MESIR periodical free wake model with *elsA* CFD uRANS solver in the context of CSD/CFD simulations has been recently implemented in HOST and validated for realistic helicopter rotor geometries and flight conditions [Rodriguez 2012]. On one hand, the Eulerian *elsA* solver is used to compute the near-body aerodynamic field (see Fig. 30(a)). On the other hand, the Lagrangian model that covers the full domain includes a lifting line model and a potential wake model (see Fig. 30(b)). The Lagrangian wake is described by MESIR, which typically uses a time step equal to 10° of azimuth. Under this value, numerical instabilities start to appear due to the important singularity of the vortex filaments.

elsA already provides a python interface that allows the exchange of data as input or output during the computation with a CGNS/Python representation. The outer state of the non-reflection condition applied at the outer boundary of the blade mesh is modified at each node during the iteration thanks to a CGNS/Python structure provided in memory to the *elsA* code.

On the other side, a specific Python module has been developed for HOST based on Python/C/Fortran architecture. This module is called by a Python script executed by HOST code during simulations. The module having the same memory

context than HOST, it is able to access the wake model data at each time step. With the geometry and the vorticity of the wake, the module computes the induced velocities on a given mesh.

Rodriguez presents a loose coupling strategy where the information exchanged by files once per revolution. The outer boundary points of the Eulerian mesh are given to the Lagrangian model for a complete rotor revolution. The Lagrangian module computes and store in files the velocities induced by the rotor lifting-lines and wakes during a complete blade revolution. Moreover, HOST provides the blade kinematics and deformations to *elsA* in each blade section and time step. On the other side, *elsA* computes the near-wall flow and provides the sectional loads to HOST. The loose coupling replaces progressively the aerodynamic loads on the blade by CFD loads. Hence at convergence the circulation used in the wake model is totally coherent with the CFD loads and so are the induced velocities.

This strategy allows different time steps in the Eulerian and in the Lagrangian codes. However, as HOST simulations are limited to a 10° time step, the frequency content provided to *elsA* is not sufficient to transfer correctly the vortex structure. To increase the frequency content, instead of interpolating the induced velocities, an interpolation of the position and vorticity in the wake is proposed. Once the wake interpolation has been performed, induced velocities are computed on the boundary nodes of the Eulerian mesh. The interpolation time step can be chosen in the range between *elsA* and HOST time steps to ensure the accuracy of the vortex structure transfer.

The validation of this coupling strategy has been done on two helicopter rotor tests cases, that focus on high-advancing speed conditions and on the prediction of blade-vortex interaction (BVI) phenomena. Results equivalent to full-uRANS computations have encouraged the present work to, first, test this approach for single-rotating propellers in high advancing ratios, and then to extend this coupling module to HOST simulations under general flight conditions with a coupling strategy between MINT free wake and *elsA* code.

APIAN Single-Rotating Propeller

The Advanced Propulsion Integration Aerodynamics and Noise (APIAN) program was an European-funded research consortium to design a high-speed ($M \sim 0.7$) six-blade single propeller on a representative 50-seats aircraft configuration. The main industrial, technical and cooperative goals were: to improve passenger comfort and reduce the airport community noise with advanced propeller-driven aircraft, to create knowledge in the noise of advanced propellers installed on the airframe, to gain knowledge on the behavior of propeller-driven aircraft in high-lift configurations, to generate an experimental aero-acoustic propeller database for future European industry needs, to validate aerodynamic and acoustic propeller prediction tools, and to push forward previous synergies between European industry, research centers and academia.



Figure 31: APIAN propeller minimum-body configuration in Onera-S1MA wind tunnel facility

The project investigated first aerodynamics and acoustics of the isolated propeller, and then the effects of installation on the aerodynamic and acoustic propeller performance.
Four wind tunnel campaigns on two propeller geometries were involved: SNAAP, a legacy geometry from the previous program, to relate propeller performance to comparable measurements; and (2) APIAN, the new propeller configuration. The wind tunnel tests were: (1) minimum-body tests at DNW-HST transonic wind tunnel facility [Custers 1999], (2) minimum-body tests at Onera/S1MA transonic facility [Crozier 1999], (3) full-aircraft tests in the same facility [Crozier 2001], and (4) full-aircraft tests in DNW-LLF subsonic facility. Moreover, a number of CFD studies were conducted by the different members of the consortium [Dumas 1998, Boyle 1999, Amato 2000, Averardo 2000, Polacsek 2000, Bousquet 2000, Bousquet 2003].

The present study uses the results obtained during the wind-tunnel tests carried out at ONERA/S1MA facility at Modane (France) in 1999 [Crozier 1999]. S1MA facility is a continuous atmospheric sub/transonic wind tunnel with a circular test section of eight-meter diameter. The test matrix included sweeps in Mach number, rotational speed (RPM) and angles of incidence. Two different pitch angles were tested for high-speed ($M \sim 0.7$) and for low-speed conditions ($M \sim 0.2$).
The wind tunnel model was instrumented to measure: (1) global loads, measured by static and rotating balances, (2) blade surface pressures, measured by several arrays of Kulites, and (3) wake velocities, measured by five-hole probes located downstream the propeller.
The wind-tunnel setup is a classical minimum-body configuration, composed of a six-bladed propeller (APIAN) mounted on a spinner, as shown in Fig.31. The whole is supported by a non-rotating cylindrical sting. The rotating parts, blades and spinner, are attached to the sting by a static and a rotating balance.

In such a configuration, balances measure the loads generated by the spinner and

the blades, yet the objective is to determine the airloads produced by the propeller blades.
In order to consider only propeller loads, balance measurements in power-on tests have been corrected by loads measured during the blade-off tests. As it has been noted by Ortun [Ortun 2012], these corrections may not be adapted for the prediction of in-plane loads, as the spinner airloads change significantly under the presence of the rotating propeller. Pressure asymmetry on the spinner skin will generate additional horizontal loads. Moreover, the spinner incidence is decreased by the acceleration of the airflow due to the propeller. This may reduce the vertical force generated by the spinner with respect to the blade-off case.

Moreover, some mismatches are observed between CFD computation results obtained by Ortun and wind-tunnel test data, mainly in terms of propeller thrust and 1P loads phase lag evolution with the incidence. Ortun explains thrust mismatches by a lack of mesh convergence and, for a particular case, he shows that differences are reduced when considering a more refined mesh. Moreover, the author evokes the possibility of an error in the spinner loads corrections, as well as some uncertainties in the CAD blade shape, whether it is a hot or a cold form, i.e. including or not deformations due to aerodynamic and inertial loads. Concerning 1P loads phase lag, it is shown in the cited article that spinner side force corrections in wind-tunnel tests were not adequate: they did not take into account side loads generated on the spinner due to the presence of the propeller.
Finally, the technical report of wind-tunnel tests [Crozier 1999], thanks to indirect check criteria, evokes an underestimation of the propeller shaft power measured by the rotating balances. Indeed, there was no direct way to check what measured the rotating balances, but data from previous minimum-body tests warned about a possible underestimation in the measured shaft power, around 10%.

AI-PX7 Contra-Rotating Open Rotor

Although a number of wind tunnel campaigns have been conducted in the last years by Airbus, for a better diffusion of the results, these experimental data have not been used in the present study. Moreover, all CROR simulations have been performed on the AI-PX7 generic open rotor configuration (see Fig. 32). This open rotor geometry was designed by Airbus within the Clean Sky JTI-SFWA European project [Negulescu 2013]. It has been used to test, validate, and develop several numerical approaches and to improve the understanding of the complex aerodynamics around open rotors (see for example [Stuermer 2008, Béchet 2011, François 2011, Giauque 2012, Colin 2012, Ben Nasr 2013]).

The geometry is an 11×9-blade pusher configuration with a rotor diameter of $D = 4.2672$m (14ft). Inlet and exhaust are not modeled in the nacelle shape. Table 6.1 gives a short overview of the AI-PX7 configuration features in high-speed conditions. The blade geometry presents a sweep distribution that varies from negative angles near the hub to positive angles near to tip, as shown in Fig. 32. Open

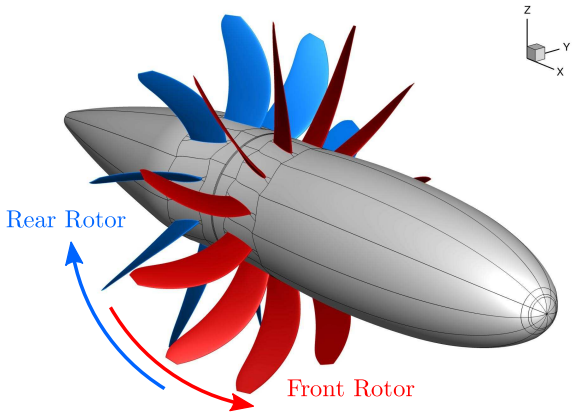


Figure 32: The generic open rotor configuration AI-PX7 designed by Airbus.

rotor blades need to be swept to decrease the magnitude of shock waves structures in high-speed conditions. The blade has a low thickness-to-chord ratio, similar to current transonic fan blades, and a low camber throughout its span. Rear rotor blades are cropped at their tip by 10% with respect to the front blade and their chord is increased in order to generate a similar thrust compared to the front rotor. Rear rotor cropping enables to decrease the impact of tip vortices convected from the front rotor to the rear rotor and thus it may reduce the overall emitted noise. The nacelle corresponds to a transonic design with the objective of diminishing as much as possible the increase in local Mach number by the nacelle. The flow is slightly accelerated by the front part of the nacelle: for example, in high-speed conditions, the Mach number increases from 0.73 in the freestream to 0.75 just upstream of the front rotor.

Chapter 1

HOST Assessment on APIAN Single Propeller Case

Contents

1.1 Parametric Study and Best Practices 73
1.2 High-Speed Simulations Assessment with Wind Tunnel Data and CFD computations 78
1.2.1 Wind Tunnel Data 78
1.2.2 *elsA* CFD Computations 78
1.2.3 HOST-MINT Simulations 80
1.2.4 Incidence Effect 83
1.2.5 Advance Ratio Effect 88
1.3 Way Forward in HOST Simulations 91

The main goal of this chapter is to assess the capability of HOST comprehensive code to predict accurately the key parameters in the preliminary design of propellers and open rotors. To do so, a representative case of an advanced single-rotating propeller has been chosen. First, a parametric study is conducted to quantify the impact of several input parameters on propeller performance and 1P loads. With this study, some best practices for propeller simulations in HOST can be established. Finally, performance and 1P loads predicted in HOST-MINT simulations are compared to wind tunnel data and CFD computations for several high speed conditions. In particular, the effect of the incidence and advance ratio are studied at constant Mach number.

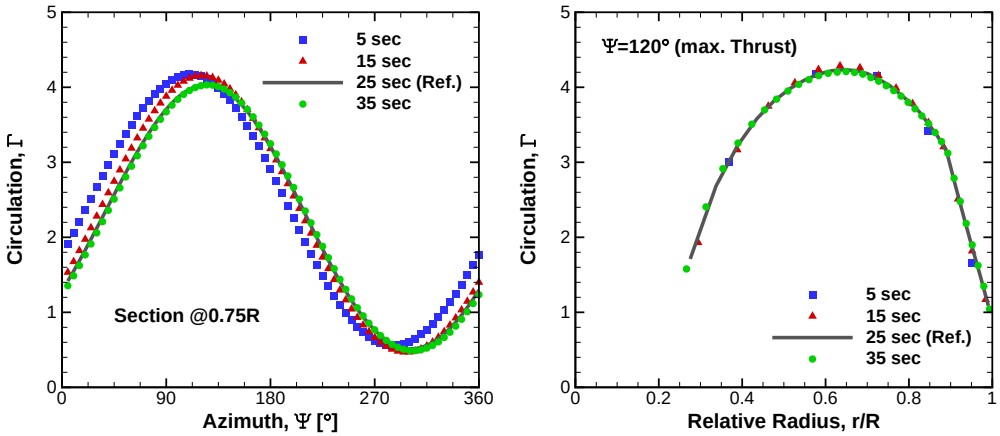
1.1 Parametric Study and Best Practices

A number of parameters in HOST-MINT simulations are assessed on a representative case of an isolated advanced propeller APIAN, described in the *Methods and Tools* Chapter, in high-speed flight conditions and under a certain incidence. The considered airflow conditions are summed up in Table 1.1, which corresponds to one of the experimental points that will be used for comparisons hereafter.

The reference HOST-MINT computation (Ref.) considers a time step equivalent to 5° of azimuth, a deformed wake of 72 panels and 25 blade sections. Table 1.2 shows the results obtained for the different cases. Each case modifies a parameter

Table 1.1: Wind tunnel test conditions for APIAN minimum-body configuration. Wind tunnel case No.1149

Mach No.	[–]	0.7
Incidence	[°]	3.
Rotational Speed	[min^{-1}]	8639.
Advance Ratio, J	[–]	3.278



(a) Azimuthal variation of Γ

(b) Radial variation of Γ

Figure 1.1: The effect of the number of sections on the blade circulation

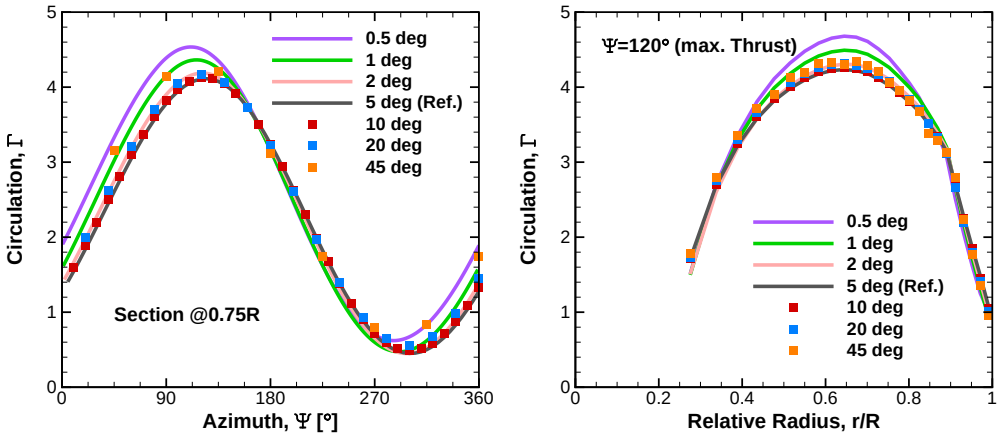
with respect to the reference case in order to assess its impact on thrust, power, and 1P load norm and phase. The percentages and the degrees represent the difference with respect to the reference.

Effect of number of blade sections. The number of blade sections has a slight impact on propeller thrust, power, and 1P load norm for a wide range of values, i.e. from 5 to 40 sections. On the contrary, the 1P load phase is very sensitive to this parameter: only a half of the phase lag is predicted when the blade uses 5 sections. The phase lag increases when increasing the number of sections, without clearly converging to a limit value.
A similar behavior can be deduced from the evolution of the circulation along a revolution (see Fig. 1.1).

When decreasing the number of blade stations without modifying the time step, the aspect ratio of the panel is increased. Currently, no refinement technique is applied on the radial direction when the aspect ratio becomes too important. Using a 2×2-point Gaussian quadrature rule can lead to numerical errors for important aspect ratios and to convergence problems in some extreme cases.

Table 1.2: Sensitivity of performance and 1P loads to several simulation parameters

	Case	Thrust [N]	Power [kW]	Norm 1P [N]	Phase 1P [°]
	Ref.	243.776	66.044	195.019	29.998°
Sections	**5**	−1.624%	−1.392%	−0.412%	−14.087°
	15	−0.159%	−0.119%	−0.287%	−3.588°
	35	+0.044%	+0.042%	+0.049%	+1.91°
	40	+0.047%	+0.043%	−0.007%	+2.693°
Time Step	**0.5**	+5.778%	+5.178%	+6.702%	−12.948°
	1	+2.283%	+1.974%	+4.871%	−8.679°
	2	+0.303%	+0.252%	+0.605%	−3.471°
	10	+0.855%	+0.774%	−0.486%	−0.837°
	20	+2.896%	+2.617%	−1.374%	−3.002°
	45	+8.236%	+7.32%	+1.076%	−10.02°
Wake Length	**9**	+6.948%	+5.957%	+3.876%	−0.3°
	18	+1.816%	+1.535%	+1.214%	+0.026°
	36	+0.33%	+0.275%	+0.179%	−0.019°
	144	−0.054%	−0.046%	+0.082%	+0.019°
No Deformation		+0.086%	+0.037%	+1.559%	−0.151°



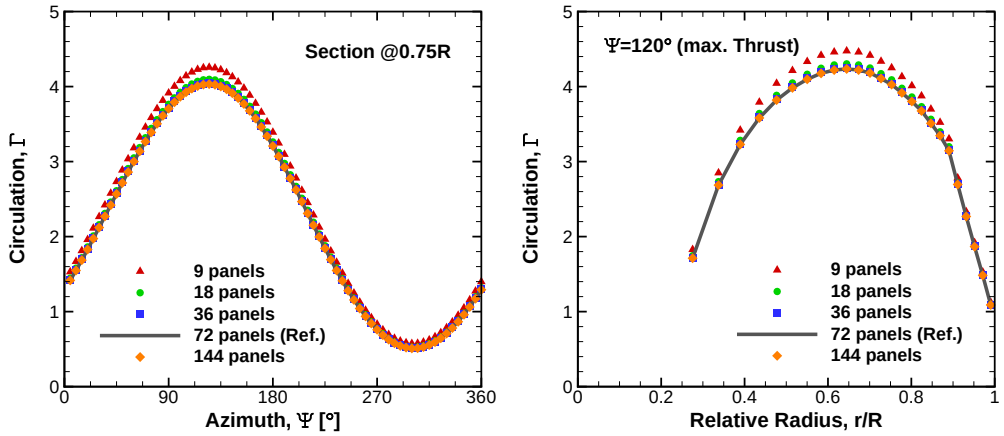
(a) Azimuthal variation of Γ at $r = 0.75R$ (b) Radial variation of Γ at $\Psi = 120^{c}irc$

Figure 1.2: The effect of time step on the blade circulation

Effect of time step. In these cases, global results appear to be more sensitive. The reference case seems to present a minimum in the thrust prediction, but differences with simulations at 2 and 10° are still small. Moreover, for very short and very long time steps, no convergence is achieved. This can be explained by the fact that the panel aspect ratio plays an important role in the accuracy of the numerical integrations. Both, very short and very long time steps imply large aspect ratios that can induce numerical errors, and can justify these differences in global performance predictions.

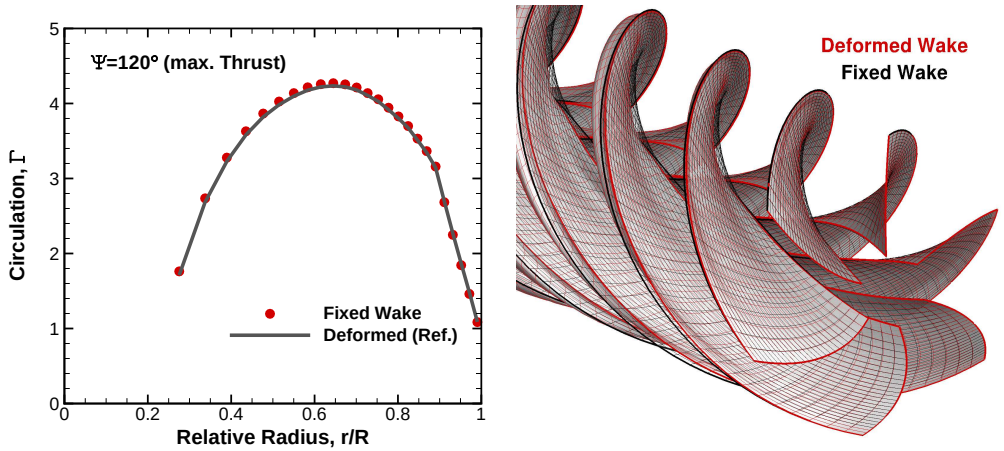
Effect of the wake length. As MINT is a free-wake model, time-marched simulations are needed to convect the wake. To reduce computational time and memory requirements, the wake is truncated above a certain number of panels. Several simulations have been computed to determine the effect of wake length, or number of panels, on the global performance, 1P loads, and blade load distribution. As it can be noticed in Table 1.2, 18 panels are enough to obtain an error of less than 2% on thrust, power, and 1P load norm. It is also noticed that 1P phase lag is almost insensitive even to wake panels that are relatively close to the blade.

Effect of the wake deformation. Wake deformation has a small impact on global propeller performance and blade loads. Only an effect of less than 2% on the 1P load norm can be attributed to the wake deformation. Nevertheless, the wake deformation is more likely to play an important role when considering the propeller in low-speed conditions or when blade-vortex interactions occur. Indeed, in low-speed cases, blades are more loaded and thus more vorticity is shed in the wake. Hence, the free wake rolls-up more quickly and presents a more deformed pattern. Because of the lower advance ratios in these conditions, the position of the returning wake may have a non-negligible impact on propeller loads.



(a) Azimuthal variation of Γ (b) Radial variation of Γ

Figure 1.3: The effect of wake length on the blade circulation



(a) Radial variation of Γ (b) Wake deformation

Figure 1.4: The effect of wake deformation on the blade circulation

To sum up, this parametric study has helped first to establish the best practices in terms of wake length and deformation for a high-speed test case in incidence. Moreover, it has helped to notice that it is not straightforward to establish a convergence criteria in terms of global performance when using singularity methods. Indeed, these type of methods being based on the outer formulation of a problem approached asymptotically, the solution is very dependent on the panel size and aspect ratio. On one side, singularity problems appear for very small panels. On the other side, the error in the numerical integration of the $\vec{v}_{\text{ind}}$ increases for large panel sizes or aspect ratios. Therefore, to determine the number of sections and the time step to be used, an analytical choice has been done based on the blade geometry characteristics and the highest frequency of the aerodynamic phenomena to be captured.

1.2 High-Speed Simulations Assessment with Wind Tunnel Data and CFD computations

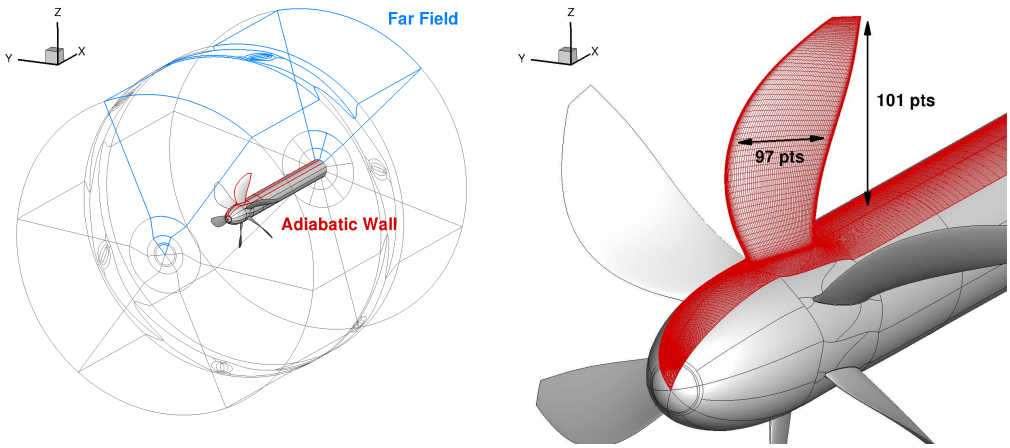
This section presents the comparison between wind tunnel data of a single-rotating propeller at high-speed conditions and several HOST-MINT simulations to assess the effect of the incidence and rotational speed on propeller performance, 1P loads, and blade load distribution. Moreover, HOST-MINT simulations are also compared to CFD uRANS computations using *elsA* solver. Local cross-section sweep and hub effects are also included in HOST-MINT simulations, in order to assess its impact on the propeller behavior.

1.2.1 Wind Tunnel Data

In order to assess HOST-MINT simulations, experimental data from wind tunnel tests at S1MA Onera facility have been used (see Methods and Tools chapter for more details). In the present study, comparisons focus only on a series of representative high-speed tests with the same blade pitch angle ($\theta_{\text{exp}} = 57.0°$). Moreover, due to the available data, only global propeller measurements could be used for code assessment. Five points of the same run varying the propeller incidence from 0 to 3° but with constant rotational speed are first considered. Then, two other points are added to the last point of the previous run, in order to assess rpm effects. In these cases the rotational speed is modified from 8600rpm to 9600rpm, while maintaining a constant incidence of 3°.

1.2.2 *elsA* CFD Computations

CFD computations have been performed using the *elsA* [Cambier 2008] uRANS solver. A full-annulus computational domain is considered, including the 6 propeller blades and the spinner downstream (see Fig. 1.5). It is meshed with a multi-block structured grid. The cylindrical domain extends 4 times the propeller radius in all directions. Autogrid [Num 2004] mesh generator has been used to generate one



(a) Boundary conditions and outer domain (b) Mesh on blade and hub

Figure 1.5: RANS mesh details for *elsA* CFD simulations

channel of the propeller (3.2 million nodes), which has then been used to generate the full propeller mesh (19.2 million nodes). All the walls (the blades and the hub) are modeled with an adiabatic condition of adherent wall; whereas the outer boundaries are modeled by a non-reflective condition, in order to prevent the reflection of acoustic waves. Infinite velocity and rotational speed are attributed to all the blocks of the mesh. A second-order centered scheme with Jameson's artificial viscosity is used for the spatial discretization [Jameson 1991]. The time discretization uses the 3-level backward Gear scheme with Newton sub-iterations [Gear 1966]. The turbulence model is Kok's k-ω with SST correction [Kok 2000]. Simulations were performed with a time step equivalent to 1° propeller rotation. Seven propeller rotations were needed to reach convergence, starting from the airflow of the case without incidence. In last rotations, 15 Gear sub-iterations were used.

Figure 1.6 shows the evolution of propeller thrust along the *elsA* simulation. The plot corresponds to the APIAN high-speed test case at 3° of incidence and it has been initialized by the convergenced high-speed case but without incidence. Note that propeller loads are converged from the 6^{th} revolution. The residual oscillations at a 6/rev frequency are due to the superposition of the six blade loads oscillating at 1/rev.

First comparisons of CFD computations at experimental blade pitch with wind tunnel test measurements showed an important thrust underestimation, as noticed by Ortun [Ortun 2012]. Thus, a change of 0.7° has been done in the blade pitch to obtain the same levels of thrust in the case without incidence ($\theta_{\text{elsA}} = 57.7°$). Then, the same pitch angle is used for the computations with the propeller in incidence.

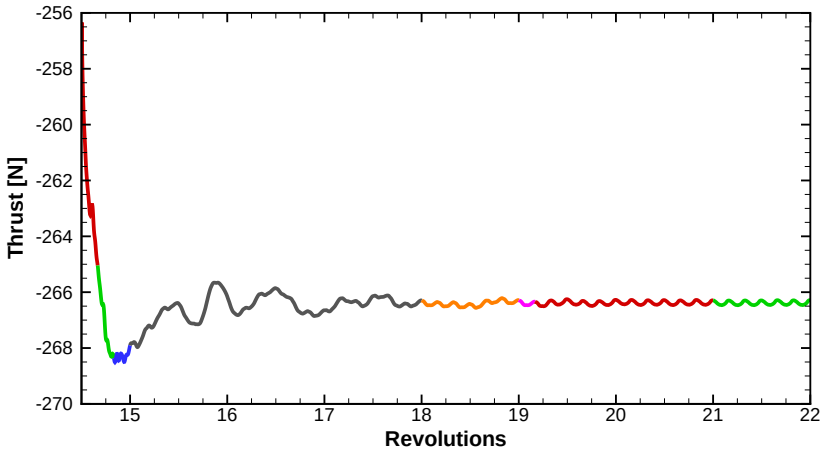


Figure 1.6: Convergence of propeller thrust for the Case No. 1149

1.2.3 HOST-MINT Simulations

HOST simulations have been performed using a time step equivalent to $5°/it$ rotation, which has proven to be a good compromise between low computational costs, i.e. several minutes of restitution time per simulation, and fair accuracy in terms of global loads, i.e. $\pm 2\%$ difference in thrust with respect to $1°/it$ simulations. A 4th-order Runge-Kutta time stepping scheme has been used. For a $5°/it$ time step simulation, a 2.5-diameter length wake is sufficient to converge in thrust, which corresponds to 55 panels in high-speed simulations.

Two parameters in HOST-MINT simulations are explained hereafter: the local sweep correction and the effects of installation.

Effects of local sweep. The effects of local sweep can be taken into account at each blade cross-section in HOST simulations by a two-dimensional correction of the Mach number, based on the swept wing theory developed by Jones [Jones 1945]. This correction considers that each cross-section at constant span position y behaves as an infinite wing of constant chord $c(y)$ at the local airfoil sweep angle $\Lambda(y)$. This induces a correction both on the airfoil Mach number and on the airfoil data as shown in Fig. 1.7. The local relative Mach number is corrected by the sweep as follows: $M_{2D} = M_{3D} \cos\Lambda$. The airfoil geometry is extracted from the cross-sections (red dashed line), normalized by the local chord and thickened $e_{2D} = e_{3D}/\cos\Lambda$ to represent the airfoil normal to the quarter-chord line (blue dashed line). Finally, the calculated lift and drag coefficients (2D) are corrected as follows to obtain the equivalent 3D aerodynamic coefficients:

$$C_{\mathrm{L}_\infty}(y) = C_{\mathrm{L}_\perp}(y)\cos^2\Lambda \quad ; \quad C_{\mathrm{D}_\infty}(y) = C_{\mathrm{D}_\perp}(y)\cos^3\Lambda \tag{1.1}$$

Figure 1.8 compares two HOST simulations with and without sweep corrections for the high-speed propeller under incidence used in the previous section. When the

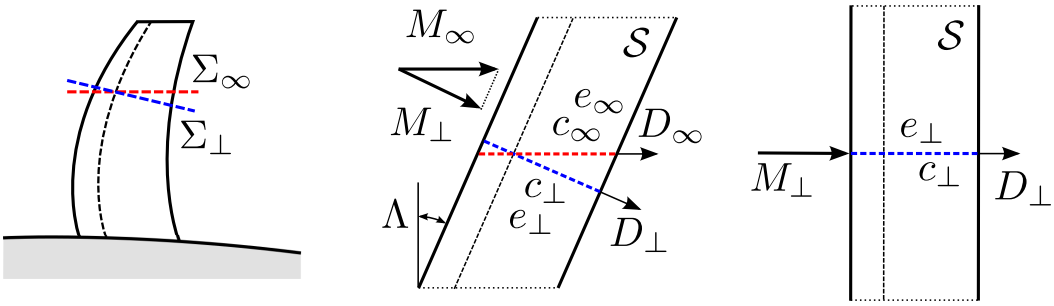


Figure 1.7: Infinite swept wing theory applied to propeller simulations

sweep correction is activated, it leads to an important decrease in the circulation along almost all the blade span. This is due to the decrease in the local Mach number due to sweep. On the contrary, when no correction is applied, the relative freestream velocity in the last blade sections reaches nearly supersonic Mach numbers. This means that airfoils close to the blade tip would present important supersonic areas and hence important shock waves would appear near the airfoil skin. Moreover, if no sweep correction was applied, it would mean that the compressibility effects on a straight blade and on a swept blade would be the same. However, experience tells that increasing the blade sweep angle tends to diminish shock waves intensity and compressibility effects.

Sweep correction decreases only the two-dimensional compressibility effects but neglects the three-dimensional structures of the shock waves. Nevertheless, this sweep correction is a first step to better account for compressibility effects on a three-dimensional blade under transonic relative velocities. This is why it is a commonly accepted practice in blade-element methods, like the approach in HOST code, to use sweep corrections on the incident Mach number and on the aerodynamic coefficients [Bousquet 1985, Gardarein 1991].

In the present study, all HOST-MINT simulations considered sweep corrections in airfoil data, as it is a first approach to better take into account the aerodynamic behavior of a swept blade.

Effects of installation. The steady effect of the nacelle or other elements of the airframe can be taken into account by a steady two-dimensional field of the perturbation velocities in Cartesian axes. The perturbation fields for each flight condition have been extracted from computations with the *elsA* CFD code on a blade-off nacelle geometry.
Moreover, a simplified wall condition is also available in HOST-MINT. It imposes a constant circulation on the first blade section and removing the effect of the root vortex filament (see Fig. 1.9).
These two corrections to account for installation effects can be activated together or separately. In this study, the perturbation field is first considered alone (*installed simulations*) and then the wall condition is added (*installed & hub model*) to assess their impact on propeller performance and blade load distribution.

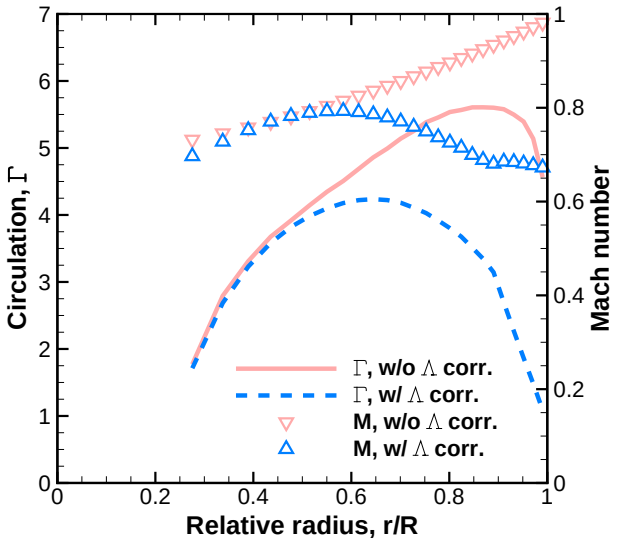


Figure 1.8: Sweep correction effect. Circulation and Mach number spanwise distribution at $\Psi = 120^{\circ}$ (maximum load).

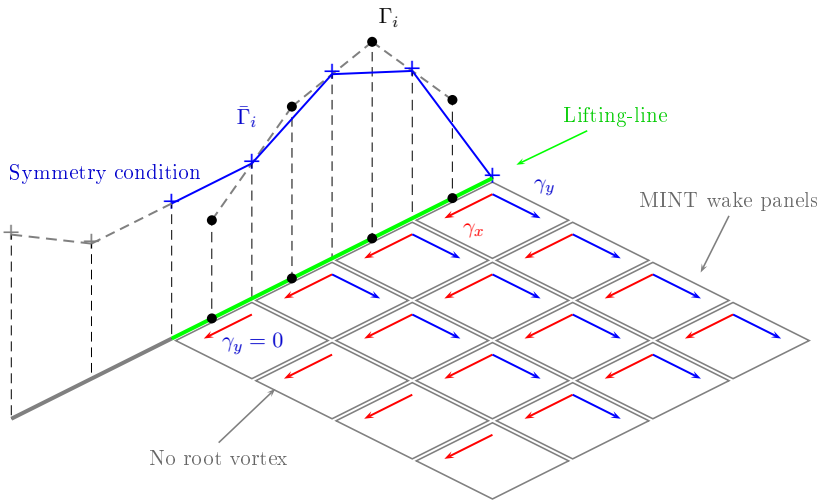


Figure 1.9: Hub model as implemented in MINT wake model

Table 1.3: Incidence sweep in APIAN experimental high-speed tests

Test number	Mach No. [–]	Incidence [°]	RPM [min^{-1}]	J [–]
1145	0.700	0.01	8623.	3.269
1146	0.699	1.00	8632.	3.268
1147	0.700	1.48	8638.	3.272
1148	0.700	2.02	8639.	3.273
1149	0.700	3.00	8639.	3.278

In the following studies, a number of HOST-MINT simulations have been computed, considering different models:

1. *Isolated* HOST-MINT simulations: only the propeller blades are taken into account, which means that no velocity perturbation field due to the spinner is considered. Moreover, relative Mach number and airfoil data are corrected to account for sweep effects.

2. HOST-MINT simulations including *installation effects*: a velocity perturbation field on the propeller disk is added to take into account the influence of the spinner on the propeller.

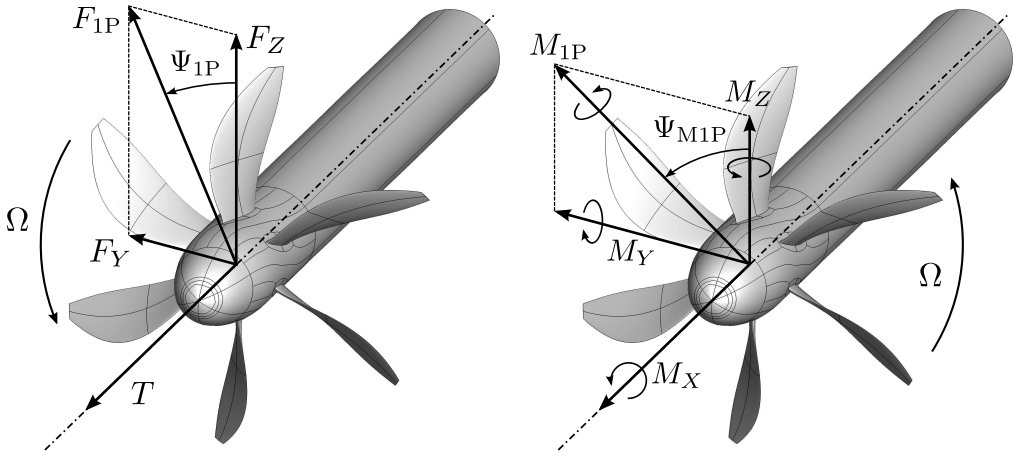
3. HOST-MINT simulations including *installation effects and the hub model*: in addition to the perturbation field, the hub model is activated in these simulations.

1.2.4 Incidence Effect

A high-speed run in the wind tunnel campaign has been chosen to compare HOST-MINT simulations with experimental data and CFD uRANS computations in *elsA*. Table 1.3 presents a summary of the main flow conditions. Simulations are performed at experimental thrust levels by changing the blade pitch in HOST-MINT and in *elsA* simulations.

Propeller performance. A number of parameters are compared hereafter: thrust coefficient (C_{TH}), power coefficient (C_{PW}), 1P load coefficient (C_{1P}), 1P load phase lag (Ψ_{1P}), 1P moment coefficient (C_{M1P}), and 1P moment phase lag (Ψ_{M1P}). They are calculated as follows:

$$\begin{aligned} C_{\text{TH}} &= \frac{T}{\rho N^2 D^4} \quad ; \quad C_{\text{PW}} = \frac{P}{\rho N^3 D^5} \\ C_{\text{1P}} &= \frac{\sqrt{F_{\text{Y}}^2 + F_{\text{Z}}^2}}{\rho N^2 D^4} \quad ; \quad \Psi_{\text{1P}} = \arctan\left(\frac{F_Y}{F_Z}\right) \\ C_{\text{M1P}} &= \frac{\sqrt{M_{\text{Y}}^2 + M_{\text{Z}}^2}}{\rho N^2 D^5} \quad ; \quad \Psi_{\text{M1P}} = \arctan\left(\frac{M_Y}{M_Z}\right) \end{aligned} \tag{1.2}$$



(a) Load terms definition

(b) Moment terms definition

Figure 1.10: Definition of loads and moments

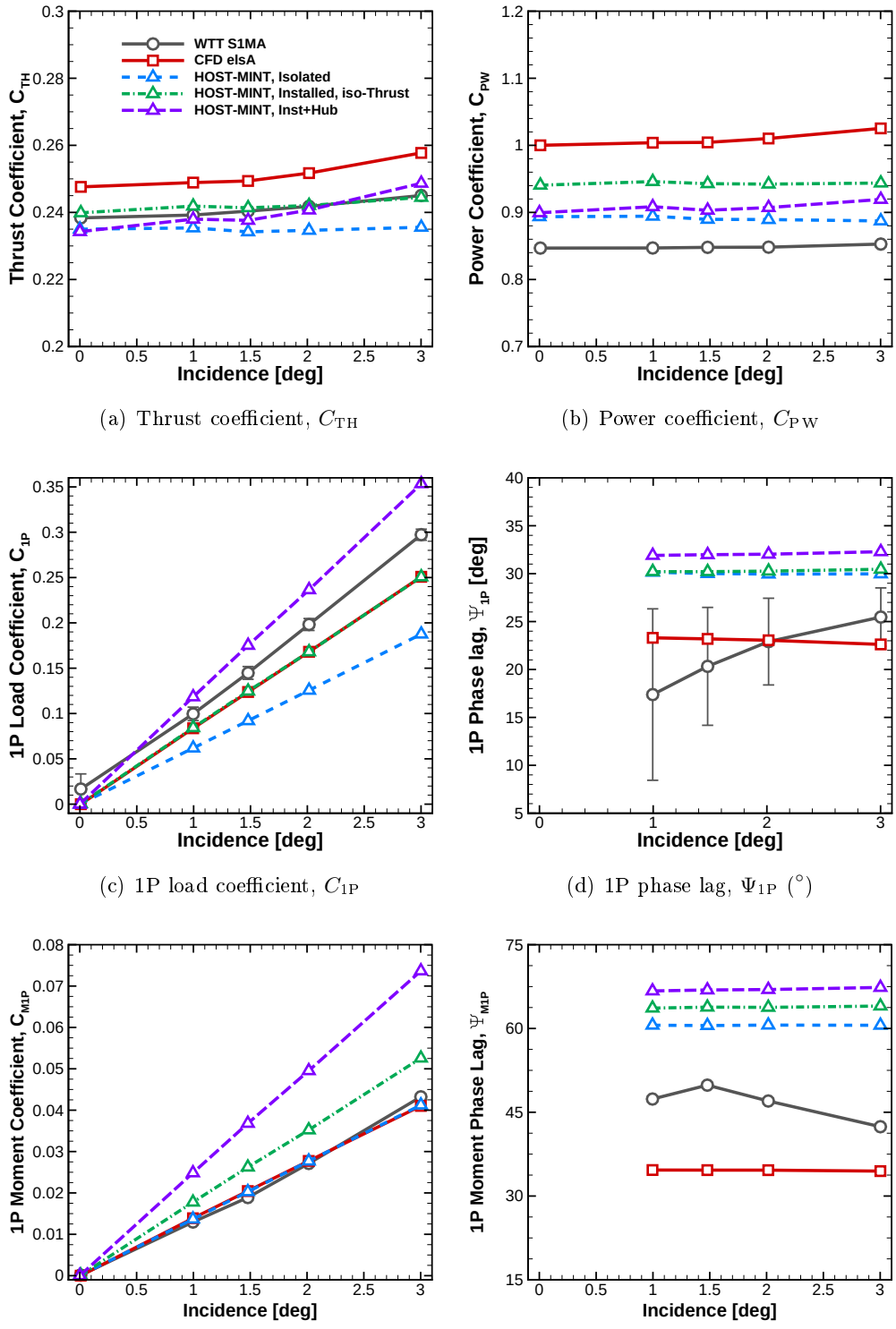
Notice first the non-zero 1P loads modulus at 0° incidence in the wind tunnel data. As it has been explained by Ortun [Ortun 2012] this may come from an error in the balances calibration. Hence, in the present study, 1P loads at zero incidence have been considered as a constant offset in the measurement of the balances for all the test cases. The plotted error bars show the upper and lower limit of the 1P loads modulus and phase when considering this offset.

Comparisons in Fig. 1.11 show a good agreement between *isolated* HOST-MINT simulations and wind tunnel test data in terms of thrust and power. However, we can also notice an underestimation of the 1P load coefficient (around 40%) and a slight overestimation of the 1P phase lag (from 5 to 15°).

When installation effects are added in HOST simulations, an underestimation of thrust is obtained. Consequently, the pitch angle should be modified by +0.7° in order to obtain the experimental thrust levels. In those cases, as shown in the upper left plot in Fig. 5.1, the power is overestimated by about 10%.

Several reasons can explain these power offsets. First, only the *cold CAD blade shape* was available for simulations, thus blade deformations were neglected in simulations. Second, as it has been explained in the *Methods and Tools* Chapter, the technical report indicated that the *rotating balances* used in the wind tunnel tests may underestimate the shaft power. Third, in order to reach experimental thrust levels, an increase of 0.7° in pitch angle was necessary in the simulations. Changing the blade pitch leads to an increase in the blade incidence and thus to an increase in the *separated boundary layer* near blade tips, which are aerodynamic conditions more difficult to be predicted correctly with RANS simulations or with two-dimensional airfoil data. Finally, neither in *elsA* CFD simulations nor in HOST airfoil data, *laminar-turbulent transition* effects are taken into account.

Notice that simulations considering *installation effects* give a 1P load norm that



(a) Thrust coefficient, C_{TH}

(b) Power coefficient, C_{PW}

(c) 1P load coefficient, C_{1P}

(d) 1P phase lag, Ψ_{1P} (°)

(e) 1P moment coefficient, C_{M1P}

(f) 1P moment phase lag, Ψ_{M1P} (°)

Figure 1.11: Incidence effect on propeller performance and 1P loads. Comparison between wind tunnel data, CFD uRANS computations and HOST-MINT simulations

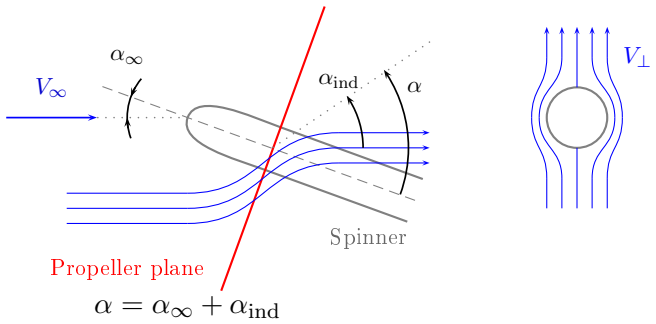


Figure 1.12: Spinner effect scheme (side and front view)

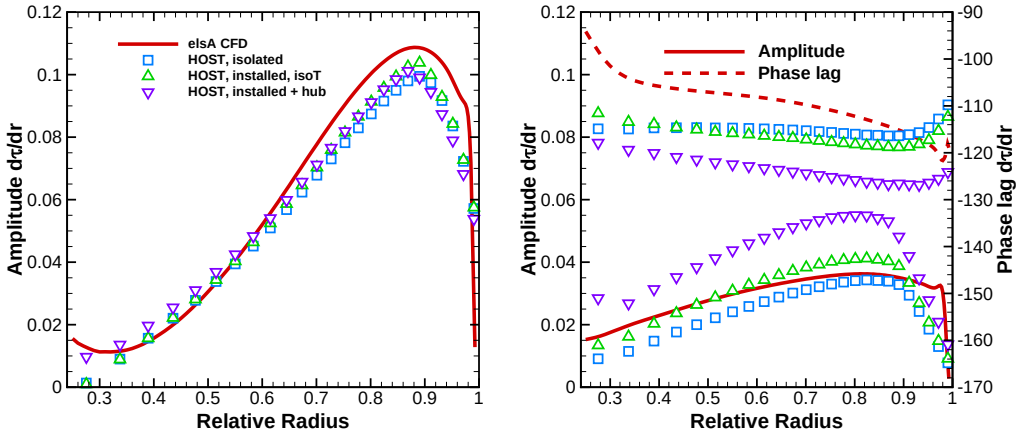
is closer to wind tunnel measurements and very close to CFD simulations. As shown by the scheme in Fig. 1.12, considering the perturbation velocities around the spinner gives an additional induced incidence to the airflow, which increases the incidence asymmetry between downward and upward moving blades, and so increases the 1P load modulus.

When regarding 1P phase lag, while CFD computations predict values within the error bars for all the incidences, it can be noticed that HOST simulations tend to overestimate these phase lags by 5° to 10°.

A very good agreement in terms of 1P moment coefficient can be observed between *isolated* HOST simulations and experimental data. However, when adding the *installation effects*, HOST-MINT tend to overestimate the norm of these in-plane moments. On the other side, significant offsets are observed in 1P moments phase lag. Even though, the levels of mismatch are similar to those obtained in *elsA* computations. These mismatches in 1P moment predictions may come from the fact that the lifting-line approach is less accurate in the prediction of loads close to the blade tips. As the contribution of a given blade section on 1P moments corresponds to the amplitude of thrust oscillations multiplied by the lever arm, a slight error in the thrust prediction near blade tips may induce important 1P moment mismatches.

Simulations considering *installation effects and the hub model* give results in terms of thrust and power that are similar to the results of *isolated* simulations. When the hub model is activated, no blade pitch modification is needed.
Notice the important contribution to the 1P load norm, when compared to *isolated* or *installed* HOST simulations. An overestimation is however observed in comparison with experimental data (around +17%). On the other side, a slight increase in 1P phase lag can be observed (+2°).
Finally, 1P moment coefficient predictions are not satisfactory both in terms of norm and phase lag.

Blade loading. In order to better understand the previous comparisons, load distributions along the blade are now considered. A common parameter to make



(a) Mode 0 (mean)

(b) Mode 1 (1/rev)

Figure 1.13: Blade load distribution modes in Case No. 1149. *elsA* computations are compared to three HOST simulations: isolated, with installation effects, and with installation effects and hub model.

this comparison is the spanwise gradient of the thrust coefficient $\partial\tau/\partial\xi$:

$$\frac{\partial\tau}{\partial\xi} = \frac{\partial T}{\partial r}\frac{R}{\rho_\infty N^2(2R)^4} \tag{1.3}$$

Figure 1.13 shows the load distribution comparison between *elsA* and the same three HOST-MINT simulations exposed in the previous paragraph. Only the two first modes of the Fast-Fourier Transform are shown: zero mode (mean value) and first mode (one per revolution, 1/rev). All HOST-MINT simulations give similar results in terms of mean blade loading (left-hand side plot), and predict correctly the load evolution for the central part of the blade. However, an underestimation can be noticed from the $0.7R$ span to the tip of the blade. This load underestimation generates the already observed thrust mismatches. Moreover, notice that the load near the blade root is not well predicted by *isolated* and *installed* HOST simulations, while the *hub effects* gets closer to *elsA*.

When focusing on the 1/rev mode, more important differences are noticed. On one side, the solid red line and the symbols around it represent the norm of the 1/rev mode, which can be linked to the norm of 1P loads. On the other side, the dashed red line and the symbols around it represent the phase lag of the 1/rev mode, which can be linked to the phase lag of 1P loads. When installation effects are considered, the 1/rev norm gets closer to *elsA* results, while keeping almost the same phase lag than in *isolated* simulations. However, important mismatches are induced when the *hub model* is considered. Notice the overestimation with respect to CFD results of both the mode norm and the mode phase lag. The implemented hub model, which should have only an important effect near the blade root, impacts in fact all the blade loading.

Table 1.4: Rotational speed sweep in APIAN experimental high-speed tests

Test No.	**Mach No.** [–]	**Incidence** [°]	**RPM** [min^{-1}]	**J** [–]
1149	0.700	3.00	8639.	3.278
1155	0.700	3.00	9064.	3.125
1163	0.700	3.00	9539.	2.969

1.2.5 Advance Ratio Effect

The *advance ratio effect* stands for the change in the aerodynamic behavior of a propeller when varying its rotational speed keeping the same infinite upstream conditions. Increasing the rotational speed N of a propeller means decreasing its advance ratio J, as:

$$J = \frac{V_\infty}{N.D} \tag{1.4}$$

where V_∞ is the freestream velocity and D is the propeller diameter.

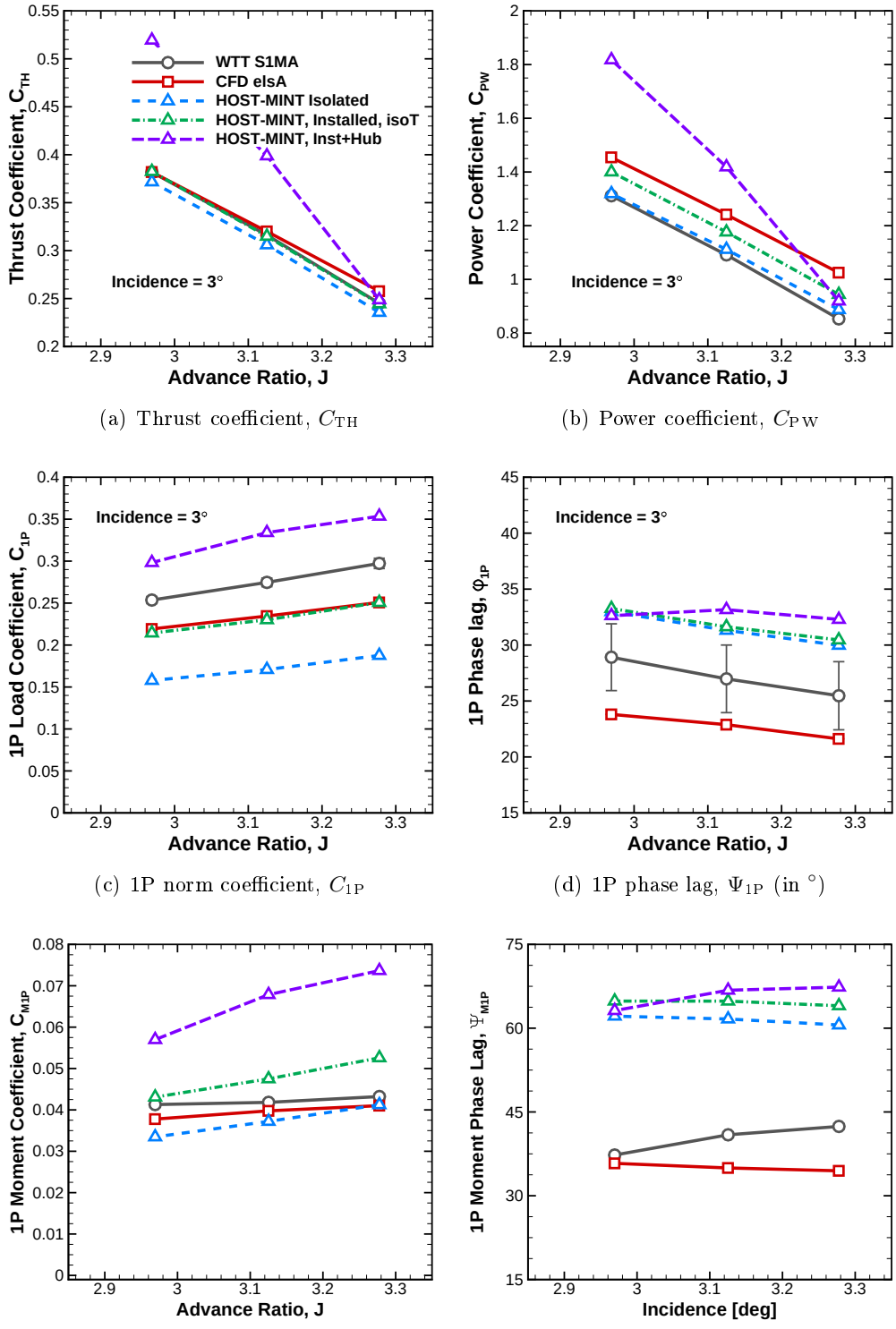
The last experimental point in the previous subsection, at 3° is now used together with two other points at different rotational speeds in order to assess HOST-MINT simulations with respect to experimental data and CFD computations. Table 5.2 shows the three considered test cases.

Comparisons between wind tunnel measurements, and isolated and installed HOST simulations have been performed (see Fig. 1.14). HOST simulations consider again the installation effects in two ways: on one side, only the perturbation field (*installed*) and, on the other side, the hub model is activated and added to the perturbation field (*inst+hub*).

Propeller performance. The same parameters as for incidence effect comparisons have been used, i.e. thrust coefficient, power coefficient, 1P load coefficient and 1P load phase lag. Based on the experimental case at 3° of incidence, the same blade pitch is used for all the cases at different rotational speeds.

The upper plots in Fig. 5.4 show that thrust and power slopes are very well captured by all HOST simulations, except when considering the hub model. As in the previous comparisons, however, a power overestimation is also noticed (about 11% offset) for the three different advance ratios, but results are still between experimental and CFD results. Again, installation effects increase 1P load modulus, getting closer to experimental results (-12%) and almost obtaining the same values as in CFD computations. 1P load phase lag is also overestimated of $\sim 5°$ for all advance ratios.

Finally, for 1P moment coefficient and 1P moment phase lag, the results are similar to what was observed in the *incidence effect* comparisons: the norm of the 1P moment in HOST installed simulations is slightly overestimated, whereas important offsets of the 1P moment phase lag can be observed. Similar to the thrust predictions,



(a) Thrust coefficient, C_{TH}

(b) Power coefficient, C_{PW}

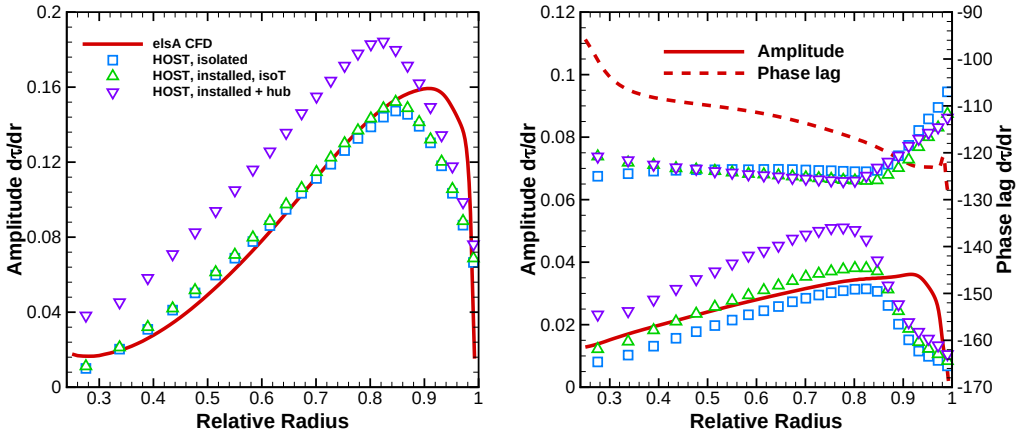
(c) 1P norm coefficient, $C_{1\mathrm{P}}$

(d) 1P phase lag, $\Psi_{1\mathrm{P}}$ (in °)

(e) 1P moment coefficient, C_{M1P}

(f) 1P moment phase lag, Ψ_{M1P} (in °)

Figure 1.14: RPM effect on propeller performance and 1P loads. Comparison between wind tunnel data, CFD uRANS computations and HOST-MINT simulations



(a) Mode 0 (mean)

(b) Mode 1 (1/rev)

Figure 1.15: Blade load distribution modes. *elsA* computations are compared to three HOST simulations: isolated, with installation effects, and with installation effects and hub model.

the hub model presents a non-satisfactory evolution for 1P moments. For these cases at high propeller incidence, however, *elsA* simulations present smaller mismatches both in terms of norm and phase lag.

Blade loading. Figure 1.15 shows the spanwise gradient of the thrust coefficient on the blade for the Case No. 1163 ($\alpha = 3°$ and $J = 2.969$). As no sufficient experimental data was available, the comparison only takes into account an *elsA* CFD computation, and the three HOST-MINT simulations previously studied: *isolated*, *installed*, and *installed with hub model*.

The left-hand side figure shows the mean value of $\partial\tau/\partial\xi$. Notice that, while *isolated* and *installed* simulations are able to follow *elsA* results in the mid-part of the blade, HOST-MINT overestimates this values when including the *hub model* effects. This fact could be already observed in the overestimation of the propeller thrust in Fig. 1.14.

On the contrary, all HOST-MINT simulations present significant mismatches in mean blade load near tips (from $0.85R$ span to blade tip). This region of the blade being highly swept and highly loaded, shows the shortcomings of the quasi two-dimensional approach in the blade element theory, and seems not to be well adapted in the current form. Further considerations on these sweep effects will be presented in the Chapters 4 and 5.

Similar results are obtained for the norm of the 1/rev mode. While *isolated* and *installed* simulations are close to *elsA* results for the mid-part of the blade, simulations considering the *hub model* overestimate *elsA* results. On the contrary, notice the important underestimation of the 1/rev norm in all HOST-MINT simulations. As it will be detailed in the study of CROR 1P loads in Chapter 6, this reduction

in blade load oscillations occurs due to the important airfoil incidences close to the blade tip. These incidences correspond to the stalled region in the two-dimensional airfoil data used in HOST, where the lift coefficient is much less sensitive to the incidence oscillation than in the linear region of the $C_L - \alpha$ polar. Thus, for the same α oscillation amplitude, much less important load oscillations are obtained.

Finally, all HOST-MINT simulations present an important overestimation of the phase lag (around $+15°$). Three zones can be distinguished in the blade: near root, medium, and near tip. Notice that the offset in the phase lag increases when approaching the blade root. This evolution can be attributed to the blade chord effects, as the blade chord effects increase when approaching the blade root. Indeed, a phase lag offset may be induced between *elsA* and HOST-MINT simulations because the point of emission of the wake is not the same: while *elsA* sheds the wake at the trailing edge, HOST-MINT sheds it from the quarter-chord line. For the near-root and near-tip regions, different 1/rev phase evolutions are observed and can be attributed to the wall effects and to the stalled region, respectively.

1.3 Way Forward in HOST Simulations

The present chapter has established some best practices in the propeller simulations using HOST. Moreover, it has shown the ability of HOST to predict propeller performance and 1P loads with a certain degree of accuracy compared to high-speed wind tunnel data and accurate uRANS simulations. When the blade pitch is adapted to achieve experimental thrust levels, the power predicted by HOST is overestimated but values are still in the zone between experimental data and CFD predictions. Moreover, by taking into account the installation effects in HOST simulations, the predictions of the 1P load norm are closer to both experimental data and CFD simulations (offsets around 10%). The time-marched scheme used in HOST simulations and the MINT free-wake model have enabled a fair prediction of 1P loads phase lag, which cannot be obtained with classical quasi-steady lifting-line methods (see [Bousquet 2003]). However, there is still a certain offset in the 1P phase lag (5 to $10°$). Finally, it has been noticed that the simplified hub model as currently implemented in HOST-MINT fails at predicting the effect of the propeller advance ratio.

An in-depth comprehension of these global results has been achieved by comparing load distributions along the blade predicted by *elsA* and HOST-MINT simulations. A Fast-Fourier Transform has helped to link the blade loading to the global propeller parameters: *mean* load values to the propeller thrust, *1/rev mode norm* to the 1P load modulus, and *1/rev mode phase lag* to the 1P load phase lag.
Good predictions of the mean and 1/rev norm blade loads were obtained for *isolated* and *installed* simulations. On the contrary, significant offsets still exists between HOST-MINT and *elsA* in the phase lag of the 1/rev mode.
Finally, blade load analysis confirmed that the hub model is not well adapted to take into account wall effects in the case of a propeller at high-speed conditions.

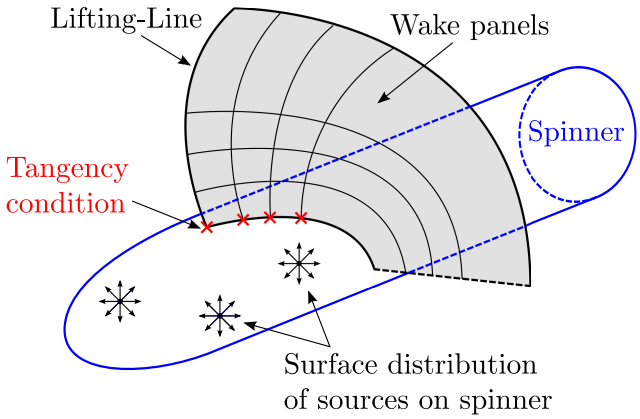


Figure 1.16: Rigorous wall effect implementation in the case of a propeller

The failure of the simplified hub model could be expected from the fact that the hub model removes the effect of the root vortex but without adding additional induced velocities to simulate the wall effect. Indeed, a rigorous implementation of the hub model should impose a tangential velocity condition to the wake panels in the blade root section in order to simulate this wall effect (see Fig. 1.16). As shown in the scheme, one solution could be a surface distribution of sources on the skin of the spinner. The intensity of the sources should be found by inverting the filled matrix of the problem, in order to impose the tangency condition to the panels at the blade root. Then, these sources should provide an additional term to the induced velocities on the calculation points and on the wake panels.
This solution, though being likely to provide a better blade load prediction close to the root, can be very CPU time-consuming depending on the number of panels used to discretize the spinner. Moreover, once the intensity of the sources is calculated, additional CPU time is needed to add the velocities induced by the sources on the calculation points and on the wake panels.
An intermediate solution could be considered in the future to better account for wall effects in HOST-MINT.

This preliminary comparison has conducted the study to a more detailed analysis of the aerodynamic mechanisms behind 1P loads, in Chapter 2, and the development and implementation of an airfoil model for unsteady airflow conditions, in Chapters 3 and 4. Finally, an Eulerian/Lagrangian coupling is going to be proposed in order to provide a better three-dimensional unsteady airflow resolution in Chapter 7.

Chapter 2

A Physical Insight into Propeller 1P loads

Contents

2.1 Theodorsen's Theory: A Two-Dimensional Analogy 93

2.2 Quantifying the Impact of Aerodynamic Mechanisms on 1P Loads 95

2.2.1 Main Contributors on 1P Load Phase Lag 98

As it has been described in *Methods and Tools* Section, HOST Blade Module uses steady two-dimensional airfoil data obtained from experimental measurements or numerical computations, thus neglecting all the unsteady phenomena on the airfoil. However, the aerodynamic behavior of an airfoil under unsteady airflow conditions at a given geometrical incidence can be very different from the steady one at the same geometrical incidence.

This chapter presents first an analytical study to estimate the characteristic reduced frequencies on the blades of an advanced propeller under a 1/rev oscillating airflow. This 1/rev oscillation aims at representing the 1/rev variation in the local angle of attack of an airfoil in the blade when the propeller is placed under a certain incidence. Then, different aerodynamic mechanisms at the origin of 1P load phase lag are assessed by a series of HOST simulations. The singularity methods, relying on linearized theories, allow a decomposition of the global solution as the superposition of different independent simpler solutions. Therefore, these methods are particularly well adapted to determine the contribution of individual aerodynamic mechanisms on a studied phenomenon.

2.1 Theodorsen's Theory: A Two-Dimensional Analogy

In a propeller working at a certain incidence with respect to the airflow, blades are experiencing a periodic incidence variation with frequency 1/rev. In order to estimate the importance of the unsteady aerodynamics, a two-dimensional analogy can be done between an isolated airfoil under a harmonic motion and a given airfoil in a blade of a propeller in incidence.

One of the first models developed to solve aeroelasticity problems for unsteady (harmonic) two-dimensional airflow was the Theodorsen's theory [Theodorsen 1935].

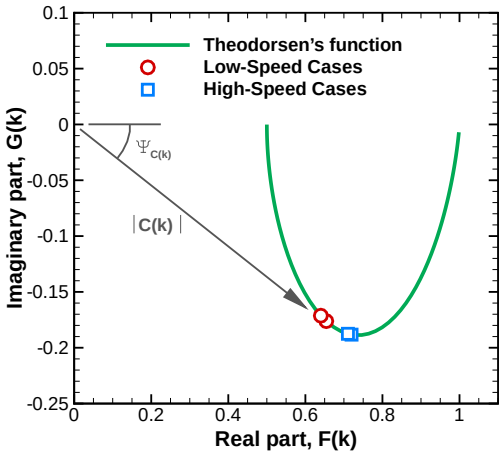


Figure 2.1: Theodorsen's function, $C(k)$

First, this model considers an incompressible two-dimensional flow around an airfoil under a heave and pitching sinusoidal motion. Second, the problem is linearized by considering small airfoil oscillations around its mean position. Finally, only the lifting problem is solved, the airfoil is assimilated to a flat plate, and hence no thickness effect is considered. Therefore, the lift and the pitching moment are obtained in terms of, on one side, the instantaneous derivatives of the airfoil motion (pitch and plunge) and, on the other side, the "history" of the airfoil motion. This second term, as we are placed in the case of a harmonic motion, depends on the complex function $C(k)$, also called Theodorsen's function, where k stands for the reduced frequency, $k = 2\pi fc/(2V_\infty)$. Theodorsen's function links the amplitude and the phase of two sinusoidal functions: on one side, the unsteady lift of an airfoil oscillating at the reduced frequency k, and, on the other side, the quasi-steady lift or the lift of an airfoil with oscillating frequency $k \to 0$.

Four representative advanced propeller test cases from APIAN wind-tunnel tests are considered to estimate the reduced frequencies linked to 1P loads. Table 2.1 shows the resulting reduced frequency k, the amplitude of Theodorsen's function $|C(k)|$, and the phase lag of Theodorsen's function $\phi_{C(k)}$ obtained for the four test cases. Figure 2.1 shows the real and imaginary part of the function in the complex plane, as well as the position of the considered test cases. We can notice that, for these reduced frequencies, Theodorsen's function predicts around 30% reduction in the amplitude and 15° of phase lag in the unsteady forces with respect to the quasi-steady case.

This analogy has shown the impact that unsteady aerodynamics can have on the prediction of airfoil loads at conditions that are similar to those of an advanced propeller. As it has been noted in the Chapter *Methods and Tools*, HOST already contains an unsteady correction. However, this correction considers only the effect of non-circulatory terms and the quasi-steady effect of the airfoil pitch motion. However, it does not consider the phase induced by the $C(k)$ function, which comes from

Table 2.1: Theodorsen's function $C(k)$ estimation for APIAN wind tunnel test conditions. Radius at 75% span $R_{75} = 0.188$m, chord at 75% span $c_{75} = 0.094$m.

Test No.	**Mach No.** [–]	**RPM** [min^{-1}]	**U** [m.s^{-1}]	**k** [–]	$\|C(k)\|$ [–]	$\phi_{C(k)}$ [°]
1145	0.7	8622	404.188	0.21	0.744	14.66
1159	0.7	9566	423.84	0.223	0.734	14.79
956	0.2	6204	189.25	0.323	0.677	15.07
972	0.2	8455	233.703	0.357	0.663	14.98

the induced velocities due to the unsteadiness in the wake circulation. While unsteady terms due to the airfoil motion tend to reduce the phase lag between unsteady and quasi-steady motion, wake terms (linked to $C(k)$ function) tend to increase this phase lag. In the following section, among other causes, this simplified unsteady model will be added in HOST simulations in order to assess its impact on propeller 1P loads.

2.2 Quantifying the Impact of Aerodynamic Mechanisms on 1P Loads

Singularity methods, like the lifting-line theory, calculate the perturbation of the velocity field at one spatial point by the addition of the influence of a series of singularities on that point (sources, sinks, doublets or vortices). The contribution of each element of the aerodynamic model can thus be easily discriminated in such kind of methods by taking into account each contribution individually. This strategy is used hereafter.

In *Physical mechanisms behind 1P loads* Subsection possible sources of 1P loads in propellers have been exposed. Among them, and focusing on 1P load phase lag, HOST is able to predict the following:

1. *Wake geometry effect*: Modeled by modifying the deformation and the convection direction of the wake. It enables to determine the contribution due to the distance between the current blade and neighbor wakes.

2. *Effect of the emitted wake* Γ: Modeled by changing the wake length. It enables to determine the contribution of the vorticity shed in the wake on induced velocities.

3. *Unsteady aerodynamic effect*: Including or not a simplified unsteady airfoil model. It enables to determine the contribution of the unsteady airflow.

On the contrary, due to model limitations, HOST will not be able to simulate hysteresis due to shock waves or dynamic stall and, as we are considering rigid blades, no aeroelastic phase lag effect is going to appear.

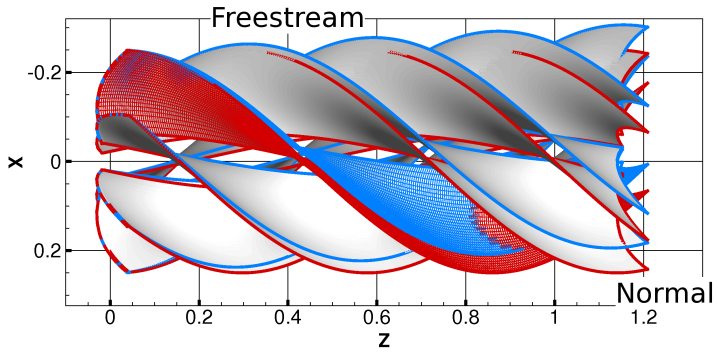


Figure 2.2: Wake convection following the freestream velocity and following the normal to the propeller plane

An Advanced Propeller Representative Case. To determine the contribution of each of the three considered sources, a study has been done taking the aerodynamic conditions of one of the available wind tunnel test cases: $M = 0.7$, 8639 rpm, 57° pitch angle, and 3° of incidence.

The *reference case* has been chosen by a study of thrust convergence: 250 wake panels, 1°/iteration, and no unsteady aerodynamic correction. The contribution of each element of the model has been quantified by comparison with this reference case (marked in red in all the tables).

Wake geometry effect. This study compares, on one side, the effect of wake deformation and, on the other side, the effect of wake convection for a prescribed wake form. Figure 2.2 shows two prescribed wakes with different convection directions: one following the freestream (V_∞) and the other following the normal to the propeller plane ($\perp$). Table 2.2 shows the thrust (T), the vertical force (F_Z), and the side force (F_Y). The last two columns show the differences with respect to the reference simulation in terms of 1P norm ($\Delta(F_{1\mathrm{P}}\%T)$) and 1P phase lag ($\Delta\phi_{1\mathrm{P}}$), where:

$$F_{1\mathrm{P}}\%T = \Delta\left(\frac{\sqrt{F_Y^2 + F_Z^2}}{T}.100\%\right) \tag{2.1}$$

It can be noticed that the wake deformation has almost no effect on phase lag prediction as deviations remain below the $\Delta\psi$ corresponding to our time step. However, convection direction, i.e. the difference in distance to the wake between the blade at $\psi = 0°$ and the one at $\psi = 180°$, has around a 10% weight in the global phase lag.

Effect of the emitted wake vorticity. Two types of simulations are compared: first, a series of simulations with different wake lengths, in order to determine the impact of near wake induced velocities; and second, a simulation for an isolated blade, in order to determine the impact of neighbor *near wakes* on the considered

Table 2.2: Full wake case test vs. Prescribed wakes (normal and V_∞):

Case	T	F_Z	F_Y	$\Delta(F_{1P}\%T)$	$\Delta\phi_{1P}$
Ref.	249.27	187.96	71.986	80.745N	20.956°
Prescribed ∞	249.14	189.76	73.883	0.991	0.317
Prescribed $\perp$	249.62	193.78	65.959	1.259	−2.159

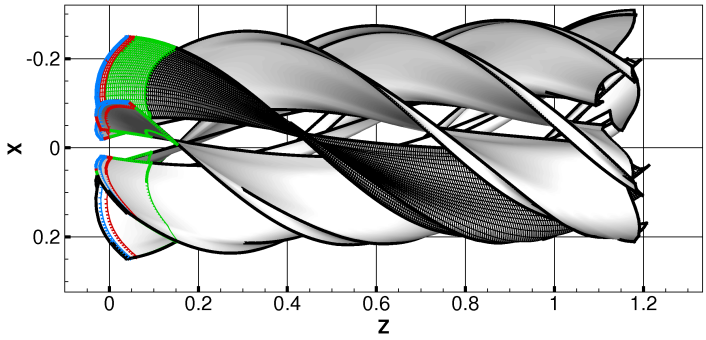


Figure 2.3: Number of panels in the wake: 2, 5, 25 and 275 (full wake)

blade. This last simulation could only be performed with a two-bladed propeller due to code limitations. Thus, we are supposing that the effect of the opposite wake is negligible. Then, the loads calculated on a blade over a cycle were used to virtually recompose a sort of six-bladed propeller in order to obtain almost constant loads and of the same order of magnitude compared to the other calculations. Figure 2.3 shows MINT wake for different number of panels: 2, 5, 25 and 275 panels. Table 2.3 shows the results obtained for these comparisons. It can be stated that, on the one hand, the near wake from the considered blade generates around 55% of the phase lag, while the neighbor near wakes add around 8%. In fact, almost all the phase lag is induced by the near wakes.

Table 2.3: Full wake vs. Near wake:

Case	T	F_Z	F_Y	$\Delta(F_{1P}\%T)$	$\Delta\phi_{1P}$
No wake	490.81	466.27	5.062	+14.261	−20.334
2 panels	440.36	318.16	69.735	−6.780	−8.593
5 panels	387.15	272.3	72.336	−7.971	−6.079
25 panels	287.76	206.56	72.281	−4.695	−1.670
2 blades, 25 panels	342.01	229.44	69.018	−10.688	−4.214
Ref.	249.27	187.96	71.986	80.745N	20.956°

Table 2.4: Full wake with or without unsteady aerodynamics:

Case	T	F_Z	F_Y	$\Delta(F_{1P}\%T)$	$\Delta\phi_{1P}$
Ref.	249.27	187.96	71.986	80.745N	20.956°
Unsteady, $1°/it$	252.29	206.07	54.68	+3.761	-6.095

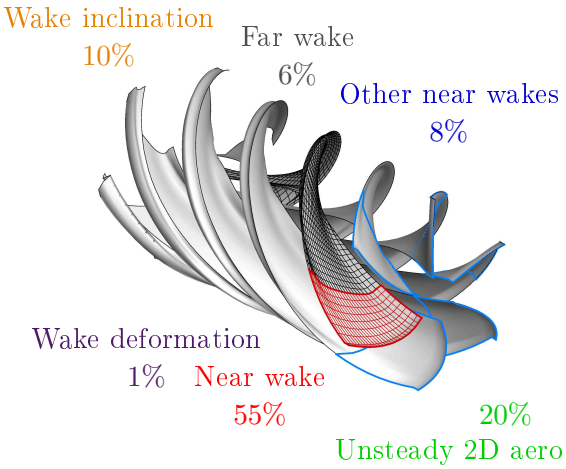


Figure 2.4: Contribution of each model element to the 1P load phase lag.

Unsteady aerodynamic terms. An additional simulation has been performed to see the impact of airfoil motion aerodynamic terms, as implemented in the official version, on the phase lag. These corrections being quasi-steady, they increase the in-phase component of the 1P loads and so they reduce the phase lag. We can notice in Table 2.4 that these terms modify the phase lag by around 20% with respect to the reference case.

2.2.1 Main Contributors on 1P Load Phase Lag

Figure 2.4 shows the contribution of each of the model elements on the prediction of 1P phase lag. The major impact coming from the *near wake* and the *unsteady airfoil corrections*, it seems interesting to deepen the study on these two domains in order to model better the key physical sources of 1P load phase lag.

As it has been explained in the *Methods and Tools* Chapter, the current unsteady model considers only the effects of the airfoil motion but neglects the unsteady contribution of the two-dimensional near wake that is shed from the trailing edge. Consequently, it will be the objective of the next Chapter to implement and assess the effect of considering the whole unsteady terms (airfoil and wake) on the 1P loads phase lag prediction. To do so, Chapters 3 and 4 present the study of two methods to implement an unsteady thin-airfoil theory in the HOST-MINT three-dimensional lifting-line code by using the matched asymptotic approaches method.

Part I

Unsteady Airfoil Model

Chapter 3

Analyzing an Unsteady Curved Lifting-Line Method (UCLL)

Contents

3.1 An Unsteady Curved Lifting-Line Theory 101
3.1.1 Theoretical Basis 101
3.1.2 A Numerical Implementation of the UCLLT 105
3.2 Outer Domain. The Singular Panel 105
3.2.1 The Doublet Formulation 106
3.2.2 The Vortex Formulation 111
3.2.3 Hess' Equivalence for Singular Panels 112
3.2.4 Current Implementation in the AILE Code 115
3.3 Inner Domain. Two-Dimensional Wake in Lifting-Line Formulation 116
3.4 Theoretical Analysis of the Model 116
3.4.1 Inner Domain. Airfoil Model 116
3.4.2 Outer Domain. The Singular Panel 118
3.4.3 Remarks on the Model 118

The main objective of this chapter is to critically analyze an unsteady curved lifting-line (UCLL) theory that can be adapted to the asymptotic approach of the lifting-line theory implemented in HOST. The solution proposed and implemented in a wing code by Muller during his PhD thesis is analyzed to understand its strengths and weaknesses.

3.1 An Unsteady Curved Lifting-Line Theory

3.1.1 Theoretical Basis

As it has been justified by Van Dyke [Van Dyke 1964], lifting-line problems can be solved with a singular perturbation formulation by introducing the Matched Asymptotic Expansion (MAE) technique into the solution of the problem. This fact was exploited by Guermond and Sellier [Guermond 1991] to extend Van Dyke's lifting-line theory to the case of swept and curved wings in unsteady flows. Under the assumption of low frequency oscillations, Devinant [Devinant 1999] proposed

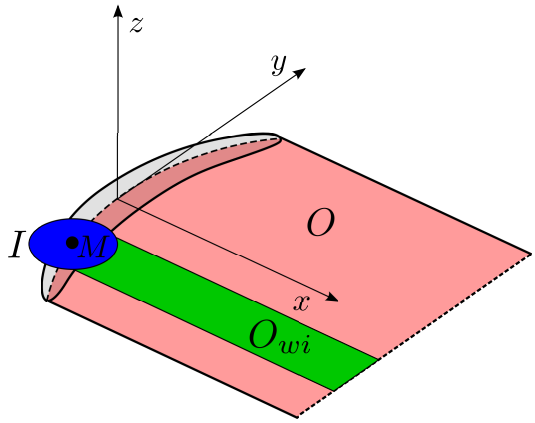


Figure 3.1: The wing and its wake are divided into several calculation domains.

a formulation of the problem adapted for numerical applications of the lifting-line theory. Based on this, Muller [Muller 2007] fully implemented Guermond's theory in the AILE code, for the unsteady simulation of swept and curved wings.

In this asymptotic approach the problem is divided into two main domains (see Fig. 3.1): the two-dimensional airfoil and its wake on one side, and a classical lifting-line problem on the other side. These two domains are linked by imposing the continuity of the wake vorticity between the inner domain (I) and the outer domain (O), which leads to the consideration of a third domain (O_{wi}).

The implicit equation of the circulation $\Gamma(M)$ can be written as indicated in Eq. (3.1).

$$\Gamma = \pi c \cos\Lambda \left(U_\infty \alpha + w_{I \cup O_{wi}} - w_{O_{wi}} + w_O + w_c \right) \tag{3.1}$$

where:

- $w_{I \cup O_{wi}}$: represents the velocity induced by the domain $I \cup O_{wi}$, which has a pure two-dimensional origin. Based on the linearized unsteady thin-airfoil theory, we obtain Eq. (3.2) for the case of a pitching and plunging airfoil.

$$\begin{aligned} w_{I \cup O_{wi}}(y,t) &= \dot{h}(y,t) + \frac{c}{2}\dot{\alpha}(y,t) \\ &+ \frac{1}{\pi c U_\infty \cos\Lambda} \int_{c/2}^{+\infty} \left(\sqrt{\frac{\nu + c/2}{\nu - c/2}} - 1 \right) \gamma_w(\nu,t) d\nu \end{aligned} \tag{3.2}$$

- $w_{O_{wi}}$: represents the two-dimensional unsteady wake in lifting-line formulation, as shown in Eq. (3.3). This term must be removed not to be considered two times in the outer and the inner domains. To solve this singular integral, Muller uses finite part integrals (FP).

$$w_{O_{wi}}(y,t) = \frac{1}{2\pi U_\infty \cos\Lambda} \mathrm{FP} \int_0^{+\infty} \frac{\gamma_y(\xi,t)}{\xi} d\xi \tag{3.3}$$

- w_O: represents the velocity induced by the outer domain, including the whole wake. For this domain, the characteristic length is the wingspan, and so the

wing is supposed to be a lifting-line. The wake is modeled by a lattice of vortex panels and vortex filaments. The expression of the velocity induced by the wake is shown in Eq. (3.4).

$$\overrightarrow{V_{\text{ind}}} = \underbrace{-\frac{1}{4\pi}\int_{\partial S}\Gamma(P)\frac{\overrightarrow{PM}\wedge\vec{dl}_P}{PM^3}}_{\text{Vortices}} \underbrace{-\frac{1}{4\pi}\int_S\frac{\vec{\gamma}\wedge\overrightarrow{PM}}{PM^3}dS_P}_{\text{Panels}} \tag{3.4}$$

where w_O is the projection of $\overrightarrow{V_{\text{ind}}}$ onto the airfoil surface along the normal to the local chord. A special treatment with finite part integrals is needed for the singular panel, i.e. the panel in contact with the calculation point.

- w_c: represents the complementary induced velocity, which takes into account the local sweep and curvature, in order to add the effect of spanwise circulation variations on the lifting line. Equation (3.5) can be deduced from the studies done by Guermond [Guermond 1990] for the case of a steady curved lifting-line by factorizing by Γ and $\partial\Gamma/\partial y$.

$$w_c(y) = a_1\Gamma(y) + a_2\frac{\partial\Gamma}{\partial y}(y) \tag{3.5}$$

where:

$$a_1 = \frac{1}{4\pi\kappa(y)}(1-\tan^2\Lambda(y)+K) \quad ; \quad a_2 = \frac{1}{2\pi}\left(K\sin\Lambda(y) + \ln\left|\frac{1+\sin\Lambda(y)}{\cos\Lambda(y)}\right|\right)$$

$$K = \frac{1}{2} + \ln\frac{c(y)\cos^2\Lambda(y)}{4b}$$

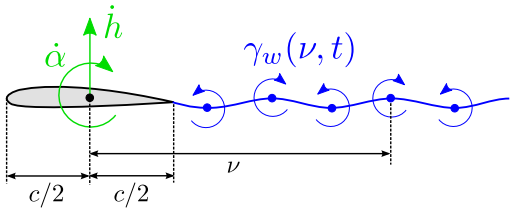
where κ stands for the local wing curvature.

The matching between the outer and inner domains is done by linking the vortex intensities of these two domains: $\gamma_w(\xi, y) = \gamma_y(\xi - c/2, y)$. Thus following Devinant [Devinant 1998] and Coppens [Le Bouar-Coppens 1999], Muller combines the terms from $I \cup O_{wi}$ and O_{wi} domains:

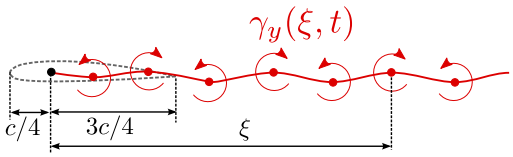
$$\begin{aligned} &w_{I\cup O_{wi}}(M,t) - w_{O_{wi}}(M,t) = \dot{h}(y,t) + \frac{c}{2}\dot{\alpha}(y,t) \\ &+\frac{1}{2\pi U_\infty\cos\Lambda}\left[\frac{2}{c}\int_0^{+\infty}\left(\sqrt{1+\frac{c}{\xi}}-1\right)\gamma_y(\xi,t)d\xi - \text{FP}\int_0^{+\infty}\frac{\gamma_y(\xi,t)}{\xi}d\xi\right] \end{aligned} \tag{3.6}$$

Theoretically, we should consider an infinite two-dimensional wake both in the lifting-line and airfoil formulations. However, if we compare the induced velocities by the wake panels and the ones induced by the two-dimensional wake in the airfoil formulation, it can be noticed that, after a certain distance both are equivalent, as shown in Eqs. (3.7) and (3.8).

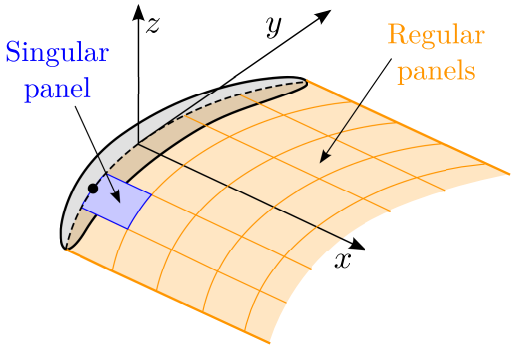
$$H = \overbrace{\frac{2}{c}\int_0^{+\infty}\left(\sqrt{1+\frac{c}{\xi}}-1\right)\gamma_y(\xi,y)d\xi}^{\text{Airfoil}} - \overbrace{\text{FP}\int_0^{+\infty}\frac{\gamma_y(\xi,y)}{\xi}d\xi}^{\text{Lifting line}} \tag{3.7}$$



(a) Inner domain, $I \cup O_{\text{wi}}$



(b) Two-dimensional wake domain, O_{wi}



(c) Three-dimensional wake domain, O

Figure 3.2: Different $\vec{v}_{\text{ind}}$ terms in the unsteady curved lifting-line theory.

$$\sqrt{1+\frac{c}{\xi}}-1=\frac{c}{2\xi}+o\left(\frac{c}{2\xi}\right) \tag{3.8}$$

If we introduce the parameter X representing the limit between the inner and the outer domains ($X \gg c/2$), the outer terms of the integrals become equivalent and so they cancel each other. Thus, we can consider only the airfoil formulation from $c/2$ to X in our wake integrals.

As the current airfoil formulation is derived from a small perturbation theory, it assumes a flat two-dimensional wake, which is not strictly true in the case of a free-wake model. Hence an additional assumption must be done: we will consider that wake deformation of the first panels, i.e. panels at distance $\xi \leq X$, has a negligible impact on induced velocities over the blade.

Finally, Eq. (3.1) can be expressed as shown in Eq. (3.9), where the color of each term corresponds to the colors in Fig. 3.2.

$$\begin{aligned}\Gamma(y,t) = {} & \pi c(y)\cos\Lambda(y)\left[U_\infty\alpha(y,t)+\dot{h}(y,t)+\frac{c(y)}{2}\dot{\alpha}(y,t)\right] \\ & +\int_0^X\left(\sqrt{1+\frac{c(y)}{\xi}}-1\right)\gamma_y(\xi,y)d\xi \\ & -\frac{c(y)\cos\Lambda(y)}{4}\int_S\Gamma(P)\vec{\nabla}_M\left(\frac{\vec{n_P}.\vec{PM}}{PM^3}\right)dS_P-\frac{c(y)}{2}\text{FP}\int_0^X\frac{\gamma_y(\xi,t)}{\xi}d\xi \\ & +\pi c(y)\cos\Lambda(y)\left[a_1\Gamma(y)+a_2\frac{\partial\Gamma}{\partial y}(y)\right]\end{aligned} \tag{3.9}$$

where we can distinguish several terms of induced velocities (see Fig. 3.2):

- The *inner domain* (thin-airfoil theory): it is composed by the quasi-steady airfoil motion term w_I and the near wake term in airfoil formulation $w_{O_{wi}}$. See the first and second lines of Eq. (3.9) and Fig. 3.2(a).

- The *outer domain* $w_O - w_{O_{wi}}$: where the wake is divided in panels and integrated by the Gauss-Legendre quadrature rule, except the singular panel, which is integrated analytically by finite part integrals. The second term removes the contribution of the near wake in the lifting-line formulation, in order not to consider it two times. See the third line of Eq. (3.9), and Figs. 3.2(c) and 3.2(b).

- The *complementary terms* w_c (from Guermond and Sellier): due to the local sweep and curvature. See the fourth line of Eq. (3.9).

3.1.2 A Numerical Implementation of the UCLLT

In his Doctoral Thesis, Muller presented the details of the numerical implementation of an unsteady curved lifting-line theory in AILE fixed-wing code. A particular attention was paid to the implementation of the finite part integrals both in the inner and the outer domains.

Only the terms in the induced velocities that involve finite part integrals are of interest here: the velocities induced by the singular panel (O domain, Fig. 3.2(c)) and the velocities induced by the near wake in lifting-line formulation (O_{wi} domain, Fig. 3.2(b)).

3.2 Outer Domain. The Singular Panel

This section presents the finite part integration of the velocities induced by the singular panel following the procedure proposed by Muller [Muller 2007]. As exposed in Chapter *Literature Review*, there are two equivalent models to represent the potential wake shed by a thin-wing: the doublet formulation and the vortex formulation. Hess showed the equivalence of these two formulation for the case of a regular panel [Hess 1972].

Muller's rationale starts by the finite part integration of the doublet formulation, which presents a simpler form for the case of a point in the plane of the wake panel. However, Muller shows that this formulation can lead to important numerical errors due to the difference between two important values of induced velocities coming from the singular panel and the regular panels, respectively.

In order to avoid these numerical errors, Muller has extended Hess' equivalence between vortex and doublet formulations to the case of a singular panel. To do so, the vortex formulation is first stated and the singular integrals are identified: the surface vorticity and the bound or lifting-line vortex. By comparison between vortex and doublet formulations, Muller deduces an expression for the singular bound vortex. The other singular integral is solved by finite parts, as done for the doublet formulation. Therefore, a final formulation is obtained for the singular panel, combining vortex and doublet formulations.

Next subsections follow Muller's rationale and put forward in the end the differences with respect to the implementation done by Muller in the AILE code.

3.2.1 The Doublet Formulation

Following Biot-Savart's law in doublet formulation, the projection along the z-axis of the *velocities induced* by the wake on a point M of the lifting-line follows:

$$w_O(M) = \frac{1}{4\pi}\int_S \frac{\Gamma(P)}{PM^3} dS_P \tag{3.10}$$

When the wake is discretized in panels, two types of terms appear in the calculation of the induced velocities. On one side, the velocities induced by the panel next to M are singular. On the other side, the velocities induced by the rest of the wake panels present regular integrals.

$$\begin{aligned} w_O(M) &= w_{\text{sing}}(M) + w_{\text{reg}}(M) \\ w_{\text{sing}}(M) &= \frac{1}{4\pi}\text{FP}\iint_{\mathcal{P}_{\text{sing}}} \frac{\Gamma(P)}{PM^3} dS_P \\ w_{\text{reg}}(M) &= \frac{1}{4\pi}\iint_{\mathcal{S}-\mathcal{P}_{\text{reg}}} \frac{\Gamma(P)}{PM^3} dS_P \end{aligned} \tag{3.11}$$

A linear evolution of the circulation Γ is assumed at each panel $\mathcal{P}$ of the wake $\mathcal{S}$. Now the singular panel $\mathcal{P}_{\text{sing}}$ is considered. For each point P in $\mathcal{P}_{\text{sing}}$ the circulation follows:

$$\forall P \in \mathcal{P}_{\text{sing}}, \quad \Gamma(P) = \Gamma(M) + (x_P - x_M)\frac{\delta\Gamma}{\delta x}(M) + (y_P - y_M)\frac{\delta\Gamma}{\delta y}(M) \tag{3.12}$$

where M is the calculation point on the lifting-line at the center of the singular panel. Defining:

$$\overrightarrow{\gamma} = \overrightarrow{n} \wedge \overrightarrow{\nabla}\Gamma = -\frac{\partial\Gamma}{\partial y}\overrightarrow{i} + \frac{\partial\Gamma}{\partial x}\overrightarrow{j} \tag{3.13}$$

It yields:

$$\gamma_x = -\frac{\partial\Gamma}{\partial y} \qquad \gamma_y = \frac{\partial\Gamma}{\partial x} \tag{3.14}$$

Thus, substituting in the expression of singular induced velocities:

$$\begin{aligned} w_{\text{sing}}(M) = \frac{\Gamma(M)}{4\pi}\underbrace{\text{FP}\iint_{\mathcal{P}}\frac{dS_P}{PM^3}}_{s_0(M)} &- \frac{\gamma_y}{4\pi}\underbrace{\text{FP}\iint_{\mathcal{P}}\frac{x_M - x_P}{PM^3}dS_P}_{s_x(M)} \\ &+ \frac{\gamma_x}{4\pi}\underbrace{\text{FP}\iint_{\mathcal{P}}\frac{y_M - y_P}{PM^3}dS_P}_{s_y(M)} \end{aligned} \tag{3.15}$$

Three surface integrals are obtained and Hadamard's finite part integrals are used to calculate their analytical value.

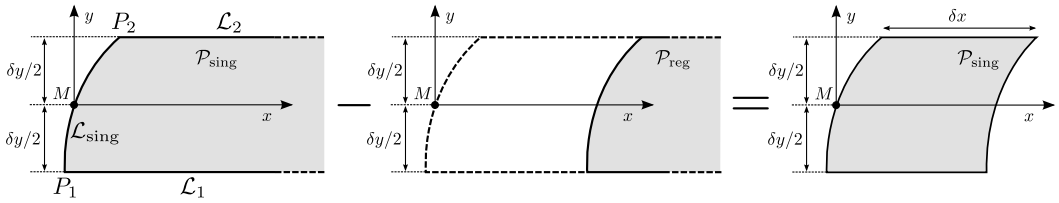


Figure 3.3: Strategy for the calculation of a finite-length singular panel.

Method for calculating singular panel $\vec{v}_{\text{ind}}$. The velocities induced by a finite singular panel are calculated in three steps (see Fig. 3.3):

1. Calculate the finite part integral for an infinite-length singular panel (left).
2. Calculate the regular integral for an infinite panel starting at δx distance from the lifting-line (center).
3. Calculate the difference between the two previous integrals to obtain the value of the finite part integral for a finite panel of δx length (right).

The integration of each of the components in Eq. (3.15) is presented hereafter. To calculate the velocities induced by the singular panel, an infinite-length panel is considered first (see left-hand side figure in 3.3). This infinite-length panel is considered to have the same circulation at the calculation point $\Gamma(M)$ than the singular panel. Moreover, the vorticity in the wake γ_x and γ_y are considered to be constant in all the points of the infinite-length panel and equivalent to the vorticity in the singular panel.

Calculation of s_0 term. The first term of the velocities induced by the singular panel is linked to the circulation at the calculation point $\Gamma(M)$:

$$\begin{aligned} s_0^{\infty}(M) &= \text{FP} \iint_{\mathcal{P}} \frac{dS_P}{PM^3} = \text{FP} \int_{-\delta y/2}^{\delta y/2} \int_{l(y_P)}^{\infty} \frac{dx_P dy_P}{(x_P^2 + y_P^2)^{3/2}} \\ &= \text{FP} \int_{-\delta y/2}^{\delta y/2} \frac{dy_P}{y_P^2} - \text{FP} \int_{-\delta y/2}^{\delta y/2} \frac{l(y_P)}{y_P^2 \sqrt{l(y_P)^2 + y_P^2}} dy_P \end{aligned} \tag{3.16}$$

Note that the terms linked to the infinite-length panel are noted with a $(\star)^{\infty}$ superscript, whereas the terms linked to the infinite-length regular panel are noted with a $(\star)^{\text{reg}}$ superscript.
The first integral in $s_0^{\infty}(M)$ yields:

$$s_{01}^{\infty}(M) = \text{FP} \int_{-\delta y/2}^{\delta y/2} \frac{dy_P}{y_P^2} = 2\text{FP} \int_{0}^{\delta y/2} \frac{dy_P}{y_P^2} = -\frac{4}{\delta y} \tag{3.17}$$

In order to solve the second integral, Guermond defined the function f as:

$$f : y \mapsto \frac{sgn(y) l(y)}{\sqrt{l(y)^2 + y^2}} \tag{3.18}$$

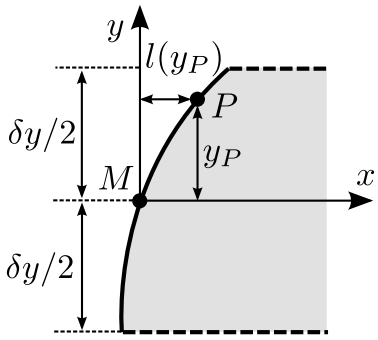


Figure 3.4: Detail of the singular vortex geometry.

Developing in Taylor's series for the considered singular vortex (see Fig. 3.4), it yields:

$$f(y) = \sin\Lambda + \frac{1}{2\kappa}y + f''(0)y^2 + \mathcal{O}(y^3) \tag{3.19}$$

where κ stands for the local radius of curvature at the calculation point M. Note also that the $sgn(y)$ is used to keep the continuity in function f.
When introducing the expression of f into the second integral, it yields:

$$s_{02}^{\infty}(M) = \sin\Lambda\,\mathrm{FP}\int_{-\delta y/2}^{\delta y/2}\frac{sgn(y_P)}{y_P^2}dy_P \tag{3.20}$$

$$+\frac{1}{2\kappa}\mathrm{FP}\int_{-\delta y/2}^{\delta y/2}\frac{sgn(y_P)}{y_P}dy_P \tag{3.21}$$

$$+f''(0)\mathrm{FP}\int_{-\delta y/2}^{\delta y/2}sgn(y_P)dy_P + \mathcal{O}(y_P) \tag{3.22}$$

The first and third integrals are zero because the function is symmetric. The second integral yields:

$$\mathrm{FP}\int_{-\delta y/2}^{\delta y/2}\frac{sgn(y_P)}{y_P}dy_P = 2\mathrm{FP}\int_{0}^{\delta y/2}\frac{dy_P}{y_P} = 2\ln\frac{\delta y}{b} \tag{3.23}$$

Note that the finite part integral yielding a logarithm has been calculated in non-dimensional variables with $b/2$ as reference length. This non-dimensional integration is necessary in a MAE approach, as finite part integrals are not homogeneous in dimensions (see Appendix A).

On the other side, the velocities induced by the infinite-length regular panel can be calculated as follows:

$$\begin{aligned} s_0^{\mathrm{reg}}(M) &= \int_{-\delta y/2}^{\delta y/2}\int_{l(y_P)+\delta x}^{\infty}\frac{dx_P dy_P}{(x_P^2+y_P^2)^{3/2}} \\ &= \int_{-\delta y/2}^{\delta y/2}\frac{1}{y_P^2}\left(1-\frac{l(y_P)-x_M+\delta x}{\sqrt{(l(y_P)-x_M+\delta x)^2+y_P^2}}\right)dy_P \end{aligned} \tag{3.24}$$

Finally, the induced velocities of the finite-length panel are obtained by removing the regular part of the infinite-length panel:

$$\begin{aligned} s_0(M) &= s_0^{\infty}(M) - s_0^{\text{reg}}(M) = -\frac{4}{\delta y} - \frac{1}{\kappa}\ln\frac{\delta y}{b} \\ &\quad - \int_{-\delta y/2}^{\delta y/2} \frac{1}{y_P^2}\left(1 - \frac{l(y_P) - x_M + \delta x}{\sqrt{(l(y_P) - x_M + \delta x)^2 + y_P^2}}\right) dy_P \end{aligned} \tag{3.25}$$

Notice that the terms linked to the infinite-length regular panel follow the same expression as the singular panel but the integration domain is shifted of δx.

Calculation of s_x. Following the same method, it is obtained:

$$\begin{aligned} s_x^{\infty}(M) &= \text{FP}\iint_{\mathcal{P}} \frac{x_M - x_P}{PM^3} dS_P \\ &= \text{FP}\int_{-\delta y/2}^{\delta y/2}\int_{l(y_P)}^{+\infty} \frac{-x_P}{\left(x_P^2 + y_P^2\right)^{3/2}} dx_P dy_P \\ &= \text{FP}\int_{-\delta y/2}^{\delta y/2} \frac{-dy_P}{\sqrt{l(y_P)^2 + y_P^2}} = \text{FP}\int_{-\delta y/2}^{\delta y/2} \frac{-y_P dy_P}{y_P\sqrt{l(y_P)^2 + y_P^2}} \end{aligned} \tag{3.26}$$

The function g is defined as follows and developed in Taylor's series:

$$g : y \mapsto \frac{sgn(y)y}{\sqrt{l(y)^2 + y^2}} \tag{3.27}$$

$$g(y) = \cos\Lambda + g'(0)y + \mathcal{O}(y^2) \tag{3.28}$$

Which yields:

$$\begin{aligned} s_x^{\infty}(M) &= -\text{FP}\int_{-\delta y/2}^{\delta y/2} \frac{sgn(y_P)g(y_P)}{y_P} dy_P \\ &\simeq -\text{FP}\int_{-\delta y/2}^{\delta y/2} \left(\cos\Lambda \frac{sgn(y_P)}{y_P} dy_P + g'(0)sgn(y_P)\right) dy_P \\ &= -2\cos\Lambda\ln\frac{\delta y}{b} \end{aligned} \tag{3.29}$$

Again, to calculate the velocities induced by the finite singular panel, the regular part must be removed:

$$\begin{aligned} s_x^{\text{reg}}(M) &= \int_{-\delta y/2}^{\delta y/2}\int_{l(y_P)+\delta x}^{+\infty} \frac{-x_P}{\left(x_P^2 + y_P^2\right)^{3/2}} dx_P dy_P \\ &= -\int_{-\delta y/2}^{\delta y/2} \frac{dy_P}{\sqrt{(l(y_P) - x_M + \delta x)^2 + y_P^2}} \end{aligned} \tag{3.30}$$

Finally, the expression for the finite singular panel is:

$$\begin{aligned} s_x(M) &= s_x^{\infty}(M) - s_x^{\text{reg}}(M) \\ &= -2\cos\Lambda\ln\frac{\delta y}{b} + \int_{-\delta y/2}^{\delta y/2} \frac{dy_P}{\sqrt{(l(y_P) - x_M + \delta x)^2 + y_P^2}} \end{aligned} \tag{3.31}$$

Calculation of s_y. The same method is followed for the third integral:

$$\begin{aligned} s_y^{\infty}(M) &= \mathrm{FP} \iint_{\mathcal{P}} \frac{y_M - y_P}{PM^3} dS_P \\ &= \mathrm{FP} \int_{-\delta y/2}^{\delta y/2} \int_{l(y_P)}^{+\infty} \frac{-y_P}{(x_P^2 + y_P^2)^{3/2}} dx_P dy_P \\ &= \mathrm{FP} \int_{-\delta y/2}^{\delta y/2} \frac{-1}{y_P} \left(1 - \frac{l(y_P)}{\sqrt{l(y_P)^2 + y_P^2}} \right) dy_P \end{aligned} \tag{3.32}$$

The function f is defined as follows and developed in Taylor's series:

$$f : y \mapsto \frac{sgn(y) l(y)}{\sqrt{l(y)^2 + y^2}} \tag{3.33}$$

$$f(y) = \sin\Lambda + \frac{1}{2\kappa} y + f''(0) y^2 + \mathcal{O}(y^3) \tag{3.34}$$

Introducing it into the integral to calculate $s_y(M)$, it yields:

$$\begin{aligned} s_y^{\infty}(M) &= \mathrm{FP} \int_{-\delta y/2}^{\delta y/2} \frac{-1}{y_P} \left(1 - sgn(y_P) f(y_P)\right) dy_P \\ &\simeq \mathrm{FP} \int_{-\delta y/2}^{\delta y/2} \left(\frac{-1}{y_P} + \frac{sgn(y_P) \sin\Lambda}{y_P} + \frac{sgn(y_P)}{2\kappa} + sgn(y_P) f''(0) y_P \right) dy_P \end{aligned} \tag{3.35}$$

and after canceling symmetric and zero functions it is obtained that:

$$s_y^{\infty}(M) = 2 \sin\Lambda \ln \frac{\delta y}{b} \tag{3.36}$$

On the other side, the regular part of the infinite panel is calculated as follows:

$$\begin{aligned} s_y^{\mathrm{reg}}(M) &= \int_{-\delta y/2}^{\delta y/2} \int_{l(y_P)+\delta x}^{+\infty} \frac{-y_P}{(x_P^2 + y_P^2)^{3/2}} dx_P dy_P \\ &= -\int_{-\delta y/2}^{\delta y/2} \frac{1}{y_P} \left(1 - \frac{l(y_P) - x_M + \delta x}{\sqrt{(l(y_P) - x_M + \delta x)^2 + y_P^2}} \right) dy_P \end{aligned} \tag{3.37}$$

In the case of a finite-length panel, the regular part of the panel extending from δx to the infinity is removed. Therefore, the calculation of $s_y(M)$ term yields:

$$\begin{aligned} s_y(M) &= s_y^{\infty}(M) - s_y^{\mathrm{reg}}(M) = 2 \sin\Lambda \ln \frac{\delta y}{b} \\ &+ \int_{-\delta y/2}^{\delta y/2} \frac{1}{y_P} \left(1 - \frac{l(y_P) - x_M + \delta x}{\sqrt{(l(y_P) - x_M + \delta x)^2 + y_P^2}} \right) dy_P \end{aligned} \tag{3.38}$$

Finite-length singular panel $\vec{v}_{\mathbf{ind}}$. The velocity induced by the singular panel in doublet formulation yields:

$$w_{\mathcal{D}}(M) = \frac{1}{4\pi}\left(\Gamma(M)s_0(M) - \gamma_y s_x(M) + \gamma_x s_y(M)\right) \tag{3.39}$$

This approach in the calculation of the induced velocities presents an important drawback: the result is the difference between two very important components, coming from the singular panel, on one side, and the regular panels, on the other side. This comes from the fact that panel edges contribution is not explicitly calculated in doublet formulation neither in singular nor in regular panels. For a wake with continuous circulation distribution, these contributions are identical but with opposite sign between one panel and its neighbor, and thus they should cancel. However, as integrals must be computed numerically, a small error in the calculation of one of the two terms can yield to very important errors in the final estimation of the induced velocity.

Therefore, similar to the Hess equivalence for regular panels [Hess 1972], Muller presents the equivalent vortex formulation for singular panels as a way to avoid this issue. In this case, the contribution of panel edges appear explicitly in the calculation of induced velocities. Thus, they can be canceled analytically between singular and regular panels, and numerical errors are avoided.

3.2.2 The Vortex Formulation

The velocity induced by the singular panel takes the following form in vortex formulation:

$$\begin{aligned} w_{\text{sing}} =& -\frac{1}{4\pi}\text{FP}\iint_{\mathcal{P}} \frac{\overrightarrow{PM}\wedge\overrightarrow{\gamma}}{PM^3} dS_P \overrightarrow{k} \\ & -\frac{1}{4\pi}\text{FP}\int_{\partial\mathcal{P}} \Gamma(P)\frac{\overrightarrow{PM}\wedge\overrightarrow{dl_P}}{PM^3}\overrightarrow{k} \end{aligned} \tag{3.40}$$

If the circulation continuity is ensured between panels, the terms linked to vortex filaments in the panel boundaries can be canceled with the same terms of neighbor panels. Thus, all the boundary vortex filaments are zero except the lifting-line. In the classical straight lifting-line theory, this vortex does not generate any induced velocity on the calculation point M. On the contrary, when considering a swept and curved wing, this term becomes singular and must be deduced by comparison between vortex and doublet formulations.

In order to compare vortex and doublet formulations, an infinite-length panel is first considered. The vortex formulation of the induced velocities in this case takes the form:

$$\begin{aligned} w_{\mathcal{T}} = & -\frac{1}{4\pi}\text{FP}\iint_{\mathcal{P}} \frac{\overrightarrow{PM}\wedge\overrightarrow{\gamma}}{PM^3} dS_P \\ -\frac{1}{4\pi}\int_{\mathcal{L}_1}\Gamma(P)\frac{\overrightarrow{PM}\wedge\overrightarrow{dl_P}}{PM^3} & -\frac{1}{4\pi}\int_{\mathcal{L}_2}\Gamma(P)\frac{\overrightarrow{PM}\wedge\overrightarrow{dl_P}}{PM^3} \\ & -\frac{1}{4\pi}\text{FP}\int_{\mathcal{L}_{\text{sing}}}\Gamma(P)\frac{\overrightarrow{PM}\wedge\overrightarrow{dl_P}}{PM^3} \end{aligned} \tag{3.41}$$

where the first integral represents the term linked to the vorticity distribution in the panel and can be developed in the same form as in the doublet formulation:

$$\begin{aligned} &\mathrm{FP}\iint_{\mathcal{P}} \frac{\overrightarrow{PM}\wedge\overrightarrow{\gamma}}{PM^3}dS_P \\ &= \gamma_y \mathrm{FP}\iint_{\mathcal{P}} \frac{x_M - x_P}{PM^3}dS_P - \gamma_x \mathrm{FP}\iint_{\mathcal{P}} \frac{x_M - y_P}{PM^3}dS_P \end{aligned} \tag{3.42}$$

The second integral in Eq. (3.41) is linked to the vortex filament $\mathcal{L}_1$ (see left-hand side picture in Fig. 3.3) and yields:

$$\begin{aligned} &\int_{\mathcal{L}_1} \Gamma(P)\frac{\overrightarrow{PM}\wedge d\overrightarrow{l_P}}{PM^3} = \int_{x_1}^{+\infty} \left(\Gamma(P_1) + (x-x_1)\gamma_y\right) \frac{\frac{\delta y}{2}dx}{\left(\left(\frac{\delta y}{2}\right)^2 + x^2\right)^{3/2}} \\ &= \frac{\delta y}{2}\left(\Gamma(P_1) - \gamma_y x_1\right)\int_{x_1}^{+\infty} \frac{dx}{\left(\left(\frac{\delta y}{2}\right)^2 + x^2\right)^{3/2}} + \frac{\gamma_y \delta y}{2}\int_{x_1}^{+\infty} \frac{xdx}{\left(\left(\frac{\delta y}{2}\right)^2 + x^2\right)^{3/2}} \\ &= \frac{2}{\delta y}\left(\Gamma(P_1) - \gamma_y x_1\right)\left(1 - \frac{x_1}{\sqrt{\left(\frac{\delta y}{2}\right)^2 + x_1^2}}\right) + \frac{\gamma_y \delta y}{2}\frac{1}{\sqrt{\left(\frac{\delta y}{2}\right)^2 + x_1^2}} \end{aligned} \tag{3.43}$$

whereas the third integral is linked to the vortex filament $\mathcal{L}_2$ and yields:

$$\begin{aligned} &\int_{\mathcal{L}_2} \Gamma(P)\frac{\overrightarrow{PM}\wedge d\overrightarrow{l_P}}{PM^3} = \int_{x_2}^{+\infty} \left(\Gamma(P_2) + (x-x_2)\gamma_y\right) \frac{\frac{\delta y}{2}dx}{\left(\left(\frac{\delta y}{2}\right)^2 + x^2\right)^{3/2}} \\ &= \frac{\delta y}{2}\left(\Gamma(P_2) - \gamma_y x_2\right)\int_{x_2}^{+\infty} \frac{dx}{\left(\left(\frac{\delta y}{2}\right)^2 + x^2\right)^{3/2}} + \frac{\gamma_y \delta y}{2}\int_{x_2}^{+\infty} \frac{xdx}{\left(\left(\frac{\delta y}{2}\right)^2 + x^2\right)^{3/2}} \\ &= \frac{2}{\delta y}\left(\Gamma(P_2) - \gamma_y x_2\right)\left(1 - \frac{x_2}{\sqrt{\left(\frac{\delta y}{2}\right)^2 + x_2^2}}\right) + \frac{\gamma_y \delta y}{2}\frac{1}{\sqrt{\left(\frac{\delta y}{2}\right)^2 + x_2^2}} \end{aligned} \tag{3.44}$$

Finally, the last integral in Eq. (3.41) is singular and it is linked to the lifting-line vortex filament $\mathcal{L}_{\mathrm{sing}}$. This singular term must be deduced by comparison between vortex and doublet formulations, as shown in the next subsection.

3.2.3 Hess' Equivalence for Singular Panels

Previous subsections have presented the doublet and vortex formulations of the velocities induced by an infinite-length singular panel. The doublet formulation has

yield to:

$$\begin{aligned} w_{\mathcal{D}} = & \frac{\Gamma(M)}{4\pi}\mathrm{FP}\iint_{\mathcal{P}}\frac{dS_P}{PM^3} \\ & -\frac{\gamma_y}{4\pi}\mathrm{FP}\iint_{\mathcal{P}}\frac{x_M - x_P}{PM^3}dS_P + \frac{\gamma_x}{4\pi}\mathrm{FP}\iint_{\mathcal{P}}\frac{y_M - y_P}{PM^3}dS_P \end{aligned} \tag{3.45}$$

whereas the vortex formulation has yield to:

$$\begin{aligned} w_{\mathcal{T}} = & -\frac{\gamma_y}{4\pi}\mathrm{FP}\iint_{\mathcal{P}}\frac{x_M - x_P}{PM^3}dS_P + \frac{\gamma_x}{4\pi}\mathrm{FP}\iint_{\mathcal{P}}\frac{x_M - y_P}{PM^3}dS_P \\ & -\frac{1}{4\pi}\int_{\mathcal{L}_1}\Gamma(P)\frac{\overrightarrow{PM}\wedge\overrightarrow{dl_P}}{PM^3} - \frac{1}{4\pi}\int_{\mathcal{L}_2}\Gamma(P)\frac{\overrightarrow{PM}\wedge\overrightarrow{dl_P}}{PM^3} \\ & -\frac{1}{4\pi}\mathrm{FP}\int_{\mathcal{L}_{\mathrm{sing}}}\Gamma(P)\frac{\overrightarrow{PM}\wedge\overrightarrow{dl_P}}{PM^3} \end{aligned} \tag{3.46}$$

Comparing Eq. (3.45) and Eq. (3.46), the colored terms cancel each other and the velocity induced by the singular filament vortex $\mathcal{L}_{\mathrm{sing}}$ takes the form:

$$\begin{aligned} \mathrm{FP}\int_{\mathcal{L}_{\mathrm{sing}}}\Gamma(P)\frac{\overrightarrow{PM}\wedge\overrightarrow{dl_P}}{PM^3} = & -\mathrm{FP}\iint_{\mathcal{P}}\Gamma(M)\frac{dS_P}{PM^3} \\ & -\int_{\mathcal{L}_1}\Gamma(P)\frac{\overrightarrow{PM}\wedge\overrightarrow{dl_P}}{PM^3} - \int_{\mathcal{L}_2}\Gamma(P)\frac{\overrightarrow{PM}\wedge\overrightarrow{dl_P}}{PM^3} \end{aligned} \tag{3.47}$$

Considering that $\Gamma(M) = [\Gamma(P_1) + \Gamma(P_2)]/2$ and replacing all the right-hand side terms by the expressions obtained in previous subsections it yields:

$$\begin{aligned} \mathrm{FP}\int_{\mathcal{L}_{\mathrm{sing}}}\Gamma(P)\frac{\overrightarrow{PM}\wedge\overrightarrow{dl_P}}{PM^3} = & \frac{2\Gamma(P_1)}{\delta y} + \frac{2\Gamma(P_2)}{\delta y} + \frac{\Gamma(M)}{\kappa}\ln\frac{\delta y}{b} \\ & -\frac{2\Gamma(P_1)}{\delta y} + \frac{2\Gamma(P_1)x_1}{\delta y\sqrt{\left(\frac{\delta y}{2}\right)^2 + x_1^2}} - \frac{2\Gamma(P_2)}{\delta y} + \frac{2\Gamma(P_2)x_2}{\delta y\sqrt{\left(\frac{\delta y}{2}\right)^2 + x_2^2}} \\ & +\frac{2\gamma_y x_1}{\delta y}\left[1 - \frac{x_1}{\sqrt{\left(\frac{\delta y}{2}\right)^2 + x_1^2}}\right] - \frac{\gamma_y\delta y}{2}\frac{1}{\sqrt{\left(\frac{\delta y}{2}\right)^2 + x_1^2}} \\ & +\frac{2\gamma_y x_2}{\delta y}\left[1 - \frac{x_2}{\sqrt{\left(\frac{\delta y}{2}\right)^2 + x_2^2}}\right] - \frac{\gamma_y\delta y}{2}\frac{1}{\sqrt{\left(\frac{\delta y}{2}\right)^2 + x_2^2}} \end{aligned} \tag{3.48}$$

The first line of the equation corresponds to the $s_0^{\infty}\Gamma(M)$ term in doublet formulation, while the other lines correspond to the filaments $\mathcal{L}_1$ and $\mathcal{L}_2$ in vortex formulation. The colored components cancel each other and the expression of the velocity induced by the singular vortex filament is obtained.

Finally, when substituting previous results in the expression of the velocities induced by a finite-length singular panel in vortex formulation, it yields (including

explicitly the vortex filaments' terms):

$$w_{\mathcal{P}}(M) = -\frac{1}{4\pi}\int_{\mathcal{S}} \frac{\overrightarrow{PM}\wedge\overrightarrow{\gamma}}{PM^3} dS_P - \frac{1}{4\pi}\int_{\mathcal{L}_{\text{sing}}} \Gamma(P)\frac{\overrightarrow{PM}\wedge d\overrightarrow{l_P}}{PM^3} + w_{\mathcal{L}_1} + w_{\mathcal{L}_2} + w_{\mathcal{L}_3} \tag{3.49}$$

As it has been shown in Eq. (3.42), the first term takes the same form as in doublet formulation. Therefore, its finite part integration yields to expressions Eq. (3.31) and Eq. (3.38). Hence, developing and combining each of the components in the previous expression, it yields:

$$w_{\mathcal{P}}(M) = I_{s0}\Gamma(M) + I_{s1}\Gamma(P_1) + I_{s2}\Gamma(P_2) + I_{sx}\gamma_x + I_{sy}\gamma_y + w_{\mathcal{L}_1} + w_{\mathcal{L}_2} + w_{\mathcal{L}_3} \tag{3.50}$$

where:

$$I_{s0} = -\frac{1}{4\pi\kappa}\ln\frac{\delta y}{b} \tag{3.51}$$

$$I_{s1} = -\frac{1}{2\pi\delta y}\frac{x_1}{\sqrt{\left(\frac{\delta y}{2}\right)^2 + x_1^2}} \tag{3.52}$$

$$I_{s2} = -\frac{1}{2\pi\delta y}\frac{x_2}{\sqrt{\left(\frac{\delta y}{2}\right)^2 + x_2^2}} \tag{3.53}$$

$$I_{sx} = \frac{1}{2\pi}\sin\Lambda\ln\frac{\delta y}{b} + \frac{1}{4\pi}\int_{-\frac{\delta y}{2}}^{\frac{\delta y}{2}} \frac{1}{s}\left(1 - \frac{\tan\Lambda s + \delta x}{\sqrt{\frac{s^2}{\cos^2\Lambda} + 2\delta x\tan\Lambda s + \delta x^2}}\right) ds \tag{3.54}$$

$$\begin{aligned} I_{sy} = {} & \frac{1}{2\pi}\cos\Lambda\ln\frac{\delta y}{b} - \frac{1}{4\pi}\int_{-\frac{\delta y}{2}}^{\frac{\delta y}{2}} \frac{ds}{\sqrt{\frac{s^2}{\cos^2\Lambda} + 2\delta x\tan\Lambda s + \delta x^2}} \\ & -\frac{x_1}{2\pi\delta y}\left[1 - \frac{x_1}{\sqrt{\left(\frac{\delta y}{2}\right)^2 + x_1^2}}\right] + \frac{\delta y}{8\pi}\frac{1}{\sqrt{\left(\frac{\delta y}{2}\right)^2 + x_1^2}} \\ & -\frac{x_2}{2\pi\delta y}\left[1 - \frac{x_2}{\sqrt{\left(\frac{\delta y}{2}\right)^2 + x_2^2}}\right] + \frac{\delta y}{8\pi}\frac{1}{\sqrt{\left(\frac{\delta y}{2}\right)^2 + x_2^2}} \end{aligned} \tag{3.55}$$

Thus, Muller extends Hess' equivalence between doublet and vortex formulations for the case of a singular panel of finite length (see Fig. 3.5). Although some mismatches in the formulation have been observed, as it will be explained hereafter, this is the key result for the integration of the singular panel using the vortex formulation. As shown by Muller, the vortex formulation is better adapted for numerical applications than doublet formulation as it cancels analytically the boundary terms.

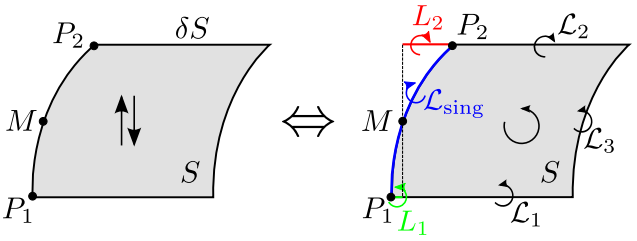


Figure 3.5: Hess and Smith equivalence for a singular panel

3.2.4 Current Implementation in the AILE Code

Some differences have been found between Muller's report and the AILE code. The velocity induced by the singular panel is calculated in AILE as follows:

$$w_{\mathcal{P}}(M) = I_{s0}\Gamma(M) + I_{s1}\Gamma(P_1) + I_{s2}\Gamma(P_2) + I_{sx}\gamma_x + I_{sy}\gamma_y \tag{3.56}$$

where:

$$I_{s0} = -\frac{1}{4\pi\kappa}\ln\frac{\delta y}{2} \tag{3.57}$$

$$I_{s1} = -\frac{1}{2\pi\delta y}\frac{x_1}{\sqrt{x_1^2 + \left(\frac{\delta y}{2}\right)^2}} \tag{3.58}$$

$$I_{s2} = -\frac{1}{2\pi\delta y}\frac{x_2}{\sqrt{x_2^2 + \left(\frac{\delta y}{2}\right)^2}} \tag{3.59}$$

$$I_{sx} = -\frac{1}{2\pi}\sin\Lambda\ln\frac{\delta y}{2} + \frac{1}{4\pi}\int_{-\frac{\delta y}{2}}^{\frac{\delta y}{2}} \frac{\tan\Lambda s + \delta x}{s\sqrt{\frac{s^2}{\cos^2\Lambda} + 2\delta x\tan\Lambda s + \delta x^2}}ds \tag{3.60}$$

$$I_{sy} = \frac{1}{2\pi}\cos\Lambda\ln\frac{\delta y}{2} - \frac{1}{4\pi}\int_{-\frac{\delta y}{2}}^{\frac{\delta y}{2}} \frac{ds}{\sqrt{\frac{s^2}{\cos^2\Lambda} + 2\delta x\tan\Lambda s + \delta x^2}} \tag{3.61}$$

A number of differences can be noticed when comparing AILE code to the results obtained in the previous subsection of the present document:

- Logarithmic functions use dimensional variables in AILE. As exposed before, this has no impact in the results as the wing span is fixed to $b = 2$ and the reference length is $b/2$.
- There is a change in the sign of I_{sx} infinite-length panel component.
- The I_{sx} regular panel component presents a singular integral, whereas the theory predicts a regular integral. This issue was not noticed because of the discrete integration along y axis.
- The differences in the I_{sy} component come from the fact that the implementation in AILE does not include the induced velocities due to the linear variation

of the circulation Γ along the left-hand side and right-hand side vortex filaments.

3.3 Inner Domain. Two-Dimensional Wake in Lifting-Line Formulation

$$w_{I\cup O_{wi}}(M,t) - w_{O_{wi}}(M,t) = \overbrace{\dot{h}(y,t) + \frac{c}{2}\dot{\alpha}(y,t)}^{\text{Airfoil motion}} + \overbrace{\frac{1}{2\pi U_\infty \cos\Lambda}\left[\underbrace{\frac{2}{c}\int_0^X \left(\sqrt{1+\frac{c}{\xi}}-1\right)\gamma_y(\xi,t)d\xi}_{\text{Airfoil formulation}} - \underbrace{\text{FP}\int_0^X \frac{\gamma_y(\xi,t)}{\xi}d\xi}_{\text{Lifting-line formulation}}\right]}^{\text{2D Wake}} \tag{3.62}$$

The last term must be calculated by finite part integrals. For a matter of simplicity, Muller assumes that the inner domain contains only the singular panel, and thus $X = \delta x$, where δx is the length of the singular panel. Taking into account the dimensional variables, the finite part integral yields:

$$\text{FP}\int_0^X \frac{\gamma_y(\xi,t)}{\xi}d\xi = \gamma_y(0,y,t)\ln\frac{2\delta x}{b} \tag{3.63}$$

where $\gamma_y(0,y,t)$ is the vorticity density of the first panel row at each y station and time t.

The second term in Eq. (3.62) contains a regular integral. Muller considers a constant evolution of γ_y along each of the wake panels, which yields:

$$\frac{2}{c}\int_0^X \left(\sqrt{1+\frac{c}{\xi}}-1\right)\gamma_y(\xi,t)d\xi = \gamma_y(0,y,t)\left(\frac{2}{u^\star+1} - \ln\frac{u^\star-1}{u^\star+1}\right) \tag{3.64}$$

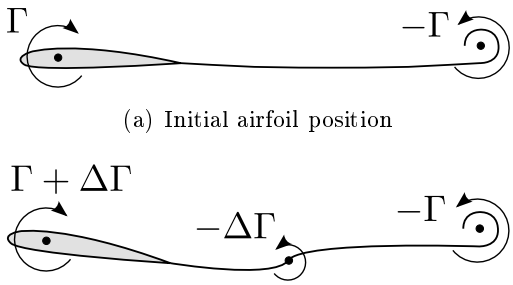
where $u^\star = \sqrt{1+c/\delta x}$.

3.4 Theoretical Analysis of the Model

This section presents an analysis of the UCLL theory proposed by Muller, focusing on the finite part integrals used to solve singularity problems. This type of approach seems to be not adapted to a discrete formulation of the problem because of three main reasons: they depend on the non-dimensional variables used to describe the problem, they impose a minimum panel span and thus limit the maximum number of panels depending on the wing aspect ratio, and they invert the sign of induced velocities introducing instabilities in the computation.

3.4.1 Inner Domain. Airfoil Model

Two-dimensional wake length. In the previous section (3.3) the hypothesis done by Muller on the calculated wake distance has been presented: $X = \delta x$. Rigorously, this imposes that the first panel must be much longer and larger than the



(a) Initial airfoil position

(b) Increase in geometrical incidence

Figure 3.6: Wake effect on an airfoil under an incidence step

local half chord. Muller considers, for example, a wing with an aspect ratio (b/c_0, span over maximum chord) of 10 and with an elliptic chord. In those cases, to respect the minimum size of the inner domain, panels should be very long and large, and thus the number of blade sections would be very limited, i.e. no more than 10 sections. This can be an important drawback to predict the form of the load distribution along the blade with an acceptable accuracy. In order to overcome this limitation, a new approach has been developed and is presented in Chapter 4.

The sign of Finite Part integrals. Consider a two-dimensional airfoil in incidence introduced into an air flow with a certain incidence. By the Kelvin's circulation theorem (see for example [Katz 2001]), it will develop an initial vortex of the same circulation Γ and of opposite sign than the circulation on the airfoil (see Fig. 3.6(a)).
Let us assume that, at a given time, the airfoil incidence is increased, as shown in Fig. 3.6(b). An increase in the airfoil circulation $\Delta\Gamma$ occurs and the shed wake contains again a vortex with the same vorticity but with opposite sign.

However, following the Biot-Savart law, these variations in the wake circulation induce velocities on the airfoil (see Eq. (3.65)). These velocities, commonly known as the downwash, tend to delay this Γ increase on the airfoil. As the effect of the vortex is inversely proportional to the distance to the airfoil and as it is convected downstream, its effect decreases with time and the airfoil circulation reaches asymptotically $\Gamma + \Delta\Gamma$.

$$w_{\text{airfoil}} = \frac{\Delta\Gamma}{2\pi x} \propto \frac{1}{x} \tag{3.65}$$

Now consider the same airfoil case, but where the unsteady two-dimensional wake term is calculated by finite part integrals:

$$w_{O_{\text{wi}}}(y,t) = \text{FP}\int_0^{\delta x} \frac{\gamma_y(\xi,t)}{\xi} d\xi = \underbrace{\ln\frac{2\delta x}{b}}_{<0}\underbrace{\gamma_y(0,y,t)}_{<0} > 0 \tag{3.66}$$

Even if the function inside the integral is positive in all the domain of integration, the non-dimensional finite part integral yields a negative value. Thus, as γ_y in the

considered case is also negative, an unphysical positive value of induced velocities (an upwash) is obtained. As the induced velocity component $w_{O_{\text{wi}}}$ is a term that is removed in the global circulation equation (3.1), its sign is negative, and hence an overestimation of the downwash is obtained. Thus, the aerodynamic incidence predicted in the two-dimensional inner domain is likely to be underestimated.

3.4.2 Outer Domain. The Singular Panel

Now consider the component of the velocities induced by the singular panel that is equivalent to the two-dimensional wake effect. Only the longitudinal variation of the circulation γ_y is considered:

$$w_{sy} = I_{sy}\gamma_y = \frac{\gamma_y}{4\pi}\left[2\cos\Lambda \underbrace{\ln\frac{\delta y}{b}}_{<0} - \int_{-\delta y/2}^{\delta y/2} \frac{ds}{\sqrt{\frac{s^2}{\cos^2\Lambda} + 2\delta x \tan\Lambda s + \delta x^2}}\right] \tag{3.67}$$

The obtained result is similar to that of the inner domain: positive induced velocities (upwash) are obtained. Thus, when the geometrical incidence is increased an additional incidence is obtained due to induced velocities, and thus the circulation also increases. This process cannot converge, as induced velocities and circulation must act in opposite senses to reach the equilibrium.

3.4.3 Remarks on the Model

This sign inversion in the induced velocities comes from the way the regularization by finite part integrals is applied. By Biot-Savart law, the velocity induced by a point in the vorticity wake on a point in the lifting-line depends on the inverse of the distance between those two points. As points get closer, their influence increase and induced velocities tend to infinity when the distance tends to zero. Guermond and Sellier [Guermond 1991] presented a method using Hadamard's finite part integrals in order to overcome the singularity problem. In their approach, the wing geometry and the wake vorticity were described using analytical functions, and therefore this enables to calculate analytically the induced velocities of all the wake on a point M_0 on the wing:

$$w_{\text{out}}(M_0) = \frac{A^{-1}}{4\pi}\text{FP}\int_{\mathcal{L}}\int_0^{+\infty} \frac{[[\psi]](v,\eta)}{[(v + x_0(\eta) - x_0(y))^2 + (y-\eta)^2]^{3/2}}\mathrm{d}\eta\mathrm{d}v \tag{3.68}$$

where $\mathcal{L}$ represents the curved lifting-line. It is important to notice that the regularization by finite part integrals is performed not only in the direction of the freestream, i.e. along the x axis, but also spanwise, i.e. along the y axis. On the contrary, Muller proposes only a regularization along the x axis, and thus it leads to unphysical induced velocity contributions.

The present analysis has shown how finite part integrals both in the inner and the outer domains inverse the sign of the singular panel contribution on induced velocities. Even if the singular panel contribution is destabilizing, the two-dimensional

wake component in the inner domain may compensate it and stabilize the whole system.
However, in the general case, the convergence cannot be ensured due to the singular panel component, as it has been noticed when implementing this methodology in HOST. Thus, finite part integrals seem not to be adapted in the present form to the calculation of a wake described with discrete panels.

The Appendix C presents an alternative form for the integration of the induced velocities in the singular panel. This new method exploits the approach proposed by Muller but finite part integrals are performed in both chordwise and spanwise directions. This enables the new approach to provide more regular induced velocities regardless both the chordwise and the spanwise size of the panel.

Chapter 4

Developing and Implementing an UCLL Method in HOST without Finite Part Integrals

Contents

4.1 The Complete Unsteady Curved Theory 121
4.2 Implementation in HOST 124
4.3 Concluding remarks 125

As explained in chapter 3, the unsteady model implementation in AILE code is not adapted to the considered case in HOST, where blades present small aspect ratios and an important number of panels due to the finite part integrals. Thus, a new approach to implement the unsteady curved lifting-line theory proposed by Guermond and Sellier [Guermond 1991] has been conceived in order to remove Hadamard's finite part integrals. This chapter presents in detail this new approach, exposes its hypothesis and limits and presents its implementation in HOST.

4.1 The Complete Unsteady Curved Theory

The asymptotic approach presented by Muller has been modified to remove two of the terms calculated in finite part integrals, in the inner and in the outer domains. Hence the implicit equation of the circulation $\Gamma(M)$ in Eq. 3.1 has been modified as follows Eq. (4.1).

$$\Gamma = \pi c \cos\Lambda \left(U_\infty \alpha + w_{I \cup O_{wi}} + w_{O \setminus O_{wi}} + w_c \right) \tag{4.1}$$

where:

- $w_{I \cup O_{wi}}$: represents the velocity induced by the domain $I \cup O_{wi}$, which has a pure two-dimensional origin. Based on the linearized unsteady thin-airfoil theory, we obtain Eq. (4.2).

$$\begin{aligned} w_{I \cup O_{wi}}(y,t) &= \dot{h}(y,t) + \frac{c}{2}\dot{\alpha}(y,t) \\ &+ \frac{1}{\pi c U_\infty \cos\Lambda} \int_{c/2}^{+\infty} \left(\sqrt{\frac{\nu + c/2}{\nu - c/2}} - 1 \right) \gamma_w(\nu,t) d\nu \end{aligned} \tag{4.2}$$

- $w_{O\backslash O_{wi}}$: represents the velocity induced by the outer domain, the whole wake except the longitudinal vorticity γ_y in the wake panels behind the considered section. For this domain, the characteristic length is the wingspan, and so the wing is supposed to be a lifting-line. The wake is modeled by a lattice of vortex panels and vortex filaments. The expression of the velocity induced by the wake is shown in Eq. (4.3).

$$\vec{V}_{\text{ind}} = \underbrace{-\frac{1}{4\pi}\int_{\partial S}\Gamma(P)\frac{\overrightarrow{PM}\wedge\vec{dl}_P}{PM^3}}_{\text{Vortices}} \underbrace{-\frac{1}{4\pi}\int_S\frac{\vec{\gamma}\wedge\overrightarrow{PM}}{PM^3}dS_P}_{\text{Panels}} \tag{4.3}$$

  The term $w_{O\backslash O_{wi}}$ corresponds to the $\vec{V}_{\text{ind}}$ component contained in the airfoil plane and normal to the local chord.

- w_c: represents the complementary induced velocity, which takes into account the local sweep and curvature, in order to add the effect of spanwise circulation variations on the lifting line. Equation (4.4) can be deduced from the studies done by Guermond [Guermond 1990] for the case of a steady curved lifting-line theory by factorizing by Γ and $\partial\Gamma/\partial y$.

$$w_c(y) = a_1\Gamma(y) + a_2\frac{\partial\Gamma}{\partial y}(y) \tag{4.4}$$

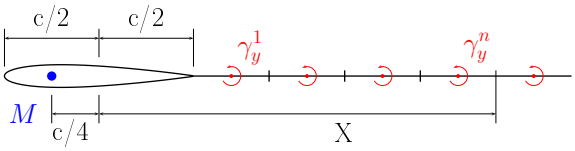
  where:

$$a_1 = \frac{1}{4\pi\kappa(y)}(1-\tan^2\Lambda(y)+K) \quad ; \quad a_2 = \frac{1}{2\pi}\left(K\sin\Lambda(y) + \ln\left|\frac{1+\sin\Lambda(y)}{\cos\Lambda(y)}\right|\right)$$

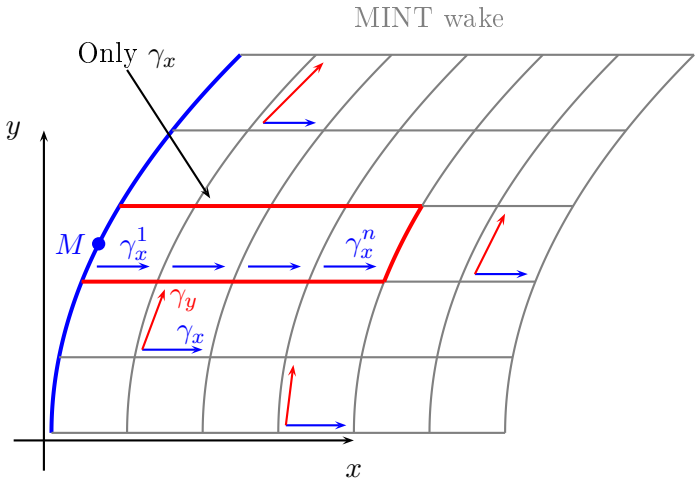
$$K = \frac{1}{2} + \ln\frac{c(y)\cos^2\Lambda(y)}{4b}$$

Again, the matching between outer and inner domains is done by linking the vortex intensities of these two domains: $\gamma_w(\xi, y) = \gamma_y(\xi - c/2, y)$. This is what the current unsteady correction implemented in HOST actually lacks: the airfoil motion effect is considered, but the two-dimensional unsteady wake effect on the airfoil is not.

Following the linearized unsteady thin-airfoil theory, the two-dimensional wake influence should be considered from the trailing edge ($\xi = c/2$) to infinity downstream. However, in the HOST code, as the airfoil is reduced to a lifting-line, wake panels shed by each section start immediately after the calculation point. In order to avoid calculating twice the velocities induced by the two-dimensional wake (see O_{wi} domain in Fig.20), a series of MINT wake panels must be treated differently in the calculation of the total induced velocity. Indeed, these panels only consider the other component of the vorticity: γ_x, i.e. the radial variation of the circulation.
Theoretically, we should consider an infinite two-dimensional wake and consider only γ_x in all the MINT wake panels behind the considered section. However, as shown in Eqs. (3.7) and (3.8), the induced velocities by MINT panels and the ones induced by



(a) Unsteady airfoil model. Inner domain



(b) MINT wake model. Outer domain

Figure 4.1: The unsteady airfoil model as implemented in HOST-MINT code

the two-dimensional wake in the airfoil formulation cancel each other after a certain distance. If we introduce the parameter X representing the limit between inner and outer domains ($X \gg c/2$), the outer terms of the integrals become equivalent and so they compensate each other. Thus, we can consider the airfoil formulation from $c/2$ to X in our wake integrals. In the current HOST implementation, X parameter has been chosen $X = 3c$. Each panel length can be estimated by considering that they are convected at the relative velocity of the section, without adding any induced velocity. This estimated panel length is then used to determine the number of panels to be considered in the two-dimensional unsteady wake, and hence to be removed from the MINT wake (as shown in Fig. 4.1).

Again, as the current airfoil formulation is derived from a small perturbation theory, it assumes a flat two-dimensional wake, which is not strictly the case in our free-wake model. Thus, an additional assumption must be done: we will consider that wake deformation of the first panels, i.e. panels at distance $\xi \leq X$, has a negligible impact on induced velocities over the blade. This hypothesis has been shown to be valid for the representative case considered in Chapter 1.

Finally, Eq. (4.1) can be expressed as shown in Eq. (4.5).

$$\begin{aligned}\Gamma(y,t) &= \pi c(y)\cos\Lambda(y)\left[U_\infty\alpha(y,t)+\dot{h}(y,t)+\frac{c(y)}{2}\dot{\alpha}(y,t)\right]\\ &+\int_0^X\left(\sqrt{1+\frac{c(y)}{\xi}}-1\right)\gamma_y(\xi,y)d\xi\\ &-\frac{c(y)\cos\Lambda(y)}{4}\int_S\Gamma(P)\overrightarrow{\nabla}_M\left(\frac{\overrightarrow{n_P}.\overrightarrow{PM}}{PM^3}\right)dS_P\\ &+\pi c(y)\cos\Lambda(y)\left[a_1\Gamma(y)+a_2\frac{\partial\Gamma}{\partial y}(y)\right]\end{aligned} \tag{4.5}$$

where we can distinguish several terms of induced velocities:

- The *inner domain* (thin-airfoil theory): composed by the quasi-steady airfoil motion term and the near wake term in airfoil formulation. The terms in the first and second lines of Eq.(4.5) correspond to the inner domain induced velocities.
- The *outer domain* w_O: where the wake is divided in panels and integrated by the Gauss-Legendre quadrature rule. A special treatment is needed for the calculation of wake panels behind the considered section, as only radial variations of circulation γ_x are considered. The third line of Eq.(4.5) corresponds to the velocities induced by the outer domain in doublet formulation.
- The *complementary terms* w_c (from Guermond and Sellier): due to the local sweep and curvature. The fourth line of Eq.(4.5) corresponds to these complementary terms.

4.2 Implementation in HOST

Figure 4.1 shows the way inner and outer domain are matched in HOST implementation. As proposed by Devinant [Devinant 1999] for the discrete problem, only one range of wake panels is considered to be in the range of the inner domain. Thus, in the outer domain (Fig. 4.1(b)) the longitudinal variation of circulation γ_y has been removed from a number of wake panels behind the considered blade section. The velocities induced by these γ_y are taken into account in the inner domain (Fig. 4.1(a)).

HOST calculates first the aerodynamic coefficients and then the circulation. Given a certain angle of attack (due to freestream velocity, rotational speed and velocities induced by the wake) and Mach number (corrected or not by the local sweep), HOST interpolates the two-dimensional aerodynamic coefficients in polar data: C_L, C_D and C_m. Unsteady corrections are applied afterward, considering a simplified 2π-slope $\partial C_L/\partial\alpha$. Equation (4.6) shows the complete lift coefficient expression.

$$C_L = C_L^{QS} + C_L^{3/4} + C_L^{\text{comp}} + C_L^{NC} + C_L^{2D_{\text{unst}}} \tag{4.6}$$

where:

- Quasi-steady term: $C_L^{QS} = C_{L_\alpha}^{\text{polar}} \dfrac{V_\perp \alpha + \dot{h} + w_{O\setminus O_{wi}}}{U_\infty}$
- Pitching motion term: $C_L^{3/4} = \pi \cos\Lambda \dfrac{c\dot{\alpha}}{U_\infty}$
- Complementary term due to sweep and curvature: $C_L^{\text{comp}} = 2\pi \cos\Lambda \dfrac{w_c}{U_\infty}$
- Non-circulatory term: $C_L^{NC} = \dfrac{\pi c \cos\Lambda}{2U_\infty^2}\left(U_\infty \dot{\alpha} + \ddot{h} - \dfrac{c\ddot{\alpha}}{4}\right)$.
- Two-dimensional unsteady wake term: $C_L^{2D_{\text{unst}}} = \dfrac{2}{U_\infty c}\displaystyle\int_0^X \left(\sqrt{1+\frac{c}{\xi}} - 1\right)\gamma_y(\xi, y)d\xi$

In order to integrate the $C_L^{2D\text{unst}}$ term we define: $u = \sqrt{1+\dfrac{c}{\xi}}$, $u^\star = u_{n+1} = \sqrt{1+\dfrac{c}{X}}$ and $u_i = \sqrt{1+\dfrac{c}{x_i}}$. It can be calculated as shown in Eq.(4.7).

$$\begin{aligned} C_L^{2D\text{unst}} &= \frac{2}{Vc}\int_0^X \left(\sqrt{1+\frac{c}{\xi}} - 1\right)\gamma_y(\xi, y)d\xi = \frac{1}{V}\int_{u^\star}^{+\infty} \frac{4u}{(u-1)(u+1)^2}\gamma_y(u, y)du \\ &= \frac{1}{V}\left[\gamma_y(0,y)\left(\frac{2}{u_1+1} - \ln\frac{u_1-1}{u_1+1}\right)\right. \\ &\left. + \sum_{i=1}^{n}\gamma_y(x_i,y)\left(\frac{2}{u_{i+1}+1} - \frac{2}{u_i+1} - \ln\frac{u_{i+1}-1}{u_{i+1}+1} + \ln\frac{u_i-1}{u_i+1}\right)\right] \end{aligned} \tag{4.7}$$

where $\gamma_y(x_i, y)$ is the circulation gradient on the i wake panel at radial y position. It has been estimated in the blade module by storing the circulation Γ in the previous time steps and calculating its gradient:

$$\gamma_y(x_i, y) = \left.\frac{\Delta\Gamma(y)}{\Delta x}\right|_i = \frac{\Gamma_{i+1,y} - \Gamma_{i,y}}{x_{i+1} - x_i} \tag{4.8}$$

4.3 Concluding remarks

As it was presented in Chapter 3, the way finite part integrals were used in the numerical implementation proposed by Muller were not adapted for the case of a blade discretized in sections that are smaller than the blade chord. Therefore, the present approach aimed at overcoming the need to solve by finite parts the singular integrals that appear in the inner and the outer domains.

To do so, the chordwise vorticity terms have been removed from the outer domain (MINT wake) and considered only in the two-dimensional airfoil model. While the lifting-line theory considers a wake shed at the quarter-chord line and thus their integrals are singular, this airfoil model considers that the wake is shed at the trailing edge and therefore the integrals of the induced velocities become regular.

This is true for the chordwise vorticity terms in the wake, but it is not the case for the spanwise terms. Hence, although being singular terms, the spanwise variation of the circulation γ_x is still calculated by a four-point Gaussian quadrature rule. This is probably the main shortcoming of the present approach, and further studies should endeavor to correct it.

Moreover, an arbitrary choice of the wake length removed from MINT and considered in the airfoil model has been done. The choice has been based on the blade chord and span dimensions. In order to fulfill the asymptotic expansions' hypothesis, X has been chosen between the blade chord c and the blade span b. Further studies should assess the sensitivity of propeller loads to the length scale X.

The next two chapters present the application of this unsteady airfoil model to the case of a propeller and an open rotor in high-speed conditions and under a certain incidence. Moreover, Chapter 6 proposes a method for analyzing the impact of several induced velocity terms on the performance and 1P loads of an open rotor in high-speed and incidence.

Chapter 5

UCLL Method Assessment on APIAN Single Propeller Case

Contents

5.1 Impact of Incidence on High-Speed HOST-MINT Simulations 128
5.2 Impact of Advance Ratio on High-Speed HOST-MINT Simulations 131
5.3 Concluding Remarks 134

The main goal of this chapter is to assess the impact of the unsteady airfoil model as implemented in HOST on the performance predictions on a single-rotating advanced propeller. As in Chapter 1, comparisons between HOST-MINT simulations, wind-tunnel measurements, and CFD computations on the APIAN six-blade propeller are presented. Moreover, the same test cases have been chosen in order to compare incidence effects and RPM effects for high-speed conditions. Finally, different HOST-MINT simulations are compared to determine the contribution of installation effects and unsteady aerodynamic corrections in the estimation of propeller performance and blade sectional loads.

Again, HOST simulations have been performed using a time step equivalent to $5°/it$, a compromise between low computational costs and a fair accuracy in global loads. A 4th-order Runge-Kutta time stepping scheme has been also used, and wake is truncated over 55 panels for these high-speed simulations.

In the following paragraphs, we expose comparisons between several types of HOST simulations:

1. *Isolated* HOST-MINT simulations: only the propeller blades are taken into account, which means that no velocity perturbation field due to the spinner is considered and no unsteady corrections are added to the aerodynamic coefficients obtained from polar data.

2. HOST-MINT simulations including *installation effects*: we add a velocity perturbation field on the propeller disk so as to take into account the influence of the spinner on the propeller.

3. HOST-MINT simulations with *unsteady and curvature corrections*: the implemented model is used on simulations that consider also installation effects.

Table 5.1: Incidence effect on APIAN high-speed test cases

Test No.	Mach No. [–]	Incidence [°]	RPM [min^{-1}]	J [–]
1145	0.700	0.01	8623.	3.269
1146	0.699	1.00	8632.	3.268
1147	0.700	1.48	8638.	3.272
1148	0.700	2.02	8639.	3.273
1149	0.700	3.00	8639.	3.278

5.1 Impact of Incidence on High-Speed HOST-MINT Simulations

Propeller "incidence effect" stands for the evolution of the propeller aerodynamic behavior when placed under different angles of incidence with respect to the airflow. Table 5.1 shows the considered test cases to study this incidence effect at high-speed conditions. Notice they are the same used in Chapter 1

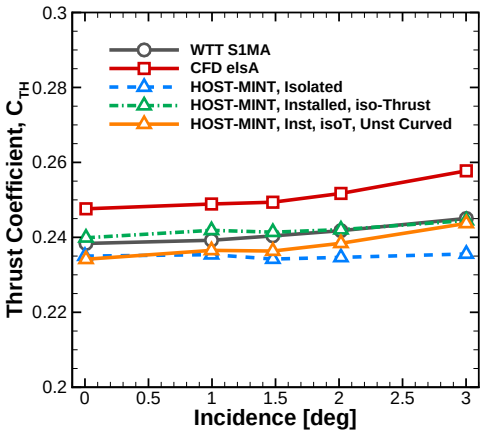
Propeller Performance. Propeller performance predictions on APIAN blade using HOST have been compared to wind-tunnel measurements and CFD computations. Six parameters have been used in the present study: the thrust coefficient (C_{TH}), the power coefficient (C_{PW}), the 1P load coefficient (C_{1P}), the 1P load phase lag (Ψ_{1P}), the 1P moment coefficient (C_{M1P}) and the 1P moment phase lag (Ψ_{M1P}).

The same CFD uRANS computations using *elsA* are again used for comparison. The propeller blade pitch has been modified of $+0.7°$ for all CFD simulations to achieve experimental thrust levels with a reasonable offset. Error bars have been added to experimental data 1P loads, considering its non-zero value in the case without incidence. These 1P loads at zero incidence have been considered as a constant offset in the measurement of the balances for all the test cases. The plotted error bars show the upper and lower limit of 1P loads modulus and phase when considering this offset.

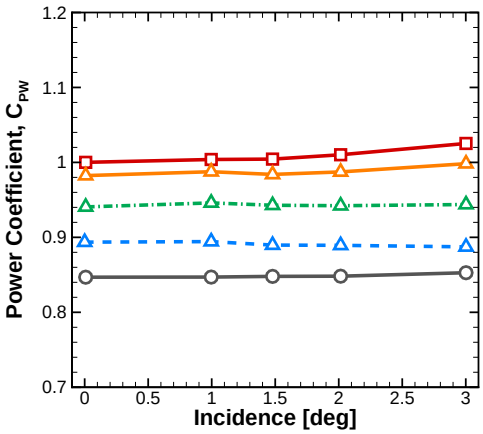
A case has been added to the comparisons in chapter 1, where the unsteady model described in Chapter 4, has been activated, as well as the velocity perturbation field (see Fig.5.1).

The unsteady model does not modify significantly the thrust, but increases the power prediction, getting closer to CFD simulations. As explained in Chapter 1, the rotating balances used in experimental tests are likely to underestimate power by $\sim 10\%$.

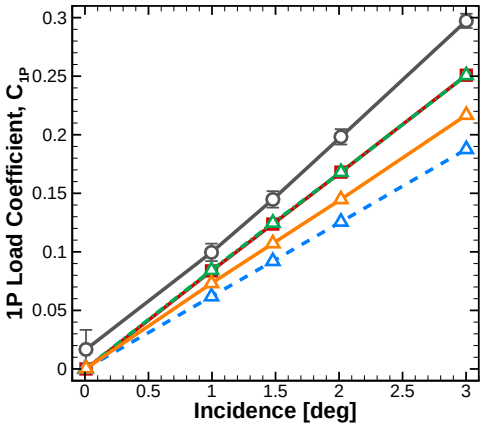
With the implemented unsteady corrections, The distribution of circulation is stored during several iterations and used to estimate their derivatives by a 2nd-order backward scheme. In the case without incidence, all unsteady terms become zero and no 1P loads arise. Besides, it can also be noticed an increase in 1P load norm



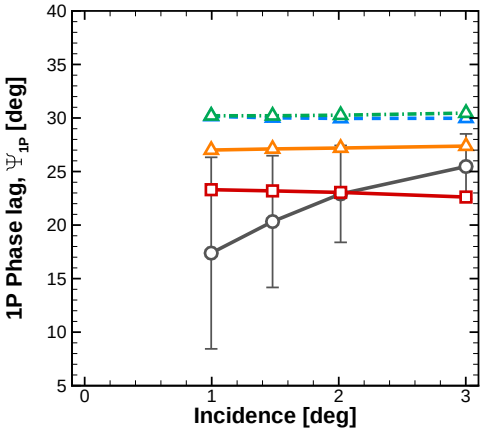
(a) Thrust coefficient, C_{TH}



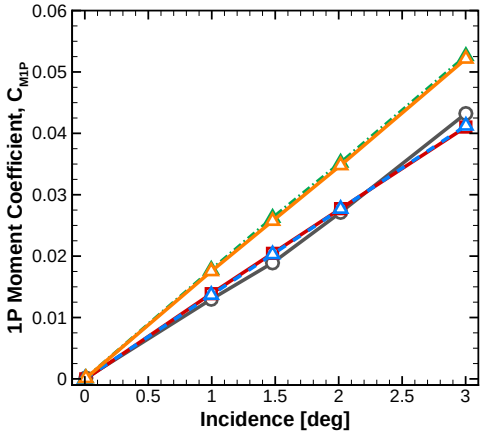
(b) Power coefficient, C_{PW}



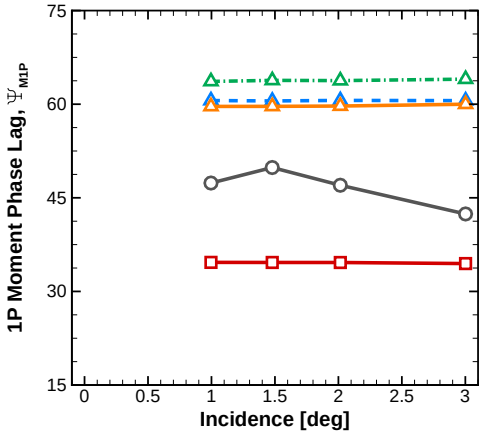
(c) 1P load coefficient, $C_{1\mathrm{P}}$



(d) 1P phase lag, $\Psi_{1\mathrm{P}}$



(e) 1P moment coefficient, C_{M1P}



(f) 1P moment phase lag, Ψ_{M1P}

Figure 5.1: Incidence effect on APIAN High-Speed simulations. Comparison between WTT data, *elsA* CFD computations and HOST-MINT simulations (isolated, with installation effects and with both unsteady corrections)

with respect to "isolated" simulations for the cases with incidence. When compared to "installed" simulations, we notice the reduction in amplitude due to the two-dimensional airfoil wake (similar to the predictions of Theodorsen's theory, see Section 2.1). The offset that still exists in 1P loads modulus can be attributed to the hub-blade mutual interaction, which is not taken into account in the blades-off velocity perturbation field.

The 1P phase lag is reduced by about 3° thanks to unsteady corrections, getting HOST simulations closer to experimental results and within the experimental error margins. Indeed, as the two-dimensional wake starts no longer from the lifting-line but from the airfoil trailing edge, the lag induced by the wake on blade loads is less important. However, a phase lag $\sim 4°$ still exists compared to CFD computations. These slight mismatches can be linked to the two-dimensional approach hypothesis of the blade element model. Indeed, notice that among all the possible sources of 1P phase lag (see Chapter 2), only a number of them can be considered in HOST simulations, and they are simulated using a quasi two-dimensional approach.

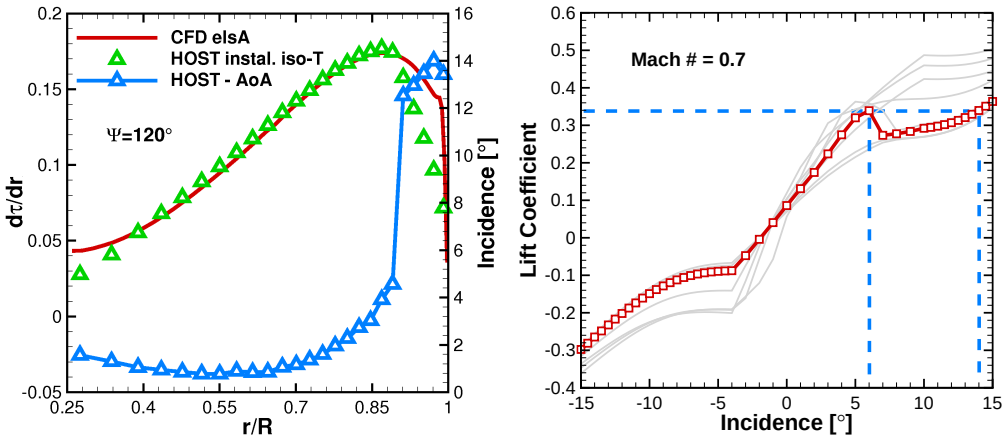
Finally, 1P moments are almost not modified by the unsteady corrections. This comes from the fact that the current implementation of the airfoil model corrects only the sectional lift, but not its pitching moment. Figures 5.1(e) and 5.1(f) put forward a shortcoming of the current unsteady model and future works should include this pitching moment correction based also on the thin-airfoil theory.

Blade sectional loads. To better understand these results, blade sectional loads have been investigated for the case at 3° of incidence in Table 5.1. HOST simulations presented before have been compared to an *elsA* CFD computation at the experimental thrust level.

Figure 5.2(a) shows the blade load comparison at a given azimuth angle between a CFD computation and an installed HOST simulation at the same thrust levels. It can be noticed that mismatches are mainly found near the root and the tip of the blade. On one side, root mismatches can be attributed to wall effects, which are not taken into account in the present lifting-line theory where $\Gamma = 0$ both at root and tip. On the other side, tip mismatches can be explained by the local incidences: close to the blade tip, HOST converges to high incidences that are after the stall point (see Fig.5.2(b)); besides, the APIAN blade presents a very important sweep angle near tip. These two factors generate important three-dimensional flow structures, that are not well captured by the two-dimensional approach used in the classical lifting-line method.

In order to improve near-tip predictions, as it has been explained in chapter 4, an additional term has been implemented in the unsteady lifting-line theory: the complementary term, which takes into account local sweep and curvature aerodynamic effects.

Figure 5.3 plots the harmonics of blade sectional loads for the same simulations as in the previous paragraph: (1) red line for the CFD computation, (2) blue squares for the *isolated simulation*, (3) green squares for the *installed simulation*, and (4) orange



(a) Blade sectional loads and incidence (b) High-speed polar curves for near-tip airfoil

Figure 5.2: Local results for APIAN high-speed conditions at 3° of incidence

Table 5.2: Advance ratio effect on APIAN high-speed test cases

Test No.	Mach No. [–]	Incidence [°]	RPM [min^{-1}]	J [–]
1149	0.700	3.00	8639.	3.278
1155	0.700	3.00	9064.	3.125
1163	0.700	3.00	9539.	2.969

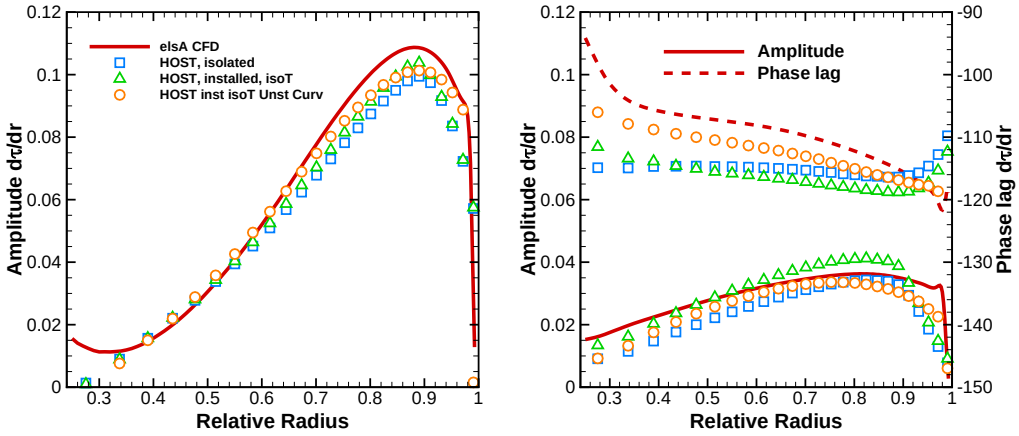
squares for the *installed simulation considering unsteady and curvature corrections*.

As it can be noticed, blade sectional loads close to the tip are better captured in the case including the curvature corrections, as the aerodynamic load is reduced in the central part of the blade and increased close to the blade tips. Moreover, this new unsteady model yields to a better prediction of the modulus and phase of the first mode all along the blade, as it can be noticed in Fig. 5.3(b). Finally, higher harmonics are negligible for all the simulations.

5.2 Impact of Advance Ratio on High-Speed HOST-MINT Simulations

Advance ratio effect stands for the evolution of the propeller aerodynamic behavior when varying its rotational speed keeping the same infinite upstream conditions. Table 5.2 shows the three considered test cases for studying the RPM effect at high-speed conditions and under 3° of incidence.

Propeller performance. Comparisons between wind-tunnel measurements and several types of HOST simulations have been performed (see Fig.5.4): isolated,



(a) Mode 0 (mean)

(b) Mode 1 (1/rev)

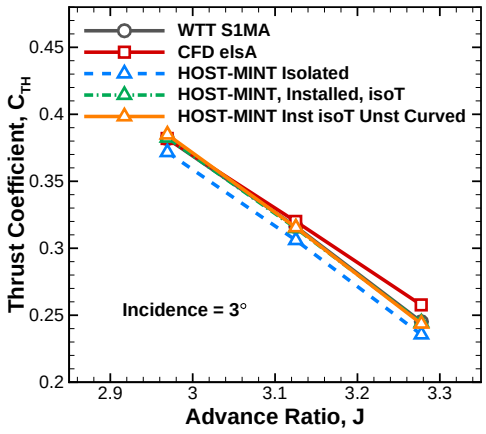
Figure 5.3: Blade load distribution modes for several HOST simulations: isolated, installed, and with unsteady & curvature corrections

installed, and with unsteady and curvature corrections' simulations. The same four parameters as for incidence effect comparisons have been used, i.e. thrust coefficient, power coefficient, 1P load coefficient and 1P load phase lag.

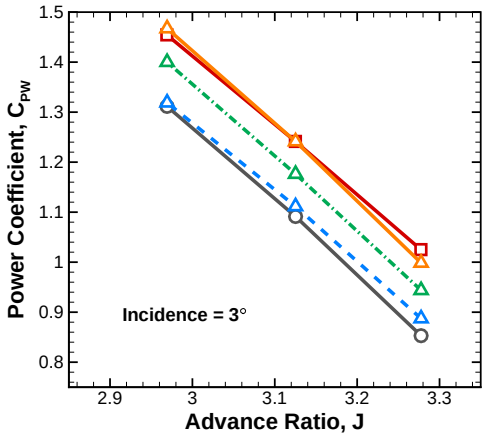
Again, thrust and power slopes are very well captured by this last HOST simulation (with installation and unsteady corrections). Although, a 11% offset in the power still exists. Nevertheless, notice that the power coefficient obtained in this last HOST simulation is still close to the predictions in *elsA* simulations. Even if installation effects increase the 1P load norm, simulations with the unsteady model show however a 20% underestimation. Finally, a very good agreement in 1P load phase lag is obtained when unsteady corrections are applied. Results when considering unsteady corrections have not exactly the same 1P phase lag evolution compared to wind-tunnel measurements. However, differences are still in the zone of uncertainty of experimental data.

Blade sectional loads. Figures 5.5 show the mean and 1/rev mode of the spanwise gradient of the thrust. The same three HOST computations used in the previous paragraph are compared to *elsA* results.

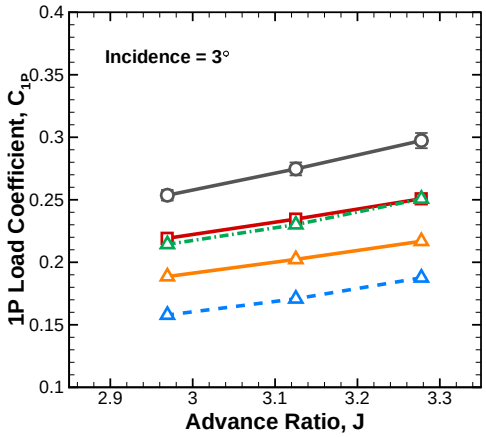
Notice that, similar to what was observed for the case 1149 ($\alpha = 3°$ and $J = 3.278$), curvature corrections increase slightly the mean and 1/rev blade loads near the blade tip. On the other side, the unsteady airfoil model reduces the 1/rev phase, thus yielding to predictions closer to CFD results, even if a 10° offset still exists. Moreover, the spanwise evolution of the 1/rev phase is also better predicted.



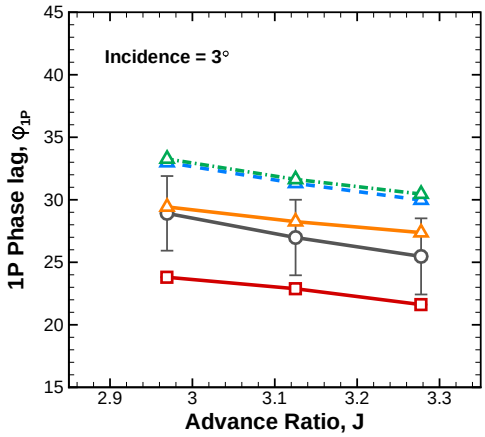
(a) Thrust coefficient, C_{TH}



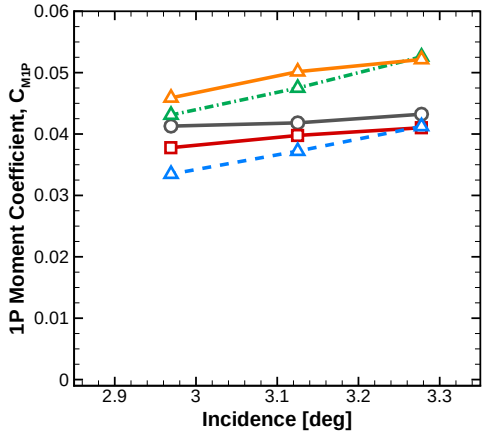
(b) Power coefficient, C_{PW}



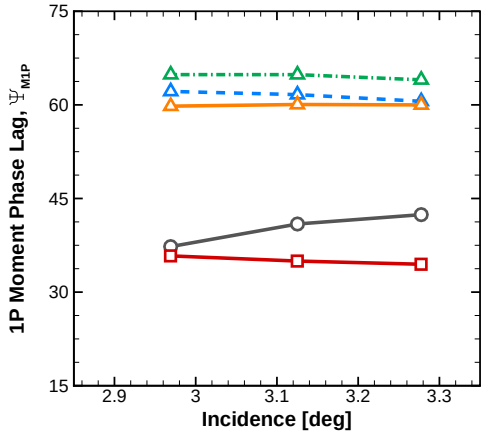
(c) 1P norm coefficient, C_{1P}



(d) 1P phase lag, Ψ_{1P}

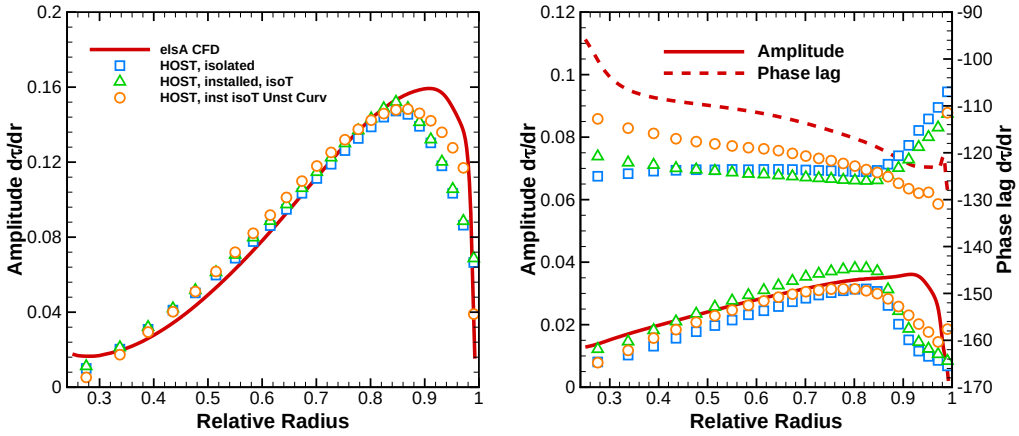


(e) 1P moment coefficient, C_{M1P}



(f) 1P moment phase lag, Ψ_{M1P}

Figure 5.4: RPM effect on APIAN High-Speed simulations. Comparison between WTT data and HOST-MINT simulations (isolated, with installation effects and with both unsteady corrections)



(a) Mode 0 (mean)

(b) Mode 1 (1/rev)

Figure 5.5: Blade load distribution modes for several HOST simulations: isolated, installed, and with unsteady & curvature corrections

5.3 Concluding Remarks

In this chapter, the benefits of including the hub effects and the unsteady airfoil model in the prediction of single propeller performance, 1P loads, and 1P moments using HOST-MINT simulations have been put forward.

The asymptotic technique proposed in Chapter 4 to link the lifting-line problem and the *unsteady airfoil model* has provided a more rigorous formulation of the complete three-dimensional problem. When applied to a number of advanced propeller cases, this asymptotic approach has yielded to a reduction in the 1P phase lag predictions, hence getting closer to experimental data and CFD results.

Finally, the *sweep and curvature effects* have been also included in the asymptotic formulation in order to improve the load distribution along the blade. The main impact of these curvature corrections has been noticed in the regions close to blade tips, where the local sweep angle becomes important ($\sim 45°$).

Nevertheless, the model is not complete, as it has been noticed in the 1P moment predictions. Indeed, the unsteady corrections are currently only applied to the airfoil lift, whereas a quasi-steady airfoil pitching moment is still considered. This leads to a significant overestimation of the 1P moment phase lag with respect to wind tunnel data and CFD predictions.

Future works should extend the airfoil model in HOST to include the unsteady pitching moment terms.

Chapter 6

UCLL Method Assessment on AI-PX7 Counter-Rotating Open Rotor Case

Contents

6.1 Test Case Description 135
6.2 Code-to-Code Assessment. elsA vs. HOST-MINT 137
6.3 Aerodynamic Mechanisms behind 1P Loads. 143
6.4 Concluding Remarks 147

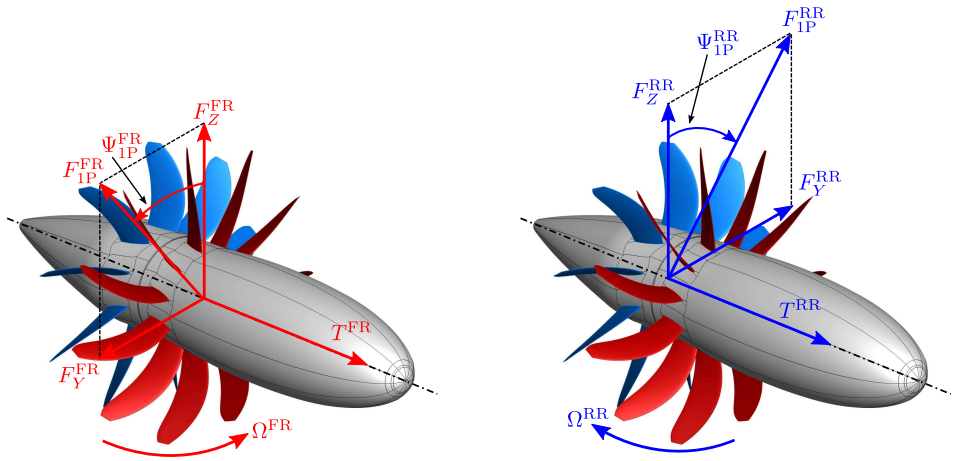
This chapter presents a code-to-code assessment between the *elsA* CFD solver and the HOST comprehensive code. The test case used for comparison is a generic contra-rotating open rotor geometry AI-PX7 designed by Airbus at high-speed conditions and at 1° of incidence. The propeller performance, blade loading, and induced velocity fields over a revolution are compared, in order to show the strengths and weaknesses of the lifting-line approach.

6.1 Test Case Description

Figure 6.1 shows the AI-PX7 Open Rotor geometry used in the present study and Table 6.1 presents the main geometrical characteristics and the flight conditions of the considered case.

Blade count (B_{FR}, B_{RR})	[–]	11 × 9
Front rotor diameter	[m]	4.2672
Rear rotor cropping	[–]	10%
Rotor-rotor spacing	[m]	0.95
Mach number	[–]	0.73
RPM	[min^{-1}]	795, -795
Incidence	[°]	1.0

Table 6.1: AI-PX7 Case Conditions



(a) Front rotor (b) Rear rotor

Figure 6.1: Load terms definition in AI-PX7 open rotor geometry

The *elsA* computation performed by François [François 2013b] has been used here. It uses a mesh with 53 million nodes, divided in a fixed far field domain and two rotating domains, one for each rotor, connected by the sliding mesh technique. This technique allows relative motions between the non-coincident interfaces and interpolates the fluxes between them.

Different HOST simulations are performed to assess the effects of installation effects and the unsteady airfoil model. HOST *isolated simulation* considers only the propeller blades, and although no nacelle is considered, the freestream Mach number is slightly increased (from 0.73 to 0.75) to simulate the mean acceleration due to the nacelle. The effects of the hub, also called *installation effects*, can be taken into account by introducing a steady velocity perturbation field for both rotors. This field is obtained from an initial CFD simulation of the nacelle in blades-off configuration. Finally, *unsteady corrections* stand for the addition of new terms in the airfoil lift calculation so as to consider its unsteady motion and the blade sweep and curvature.

While the *elsA* computation has been performed in 8 days on 128 cores and with a time step equivalent to a rotation of 0.5°, HOST simulations have been performed in 11 hours on 8 cores and with an equivalent 2° time step, for a matter of reasonable computational costs in a design process. In fact, the computational cost of HOST simulations are of the order of $O(N_{\text{step}}^3)$ due to the simulation time, $O(N_{\text{step}})$, and the free convection of the wake, $O(N_{\text{step}}^2)$, where N_{step} is the number of time steps. Moreover, as in HOST there is no interpolation between rotors and no viscous diffusion, the wake propagation is less sensitive to time step in HOST simulations than in *elsA* computations. Thus, a 2° time step simulation has proven to be a good compromise to capture the main part of the interaction between rotors, i.e. the effect of incidence. Indeed, as the main frequency of the incidence effect is a full revolution, 180 time steps are computed per period, which is largely sufficient to capture this mechanism. Moreover, blade-wake interactions might also be captured

with a certain accuracy, as 8 time steps are computed per blade passage period.

6.2 Code-to-Code Assessment. elsA vs. HOST-MINT

This section presents the main results obtained with HOST and compared with the reference simulation using *elsA*. First, propeller performance are presented, then the global blade thrust is compared, and finally, the blade thrust distribution is presented, i.e. the contribution of each section to the thrust.

Open Rotor Performance. Table 6.2 shows the propeller performance comparison between *elsA* simulation and three HOST simulations: *isolated*, with *installation effects*, and with both *installation and unsteady corrections*. For HOST simulations, the blade pitch has been adapted in order to obtain the same global thrust level $T = T_{\mathrm{FR}} + T_{\mathrm{RR}}$ and power ratio $P_{\mathrm{FR}}/P_{\mathrm{RR}}$ than in *elsA*. Acceptable pitch angle modifications, i.e. around 1°, are required in order to achieve the *elsA* thrust and power ratio levels. These pitch angles are going to be used in the rest of the study for comparing the different cases.

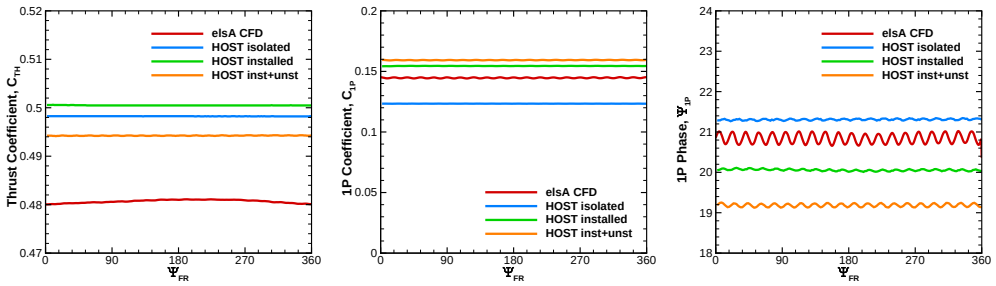
		elsA CFD	**Δ Isolated**	**Δ w/Installation**	**Δ w/Inst+Unst**
θ^{FR}	[°]	62.50	-1.22°	-1.36°	-1.36°
θ^{RR}	[°]	62.50	-0.28°	-0.17°	-0.17°
Thrust	[N]	20320	0.575%	0.458%	-0.87%
Power Ratio		1.25	1.46%	0.893%	0.00%

Table 6.2: AI-PX7 Performance. Comparison between *elsA* and HOST-MINT results (isolated, installed and installed+unsteady)

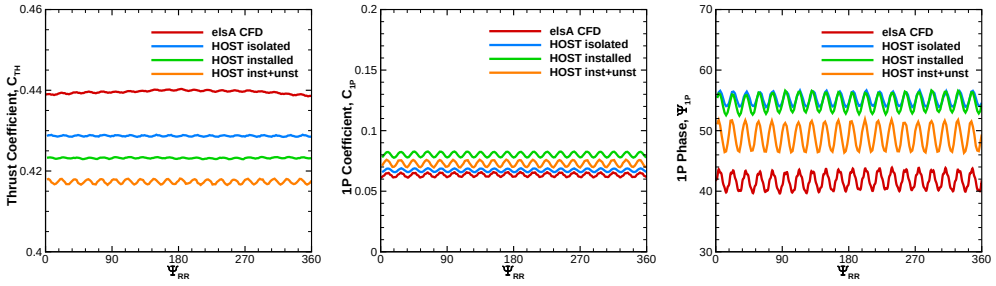
Rotor Performance and In-Plane Loads. Figure 6.2 shows the thrust coefficient, the in-plane loads coefficient and the in-plane phase lag for front and rear rotors respectively. These parameters are defined as follows:

$$C_{\mathrm{TH}}^{\mathrm{FR}} = \frac{T_{\mathrm{FR}}}{\rho_\infty N_{\mathrm{FR}}^2 (2R_{\mathrm{FR}})^4} \quad ; \quad C_{\mathrm{1P}}^{\mathrm{FR}} = \frac{\sqrt{F_{\mathrm{Y_{FR}}}^2 + F_{\mathrm{Z_{FR}}}^2}}{\rho_\infty N_{\mathrm{FR}}^2 (2R_{\mathrm{FR}})^4} \quad ; \quad \phi_{\mathrm{1P}}^{\mathrm{FR}} = \arctan \frac{F_{\mathrm{Y_{FR}}}}{F_{\mathrm{Z_{FR}}}}$$
$$C_{\mathrm{TH}}^{\mathrm{RR}} = \frac{T_{\mathrm{RR}}}{\rho_\infty N_{\mathrm{FR}}^2 (2R_{\mathrm{FR}})^4} \quad ; \quad C_{\mathrm{1P}}^{\mathrm{RR}} = \frac{\sqrt{F_{\mathrm{Y_{RR}}}^2 + F_{\mathrm{Z_{RR}}}^2}}{\rho_\infty N_{\mathrm{FR}}^2 (2R_{\mathrm{FR}})^4} \quad ; \quad \phi_{\mathrm{1P}}^{\mathrm{RR}} = \arctan \frac{F_{\mathrm{Y_{RR}}}}{F_{\mathrm{Z_{RR}}}} \tag{6.1}$$

Several remarks can be done on these figures. First, the total thrust level is obtained with a slight overestimation of the front rotor thrust (+3.5%) and a slight underestimation of the rear one (−3.5%). These differences can be explained by a lack of induced velocities from the rear rotor on the front rotor. Indeed, as HOST is



(a) Front Thrust coefficient (b) Front 1P coefficient (c) Front 1P phase



(d) Rear Thrust coefficient (e) Rear 1P coefficient (f) Rear 1P phase

Figure 6.2: Front and Rear Rotor performance comparison

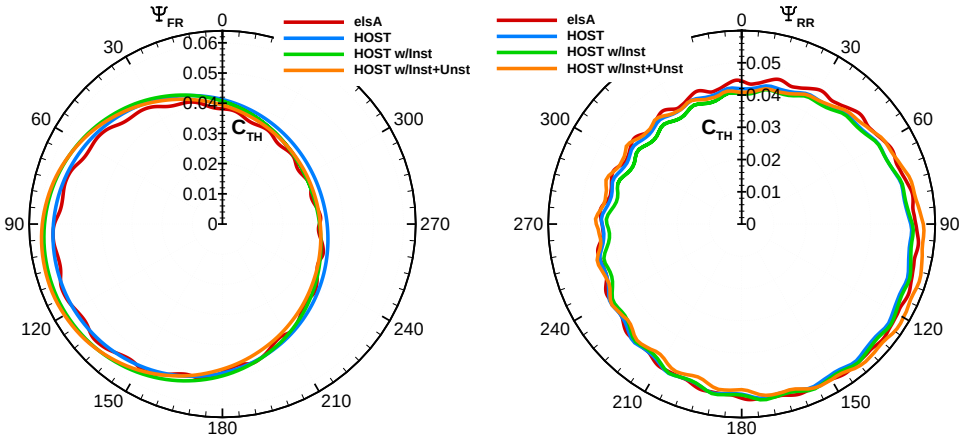
based on the lifting-line theory, the blade is reduced to the quarter-chord line, and thus chord effects are not well captured. In this open rotor configuration, even if results are still satisfactory, this deficiency starts to appear.

When comparing in-plane loads, it can be noticed how installation effects play an important role in predicting better their magnitude, i.e. differences are reduced from -17% to $+10\%$ for the worst case. Besides the magnitude of rear rotor in-plane loads is slightly modified by installation effects.

The mean value of the rear rotor in-plane phase lag are closer to *elsA* results when using the unsteady airfoil model, i.e. from $+12°$ to $+7°$. The amplitude of the blade load oscillation is however slightly overestimated. On the other side, the offset of front rotor phase lag is increased due to installation effects and the unsteady model, but values are still in the level of resolution of the simulations, i.e. $2°$.

Blade thrust. Figure 6.3 plots the blade thrust evolution along a cycle. It compares *elsA* computation with the three HOST simulations.

Notice that the thrust coefficient is slightly overestimated in the downward moving blade when adding installation effects.Notice also the lack of oscillations in the front blade loads. This can be explained by the fact that lifting-line methods reduce the blade to its quarter-chord line, and therefore the distance between rotors is more important than in the real blade geometry. Indeed, as the distance between the quarter-chord lines of both rotors is more important than the distance between



(a) Front rotor (b) Rear rotor

Figure 6.3: Blade loading along a cycle. *elsA* compared to HOST simulations

the trailing-edge of the front blade and the leading-edge of the rear blade, the effects from rear rotor on the front rotor are underestimated.

Regarding the rear blade loads, even if all HOST simulations match reasonably well with CFD, a slight underestimation appears in the upper part of the blade cycle. Morerover, the amplitude of the rear blade load oscillations is correctly captured and it is due to the passage of the front rotor wakes across the rear rotor. Notice however that a certain phase lag appears in the peaks between HOST and CFD. This can be explained by a difference in the point of emission of the wake panels: while in *elsA* they are convected from the trailing edge, HOST does it from the quarter-chord line.

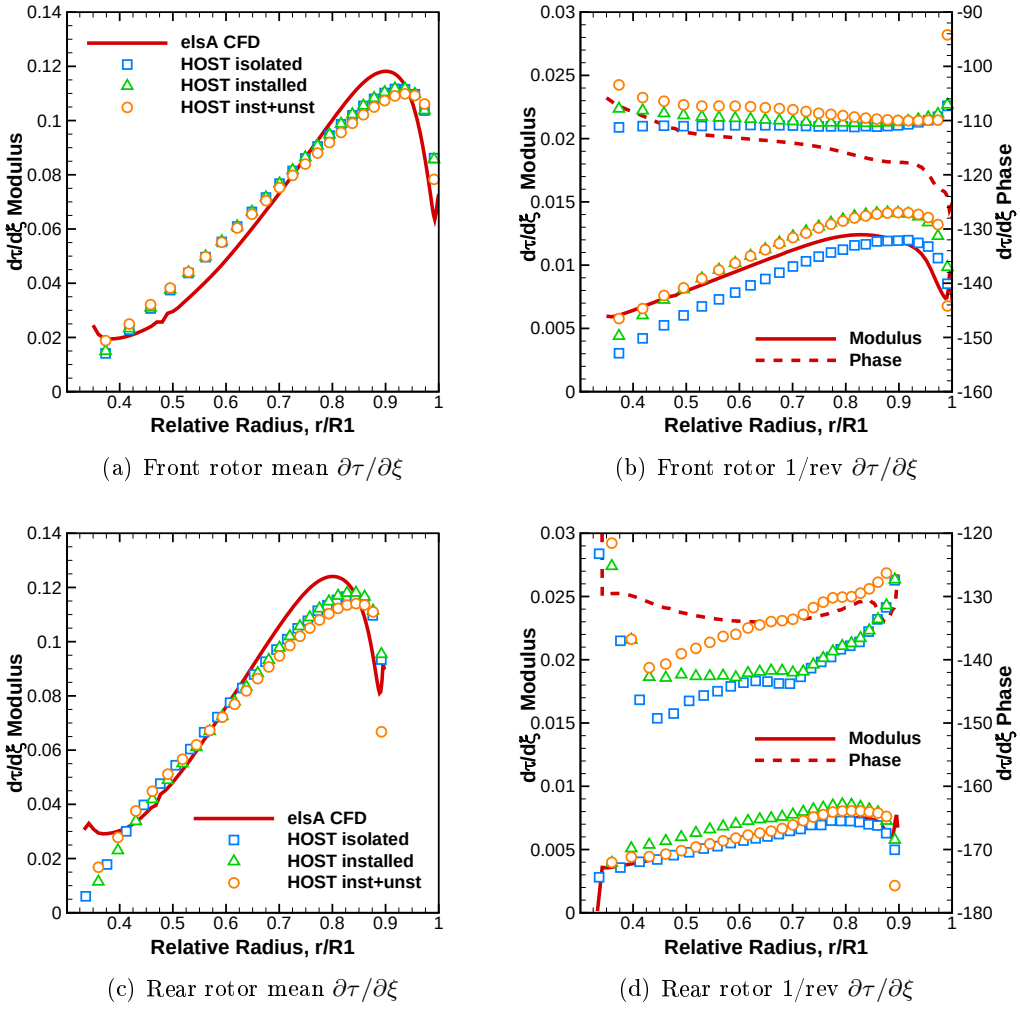
Blade thrust distribution. Figure 6.4 shows the thrust coefficient distribution along the blade $\partial\tau/\partial\xi$ for the same four simulations. The thrust coefficient distribution is defined as follows:

$$\frac{\partial\tau_{\mathrm{FR}}}{\partial\xi_{\mathrm{FR}}} = \frac{\partial T_{\mathrm{FR}}}{\partial\xi_{\mathrm{FR}}} \frac{R_{\mathrm{FR}}}{\rho_\infty N_{\mathrm{FR}}^2 (2R_{\mathrm{FR}})^4} \quad ; \quad \frac{\partial\tau_{\mathrm{RR}}}{\partial\xi_{\mathrm{RR}}} = \frac{\partial T_{\mathrm{RR}}}{\partial\xi_{\mathrm{RR}}} \frac{R_{\mathrm{RR}}}{\rho_\infty N_{\mathrm{FR}}^2 (2R_{\mathrm{FR}})^4} \tag{6.2}$$

where the front rotor parameters (rotational speed N_{FR} and propeller radius R_{FR}) are used as the reference for both rotor coefficients.

Left-hand figures show an important wall effect on the front and rear mean blade loads, which is not captured by HOST as no hub model is implemented, i.e. circulation is imposed to zero at the root section. In the central part of the blade, $\partial\tau/\partial\xi$ is overestimated. Finally, the blade maximum loading is underestimated and slightly closer to the blade tip. No significant difference is observed between HOST simulations.

Right-hand side figures show the first mode of $\partial\tau/\partial\xi$. Installation effects increase these oscillations on both rotors. The unsteady model corrects slightly the modulus



(a) Front rotor mean $\partial\tau/\partial\xi$

(b) Front rotor 1/rev $\partial\tau/\partial\xi$

(c) Rear rotor mean $\partial\tau/\partial\xi$

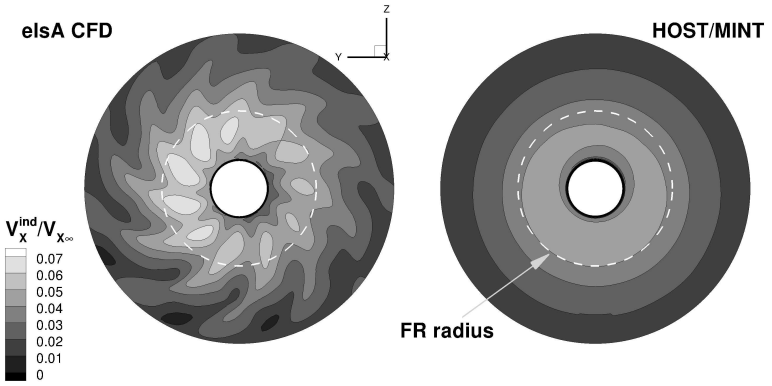
(d) Rear rotor 1/rev $\partial\tau/\partial\xi$

Figure 6.4: Discrete Fourier Transform of the front and rear rotors $\partial\tau/\partial\xi$

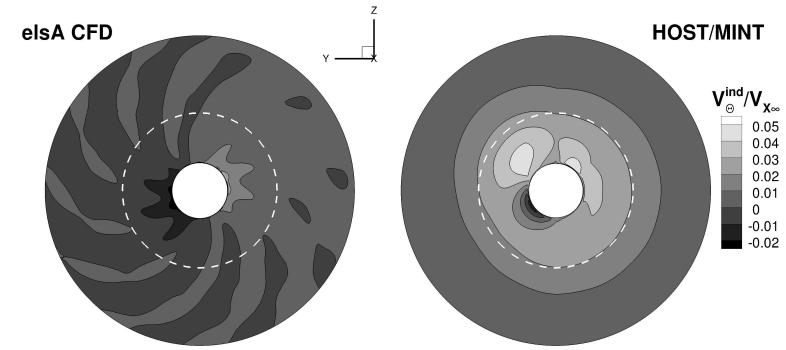
on the rear blade and reduces the phase lag, getting significantly closer to *elsA* results in an important part of the blade.

Induced Velocity Fields. This paragraph compares the axial and circumferential induced velocities as predicted by *elsA* and HOST-MINT for two planes normal to the rotating axis: one upstream the front rotor and the other one between the rotors (see figures 6.5 and 6.6). The circumferential component for the first and the second plane are calculated respectively in the direction of rotation of the front and the rear rotor.

For the plane upstream the front rotor (figures 6.5(a) and 6.5(b)), important mismatches are observed. Nevertheless, as it has been shown in the previous paragraph, the comparison between blade loads predicted by *elsA* and HOST are very similar. To explain this it must be considered that the upstream plane is very close to the

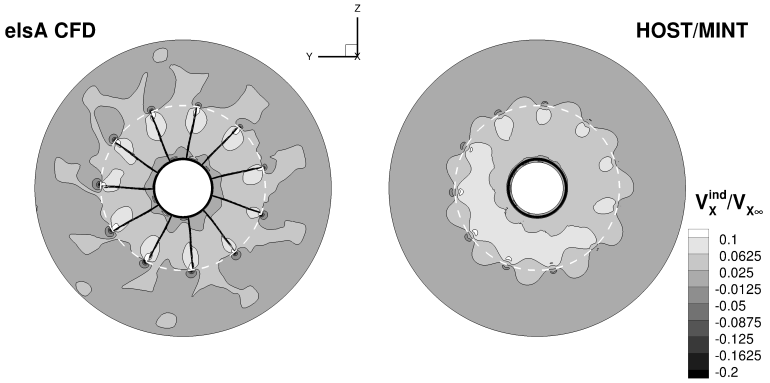


(a) Non-dimensional axial velocity, $V_{\mathrm{X}}^{\mathrm{ind}}/V_{X\infty}$

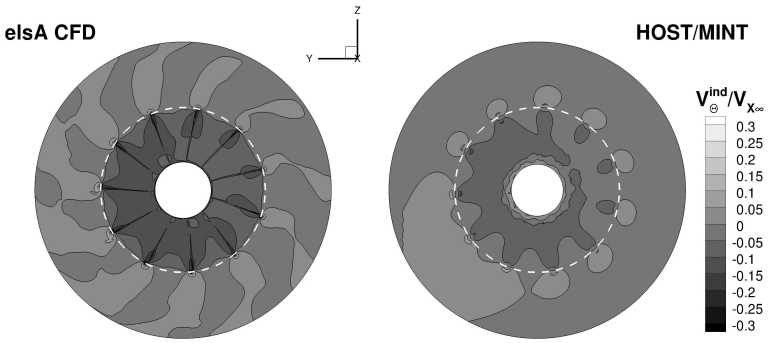


(b) Non-dimensional circumferential velocity, $V_{\theta}^{\mathrm{ind}}/V_{X\infty}$

Figure 6.5: Comparison between *elsA* and HOST-MINT results for an x-plane upstream the front rotor



(a) Non-dimensional axial velocity, $V_{\mathrm{X}}^{\mathrm{ind}}/V_{X\infty}$



(b) Non-dimensional circumferential velocity, $V_{\theta}^{\mathrm{ind}}/V_{X\infty}$

Figure 6.6: Comparison between *elsA* and HOST-MINT results for an X-slice between rotors

leading edge of the blade, and so the passage of the blade is very well captured in *elsA*. It is not the case in HOST-MINT, as the blade is reduced to its quarter-chord line. Therefore, this comparison shows that volume effects are not negligible in the field near the blade.

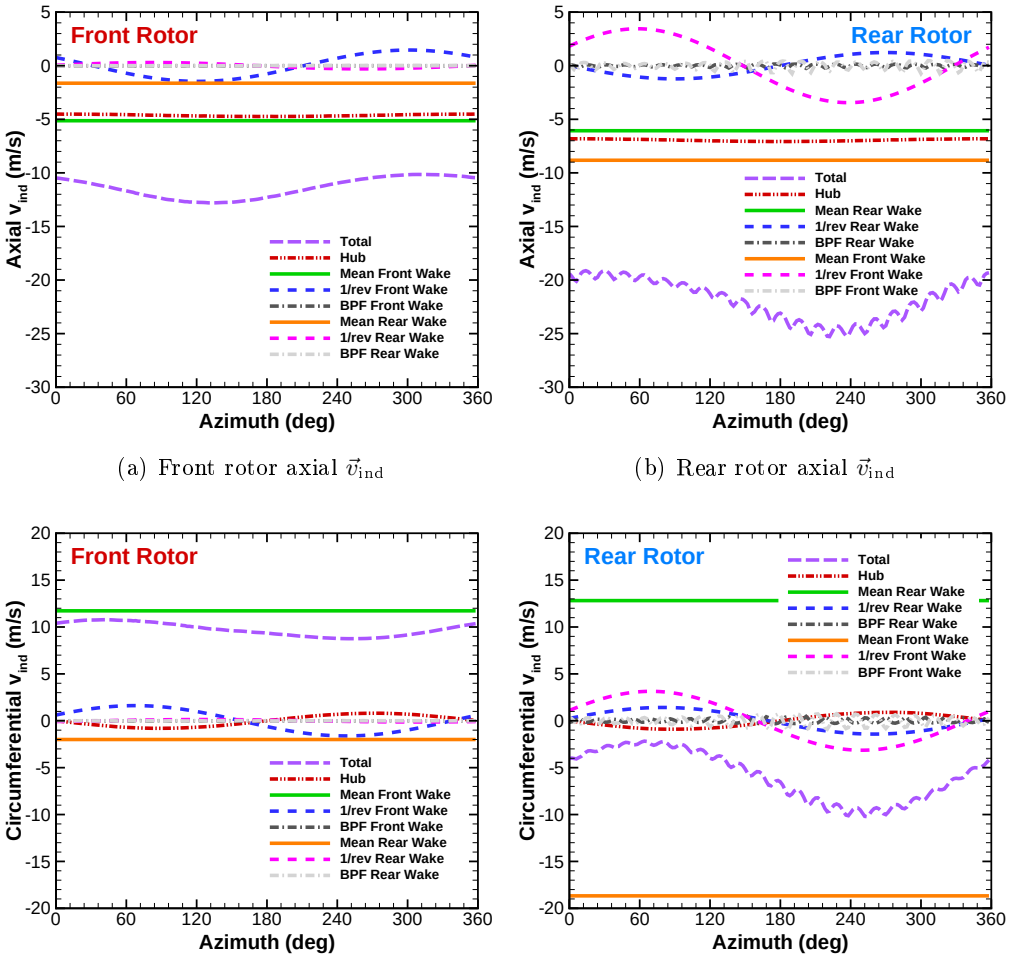
In figures 6.6(a) and 6.6(b), even if some differences can be observed, the general pattern is well captured by HOST-MINT, specially the circumferential component. The axial component calculated by HOST-MINT presents higher values in the zone of the downward moving blade, which are less evident in *elsA* results. On the contrary, this zone of higher circumferential induced velocities is noticed both in HOST and *elsA* results. As HOST-MINT considers a potential wake, no velocity deficit is observed due to the viscous effects in the wake. Moreover, similar to what was observed for the rear rotor blade loads, a certain phase lag in the tip vortex position can be observed due to a difference in the emission points of the wake.

6.3 Aerodynamic Mechanisms behind 1P Loads.

The last section of this study is devoted to the analysis of the aerodynamic mechanisms behind open rotor 1P loads. Singularity methods like the lifting-line theory are particularly well adapted to this type of study. They allow a decomposition of the induced velocities in different terms and, by removing one term at each simulation, its impact can be quantified.

Description of the method. From a purely geometrical approach, 1P loads can be attributed to a difference in the relative velocities of the downward and the upward moving blades, which generates a difference in their loads and thus a net force in the propeller plane. However, the impact of induced velocities, $\vec{v}_{\text{ind}}$, on 1P loads cannot be neglected as it has been shown in section 6.2. To analyze their contribution, $\vec{v}_{\text{ind}}$ are going to be decomposed in several components. A quantification of the impact of one single $\vec{v}_{\text{ind}}$ component on thrust and 1P loads should be estimated by removing that component from a HOST simulation and comparing the results with respect to the original simulation.

The induced velocities $\vec{v}_{\text{ind}}$ represent the influence of the potential wakes, the installation effects and the airfoil motion relative to the airflow. These different contributions are added in the lifting-line methods to calculate the total $\vec{v}_{\text{ind}}$ on each blade section and therefore to obtain the aerodynamic behavior of the different blade sections of the propeller.
Hence a decomposition of the $\vec{v}_{\text{ind}}$ can be done as follows: (a) *unsteady corrections* due to the airfoil motion; (b) *installation effects* due to the hub; (c) *auto-induced velocities*, $\vec{v}_{\text{ind}}$ by the wake of a propeller on the propeller itself; and (d) *mutually-induced velocities*, $\vec{v}_{\text{ind}}$ by the wake of the other propeller. Both, auto- and mutually-induced velocities are decomposed in mean value (mode 0), 1/rev or incidence mode (mode 1), and the Blade Passing Frequency mode (mode BPF). Figure 6.7 shows, for a given radial position ($r = 0.75R$), the decomposition of the axial and circumfer-



(a) Front rotor axial $\vec{v}_{\text{ind}}$

(b) Rear rotor axial $\vec{v}_{\text{ind}}$

(c) Front rotor circumferential $\vec{v}_{\text{ind}}$

(d) Rear rotor circumferential $\vec{v}_{\text{ind}}$

Figure 6.7: Decomposition of the induced velocities $\vec{v}_{\text{ind}}$ for the front and the rear rotors.

ential components of the $\vec{v}_{\text{ind}}$ into its different terms. Note that negative axial $\vec{v}_{\text{ind}}$ tend to diminish the aerodynamic incidence of the blade section, whereas negative circumferential $\vec{v}_{\text{ind}}$ tend to increase it.

Figure 6.8 plots the contribution of each $\vec{v}_{\text{ind}}$ component on thrust, 1P load norm, and 1P load phase. Notice that the percentage value accounts for the importance of the impact of each component, whereas the sign accounts for its positive or negative contribution. Moreover, percentages in red should be considered carefully, as they are a consequence of non-linear effects, as it will be explained hereafter. These results have been obtained by storing the $\vec{v}_{\text{ind}}$ field for a complete CROR simulation and then removing one $\vec{v}_{\text{ind}}$ component at each simulation, in order to quantify its impact.

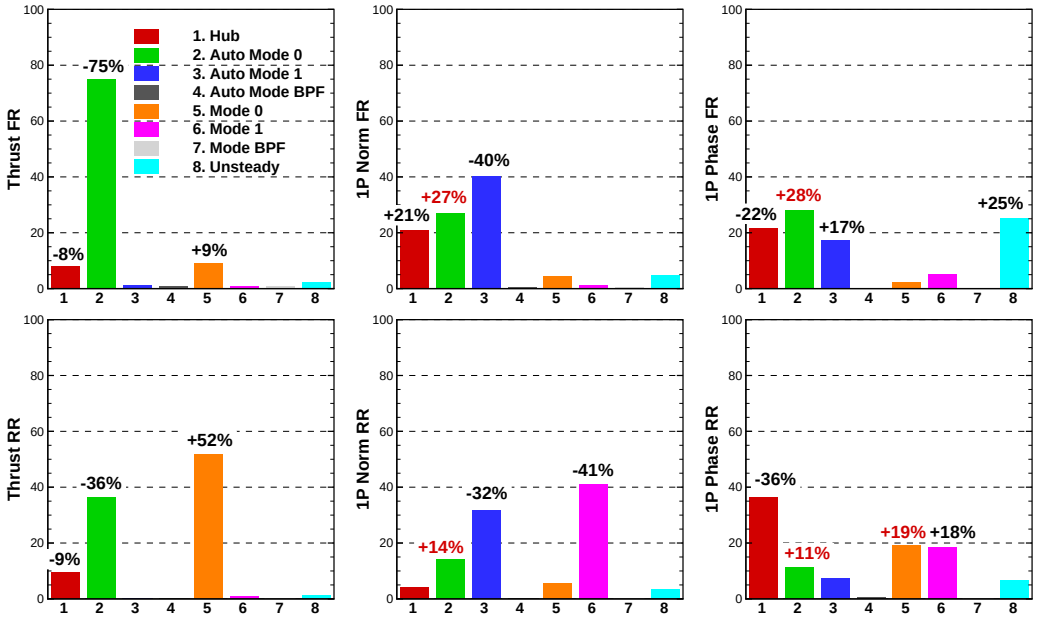


Figure 6.8: Contribution of the $\vec{v}_{\text{ind}}$ terms on the thrust, the 1P load norm, and the 1P load phase lag of front and rear rotors.

Aerodynamic mechanisms of Thrust. The mean value of $\vec{v}_{\text{ind}}$ is composed mainly of an axial and a circumferential component, i.e. the swirl. In the present method both components are considered together. Notice the mean value of $\vec{v}_{\text{ind}}$ is the main mechanism impacting the propeller thrust. However, the impact of auto-induced and mutually-induced velocities is not the same. On one side, in the case of auto-induced velocities, both axial and swirl components decrease the local angle of attack and hence the thrust. On the other side, in the case of mutually-induced velocities, the swirl increases the angle of attack whereas axial component decreases it, but the overall effect tends to increase the angle of attack.

The front rotor thrust predicted by HOST is almost not affected by the rear rotor wake. Thus we can consider that its response will be similar to the case of a single propeller in incidence. On the contrary, the rear rotor thrust is more impacted by the front rotor mean $\vec{v}_{\text{ind}}$ (bar 5) than by its auto-induced velocity (bar 2). Furthermore, the contribution of the swirl of the front rotor wake increases the blade incidence and thus the rear rotor thrust.

Finally, as the hub tends to accelerate the airflow in the axial and upward directions, it has a negative impact on the thrust of both rotors (bar 1), though it is less important than the wake components (-9%).

Aerodynamic mechanisms of 1P load norm. The main $\vec{v}_{\text{ind}}$ mechanism impacting 1P load norm is the first mode of the wake (bars 3 and 6), due to the propeller incidence. Indeed, the vorticity shed in the wake is linked to the evolution of the angle of attack of the blade and acts in the opposite direction. For example,

an increase in the angle of attack generates a wake with more vorticity and more $\vec{v}_{\text{ind}}$ which tend to reduce the angle of attack. As the 1P load norm is directly related with the oscillation of the angle of attack of the blades, both auto- and mutually-induced velocities tend to reduce this 1P load norm. As for the thrust, the most important contribution on the 1P load norm of the rear rotor is the first mode of the front rotor wake. This helps to explain what was noticed in section 6.2: that front rotor wake reduces the rear rotor incidence and thus the 1P load norm.

Notice the important contribution of the mean $\vec{v}_{\text{ind}}$ (bar 2). As plotted in the scheme of Fig. 6.9, this is due to non-linear airfoil data, which is not desired in the present linear analysis of the 1P loads. Indeed, when removing the mean $\vec{v}_{\text{ind}}$ from the input perturbation files, the local incidence increases up to values after the airfoil stall angle. As it is shown in the figure, for a given incidence oscillation and when removing the mean $\vec{v}_{\text{ind}}$ contribution, the lift coefficient does not almost oscillate. Consequently, the method predicts a very important but unphysical contribution of the mean $\vec{v}_{\text{ind}}$ on the 1P load norm and phase lag. This would not be the case if the angle of attack remained around the working point and inside the range of incidences where the airfoil data is linear. Therefore, the percentages of the impact of mean auto-induced and mutually-induced velocities on the 1P load norm and phase lag (bars 2 and 5) should be considered carefully.

Finally, similar to what has been obtained for the single propeller, the hub in incidence has a positive contribution on the 1P load norm as it accelerates the airflow upwards , increasing the difference in relative velocity seen by the downward moving blade and the upward moving blade, and thus increasing the rotor vertical force and consequently increases the 1P load norm (bar 1).

Aerodynamic mechanisms of 1P load phase. One of the most important contributions comes from the installation effects (bar 1). Indeed, as it has been explained in the previous paragraph, the hub increases the vertical force generated by the propeller without modifying its side force. This is why installation effects tend to reduce 1P load phase lag.

Notice also that the unsteady airfoil model has an important positive contribution on the phase lag (bar 8). In addition to the $\vec{v}_{\text{ind}}$ from the airfoil motion, this model includes the effect of the near wake. The first one tends to accelerate the lift evolution when the incidence is modified, whereas the second one tends to lag it. The overall contribution is an increase in the lag between incidence and lift, which generates an increase in 1P load phase lag.
As explained before, the mean $\vec{v}_{\text{ind}}$ has a non-linear impact on 1P load norm and phase lag, and should be considered carefully (bars 2 and 5).

The first mode of $\vec{v}_{\text{ind}}$ (bars 3 and 6) tend to decrease the amplitude and lag the blade loading oscillation due to the propeller incidence. This explains why 1P load phase lag of the rear rotor is around two times the one of the front rotor. Figure 6.10 tries to illustrate how the front rotor induced velocities contribute to lag the angle of attack of a blade section of the rear rotor. First, the dashed curve represents the

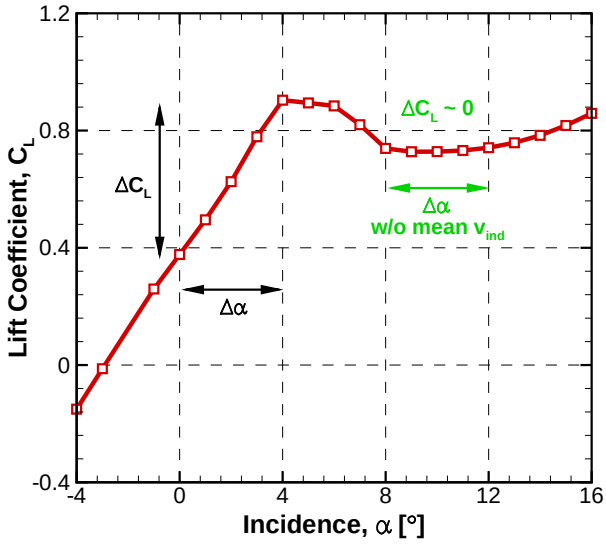


Figure 6.9: Example of two-dimensional airfoil data and the oscillation of angle of attack due to the incidence along a blade cycle. Comparison between the case with and the case without mean induced velocities.

angle of attack of a single propeller induced by its wake; its minimum value is found in the downward moving blade zone, because there the wake has more vorticity. Second, the dash-dotted curve represents the angle of attack induced by the front rotor wake; its minimum value is placed around 270°, where the front rotor wake has more vorticity. Finally, the solid curve shows the addition of both contributions, as in the case of a CROR. It presents a reduction of the amplitude of the $\Delta\alpha$ and an increase in its phase with respect to the single propeller case.

Finally, the contribution of the BPF modes in HOST simulations is negligible (bars 4 and 7). However, an analysis of the sensitivity of 1P phase lag to time step presented by François et al. [François 2013b], puts forward that the BPF modes have an impact of around 3.5° for the front rotor (−17%) and 3° for the rear rotor (−7%). These offsets can be a consequence of the three reasons exposed in section 6.2: using different time steps, neglecting viscous effects in HOST, and reducing the blade to its quarter-chord line in HOST.

6.4 Concluding Remarks

A detailed code-to-code assessment between *elsA* CFD solver and HOST lifting-line code, has been performed on a generic contra-rotating open rotor geometry (AI-PX7) at high-speed conditions and at 1° of incidence. Three different types of HOST simulations have been performed in order to assess the impact of nacelle effects and unsteady corrections on aerodynamic performance and 1P loads.
The total thrust and power ratio target values have been achieved for all HOST

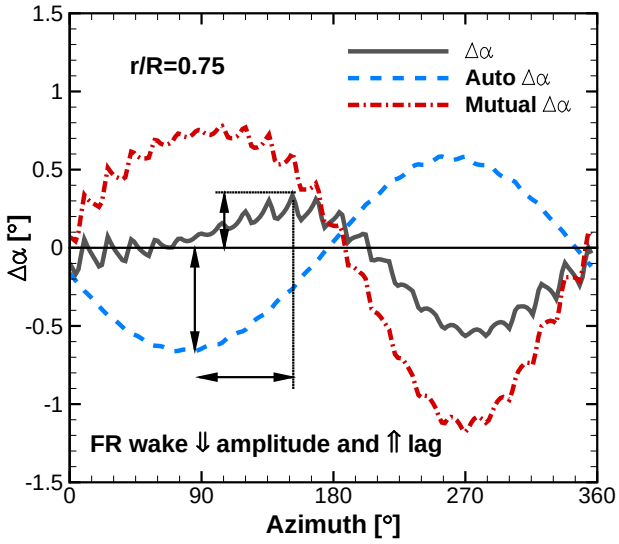


Figure 6.10: Angle of attack evolution during a revolution for a rear rotor blade section. Auto-induced and mutually-induced $\Delta\alpha$ are plotted together with the total $\Delta\alpha$ for a given blade section

simulations within reasonable pitch angles modifications, i.e. $\sim 1.36°$. On the one hand, offsets obtained in 1P loads modulus have been reduced when adding the effect of the nacelle. On the other hand, the unsteady airfoil model implemented in HOST allows reducing mismatches on the rear rotor 1P loads phase lag.
Fair results have been obtained for global blade thrust, even though the comparison has also highlighted some shortcomings of the present method in the prediction of the rear potential effect on the front rotor. This phenomenon has been explained by the fact that chord effects are not considered in lifting-line methods, and they become important for rotors that are close one to each other.
In the comparisons of thrust distribution along the blade, the shape predicted by *elsA* was also obtained in HOST, but with some minor offsets. They were noticed near the blade root due to the wall effect. Moreover, acceptable differences in maximum mean loads were also observed (-8%) and their position was slightly closer to the blade tip than in *elsA* simulations. The first harmonic was well captured by all HOST simulations, though installation effects overestimate its amplitude on the front blade. Unsteady corrections reduced the phase lag of the first mode, and thus results get closer to *elsA* ones.
Induced velocity fields have shown, on one side, the impact of neglecting chord effects in HOST and, on the other side, the capacity to capture correctly the potential effect of the tip vortices and the global effect of the front wake on the rear rotor.

A method to identify the mechanisms governing thrust and 1P loads has been presented. Though some non-linear effects appear in some of the results, the method enables to determine the quantitative impact of each mechanism on global performance of open rotors.

The front rotor behavior predicted by HOST is very close to the one of a single-rotating propeller, as the rear rotor has a very small contribution on its performance and 1P loads ($< 10\%$). These results have to be analyzed taking into account what has been exposed in section 6.2, i.e. that HOST simulations neglect chord effects, leading to an underestimation of the potential effect of the rear rotor on the front rotor.
On the contrary, the most important mechanism on the rear rotor response is the front rotor wake effect. Indeed, more than 50% of its thrust is due to the combination of positive axial and negative circumferential $\vec{v}_{\text{ind}}$ from the front rotor wake. Moreover, this wake decreases the 1P load norm (-41%) and increases its phase lag significantly ($+18\%$).
Finally, while installation effects play an important role in the prediction of 1P loads for both rotors, the unsteady corrections have shown to be important for the 1P phase lag, mainly in the case of the front rotor, where more important incidence variations occur.

The next chapters will be devoted to the implementation and first validation tests of a coupling strategy between a HOST simulation and an *elsA* near-wall mesh in order to obtain a moderate-cost methodology that takes into account three-dimensional, chord, compressibility, and viscosity effects in propeller and open rotor cases.

Part II

Code Coupling

Chapter 7

Development of a Coupling Strategy between HOST-MINT and elsA Codes

Contents

7.1 Current Coupling between HOST/MESIR and elsA 154
7.1.1 HOST/MESIR-elsA Coupling Strategy 154
7.1.2 Main Advantages and Shortcomings of the Strategy 155
7.2 Implementation of a One-Way Coupling between elsA and HOST-MINT codes 156
7.3 Assessment of MESIR and MINT Coupling Strategies for Single Propellers 157
7.3.1 Induced velocity fields 159
7.3.2 Induced Velocities Interpolation Time Step 165
7.4 Coupling Strategy Assessment on APIAN Single Propeller Case 168
7.4.1 Test Case Description. 168
7.4.2 Blade Loading 169
7.4.3 Propeller Performance 169
7.4.4 Blade Load Distribution 170
7.4.5 Pressure on Blade Skin 171
7.4.6 Flow Analysis 173
7.5 Induced Velocity Fields 174
7.6 Concluding Remarks 177

This chapter presents the state-of-art of the coupling between HOST and *elsA* codes for the simulation of single-rotating propellers. In the current coupling strategy, the HOST simulation uses the MESIR wake model, which restricts the number of applications of this coupling strategy. These restrictions have been identified and are described in the present chapter.

Moreover, in order to address some of the current restrictions, instead of using the MESIR wake model, a new coupling strategy using MINT high-order free-wake model has been partially implemented. A first step in the validation of this new

approach has been done by comparing two HOST-*elsA* coupled computations using MESIR and MINT wake models, respectively.

7.1 Current Coupling between HOST/MESIR and elsA

This section details the current coupling strategy implemented in HOST and *elsA* codes. Moreover, the main advantages and shortcomings are listed and studied.

As described in the *Methods and Tools* chapter, the current coupling strategy uses the induced velocities calculated by MESIR wake model on the boundaries of a near-wall mesh around one blade of the propeller, whereas the blade loads calculated by *elsA* are given as an input to HOST-MESIR. This strategy allows to consider a reduced volume of the problem.

7.1.1 HOST/MESIR-elsA Coupling Strategy

Figure 7.1 shows a scheme of the loose coupling strategy already implemented between HOST and *elsA* codes. The periodicity hypothesis in MESIR wake model allows to couple both codes once per revolution, instead of doing it at each time step. This reduces significantly the code-to-code communication time.

Coupled simulations start with an *elsA* computation of a near-wall mesh around the blade. As it will be shown hereafter, the mesh used in the present study extends around the blade wall for a distance of the order of the maximum of the blade chord. A full revolution is computed considering non-reflective boundary conditions (BC) in the outer mesh boundaries. This non-reflective BC imposes the freestream state of the conservative variables for the incoming inflow all along the simulation. The RVA module extracts the surface mesh of the outer BC at each time step.
On the other side, HOST/MESIR simulations run until the circulation on all the blade sections is converged. To achieve this convergence, the vorticity and the position of the wake panels is modified iteratively.
This time, the RVA module uses these wake data to compute the velocity induced on each node of the surface mesh extracted from the outer boundary of the flow domain computed with *elsA*. The vortex filaments in the wake are considered as distributed singularities and hence Biot-Savart's law is used to compute the velocity they induce on the mesh nodes. These induced velocities are stored in a series of files for a complete blade revolution.
These files are then used in another revolution of the *elsA* computation, using the HOST/MESIR data to replace the freestream state in the non-reflective BC. With this, the velocities induced by the far wake and the effect of the other blades is taken into account in the airflow around the blade.
During the *elsA* computation, pressure and viscous forces on the blade skin are integrated to obtain a spanwise distribution of the blade load. At the end of the computation, these loads are provided to HOST/MESIR in order to correct the initial load prediction.

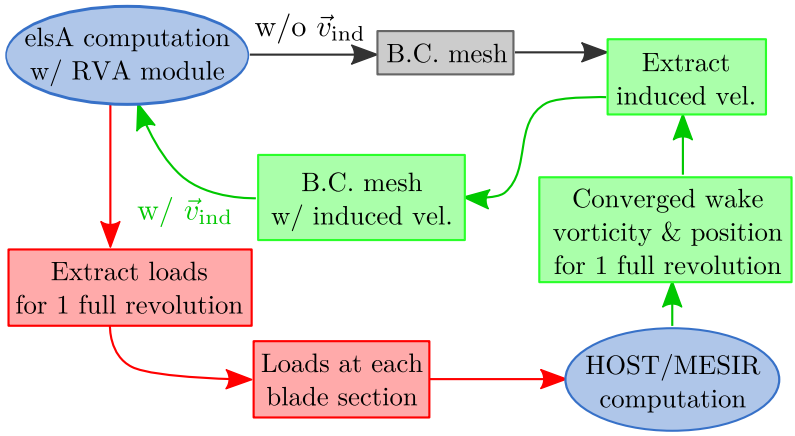


Figure 7.1: Loose coupling strategy between HOST/MESIR and *elsA* simulations.

This loop is repeated until the loads predicted by *elsA* and those predicted by HOST match.

7.1.2 Main Advantages and Shortcomings of the Strategy

As it has been explained before, a one per revolution coupling strategy already exists between *elsA* and HOST-MESIR codes. This strategy presents theoretically the advantage to reduce the computational domain of the CFD method to the near field around one blade of the propeller. Therefore, important meshing and computational cost reduction might be expected from this with respect to full-annulus uRANS simulations. Besides, the method can be applied to general airflow conditions like a full-annulus simulation. Moreover, with respect to lifting-line simulations, a much better definition of the aerodynamics of the near blade domain might be also obtained.

On the other side, a number of shortcomings have been detected in the current implementation and have been addressed with a new coupling strategy presented in the next subsection:

- The periodicity hypothesis in MESIR wake model allows a rigorous implementation of a loose coupling strategy, as data is exchanged once per revolution. However, the periodicity hypothesis, although reducing the computational costs, it limits the field of application of this stratedy to *stabilized periodic flight conditions*. Therefore, it does not enable non-periodical simulations, like for example, the simulation of a maneuver of an helicopter or the whirl flutter of a propeller.

- MESIR wake model can only take into account the *influence of one wake element*, thus limiting its application to single rotors or propellers. This is a minor drawback for classical helicopter configurations, but can be limiting in the case of a rotorcraft with two co-axial rotors or a rotor and one or more propellers. In addition, it is a major drawback in the case of open

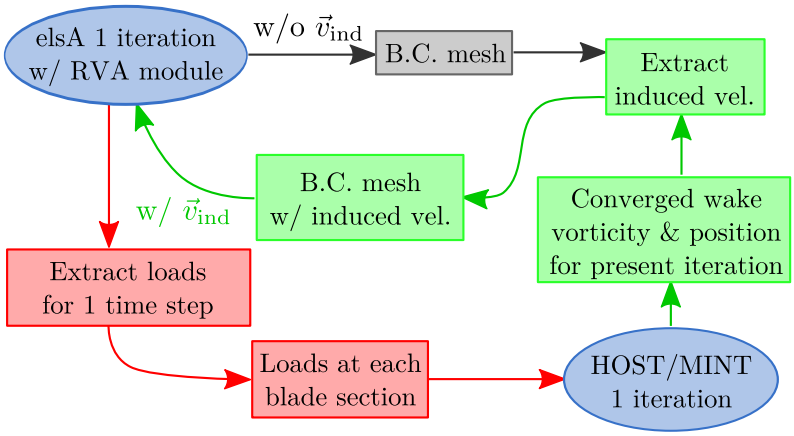


Figure 7.2: Tight coupling strategy between HOST-MINT and *elsA*.

rotor simulations, because the mutual effect between the front rotor and the rear rotor is completely neglected. As it has been shown in Chapter 6, this rotor-rotor interaction cannot be neglected mainly to predict the rear rotor aerodynamic behavior.

- MESIR is a *low-order wake model* that describes the wake vorticity as a lattice of vortex filaments. This approach presents a very singular behavior when the calculation point is close to the wake and thus regularization techniques are necessary to avoid too important values of the induced velocities, which are generally not physical.

7.2 Implementation of a One-Way Coupling between elsA and HOST-MINT codes

The shortcomings in the coupling strategy using MESIR wake model have motivated the implementation of a more flexible one using MINT high-order free-wake model. In the present work, the one-way coupling has been done under the form of a loose coupling, i.e. the exchange of information takes place once per propeller revolution.

The strategy partially implemented to couple HOST-MINT and *elsA* codes allows theoretically both tight and loose coupled simulations. The loose coupling loop follows a scheme similar to the scheme in Fig. 7.1. Here Fig. 7.2 shows the scheme of the tight coupling loop, where the exchange of information is no longer done once per revolution, but at each physical time step or iteration. Therefore, notice that no periodicity constraint is needed here, and thus the methodology can be extended to a very large scope of applications. However, it must be also noticed that a tight coupling strategy implies a much more important exchange of information between codes. Currently, this exchange is done by files, but a much faster memory exchange could be implemented in the future.

The present work focuses only on the implementation of a one-way coupling

Table 7.1: Conditions for APIAN minimum-body configuration. From wind tunnel case No.1149

Mach No.	[–]	0.7
Incidence	[°]	3.
Rotational Speed	[min^{-1}]	8639.
Advance Ratio, J	[–]	3.278

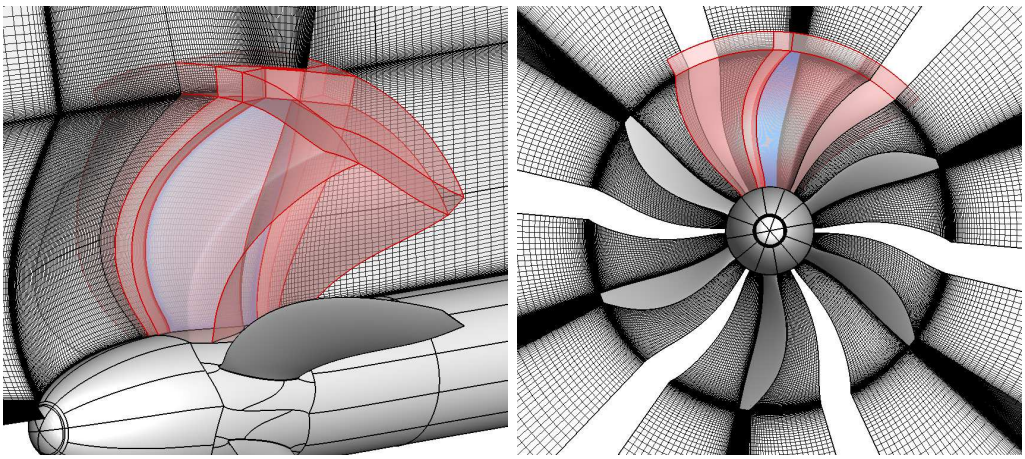
between HOST and *elsA*, and its assessment in a loose coupling strategy. Regarding the scheme in Fig. 7.1, the induced velocities during a full revolution are transmitted from HOST to *elsA* in order to account for the effect of the other blades and wakes. However, the loads predicted by *elsA* are not communicated to the HOST Blade Module and hence the loop is not closed.

7.3 Assessment of MESIR and MINT Coupling Strategies for Single Propellers

This section presents a first assessment of the two coupling strategies between *elsA* and HOST codes presented before. To do this assessment, the APIAN single propeller test case in high-speed conditions and at 3° of incidence is considered (see Table 7.1). The full-annulus *elsA* uRANS case presented in Chapter 1 is used as a reference.

As described in the previous sections, both coupling strategies presented in this study perform their uRANS computations on a near-wall mesh around the blade. Figure 7.3 shows a detailed view of the RANS mesh used in coupled computations (in red). Moreover, the full-annulus RANS mesh used in previous *elsA* simulations is plotted in black. Note that the figure does not plot a slice of the mesh, but it follows one mesh surface. Therefore, due to the form of the channel, some gaps appear as it can be observed in Fig. 7.3(b).
Comparing both meshes, it can be noticed that the near-wall mesh is an extraction of a part of the full-annulus mesh. This near-wall mesh has 1.53 million points, distributed automatically by the Autogrid mesher in order to capture the viscous effect in the boundary layer close to the blade wall, as well as the downward propagation of the wake.

A number of uRANS simulations on this near-wall mesh have been performed and compared to the reference simulation. All the walls (blades and hub) are modeled with an adiabatic condition of adherent wall, whereas the outer boundaries are modeled by a non-reflective condition. This outer condition is modified in the coupled simulations to account for the effect of the other blades and wakes. Infinite velocity and rotational speed are attributed to all the blocks of the mesh. A second-order centered scheme with Jameson's artificial viscosity is used for the spatial discretization. The time integration algorithm uses a backward Euler scheme



(a) Side view. J-slices of the mesh.

(b) Front view. I-slices of the mesh.

Figure 7.3: APIAN mesh slices for uRANS simulations in *elsA*. The near-wall mesh (in red) uses the same discretization than in the full-annulus mesh (in black).

with Gear sub-iterations. The turbulence model is Kok's k-ω with SST correction. Simulations are performed with a time step equivalent to 1° of propeller rotation.

In each *elsA* simulation, the outer boundary conditions have been treated differently to account for the effect of other blades and wakes:

- No induced velocities $\vec{v}_{\text{ind}}$ in the outer BC's.
- HOST/MESIR $\vec{v}_{\text{ind}}$: induced velocities computed by HOST/MESIR routines.
- HOST-MINT $\vec{v}_{\text{ind}}$: induced velocities computed by HOST-MINT routines.
- HOST-MINT $\vec{v}_{\text{ind}}$ without vortex reg.: the regularization around the vortex filaments has been removed.
- HOST-MINT $\vec{v}_{\text{ind}}$ new panel reg.: together with the suppression of the regularization in vortex filaments, the panel regularization has been modified.
- HOST-MINT $\vec{v}_{\text{ind}}$ with analytical vortex: as in MESIR wake model, velocities induced by vortex filaments are computed analytically.

The polar plot in Fig. 7.4 shows the blade load evolution along the different near-wall simulations.
The CFD simulations on the near-wall mesh have been first performed considering a non-reflection condition on the outer BC's. Due to the small mesh dimensions, the global blade loads were converged after the first complete revolution. The third revolution was used to extract the blade loads without considering MINT $\vec{v}_{\text{ind}}$.
Then, starting from the previous converged simulation, the different MINT $\vec{v}_{\text{ind}}$ were added to the outer BC's. Three revolutions were needed to converge blade loads and the fourth revolution was used to extract the blade loads.

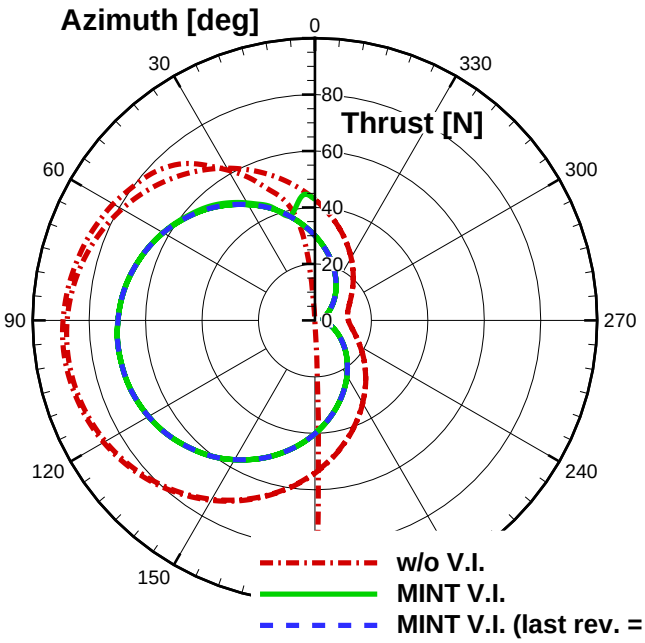


Figure 7.4: Thrust convergence for near-wall case with $\vec{v}_{\text{ind}}$ from HOST-MINT.

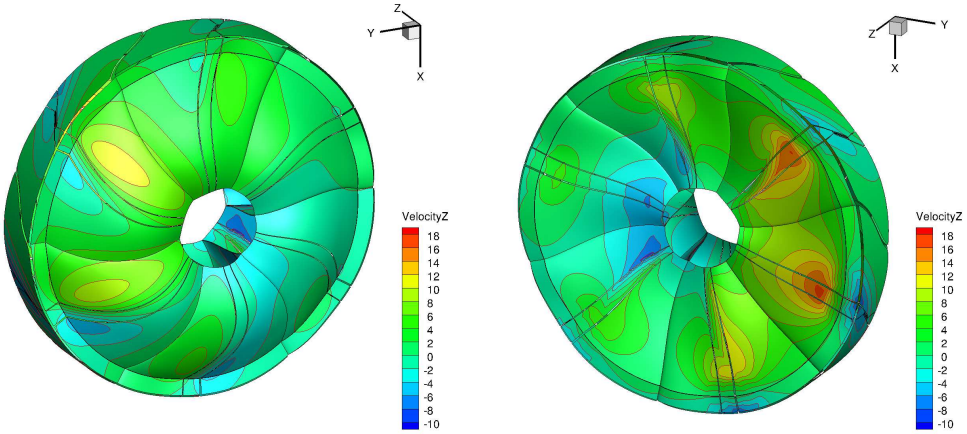
7.3.1 Induced velocity fields

In order to assess the next coupling methodology, the induced velocities $\vec{v}_{\text{ind}}$ from MINT wake model are compared here to the velocities induced by MESIR. Figure 7.5 shows the comparison between the axial $\vec{v}_{\text{ind}}$ component obtained from both wake models for six different azimuthal positions of the computed blade. Left-hand side figures plot a view of the front part of the BC mesh, whereas right-hand side figures show its back part. The third row of figures show the differences between both approaches in m/s. A number of differences can be observed in both sides.

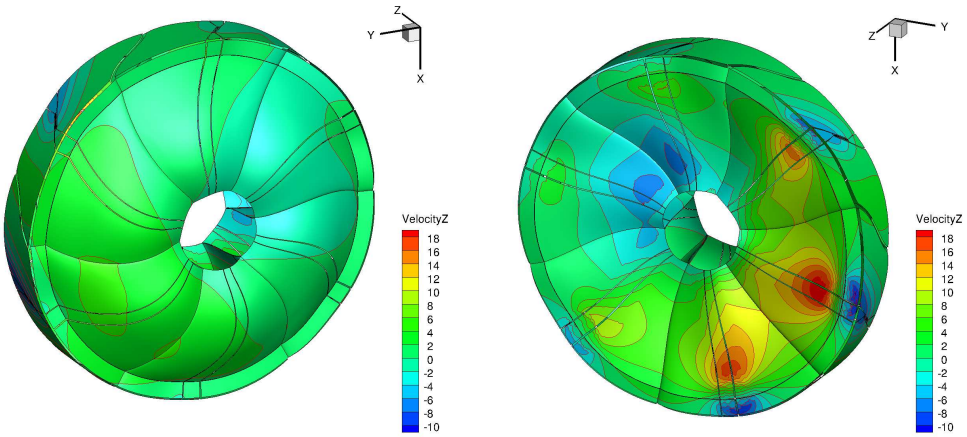
In the front view, MINT predicts a much more smoothed $\vec{v}_{\text{ind}}$ field than MESIR. Notice in particular that, near the bound vortex in the quarter-chord line of the blade, important axial induced velocities are obtained with MESIR, and not with MINT. These differences seem to come from the different treatment of the vortex filaments: different regularization radius and different integration methods, i.e. analytical in MESIR and numerical in MINT.

In the rear view, the general pattern is the same between MESIR and MINT. The passage of the wakes across the mesh can be noted by important axial induced velocities, mainly near the blade tips. The intensity of these tip vortices and the wake varies depending on the azimuthal position, and hence also the induced velocities. Notice in particular the negative sign of the axial $\vec{v}_{\text{ind}}$ in the upward moving blade, where the blade circulation diminishes and hence negative vorticity is shed in the wake.

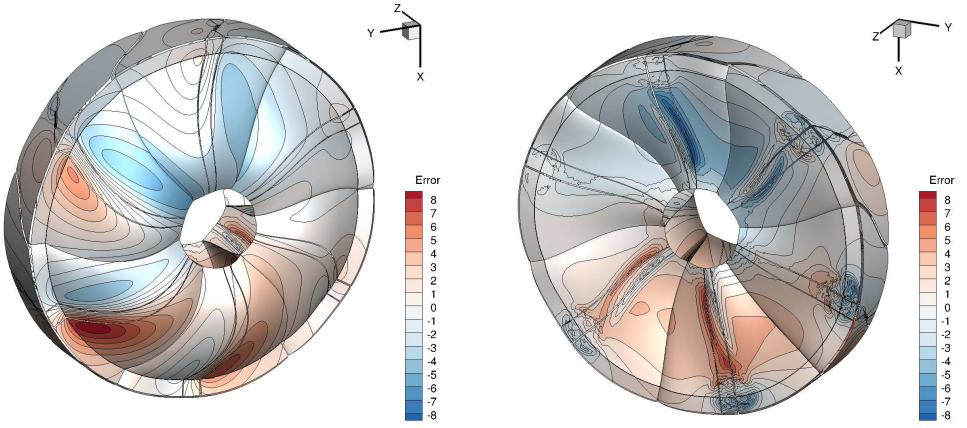
Nevertheless, a number of differences can be noticed between both predictions. First, the intensity of the tip vortices is overestimated in MINT for the downward moving



(a) MESIR wake



(b) Original MINT wake



(c) Error in $\vec{v}_{\text{ind}}$ wrt MESIR

Figure 7.5: Axial $\vec{v}_{\text{ind}}$ from MESIR and MINT wake models.

blade. Second, oscillations in the induced velocities can be observed in iso-lines predicted by MINT, mainly close to tip vortices, which are not found in MESIR. Finally, MINT panel regularization leads to a smoother effect on the $\vec{v}_{\text{ind}}$ compared to the regularized lattice of vortices in MESIR.

In order to assess the origin of these differences with respect to MESIR, a number of tests and modifications have been done in MINT $\vec{v}_{\text{ind}}$ extraction routines:

- *Regularization of vortex filaments*: compare with and without vortex regularization
- *Regularization of vortex panels*: compare two types of panel regularization
- *Integration of vortex filaments*: compare numerical and analytical integration of the vortex $\vec{v}_{\text{ind}}$.

Their induced velocity fields are presented and compared hereafter.

Regularization of vortex filaments. The velocities induced by vortex filaments are calculated in MINT by the two-point Gaussian quadrature rule. When the calculation point gets close to the Gauss points, induced velocities become singular. Therefore, a regularization method is needed to avoid too important unphysical induced velocities. In MINT, a linear regularization is applied when distances become too small, as shown in the scheme in Fig. 7.6. This regularization method models in a rough way the viscous core of a cylindrical vortex with constant radius. Notice that, as the regularization radius is an arbitrary value, an incorrect choice may lead to two possible extremes: on one side, if the radius is too small, induced velocities may be too important for calculation points close to the vortex thus avoiding the MINT simulation to converge; on the other side, if the radius is too important, all the induced velocities from the vortex surrounding the calculation point might be almost erased. Therefore, an equilibrium must be found in the choice of this regularization distance.

First comparisons of the velocities induced by MESIR and MINT wake models showed an important underestimation of the effect of the vortex in MINT. Therefore, the vortex filament regularization was removed in order to see the contribution of vortices without any regularization. Figure 7.7 shows the comparison between the velocities induced by MESIR and MINT on the outer mesh of the APIAN blade.

Notice that, removing the regularization reduces significantly the mismatches between MESIR and MINT predictions on the front part of the surface mesh. The $\vec{v}_{\text{ind}}$ on the rear part of the mesh are almost unchanged. Next comparisons will use non-regularized vortices in MINT for the computation of $\vec{v}_{\text{ind}}$.

These results put forward the importance in the choice of a regularization distance for the computation of induced velocities. The effect of this parameter should be further investigated in HOST-MINT simulations in order to establish some best practices in the case of propellers and open rotors.

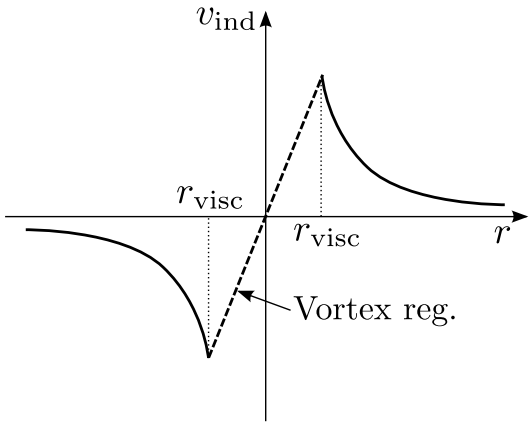


Figure 7.6: Scheme of the regularization of velocities induced by vortex filaments in MINT.

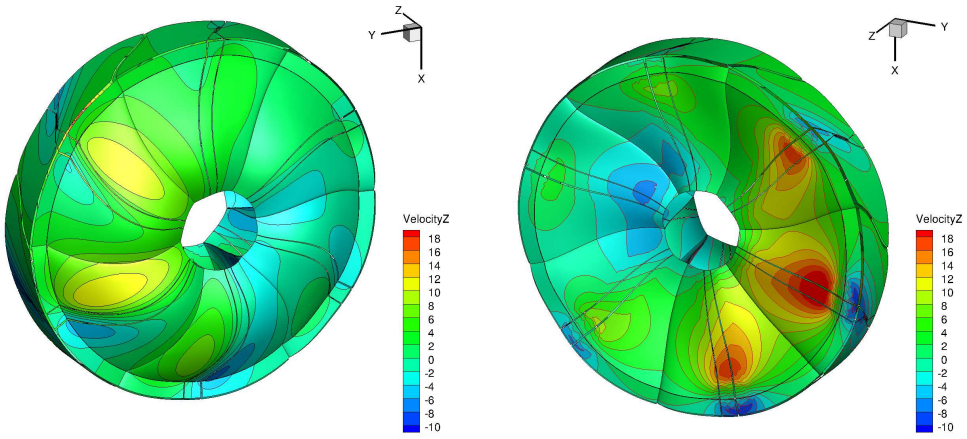
Regularization of vortex panels. The velocities induced by MINT wake panels are calculated using the four-point Gaussian quadrature rule applied to Biot-Savart's law. Similar to vortex filaments, this numerical integration of panels containing a certain vorticity is also singular when the calculation point gets closer to one of the Gauss points. Therefore, a regularization strategy is needed to avoid too important induced velocities.

Current MINT version determines a regularization distance depending on the size of the considered panel and an arbitrary input value. This time, however, when the calculation point is inside the regularization distance of a Gauss point, a zero contribution is considered. This regularization has shown to produce oscillations when the calculation points get close to the wake panels (see Fig. 7.5). In order to remove these oscillations, another regularization strategy has been implemented. Figure 7.8 shows both, the original and the new panel regularization for the extraction of $\vec{v}_{\text{ind}}$. Instead of considering a zero contribution inside of the regularization radius, constant $\vec{v}_{\text{ind}}$ are considered in this inner region. Notice that the step in $\vec{v}_{\text{ind}}$ is no longer placed at the regularization radius (dashed red line), but at the panel plane (dashed blue line), which corresponds better to the effect of a potential wake.

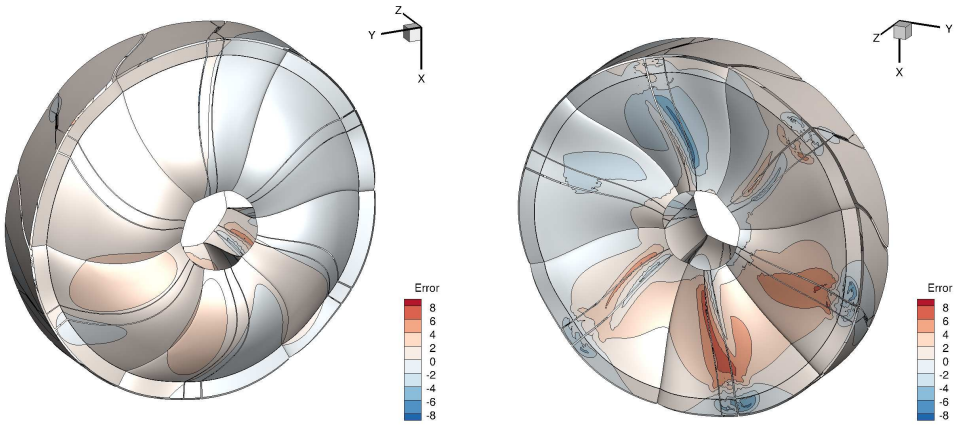
Figure 7.9 shows the comparison between the velocities induced by MESIR and MINT with the original and the new panel regularization.

The front part of the mesh presents a $\vec{v}_{\text{ind}}$ prediction that is very similar to the ones with the original panel regularization. On the contrary, the effect of the new regularization can be mainly noticed when the wake crosses the surface mesh. In those cases, when the grid points are very close to the Gauss points in the wake panels, the regularization strategy acts and removes the effect of some of the Gauss points. This leads to unphysical oscillations of the $\vec{v}_{\text{ind}}$ on points near the potential wake panels.

The new regularization approach smooths these oscillations, as no discontinuity in the $\vec{v}_{\text{ind}}$ is imposed at the regularization radius r_{visc}. However, differences in tip



(a) Axial $\vec{v}_{\text{ind}}$ in MINT w/o regularization



(b) Error in $\vec{v}_{\text{ind}}$ wrt MESIR

Figure 7.7: Potential induced velocities on the outer BC's of a near-wall APIAN mesh.

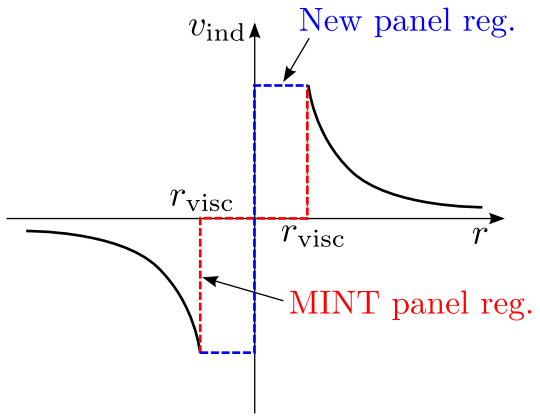
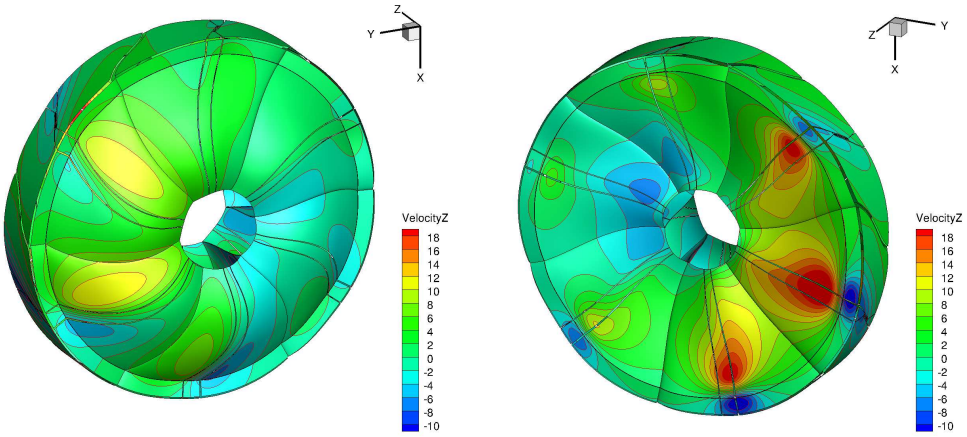
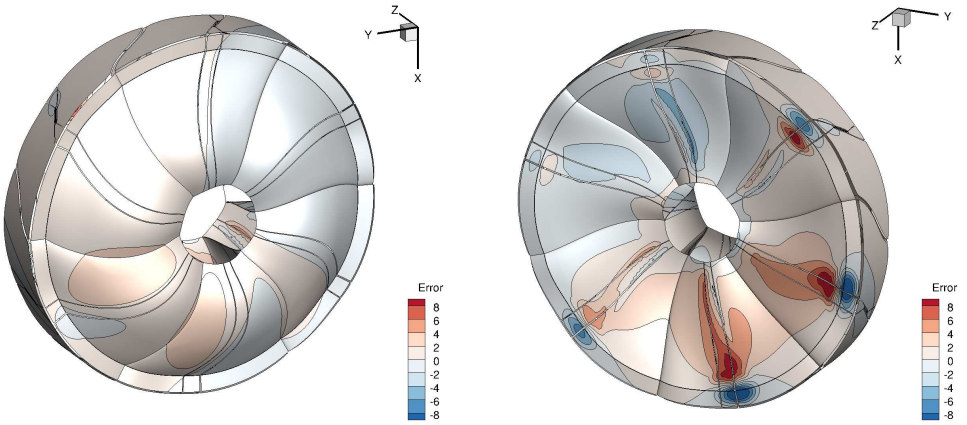


Figure 7.8: Scheme of the current and modified $\vec{v}_{\text{ind}}$ regularization by vorticity panels in MINT.



(a) Axial $\vec{v}_{\mathrm{ind}}$ in MINT w/ new panel regularization



(b) Error in $\vec{v}_{\mathrm{ind}}$ wrt MESIR

Figure 7.9: Potential induced velocities on the outer BC's of a near-wall APIAN mesh.

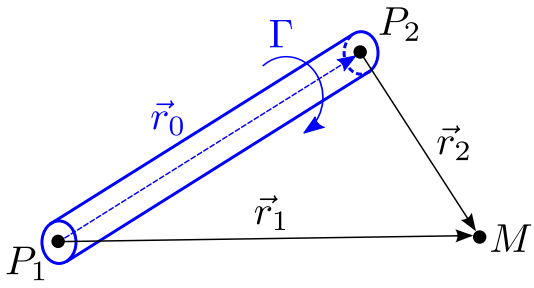


Figure 7.10: The velocity induced on a point by a finite straight vortex filament of constant circulation Γ.

vortex and wake smoothness still exist. Again, the effect of panel regularization distance should be assessed in order to fix some best practices for propeller and open rotor cases.

Analytical vs. numerical vortex filaments integration. MESIR models the wake as a lattice of vortex filaments with constant circulation. To predict the effect of these vortices on the outer BC mesh, it computes analytically the integrals given by Biot-Savart's law.
On the contrary, MINT wake considers a wake where vortex panels have a constant vorticity density $\vec{\gamma}$ and where vortex filaments have a linear variation of the circulation Γ. In MINT, instead of using an analytical solution of the integrals, the two-point Gaussian quadrature rule is used for the integration of vortex filaments, and four-point Gaussian quadrature rule for the integration of vortex panels.

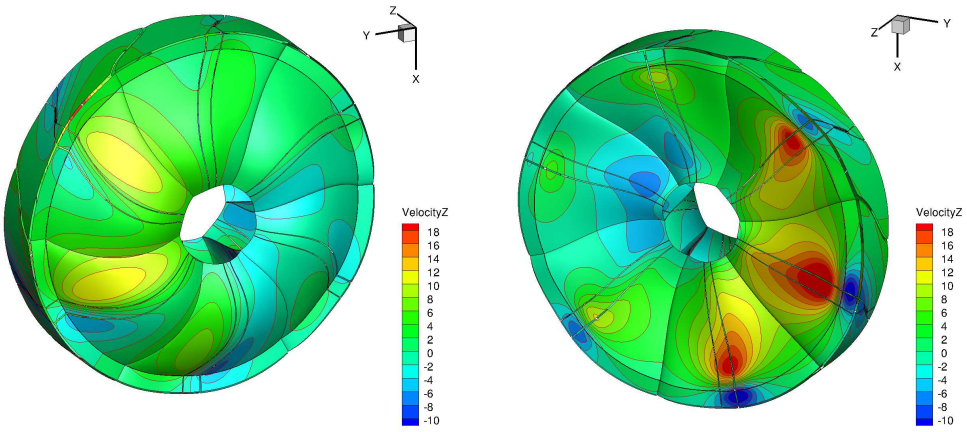
In order to assess the accuracy of this discrete integration, an analytical integration of the vortex filaments has been implemented in MINT, but considering a constant circulation for a matter of simplification. As circulation varies linearly in this wake model, the mean value of the circulation in the straight vortex filament is taken for the computation of the induced velocities. The analytical expression to calculate the induced velocities of a vortex filament with constant circulation follows (see Fig. 7.10):

$$\vec{v}_{\text{ind}} = \frac{\Gamma}{4\pi} \frac{\vec{r}_1 \wedge \vec{r}_2}{|\vec{r}_1 \wedge \vec{r}_2|^2} \vec{r}_0 . \left(\frac{\vec{r}_1}{|\vec{r}_1|} - \frac{\vec{r}_2}{|\vec{r}_2|} \right) \tag{7.1}$$

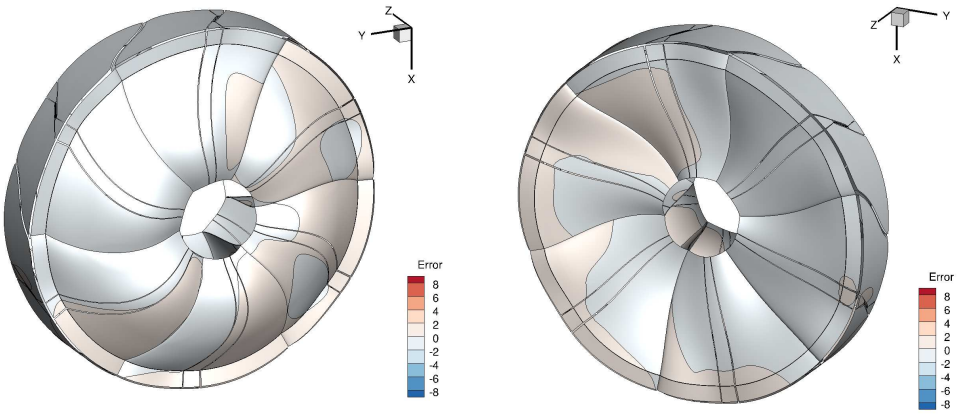
Figure 7.11 shows the comparison between numerical and analytical integration of the vortex filaments, with respect to MESIR $\vec{v}_{\text{ind}}$. Very small differences between both integration techniques confirms that the numerical integration is sufficient for the prediction of $\vec{v}_{\text{ind}}$ even for calculation points that are relatively close to the bound vortex, as it is the case for the front part of the BC mesh. Therefore, the two-point Gaussian quadrature rule is retained for the bound vortex.

7.3.2 Induced Velocities Interpolation Time Step

Another step in the validation of the method has been the study of the blade load sensitivity to the $\vec{v}_{\text{ind}}$ interpolation time step.



(a) Axial $\vec{v}_{\text{ind}}$ in MINT w/ analytical vortex integration



(b) Differences in $\vec{v}_{\text{ind}}$ wrt MINT w/ numerical integration

Figure 7.11: Potential induced velocities on the outer BC's of a near-wall APIAN mesh.

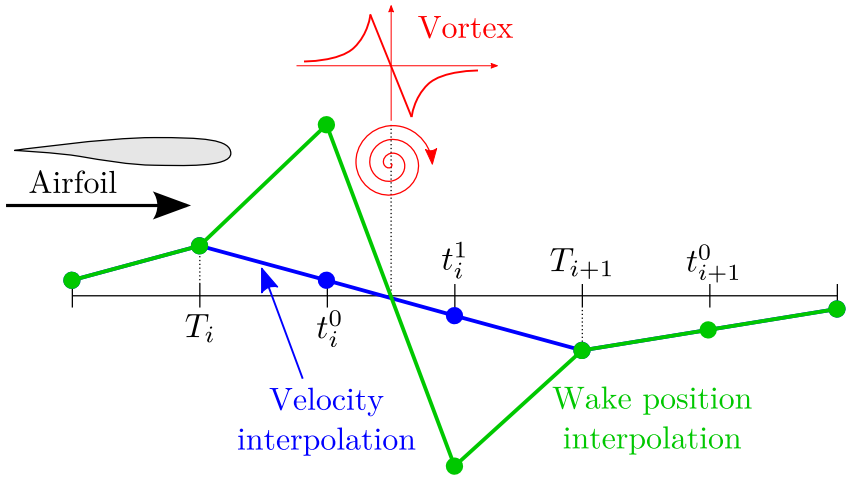


Figure 7.12: Two interpolation strategies to capture a vortex passage. $T_\star$ correspond to the physical time steps, whereas $t_\star$ correspond to the interpolation time steps.

The velocities induced by the MINT wake on the outer BC's mesh can be extracted with a time step that can be different from the one in HOST-MINT simulations. When this occurs, an interpolation is needed. As HOST-MINT uses a Lagrangian description of the airflow, instead of interpolating the induced velocities between two HOST-MINT steps, the interpolation is done on the position and the vorticity of the wake panels.

The scheme in Fig. 7.12 represents the case of a vortex interaction, where T_i and T_{i+1} are two consecutive time steps in a HOST-MINT simulation, and t_i^0, t_i^1, and t_{i+1}^0 are the intermediate time steps where the induced velocities are extracted. The scheme considers a fixed vortex and an airfoil advancing from the left to the right, and hence interacting with the vortex. Two curves represent the evolution of the induced velocities depending on the interpolation strategy. The figure shows how the interpolation based on the wake position allows a better capture of the problem unsteadiness than the direct interpolation of the induced velocities.

Moreover, since the *elsA* simulations can be performed at a different time step, usually smaller than the HOST-MINT time steps, an interpolation is needed to provide a field of $\vec{v}_{\text{ind}}$ at each time step to the outer BC's.

In the considered case, three different extraction time steps have been considered in HOST-MINT: 5°/it, 2°/it, and 1°/it. Meanwhile, all HOST-MINT simulations have been performed at 5°/it and all *elsA* simulations at 1°/it. Figure 7.13 shows the CFD blade load comparison between these three cases. Note that no significant differences are observed between these three interpolation time steps. In this particular case of a single propeller in incidence, as it is noticed in the figure, the dominant mode in the blade loads is the incidence, a 1/rev mode. Therefore, even a 5°/it interpolation is sufficient to capture correctly this phenomenon in CFD simulations in the near-wall mesh.

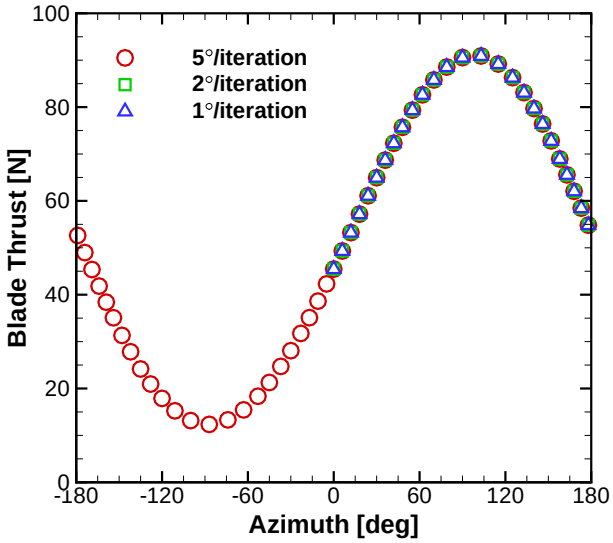


Figure 7.13: The MINT interpolation time step effect on CFD blade loads. Comparison between 5°/it, 2°/it, and 1°/it interpolations.

Table 7.2: Wind tunnel test conditions for APIAN minimum-body configuration. Wind tunnel case No.1149

Mach No.	[–]	0.7
Incidence	[°]	3.
Rotational Speed	[min^{-1}]	8639.
Advance Ratio, J	[–]	3.278

7.4 Coupling Strategy Assessment on APIAN Single Propeller Case

This section presents the code-to-code assessment of the one-way coupling strategy that has been implemented in HOST-MINT and *elsA*. A comparison between a full-annulus *elsA* simulation and a near-wall coupled simulation is detailed hereafter.

7.4.1 Test Case Description.

A representative case of APIAN single propeller has been chosen for the assessment of the new coupling strategy between HOST and *elsA*. High-speed flight conditions and 3° of incidence are considered here. The airflow conditions are summed up in Table 7.2, which corresponds to the same experimental point than in Chapter 1.

In this chapter, a near-wall mesh simulation with HOST-MINT $\vec{v}_{\text{ind}}$ without vortex regularization and with the new panel regularization is considered. This simulation is compared when possible to experimental data from wind-tunnel tests, to a CFD full-annulus *elsA* simulation, and to a HOST-MINT simulation with instal-

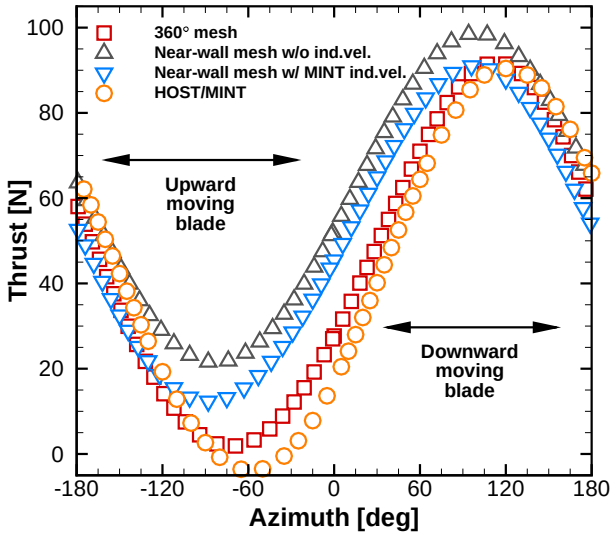


Figure 7.14: Blade thrust along a revolution. Comparison between *elsA* 360° mesh, near-wall mesh w/o $\vec{v}_{\text{ind}}$, HOST-MINT simulation, and near-wall mesh w/ $\vec{v}_{\text{ind}}$ from HOST-MINT.

lation effects and the unsteady model corrections (already presented in Chapter 5).

7.4.2 Blade Loading

Figure 7.14 shows the thrust generated by the reference blade along a complete revolution. A number of simulations are here compared: a full-annulus CFD simulation, a near-wall mesh with non-reflection conditions at the outer BC's, a HOST-MINT simulation with installation effects and unsteady corrections, and, finally, a near-wall mesh with MINT induced velocities (new coupling strategy).

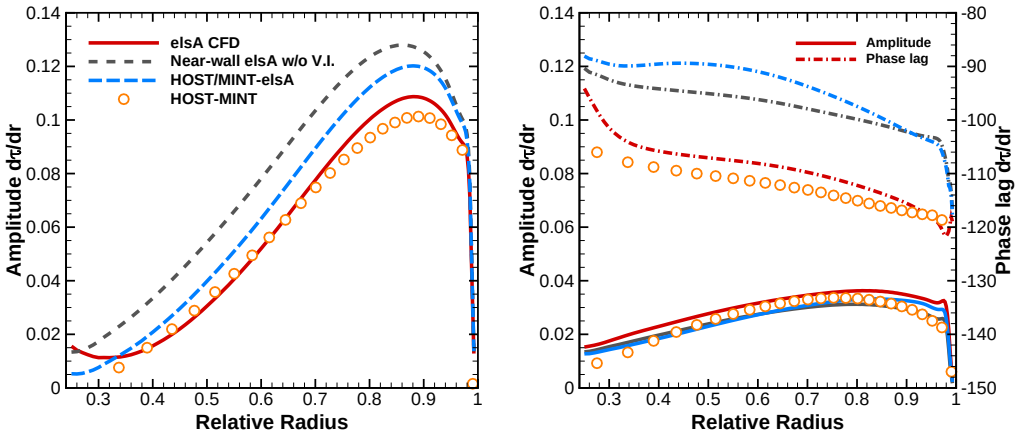
Notice that, while loads predicted by the HOST-MINT simulation are close to full-annulus *elsA* predictions, both near-wall simulations overestimate loads along the major part of the revolution. When comparing both near-wall simulations, it is observed that MINT induced velocities at the outer BC's diminish the mean blade loads and reduce slightly the load phase lag. Finally, the main differences are noticed in the load phase lag: both near-wall simulations present an important underestimation of the blade load phase lag. As it will be shown hereafter, this will induce an important underestimation of the 1P load phase lag.

7.4.3 Propeller Performance

Table 7.3 shows the comparison between the same simulations presented in the previous subsection: the full-annulus CFD simulation, the HOST-MINT simulation, and the coupled HOST-MINT and *elsA* simulation. Moreover, the available wind tunnel data has been added as a reference.

	WTT	elsA 360°	HOST-MINT	Coupled MINT-elsA
Blade pitch [°]	57.0	+0.7°	+0.7°	+0.7°
Thrust [N]	253.34	+5.147%	−0.604%	+19.42%
1P Norm [N]	307.31	−15.60%	−20.56%	−30.36%
1P Phase [°]	25.47°	−2.85°	+1.9°	−19.24°

Table 7.3: APIAN propeller performance and 1P loads comparison



(a) Mean load

(b) Mode 1 (1/rev)

Figure 7.15: Spanwise distribution of the blade thrust. Comparison between full-annulus CFD simulation, HOST-MINT simulation, near-wall mesh w/o $\vec{v}_{\text{ind}}$, and near-wall mesh w/ MINT $\vec{v}_{\text{ind}}$.

As explained before, only a one-way coupling has been implemented between HOST-MINT and near-wall *elsA* simulations. Therefore, even if the HOST-MINT simulation is performed at the blade pitch to reach experimental thrust levels, the loads predicted by the near-wall *elsA* simulation may not be the same as in experimental data.

Indeed, in the present case, a $\sim 20\%$ overestimation of the thrust is obtained for the coupled simulation. Moreover, the 1P load norm is underpredicted by $\sim 30\%$ and the 1P phase lag is largely underpredicted ($\sim -19°$).

7.4.4 Blade Load Distribution

In this subsection, the study focuses on the comparison of the thrust spanwise distribution along the blade. Again, all the previous simulations are compared, but no experimental data is available.

Figure 7.15 plots the mean and the 1/rev mode of the blade thrust spanwise distribution. The left-hand side figure shows how the induced velocities in the outer

BC's reduce the mean thrust along all the blade span in the simulation on the near-wall domain. However, the effect of induced velocities seems to be insufficient to reach the CFD predictions on the full-annulus mesh.

Besides, the right-hand side figure shows the 1/rev mode of the blade thrust distribution. The gray dashed curves represent the blade loads obtained in a simulation on a near-wall domain without including any induced velocities to the freestream conditions at the BC. It can be noticed that the mean value is better predicted close to the blade tips in the simulation on the near-wall domain when the MINT induced velocities are added (blue long-dashed curves). On the contrary, induced velocities reduce even more the phase lag in the mid-span area, and therefore they increase the offset with respect to the reference full-annulus simulation.

7.4.5 Pressure on Blade Skin

This subsection compares the pressure coefficient K_{P} on the skin of the reference blade. The pressure coefficient for propellers differs from the fixed-wings:

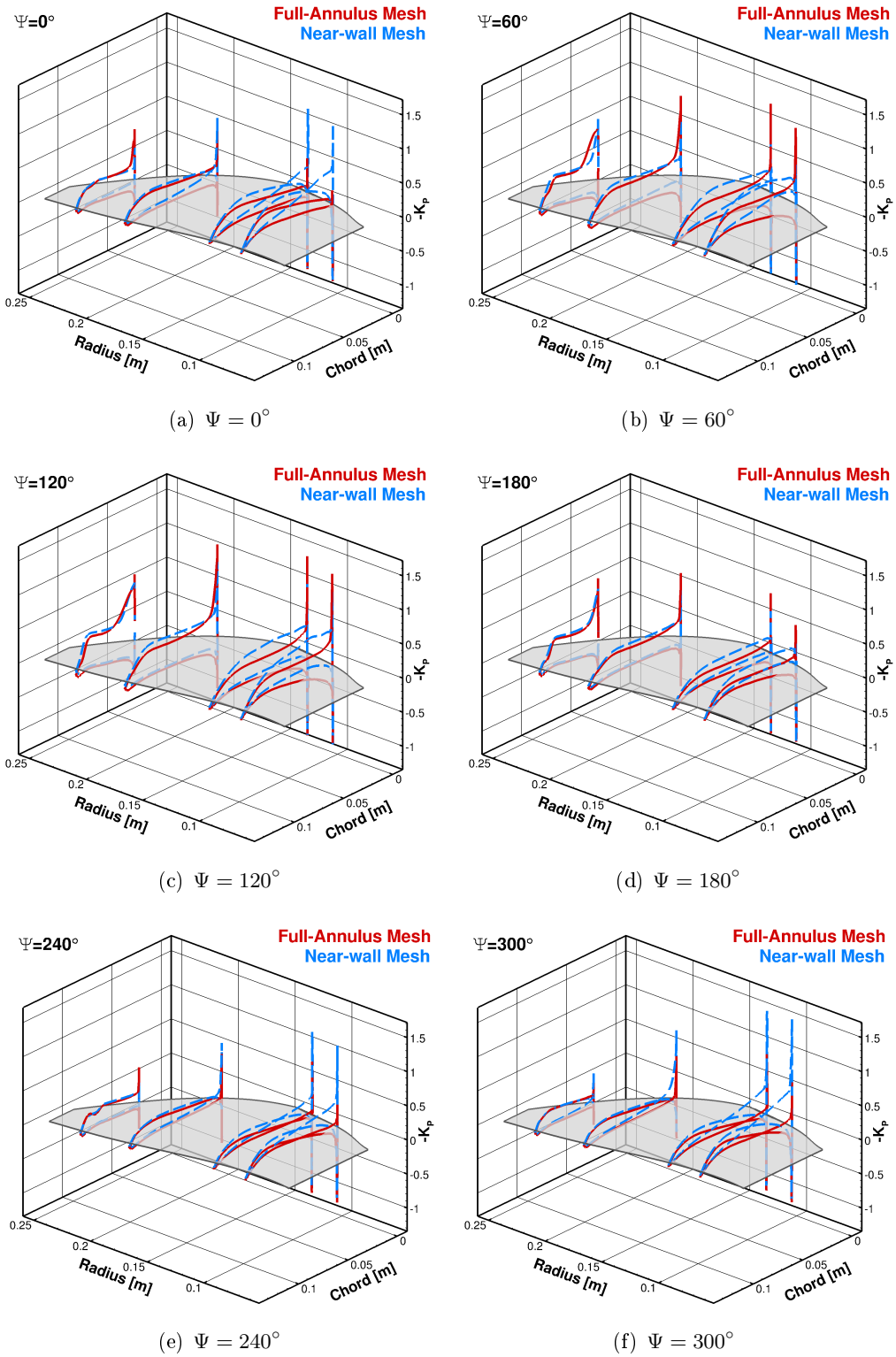
$$K_{\mathrm{P}} = \frac{p - p_\infty}{1/2\rho_\infty(V_\infty^2 + (\Omega r)^2)} \tag{7.2}$$

Figure 7.16 shows the comparison of $-K_{\mathrm{P}}$ between the reference full-annulus simulation (solid red curves) and the near-wall CFD simulation with MINT induced velocities (dashed blue curves). The six subfigures represent six different azimuthal positions of the reference blade: 0°, 60°, 120°, 180°, 240°, and 300°. Each subfigure plots the pressure coefficient at four representative blade sections: close to the blade root ($r/R = 0.4$), at the maximum chord ($r/R = 0.5$), at the theoretical maximum blade load ($r/R = 0.75$), and close to the blade tip ($r/R = 0.9$). Note that the plotted form of the blade corresponds to the untwisted geometry of the APIAN chord line.

First, a fairly good agreement can be observed for the two section closest to the blade tip, i.e. $r/R = 0.75$ and $r/R = 0.9$. Even if some mismatches appear in the peak of expansion on the suction side, the global form of the pressure is capture by the CFD simulation on a near wall mesh.

On the contrary, important differences are noticeable in the two sections closest to the blade root. The main difference comes from an underestimation of the pressure for both the suction and the pressure sides (see for example Fig. 7.16(c)).

These offsets close to the blade root may be explained by two facts. On one side, the near-wall mesh is narrower close to the blade root than close to the blade tip. Therefore, non-reflective boundary conditions may not be adapted for such small distances. On the other side, as HOST-MINT simulations do not consider the effect of the nacelle, an important vortex is shed at the blade root. This root vortex may modify the pressure distribution for the sections that are close to the blade root.



(a) $\Psi = 0^\circ$

(b) $\Psi = 60^\circ$

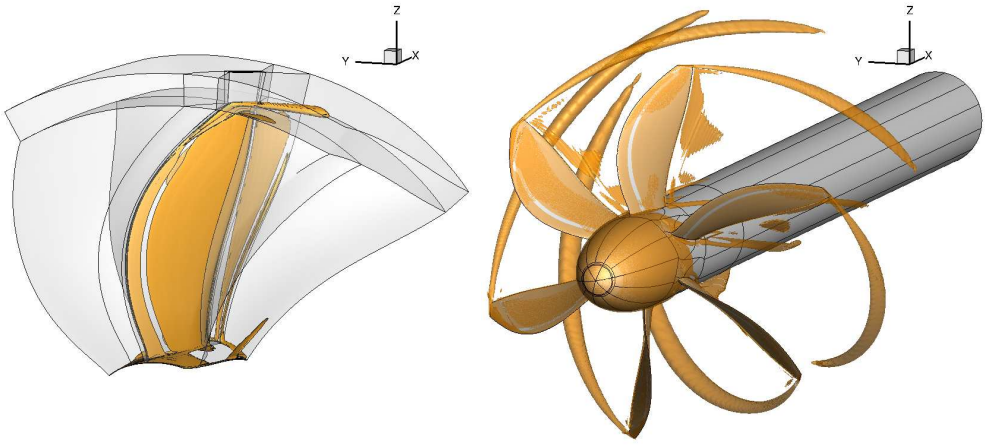
(c) $\Psi = 120^\circ$

(d) $\Psi = 180^\circ$

(e) $\Psi = 240^\circ$

(f) $\Psi = 300^\circ$

Figure 7.16: Pressure coefficient on the blade skin. Comparison between CFD results on full-annulus mesh and on near-wall mesh.



(a) Near-wall computation (b) 360° computation

Figure 7.17: Iso-surface 10^6 of Q-criterion on uRANS computations in *elsA*. Comparison between full-annulus mesh and near-wall mesh w/ MINT $\vec{v}_{\text{ind}}$ at azimuth $\Psi = 0°$.

7.4.6 Flow Analysis

In order to better understand the mismatches observed between full-annulus and near-wall simulations, a detailed flow analysis is here presented.

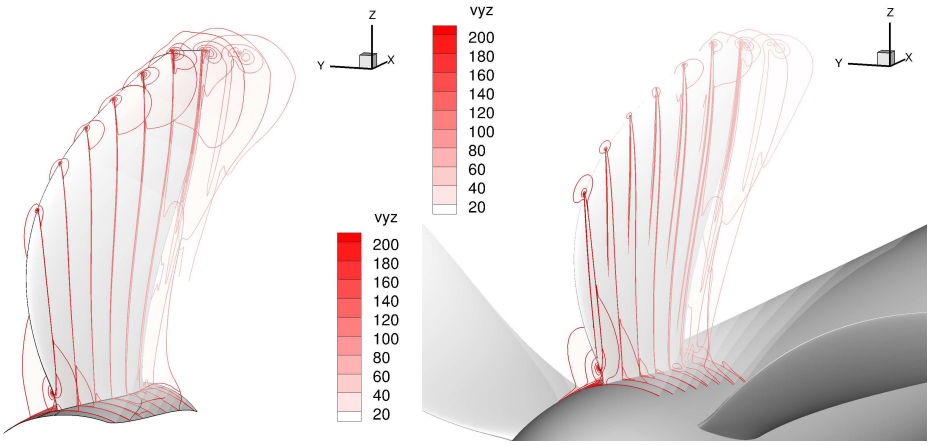
Vortex detection with the Q-criterion. The Q-criterion is a way to detect vortices in a flow and it is defined as follows:

$$Q = \frac{1}{2}\left(|\overline{\overline{\Omega}}|^2 - |\overline{\overline{S}}|^2\right) \tag{7.3}$$

where $\overline{\overline{S}} = \frac{1}{2}\left(\nabla\vec{v} + (\nabla\vec{v})^T\right)$ is the rate-of-strain tensor, and $\overline{\overline{\Omega}} = \frac{1}{2}\left(\nabla\vec{v} - (\nabla\vec{v})^T\right)$ is the vorticity tensor.

Figure 7.17 shows the iso-surface 10^6 of Q-criterion for two CFD simulations, one considering a full-annulus mesh and the other considering a near-wall mesh around the reference blade. From the comparison of these two plots, no significant difference can be observed in the development of the blade tip vortex, at least for this azimuthal position.
Therefore, a further analysis of the local velocities in the field should be done to detect the differences in blade incidence at a given time step.

Velocities in mesh slices. A number of slices have been extracted from the results obtained with the full-annulus and the near-wall mesh. Figure 7.18 shows the norm of the velocities in the plane Y-Z at azimuth angle $\Psi = 0°$ obtained with both simulations. It can be noticed that the intensities of the blade root vortex and the leading-edge vortex are more important in the near-wall computation than in the



(a) Near-wall computation (b) 360° computation

Figure 7.18: Norm of the in-plane velocity for two uRANS computations in *elsA*. Comparison between full-annulus mesh and near-wall mesh w/ MINT $\vec{v}_{\text{ind}}$ at azimuth $\Psi = 0°$.

full-annulus one. If this result is compared with the pressure coefficients obtained in Fig. 7.16(a), it can be noticed that, in the near-wall simulation, an inversion of the curves exists close to the blade root. This implies a negative contribution to the blade loads, and hence a different intensity and form of the root vortex.

7.5 Induced Velocity Fields

In order to prepare open rotor coupled simulations, the velocities induced by elsA and HOST are compared in representative positions of the flow field. Two planes, one upstream and one downstream the propeller are considered here. In *elsA* simulations, the planes are a X-slice in the mesh.

In classical CFD computations there is no direct access to the velocities induced by the propeller blades. To estimate them, it must be assumed that the velocity field is the superposition of the velocity field around a blade-off nacelle and the field around the propeller blades without nacelle. This hypothesis might be correct at first order, but neglects the interaction between the hub and the blade, and its effect on the airflow. Figure 7.19 shows the considered geometry and the two planes of interest in red.

On the contrary, in HOST, the velocities induced by the propeller are directly obtained. Indeed, singularity methods assume that the velocity field is the superposition of the elementary fields generated by each singularity. Thus, the velocities induced by the propeller blades and their wakes on the considered X-planes can be calculated at each time step by Biot-Savart's law.

The main goal of this comparison is to estimate the induced angle of attack that a propeller rotating in the opposite sense may see if it was located upstream

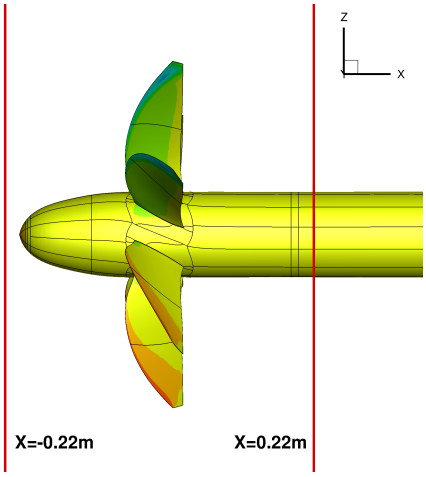


Figure 7.19: Side view of APIAN propeller and two considered X-planes (in red)

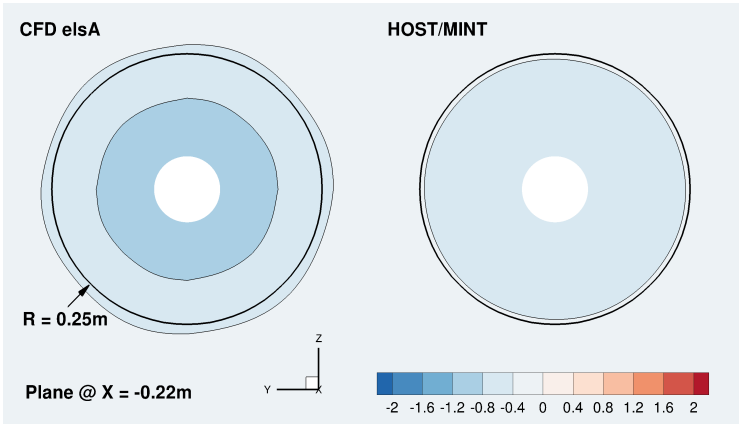


Figure 7.20: Induced angle of attack on the upstream X-plane. Comparison between *elsA* and HOST.

or downstream the APIAN propeller. The ratio between the rotor-to-rotor distance and the maximum blade chord has been chosen from a generic contra-rotating open rotor geometry, AI-PX7: $(d/c)_{\text{APIAN}} = (d/c)_{\text{AIPX7}}$, $d_{\text{APIAN}} = 0.22\text{m}$.

Figures 7.20 and 7.21 show the induced angle of attack predicted by HOST and *elsA* at an X-plane upstream the propeller and downstream the propeller, respectively. It considers the angle difference $\Delta\beta$ in the relative velocity when adding the induced velocities (see Fig. 7.22). The point of view is in front of the X-planes and the propeller turns counterclockwise.

A noticeable underestimation of the induced angle of attack on the upstream plane can be noticed in HOST simulations. This induced angle of attack is directly linked to the induced velocities. Remember that a similar phenomenon had been already observed in the front rotor of AI-PX7 open rotor case. In both cases, the underestimation of the induced velocities can be attributed to the lifting-line

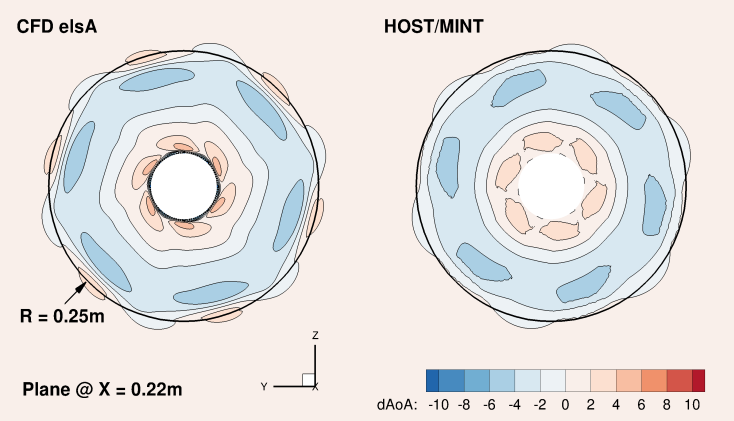


Figure 7.21: Induced angle of attack on the downstream X-plane. Comparison between *elsA* and HOST.

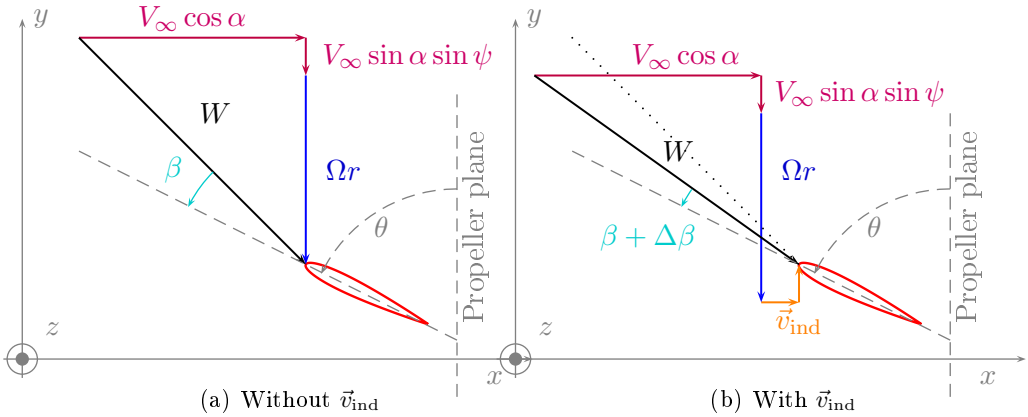


Figure 7.22: Velocity triangles considering or not the induced velocities

hypothesis reducing all the blade to its quarter-chord line.

On the contrary, a good prediction of the induced angle of attack is obtained for the downstream plane. In this case, the chord effects are less important than the effect of the wake going through the X-plane. Notice however, that the main differences are mainly observed near the root and the tip of the blade: *elsA* predicts more important root and tip wake effects on the induced angle of attack. Nevertheless, these comparisons show that the general patterns are very close, and therefore, *elsA* and HOST simulations are expected to present similar aerodynamic angles of attack.

7.6 Concluding Remarks

The current coupling strategy between the HOST-MESIR comprehensive code and the *elsA* CFD code has been analyzed and its main advantages and drawbacks have been put forward. In order to overcome with some of the main shortcomings of this method, a new coupling strategy using the MINT free-wake model has been partially implemented and assessed first with respect to MESIR coupling strategy.

A number of modifications in the extraction of the induced velocities have been performed in order to obtain results in MINT that are closer to MESIR predictions. The modifications have focused on the vortex and panel regularization techniques used in HOST-MINT simulations, which have shown to be unadapted for coupled simulations.

The second part of the validation process has been a comparison between full-annulus *elsA* simulation and a coupled HOST-MINT and *elsA* simulation. Significant differences have been observed mainly on the prediction of the 1P load phase lag, which is largely underestimated in the coupled simulation.

Finally, a comparison between the induced flows in the full-annulus and in the near-wall simulations has been performed in order to prepare future contra-rotating open rotor coupled simulations. Two X-slices, one upstream and one downstream the blade, in order to assess the angle of attack induced by the propeller. These slices have been placed at distances that are representatives of the case of an open rotor. Therefore, the induced angles of attack are likely to represent the interaction between both rotors in a real open rotor case.
For this case, encouraging results have been obtained as both, full-annulus and reduced-domain simulations, yield to very similar induced angles of attack for both the upstream and the downstream X-slices.

Conclusion

Due to the increase in fuel prices, airframe and engine manufacturers are looking for step-changing technologies that might enable them to produce more efficient and cleaner aircraft by 2020 and later. Among a number of emerging concepts, the contra-rotating open rotor engine is likely to be an interesting option for the significant reduction of the aircraft fuel consumption and polluting emissions. Nevertheless, a number of key aspects are not still sufficiently mastered from the early development steps of the engine. Therefore, manufacturers are investing in the development of methodologies adapted for preliminary design phases in order to assess some of these key parameters.

In the present thesis, the objective was to provide moderate-cost methodologies for the aerodynamic simulation of contra-rotating open rotors. The key parameters to be assessed in the preliminary aerodynamic design of an open rotor are, on one side, the prediction of the engine performance and, on the other side, the in-plane loads generated by the engine installation or by the aircraft incidence. Moreover, during the first design steps, rapid and flexible simulation tools should be provided to designers enabling them to explore a large scope of engine configurations and test cases in a reasonable computational time.

Following these criteria, a study of the different available simulation methods has been conducted. The main assets and drawbacks of each method have been put forward and the choice of a method based on the unsteady lifting-line theory has been justified. The HOST comprehensive code for aero-mechanical simulation of rotorcraft has been chosen and adapted for the simulation of single and contra-rotating propellers. The subsequent chapters have been devoted, first, to assess the HOST code for the aerodynamic simulation of propellers and CROR in incidence; second, to improve the blade-element model to account for unsteady aerodynamics; third, to provide a better insight into the mechanisms governing the in-plane loads; and fourth, to explore HOST-elsA coupling strategies for propellers.

Chapter 1 has provided a first assessment of the HOST code for single propeller test cases in minimum-body configuration and in high-speed conditions. A number of best practices for future simulations have been established and justified.
Then, wind tunnel data and more advanced CFD simulations have been used to assess the accuracy of HOST simulations in the prediction of propeller performance and in-plane loads. In addition, the blade load distributions have also been compared. Moreover, two models to account for the effects of the spinner have also been tested and compared to experimental data and CFD simulations.
Despite the uncertainties in experimental data, satisfactory results have been obtained in HOST simulations when the effects of spinner were taken into account. HOST has shown to capture correctly the incidence effect (α-effect) and the rotational speed effect (J-effect). Nevertheless, some offsets were still noticed in the prediction of propeller in-plane loads. A deeper insight into the origin of these in-

plane loads has been necessary as these loads are critical for the dimensioning of the engine installation, for the aicraft handling qualities, and for aeroelastic phenomena.

Previous works found in the literature had tried to understand the in-plane loads from a global approach provided by experimental data or CFD simulations. However, to the author's knowledge, no deep analysis on the in-plane loads has been previously done based on singularity methods. This type of approaches is based on the linear superposition of the effect of a number of elements in the space (the singularities) to determine the global airflow. This property has been used in Chapter 2 to estimate the contribution of a number of aerodynamic mechanisms at the origin of propeller in-plane loads. This has led to a better understanding of these mechanisms and provides a precious tool for engine designers aiming at mastering these undesired loads.

The unsteadiness in the relative airflow seen by the blade has been identified as one of the main contributors to predict correctly the in-plane loads. Besides, it has also been shown that the unsteady corrections in the official HOST version does not implement rigorously the unsteady airfoil theory. Therefore, Chapters 3 and 4 have been devoted to the theoretical analysis, development, and implementation of an unsteady airfoil model that enables, on one side, to correct the quasi-steady airfoil data to include the loads due to airflow unsteadiness and, on the other side, to account for the local blade sweep and curvature. In Chapter 3 a first model based on previous works has been theoretically analyzed and has shown important shortcomings. Hence, it has been necessary to re-develop an unsteady airfoil model to be implemented in the HOST code, as exposed in Chapter 4. Again, the main shortcomings of the implemented model have been put forward.

The unsteady model implemented in HOST has been assessed in Chapter 5 by comparison with previous HOST simulations, experimental data, and CFD simulations. Very satisfactory results have been obtained in terms of propeller performance, in-plane loads, and blade load distributions. In particular, an improvement in the prediction of in-plane loads phase lag and blade load distribution have been remarked thanks to the unsteady airfoil model.

A similar study has been conducted in Chapter 6 for the case of a generic open rotor geometry (AI-PX7) in isolated configuration, in high-speed conditions and in incidence. The assessment of the HOST code has been done by comparing its results with CFD simulations. Again, satisfactory results have been obtained in terms of global performance and in-plane loads, as well as in terms of blade load distribution. Taking into account the effects of the nacelle and including the unsteady airfoil model has provided more in-plane loads that are closer to CFD results. Nevertheless, it has also been noted the importance of chord and volume effects in open rotor simulations. Indeed, due to the fact that these effects are neglected in HOST, an underestimation of the potential interaction between rotors has been noticed.

In order to complete the insight into in-plane load mechanisms in Chapter 2, the second part of the Chapter 6 has been devoted to the study of the mechanisms behind open rotor in-plane loads. Again, this method provides a useful tool for designers as it enables rapid sensitivity studies of open rotor performance and in-

plane loads to an important number of key design parameters.

The last chapter of this thesis (Chapter 7) is devoted to an exploratory study of the coupling between the *elsA* CFD code and the HOST comprehensive code for propeller simulations. The interest of this type of simulations lies in the fact that the CFD simulation domain is reduced to a small volume around one blade of the propeller. The effect of the other blades is provided by the induced velocities calculated in a more rapid code, HOST in the present study. This approach is likely to reduce computational costs with respect to full CFD simulations, while maintaining a large scope of applications, including installed configurations or incidence effects. The state-of-art in this field is summarized and its shortcomings are exposed. Then, a new coupling strategy is proposed and partially implemented. First comparisons between both coupling strategies on a single propeller test case show similar results, although a number of modifications in the computation of induced velocities have been necessary. On the contrary, when comparing this new coupling strategy with CFD simulations of a complete propeller, important mismatches can be noticed. Further studies should be conducted to better understand the origin of these mismatches and to solve them. Moreover, for the moment, only a one-way coupling strategy has been implemented. Future HOST versions are likely to be more adapted for complete coupled HOST-*elsA* simulations.

To sum up, this thesis has provided a better insight into the comprehension of the in-plane load mechanisms, as well as a preliminary design tool for the aerodynamic simulation of open rotors. These are two key steps for the integration of open rotors on future Airbus aircraft.

Moreover, this thesis has opened a number of fields to be explored: (1) HOST simulations have shown a lack of accuracy in the prediction of loads close to the blade root. Therefore, a hub model based on singularity methods might be a way to improve the predictions in this area. (2) The unsteady airfoil model currently implemented still neglects the singularity of the spanwise vortices in the wake. A more rigorous model allowing a correct regularization of the wake should improve the stability of HOST simulations (3) In order to reduce the computational time, fast multipole techniques are being investigated at Onera for the integration of the induced velocities, promising important gains in computational time. (4) Continue with the development of a full HOST-*elsA* coupling strategy for the simulation of propellers and contra-rotating open rotors. (5) Increasing the number of HOST applications: including aeroelastic simulations, or using the MINT wake for rapid aeroacoustic simulations.

Appendix A

Finite Part Integrals

This chapter details the theory behind finite part integrals as used by Gallois [Gallois 2003] and Muller [Muller 2007] in their respective Ph.D. thesis. The chapter starts with a definition of Cauchy's Principal Value integral. Then, the Finite Part integral defined by Hadamard as the generalization of Cauchy's Principal Value is detailed.

A.1 Principal Value of a Singular Integral

From the formalization of the lifting-line problem, Prandtl [Prandtl 1923] has discovered the importance of the correct computation of singular integrals. In particular, he had to consider the Principal Value of the following integral: $\mathrm{PV}\int_a^b \frac{\partial\Gamma}{\partial y}\frac{dy}{y-c}$.

In a more general case, the Principal Value integrals are used in integrals of the form:

$$\begin{aligned}\mathrm{PV}\int_a^b \frac{\psi(x)dx}{x-c} &= \lim_{\varepsilon\to 0}\left(\int_a^{c-\varepsilon}\psi(x)\frac{dx}{x-c}+\int_{c+\varepsilon}^b \psi(x)\frac{dx}{x-c}\right)\\ &= \int_a^b \frac{\psi(x)-\psi(c)}{x-c}dx+\psi(c)\mathrm{PV}\int_a^b\frac{dx}{x-c}\\ &= \int_a^b \frac{\psi(x)-\psi(c)}{x-c}dx+\psi(c)\ln\frac{b-c}{c-a}\end{aligned} \tag{A.1}$$

for a function $\psi(x)$ continuous in all the $[a,b]$ interval. The first integral is improper but convergent. The second integral has been solved by Principal Values as follows:

$$\int_a^b\frac{dx}{x-c}=\lim_{\varepsilon_1,\varepsilon_2\to 0}\left(\int_a^{c-\varepsilon_1}\frac{dx}{x-c}+\int_{c+\varepsilon_2}^b\frac{dx}{x-c}\right)=\ln\frac{b-c}{c-a}+\lim_{\varepsilon_1,\varepsilon_2\to 0}\ln\frac{\varepsilon_1}{\varepsilon_2} \tag{A.2}$$

To calculate the Principal Value integral, it is imposed that $\varepsilon_1=\varepsilon_2$, thus yielding:

$$\mathrm{PV}\int_a^b\frac{dx}{x-c}=\ln\frac{b-c}{c-a} \tag{A.3}$$

The singular term in the integral has disappeared.

A.2 Hadamard's Finite Part Integrals

When considering higher order singularities, Principal Value integrals cannot be used because the regular part does not become zero when $\varepsilon\to 0$. This type of integrals are common in potential methods for aerodynamics. To solve them, Hadamard

[Hadamard 1932] proposed a Finite Part interpretation of the integrals, similar to Cauchy's Principal Value.

A function $g : [a, b]\backslash\{x_0\} \to \mathbb{R}$ continuous in all its definition interval is considered. The integral can be expressed as follows:

$$\mathcal{J}(\varepsilon) = \int_a^{x_0-\varepsilon} g(x)dx + \int_{x_0+\varepsilon}^b g(x)dx \tag{A.4}$$

$\mathcal{J}(\varepsilon)$ integral can be written as the sum of a regular part $\mathcal{R}(\varepsilon)$ and an irregular part $\mathcal{I}(\varepsilon)$. Hence, the Hadamard's Finite Part integral is defined as:

$$\mathrm{FP}\int_a^b g(x)dx = \lim\left[\int_a^{x_0-\varepsilon} g(x)dx + \int_{x_0+\varepsilon}^b g(x)dx - \mathcal{I}(\varepsilon)\right] = \lim_{\varepsilon\to 0}\mathcal{R}(\varepsilon) \tag{A.5}$$

In this case, the irregular part of the integral appears explicitly. It can be considered that Cauchy's Principal Value is a particular type of Hadamard's Finite Part integrals where the irregular part becomes zero when $\varepsilon \to 0$.

The general problem can be formulated as:

$$H^n_{f,a,b} = \mathrm{FP}\int_a^b \frac{f(x)dx}{(b-x)^{1+n}}\,,\ n \in \mathbb{N}^* \tag{A.6}$$

If the function $f^{(n+1)}(x)$ exists and is continuous in $[a, b]$, then it can be developed in Taylor series as follows:

$$f(x) = \sum_{k=0}^{n} \frac{(-1)^k f^{(k)}(b)(b-x)^k}{k!} + O\left((b-k)^{n+1}\right) \tag{A.7}$$

Thus, the integral yields:

$$\begin{aligned} H^n_{f,a,b} &= \int_a^b \frac{f(x) - (-1)^k f^{(k)}(b)(b-x)^k/k!}{(b-x)^{1+n}}dx + \sum_{k=0}^{n}\frac{(-1)^k}{k!}f^{(k)}(b)\mathrm{FP}\int_a^b \frac{dx}{(b-x)^{1+n-k}} \\ &= \int_a^b \frac{f(x) - (-1)^k f^{(k)}(b)(b-x)^k/k!}{(b-x)^{1+n}}dx + \sum_{k=0}^{n}\frac{(-1)^{k+1}f^{(k)}(b)}{(n-k)(a-b)^{n-k}k!} \end{aligned} \tag{A.8}$$

The Finite Part integral defined in Eq. A.8 is also valid when the singularity is not in the boundaries of integration. In the case of the lifting-line as implemented in HOST, the singularity is placed in the middle of the panels, and thus finite part integrals are divided in two intervals.

Gallois [Gallois 2003] has compared a number of numerical integration methods of these finite part integrals with the analytical approach. It has been noticed that the convergence of numerical methods was much slower than the convergence of the analytical one. Thus, this option has also been chosen to integrate finite parts in the integration of the induced velocities of the singular panel.

Muller lists a number of properties of Finite Part integrals [Muller 2007]:

- *Unique definition of the Finite Part*: $\mathcal{I}(\varepsilon)$ is defined as a generalized polynomial of the form: $\sum_{i<-1}\sum_{j>0} a_{i,j}\varepsilon^i(\ln\varepsilon)^j$ [Guermond 1990].

- The sign of the function on the interval $[a,b]$ does not provide any information of the *sign of the Finite Part integral*: for example, the Finite Part integration of the positive $1/x^2$ function in the interval $[0,1]$ yields:

$$\mathrm{FP}\int_0^1 \frac{dx}{x^2} = \lim_{\varepsilon\to 0}\left(\int_\varepsilon^1 \frac{dx}{x^2} - \mathcal{I}(\varepsilon)\right) = \lim_{\varepsilon\to 0}\left(-1+\frac{1}{\varepsilon}-\frac{1}{\varepsilon}\right) = -1 \tag{A.9}$$

- *Finite Part integrals are not invariant to variable changes*:

$$\mathrm{FP}\int_0^1 \frac{dx}{x} = 0 \tag{A.10}$$

whereas if the variable change $u = 2x$ is applied, it yields:

$$\mathrm{FP}\int_0^2 \frac{du}{u} = \ln 2 \tag{A.11}$$

Appendix B

Sweep Effect

This appendix details the simplified swept-wing theory implemented in HOST Blade Module. It is a first correction to the two-dimensional airfoil data in order to consider the effect of the local sweep angle on the aerodynamic behavior of the airfoil. In the present work, only the Mach number correction has been considered, whereas the incidence is left unchanged. Moreover, as it will be detailed hereafter, the lift and drag coefficients are also corrected in the airfoil data to account for the local sweep.

Figure B.1 shows the steps to predict the aerodynamic behavior of each blade section when the sweep correction is activated in the HOST code. The left-hand side figure represents the studied blade where one of the calculated section has been highlighted in red (Σ_∞ section). The Blade Module in HOST is based on the blade-element method, which considers that the aerodynamic behavior of each blade section is similar to an infinite-span wing. Remember that, as explained in the *Methods and Tools* chapter, the effect of the other blade sections and the effect of the other blades are taken into account in the inflow velocity computed by the wake model.

The aerodynamic behavior of an infinite-span wing with a certain sweep angle Λ has been studied very early in the wing design for high-speed aircraft [Jones 1945]. The figure in the center represents Jones' hypothesis, which considers that a swept wing of infinite span meeting an airflow at a certain velocity (V_∞) behaves as a non-swept wing of the same geometry but meeting an airflow with lower velocity ($V_\perp$). The relation between these two velocities is:

$$V_\perp = V_\infty \cos\Lambda \tag{B.1}$$

Jones' theory for swept wings considers the flow perpendicular to the wing, but neglects the effect of the flow parallel to the wingspan.

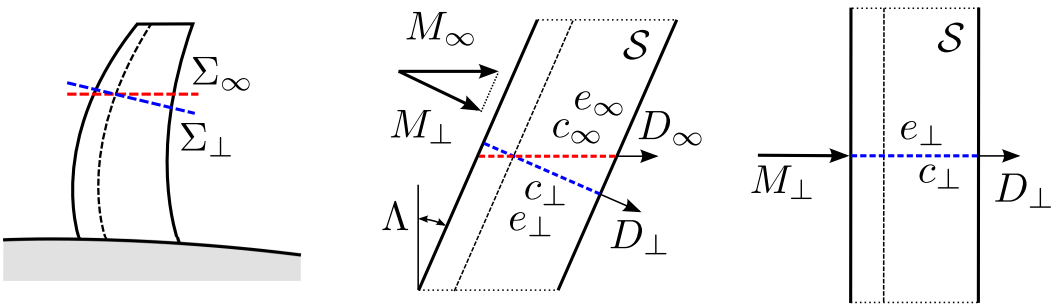


Figure B.1: Sweep correction hypothesis in the blade-element theory.

Therefore, to estimate the behavior of the swept wing, another section can be defined perpendicular to the sweep angle, highlighted in blue and noted as $\Sigma_\perp$. This section has a different chord ($c_\perp$) and relative thickness ($e_\perp/c_\perp$). The local chord of section $\Sigma_\perp$ follows:

$$c_\perp = c_\infty \cos\Lambda \tag{B.2}$$

and the relative thickness follows:

$$\frac{e_\perp}{c_\perp} = \frac{e_\infty}{c_\infty} \cos\Lambda \tag{B.3}$$

However, the span of the section is the same: $b_\infty = b_\perp$.

Based on equations (B.1), (B.2), and (B.3), a relation can be found between the expressions of the aerodynamic forces in Σ_∞ and $\Sigma_\perp$. First, the lift follows:

$$L_\infty = \frac{1}{2}\rho_\infty V_\infty^2 c_\infty b_\infty C_L^\infty \quad \text{and} \quad L_\perp = \frac{1}{2}\rho_\infty V_\perp^2 c_\perp b_\perp C_L^\perp \tag{B.4}$$

which yields to:

$$L_\infty = L_\perp \quad \Rightarrow \quad V_\infty^2 C_L^\infty = V_\perp^2 C_L^\perp \quad \Rightarrow \quad C_L^\infty = C_L^\perp \cos^2\Lambda \tag{B.5}$$

And the drag follows:

$$D_\infty = \frac{1}{2}\rho_\infty V_\infty^2 c_\infty b_\infty C_D^\infty \quad \text{and} \quad D_\perp = \frac{1}{2}\rho_\infty V_\perp^2 c_\perp b_\perp C_D^\perp \tag{B.6}$$

hence yielding to:

$$D_\infty = D_\perp \cos\Lambda \quad \Rightarrow \quad V_\infty^2 C_D^\infty = V_\perp^2 C_D^\perp \cos\Lambda \quad \Rightarrow \quad C_D^\infty = C_D^\perp \cos^3\Lambda \tag{B.7}$$

These sweep corrections have been used in all HOST-MINT simulations in the present Thesis. Therefore, the velocity seen by each blade section is corrected following the Eq. B.1, whereas the lift and the drag coefficients have been corrected in the airfoil data following Eqs. (B.5) and (B.7).

Appendix C

Alternative Form of the Singular Panel Integration

A two-dimensional regularization by finite part integrals is proposed, by establishing at each blade section a parabolic equation to model the form of the whole blade (see Fig. C.1). Similarly to what was proposed by Muller, the finite singular panel is calculated by the difference between a singular parabolic wake and the same wake except the surface of the singular panel. The difference of this approach with respect to the one proposed by Muller is that the infinite panel $\mathcal{S}$ extends not only chordwise but also spanwise.

C.1 Development of the Singular Panel Integration

C.1.1 The Complete Parabolic Wake

The velocity induced by the singular parabolic wake in doublet formulation has been decomposed as follows:

$$w_{\text{ind}}^{\infty}(M) = \frac{1}{4\pi}\Bigg(\Gamma(M) \underbrace{\text{FP} \iint_{\mathcal{S}} \frac{dS}{PM^3}}_{s_0^{\infty}} - \gamma_y(M) \underbrace{\text{FP} \iint_{\mathcal{S}} \frac{x_M - x_P}{PM^3} dS}_{s_x^{\infty}} + \gamma_x(M) \underbrace{\text{FP} \iint_{\mathcal{S}} \frac{y_M - y_P}{PM^3} dS}_{s_y^{\infty}} \Bigg) \tag{C.1}$$

Each of the integral terms is developed for a singular panel in $(x, y) \in ([0, +\infty], [0, b])$, where b is the blade span length. At each blade section M, a local frame is considered, as shown in Fig. C.2.

Calculation of s_0^{∞} term. The integral is expanded to solve it in finite parts:

$$\begin{aligned} s_0^{\infty}(M) &= \text{FP} \int_{-y_M}^{b-y_M} \int_{l^{\star}(y)}^{+\infty} \frac{dxdy}{(x^2+y^2)^{3/2}} \\ &= \underbrace{\text{FP} \int_{-y_M}^{b-y_M} \frac{dy}{y^2}}_{s_{01}^{\infty}} - \underbrace{\text{FP} \int_{-y_M}^{b-y_M} \frac{l^{\star}(y)}{y^2\sqrt{l^{\star}(y)^2+y^2}} dy}_{s_{02}^{\infty}} \end{aligned} \tag{C.2}$$

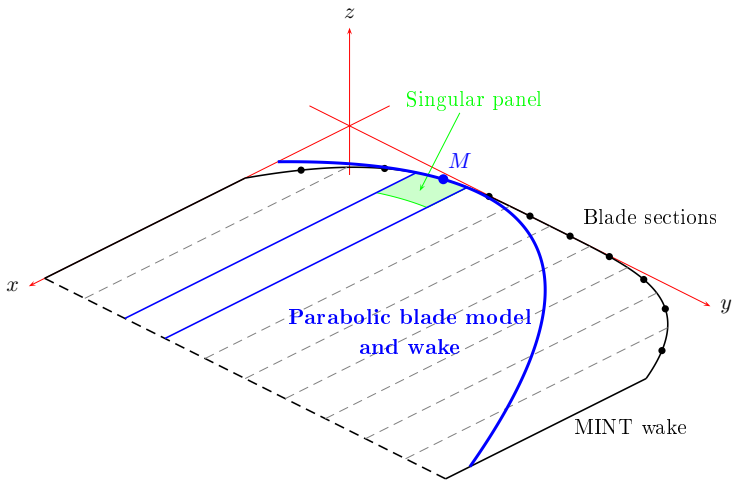


Figure C.1: Parabolic blade and wake models to calculate finite singular panel $\vec{v}_{\text{ind}}$

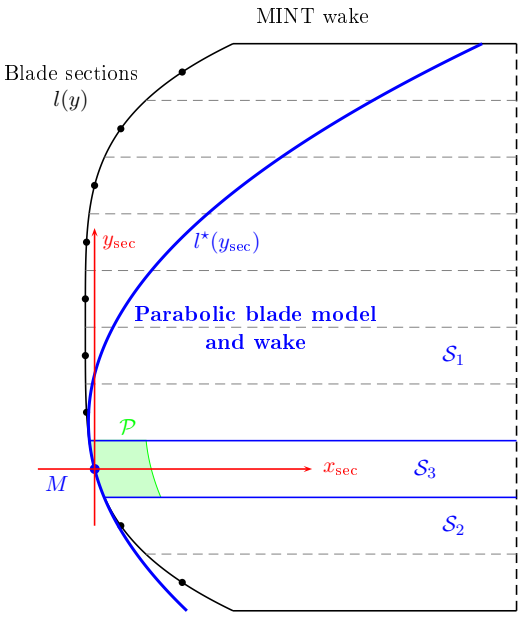


Figure C.2: Local reference frame for singular panel $\vec{v}_{\text{ind}}$ calculation

The first integral yields:

$$s_{01}^{\infty} = \mathrm{FP}\int_{-y_M}^{b-y_M} \frac{dy}{y^2} = \frac{-b}{y_M(b-y_M)} \tag{C.3}$$

For the second integral the function $f(y)$ is defined and developed in Taylor's series around $y = 0$ as follows:

$$f(y) = \frac{sgn(y)l^{\star}(y)}{\sqrt{l^{\star}(y)^2 + y^2}} = \sin\Lambda + \frac{y}{2\kappa} + \frac{f''(0)y^2}{2} + \mathcal{O}(y^3) \tag{C.4}$$

where $f''(0)$ can be calculated if a parabolic model of the blade form is considered, $l^{\star}(y) = k_1 y^2 + k_2 y + k_3$, passing by the section origin O_{sec} at the calculation point M, with the first derivative $dl^{\star}/dy(0) = \tan\Lambda$, and a curvature radius κ at O_{sec}. Note that each parabolic wake is calculated for a local frame OXY_{sec} centered at the calculation point $M = [l(y_M), y_M]$. The constants in the parabolic equation are:

$$k_1 = (1+\tan^2\Lambda)^{3/2}/(2\kappa)\ , \quad k_2 = \tan\Lambda \quad \text{and} \quad k_3 = 0 \tag{C.5}$$

Which in the end yields to :

$$f''(0) = \frac{-3k_1^2 k_2}{(1+k_2^2)^{5/2}} \tag{C.6}$$

Thus, the second term yields:

$$\begin{aligned} s_{02}^{\infty} &= \mathrm{FP}\int_{-y_M}^{b-y_M} \frac{l^{\star}(y)}{y^2\sqrt{l^{\star}(y)^2+y^2}}dy \\ &\sim \sin\Lambda \mathrm{FP}\int_{-y_M}^{b-y_M} \frac{sgn(y)}{y^2}dy + \frac{1}{2\kappa}\mathrm{FP}\int_{-y_M}^{b-y_M}\frac{sgn(y)}{y}dy + \frac{f''(0)}{2}\mathrm{FP}\int_{-y_M}^{b-y_M} sgn(y)dy \\ &= \sin\Lambda\frac{b-2y_M}{y_M(b-y_M)} + \frac{1}{2\kappa}\ln\left[\frac{4y_M(b-y_M)}{b^2}\right] + \frac{-3k_1^2k_2}{2(1+k_2^2)^{5/2}}(b-2y_M) \end{aligned} \tag{C.7}$$

Calculation of the s_x^{∞} term.

$$\begin{aligned} s_x^{\infty} &= \mathrm{FP}\int_{-y_M}^{b-y_M}\int_{l^{\star}(y)}^{+\infty} \frac{-xdxdy}{(x^2+y^2)^{3/2}} \\ &= \mathrm{FP}\int_{-y_M}^{b-y_M} \frac{-dy}{\sqrt{l^{\star}(y)^2+y^2}} = \mathrm{FP}\int_{-y_M}^{b-y_M}\frac{-ydy}{y\sqrt{l^{\star}(y)^2+y^2}} \end{aligned} \tag{C.8}$$

A function $g(y)$ is defined and developed in Taylor's series as follows:

$$g(y) = \frac{sgn(y)y}{\sqrt{l^{\star}(y)^2+y^2}} = \cos\Lambda + g'(0)y + \mathcal{O}(y^2) \tag{C.9}$$

Again, the term $g'(0)$ can be calculated by supposing that the shape of the blade is parabolic. It yields:

$$g'(0) = \frac{-k_1k_2}{(1+k_2^2)^{3/2}} \tag{C.10}$$

Thus, the s_x^∞ term yields:

$$\begin{aligned} s_x^\infty &= -\mathrm{FP}\int_{-y_M}^{b-y_M} \frac{sgn(y)g(y)}{y}dy \\ &= -\mathrm{FP}\int_{-y_M}^{b-y_M} \cos\Lambda\frac{sgn(y)}{y}dy - \mathrm{FP}\int_{-y_M}^{b-y_M} g'(0)sgn(y)dy \\ &= -\cos\Lambda\ln\left[\frac{4y_M(b-y_M)}{b^2}\right] - \frac{-k_1k_2}{(1+k_2^2)^{3/2}}(b-2y_M) \end{aligned} \tag{C.11}$$

Calculation of s_y^∞ term.

$$\begin{aligned} s_y^\infty(M) &= \mathrm{FP}\int_{-y_M}^{b-y_M}\int_{l^\star(y)}^{+\infty} \frac{ydxdy}{(x^2+y^2)^{3/2}} \\ &= \mathrm{FP}\int_{-y_M}^{b-y_M} \frac{-1}{y}\left(1-\frac{l^\star(y)}{\sqrt{l^\star(y)^2+y^2}}\right)dy \end{aligned} \tag{C.12}$$

Using again $f(y)$ function, the term can be developed as follows:

$$\begin{aligned} s_y^\infty(M) &= \mathrm{FP}\int_{-y_M}^{b-y_M}\left(\frac{-1}{y}+\frac{sgn(y)\sin\Lambda}{y}+\frac{sgn(y)}{2\kappa}+\frac{f''(0)}{2}sgn(y)y\right)dy \\ &= \ln\frac{y_M}{b-y_M}+\sin\Lambda\ln\left[\frac{4y_M(b-y_M)}{b^2}\right]+\frac{1}{2\kappa}(b-2y_M) \\ &+\frac{-3k_1^2k_2}{4(1+k_2^2)^{5/2}}[(b-y_M)^2+y_M^2] \end{aligned} \tag{C.13}$$

C.1.2 The Regular Part of the Parabolic Wake

After having integrated in finite parts all the parabolic wake, the regular parts are removed in order to account only for the velocities induced by the singular panel at the considered blade section.

When considering the velocities induced by the whole parabolic wake except the singular panel, all the integrals are regular and hence they can be easily computed numerically. Although the expressions to integrate the regular part of the parabolic wake are the same as in the previous subsection, in this case, the domain is divided in three areas: both sides of the singular panel (1 and 2) and the infinite wake downstream the singular panel (3) (see Fig. C.2).

Similar to what has been done for the singular parabolic wake, the velocities induced by the regular parts of the parabolic wake $\mathcal{S}-\mathcal{P}$ are decomposed as follows:

$$\begin{aligned} w_{\mathrm{ind}}^{\mathrm{reg}}(M) = \frac{1}{4\pi}\Bigg(&\Gamma(M)\underbrace{\iint_{\mathcal{S}-\mathcal{P}}\frac{dS}{PM^3}}_{s_0^{\mathrm{reg}}} \\ &-\gamma_y(M)\underbrace{\iint_{\mathcal{S}-\mathcal{P}}\frac{x_M-x_P}{PM^3}dS}_{s_x^{\mathrm{reg}}}+\gamma_x(M)\underbrace{\iint_{\mathcal{S}-\mathcal{P}}\frac{y_M-y_P}{PM^3}dS}_{s_y^{\mathrm{reg}}}\Bigg) \end{aligned} \tag{C.14}$$

Calculation of s_0^{reg} term.

$$\begin{aligned} s_0^{\text{reg}} = &\int_{-\delta y/2}^{\delta y/2} \int_{l^\star(y)+\delta x}^{+\infty} \frac{dxdy}{(x^2+y^2)^{3/2}} \\ &+ \int_{\delta y/2}^{b-y_M} \int_{l^\star(y)}^{+\infty} \frac{dxdy}{(x^2+y^2)^{3/2}} + \int_{-y_M}^{-\delta y/2} \int_{l^\star(y)}^{+\infty} \frac{dxdy}{(x^2+y^2)^{3/2}} \end{aligned} \tag{C.15}$$

where the three integrals correspond to the infinite wake downstream the singular panel, the left-hand side wake surface, and the right-hand side surface, respectively.

Calculation of the s_x^{reg} term.

$$\begin{aligned} s_x^{\text{reg}} = &\int_{-\delta y/2}^{\delta y/2} \int_{l^\star(y)+\delta x}^{+\infty} \frac{-xdxdy}{(x^2+y^2)^{3/2}} \\ &+ \int_{\delta y/2}^{b-y_M} \int_{l^\star(y)}^{+\infty} \frac{-xdxdy}{(x^2+y^2)^{3/2}} + \int_{-y_M}^{-\delta y/2} \int_{l^\star(y)}^{+\infty} \frac{-xdxdy}{(x^2+y^2)^{3/2}} \end{aligned} \tag{C.16}$$

where the three integrals correspond to the infinite wake downstream the singular panel, the left-hand side wake surface, and the right-hand side surface, respectively.

Calculation of the s_y^{reg} term.

$$\begin{aligned} s_y^{\text{reg}} = &\int_{-\delta y/2}^{\delta y/2} \int_{l^\star(y)+\delta x}^{+\infty} \frac{-ydxdy}{(x^2+y^2)^{3/2}} \\ &+ \int_{\delta y/2}^{b-y_M} \int_{l^\star(y)}^{+\infty} \frac{-ydxdy}{(x^2+y^2)^{3/2}} + \int_{-y_M}^{-\delta y/2} \int_{l^\star(y)}^{+\infty} \frac{-ydxdy}{(x^2+y^2)^{3/2}} \end{aligned} \tag{C.17}$$

where the three integrals correspond to the infinite wake downstream the singular panel, the left-hand side wake surface, and the right-hand side surface, respectively.

C.1.3 The Complete Expression

The expression for the integration of the singular panel $\mathcal{P}$ is obtained by removing the effect of the regular parts of the parabolic wake $\mathcal{S} - \mathcal{P}$ to the velocities induced by the complete parabolic wake $\mathcal{S}$. Therefore, based on the previous results, the expression for the velocities induced by the singular panel yields:

$$w_{\mathcal{P}} = w_{\text{ind}}^{\infty} - w_{\text{ind}}^{\text{reg}} = \Gamma(M)(s_0^{\infty} - s_0^{\text{reg}}) - \gamma_y(s_x^{\infty} - s_x^{\text{reg}}) + \gamma_x(s_y^{\infty} - s_y^{\text{reg}}) \tag{C.18}$$

Future studies are still necessary in order to assess this new approach for the integration of the singular panel by finite part integrals. In particular, the most important decision is probably the choice of the singular panel size ($\delta x \times \delta y$). These lengths determine in fact the limit of the finite part regularization and have a significant impact on the global induced velocities, as highlighted in Chapter 3.

Appendix D

Résumé en français

Contents

D.1 Introduction 195
D.2 Un aperçu des mécanismes à l'origine des efforts 1P 196
D.2.1 Les mécanismes physiques à l'origine des efforts 1P 196
D.2.2 Une méthode pour quantifier les mécanismes sur les efforts 1P 197
D.3 Développement et implémentation d'une méthode de ligne portante courbe et instationnaire 199
D.4 Évaluation de la méthode de ligne portante courbe et instationnaire dans le cas d'hélice simple APIAN 201
D.5 Évaluation de la méthode de ligne portante courbe et instationnaire dans le cas de l'Open Rotor AI-PX7 202
D.5.1 Évaluation de HOST-MINT dans un cas d'open rotor 202
D.5.2 Un aperçu dans les mécanismes des efforts 1P 204
D.6 Développement d'une méthodologie de couplage entre les codes HOST et elsA 206
D.7 Conclusions 208

D.1 Introduction

Depuis quelques années, la hausse du prix des carburants pousse les avionneurs et les motoristes à étudier des technologies révolutionnaires permettant de produire des avions plus efficients et plus propres à horizon 2020 et au-delà. Parmi des nombreux concepts qui émergent, le *contra-rotating open rotor*[1] semble être une option attractive pour la réduction significative de la consommation spécifique de carburant et des émissions polluantes. Cependant, un certain nombre de domaines clés ne sont pas encore suffisamment maîtrisés dès les premières phases de la conception d'un nouveau moteur. C'est pour cela que les industriels investissent dans le développement de méthodologies qui soient adaptées à chaque phase de la conception pour pouvoir évaluer correctement ces paramètres clés.

Cette thèse porte sur le développement de méthodologies à coût modéré pour les phases de conception préliminaire des *open rotor*. Les paramètres principaux qui doivent être maîtrisés pendant les phases de conception préliminaire sont, d'un

[1] Aussi appelé *open rotor* : moteur à doublet d'hélices contrarotatives.

côté, la prédiction des performances aérodynamiques des hélices et, d'un autre côté, les efforts dans le plan hélice[2] générés par les effets d'installation ou par l'incidence du moteur. En outre, pendant ces premières phases de conception, les outils de simulation fournis aux concepteurs doivent être très rapides et très souples, afin de permettre l'exploration d'une large variété de configurations de moteur dans un temps de calcul raisonnable.

Suivant ces critères, une étude des différentes méthodes disponibles a été réalisée. Les principaux atouts et limites de chaque méthode ont été mis en avant et le choix d'une méthode basée sur la théorie de la ligne portante courbe et instationnaire a été justifiée. HOST, un code pour la simulation aéro-mécanique des hélicoptères, e été choisi et adapté pour la simulation des hélices simples et contrarotatives.

Cette thèse est donc structurée de la façon suivante : en premier lieu, une étude pour approfondir la compréhension de l'origine des efforts 1P a été menée; en deuxième lieu, le modèle d'élément de pale a été amélioré pour prendre en compte plus rigoureusement l'aérodynamique instationnaire des profils 2D et les effets de flèche et de courbure de pale; en troisième lieu, le code HOST et les modèles instationnaire et d'effets d'installation ont été évalués pour la simulation des hélices simples et des CROR à l'aide des données expérimentales et des simulations CFD plus avancées et plus précises; et enfin, la dernière partie de la thèse a été consacrée à une étude exploratoire du couplage entre les codes HOST et *elsA*[3].

D.2 Un aperçu des mécanismes à l'origine des efforts 1P

Cette section offre, d'un côté, une explication des différents termes qui contribuent à la génération des efforts dans le plan hélice (les efforts 1P) et, d'un autre côté, elle développe une méthode pour la quantification de l'impact des différents mécanismes sur ces efforts.

D.2.1 Les mécanismes physiques à l'origine des efforts 1P

Dans le cas général d'une hélice dans un écoulement non uniforme sur son plan de rotation, chaque pale développe des efforts instationnaires le long d'un tour de pale complet. La contribution des efforts des différentes pales à un instant donné peut ainsi conduire à un effort net de l'hélice qui ne soit pas aligné avec l'axe de rotation de l'hélice. Dans ce cas de figure, la force résultante peut être décomposée en un vecteur parallèle à l'axe de rotation de l'hélice, la traction, et en un vecteur dans le plan de rotation de l'hélice, appelé souvent l'*effort 1P*. Comprendre les mécanismes qui régissent le module et la direction de cet effort reste un enjeu majeur pour le développement des avions propulsés par des CROR.

Le module des efforts 1P. Dans le développement des moteurs à hélices, l'apparition d'un effort non négligeable dans le plan hélice a été constaté très tôt

[2] Aussi appelés *efforts 1P*.

[3] Ensemble Logiciel pour la Simulation Aérodynamique, solveur CFD de l'Onera.

pour le cas d'une hélice dans un écoulement avec une certaine incidence. En effet, l'incidence constitue le cas le plus simple d'écoulement non uniforme dans le plan hélice.

Dû à la vitesse de rotation de l'hélice, l'incidence de l'écoulement amont induit une variation de l'angle et de la vitesse de l'écoulement vu par la pale. Ces variations de vitesse et d'incidence génèrent à leur tour une variation dans les efforts développés par la pale : plus l'incidence et la vitesses sont importantes, plus les efforts sur la pale seront importants. L'addition de ces efforts sur le plan de l'hélice et leur addition conduisent à un effort net dans le sens de l'incidence de l'hélice, couramment un *effort vertical*.

Cependant, cette explication purement "géométrique" explique seulement l'existence d'un effort parallèle à la projection de la vitesse d'avancement dans le plan de l'hélice, mais pas celle d'un effort perpendiculaire à cette direction, couramment appelé *effort latéral*.

La phase des efforts 1P. À l'effort vertical dû à la variation d'incidence et de vitesse relative de la pale s'ajoute un effort latéral qui peut être aussi compris comme un déphasage de l'effort par rapport la variation de l'incidence et de la vitesse de l'écoulement vu par la pale. Ce phénomène de déphasage est plus complexe, et un bon nombre de mécanismes peuvent l'impacter. Au cours de ces travaux de thèse, l'étude s'est focalisés sur deux d'entre eux, reproductibles par les calculs HOST employés pour leur analyse :

- *La distance entre la pale et les sillages* : la pale descendante lâche un sillage plus chargé en vorticité que celui de la pale montante. À cause de l'inclinaison du sillage, la pale à $\Psi = 0°$ est plus près du sillage de la pale descendante que la pale à $\Psi = 180°$. C'est pour cela que, l'incidence de la pale à $\Psi = 0°$ est plus faible que celle de la pale à $\Psi = 180°$, et il en est donc de même pour la force latérale développée. L'intégration des efforts sur les pales pourrait donc expliquer la force latérale qui apparaît dans le plan hélice.

- *Les effets de l'instationnarité de l'écoulement sur la pale et le sillage proche* : par analogie avec le cas d'un profil 2D oscillant, chaque pale dans une hélice en incidence voit un écoulement variant en 1/rev à une certaine fréquence, et développe des forces aérodynamiques instationnaires à cette même fréquence 1/rev, mais avec un certain déphasage. Ce déphasage serait généré par l'effet induit par le sillage proche sur la pale, comme dans le cas d'un profil oscillant.

D.2.2 Une méthode pour quantifier les mécanismes sur les efforts 1P

Les méthodes de singularités, comme la ligne portante, calculent la perturbation du champ de vitesses par la superposition de l'influence d'une série de singularités (sources, puits, doublets ou tourbillons) sur chaque point du domaine. C'est ainsi

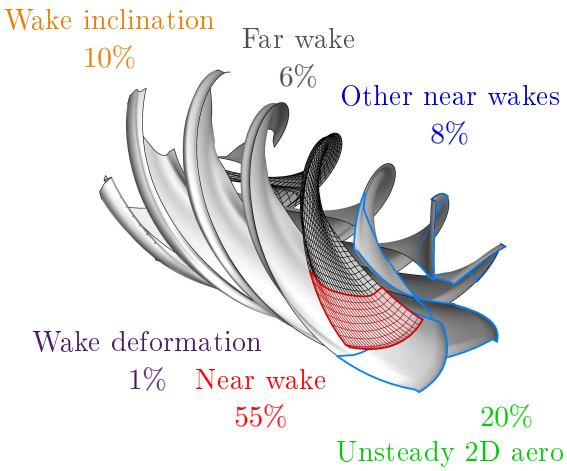


Figure D.1: Contribution de chaque élément du modèle à la phase des efforts 1P.

que, la contribution de chaque élément du modèle peut être facilement discriminée dans ce type de méthodes en prenant individuellement chaque contribution.

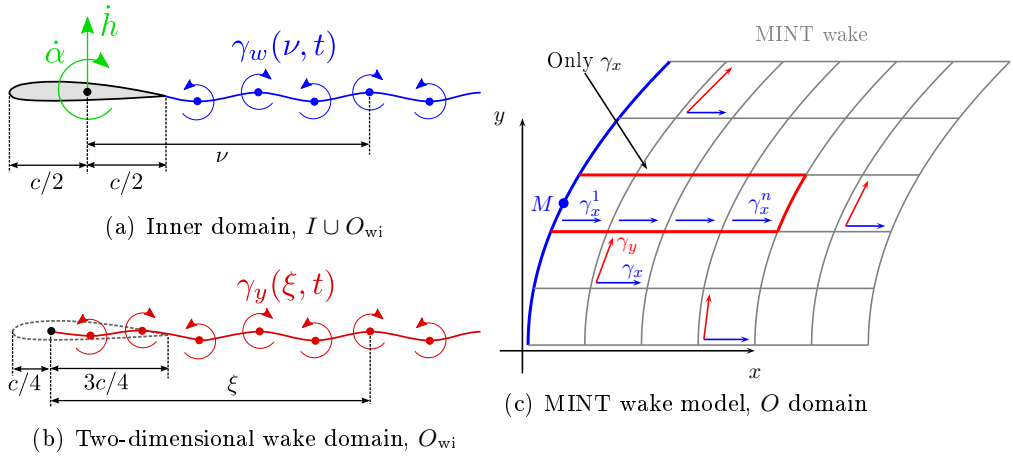
Cette approche a été utilisée dans les simulations avec HOST pour la quantification des mécanismes aérodynamiques à l'origine des efforts 1P. Les trois effets décrits précédemment ont été modélisés dans HOST par:

1. *La géométrie du sillage* : cet effet est modélisé par la modification de la déformation et de la direction de convection du sillage. Cela permet de déterminer la contribution qu'a la distance entre la pale et les autres sillages sur les efforts 1P.

2. *La vorticité instationnaire émise dans le sillage* : cet effet est modélisé par le changement dans la longueur du sillage prise en compte dans le calcul. Le sillage est donc tronqué au bout d'un certain nombre de panneaux, ce qui sert à régler cette longueur de sillage. Cela permet de déterminer l'impact de la vorticité lâchée à chaque instant dans le sillage sur les efforts 1P.

3. *L'aérodynamique instationnaire du profil* : cet effet est modélisé par l'activation d'un modèle simplifié de profil instationnaire. Cela permet de déterminer la contribution des instationnarités dans l'écoulement sur les efforts 1P.

La Fig. D.1 montre la contribution de chacun des éléments du modèle dans la prédiction de la phase des efforts 1P. L'impact le plus important venant du *sillage proche de la pale* et des effets *instationnaires sur le profil*, il paraît intéressant d'approfondir ces deux domaines dans les études à venir.



(a) Inner domain, $I \cup O_{\text{wi}}$

(b) Two-dimensional wake domain, O_{wi}

(c) MINT wake model, O domain

Figure D.2: Different $\vec{v}_{\text{ind}}$ terms in the unsteady curved lifting-line theory.

D.3 Développement et implémentation d'une méthode de ligne portante courbe et instationnaire

Une première étude a été menée pour évaluer une approche de méthode de ligne portante courbe et instationnaire proposée par Muller au cours de sa thèse [Muller 2007]. Il a été montré que cette approche par des intégrales en Partie Finies n'était pas adaptée pour les cas considérés dans le code HOST, où les géométries de pale présentent un allongement relativement faible.

C'est ainsi qu'une nouvelle approche qui implémente la théorie unifiée de la ligne portante développée par Guermond et Sellier [Guermond 1991] est ici proposée. La différence principale de cette approche vis-à-vis de celle proposée par Muller est de s'affranchir des intégrales en Partie Finies pour l'intégration des termes singuliers dans le calcul des vitesses induites.

Comme il avait été justifié par Van Dyke [Van Dyke 1964], le problème de la ligne portante étant un problème de perturbations singulières, il peut être résolu en développant la solution du problème par la technique des développements asymptotiques raccordés. Ceci a été utilisé par Guermond et Sellier [Guermond 1991] pour étendre la théorie de Van Dyke au cas d'une ligne portante courbe et dans un écoulement instationnaire sinusoïdal. Sous l'hypothèse de basses fréquences, Devinant [Devinant 1999] a démontré que cette théorie pouvait être appliquée au cas d'un mouvement instationnaire non-périodique. Enfin, Muller a implémenté cette théorie dans un code académique pour la simulation d'ailes courbes dans des écoulements instationnaires [Muller 2007].

Dans cette approche asymptotique, le problème est divisé en deux domaines (voir la Fig. 3.2) : d'un côté, le domaine du profil 2D (domaine intérieur I) et, d'un autre côté, le problème classique de la ligne portante 3D (domaine extérieur, O). Ces deux domaines sont reliés en imposant une continuité dans la vorticité du sillage entre le domaine intérieur I et le domaine extérieur O, ce qui conduit à la considération

d'un troisième domaine O_{wi}, lié au sillage 2D instationnaire derrière le profil.

L'équation implicite de la circulation peut être écrite:

$$\Gamma = \pi c \cos\Lambda \left(U_\infty \alpha + w_{I \cup O_{\text{wi}}} + w_{O \setminus O_{\text{wi}}} + w_c \right) \tag{D.1}$$

où:

- $w_{I \cup O_{wi}}$: il représente la vitesse induite par le domaine $I \cup O_{wi}$, qui a une origine purement 2D. Basé sur la théorie de profil instationnaire linéarisée, on obtient:

$$\begin{aligned} w_{I \cup O_{wi}}(y,t) \quad &= \dot{h}(y,t) + \frac{c}{2}\dot{\alpha}(y,t) \\ &+ \frac{1}{\pi c U_\infty \cos\Lambda} \int_{c/2}^{+\infty} \left(\sqrt{\frac{\nu + c/2}{\nu - c/2}} - 1 \right) \gamma_w(\nu,t) d\nu \end{aligned} \tag{D.2}$$

- $w_{O \setminus O_{wi}}$: ce terme représente la vitesse induite par le domaine extérieur, ce qui inclut tout le sillage sauf la vorticité longitudinale γ_y dans les panneaux du sillage derrière la section de calcul. Dans ce domaine, la longueur caractéristique est l'envergure de la pale, et donc on considère que celle-ci se réduit à une ligne portante le long du quart de corde de la vraie géométrie. Le sillage est modélisé par un réseau de lanières et de panneaux de vorticité. Les vitesses induites par ces singularités peuvent donc être calculées par:

$$\vec{V}_{\text{ind}} = \underbrace{-\frac{1}{4\pi} \int_{\partial S} \Gamma(P) \frac{\overrightarrow{PM} \wedge \vec{dl}_P}{PM^3}}_{\text{Vortices}} \underbrace{- \frac{1}{4\pi} \int_S \frac{\vec{\gamma} \wedge \overrightarrow{PM}}{PM^3} dS_P}_{\text{Panels}} \tag{D.3}$$

  Le terme $w_{O \setminus O_{wi}}$ correspond à la composante de la $\vec{V}_{\text{ind}}$ qui est contenue dans le plan du profil et qui est normale à la corde locale.

- w_c: ce terme représente les vitesses induites complémentaires, qui prennent en compte la flèche et la courbure locales de la pale. Ceci permet d'ajouter l'effet de la variation radiale de circulation dans la ligne portante. A partir des études de Guermond [Guermond 1990], on peut déduite l'expression suivante en factorisant par Γ et $\partial\Gamma/\partial y$:

$$w_c(y) = a_1 \Gamma(y) + a_2 \frac{\partial \Gamma}{\partial y}(y) \tag{D.4}$$

  où:

$$a_1 = \frac{1}{4\pi\kappa(y)}(1 - \tan^2\Lambda(y) + K) \quad ; \quad a_2 = \frac{1}{2\pi}\left(K \sin\Lambda(y) + \ln\left| \frac{1 + \sin\Lambda(y)}{\cos\Lambda(y)} \right| \right)$$

$$K = \frac{1}{2} + \ln \frac{c(y)\cos^2\Lambda(y)}{4b}$$

La continuité de la vorticité entre le domaine intérieur et extérieur permet d'établir le lien entre ces deux domaines: $\gamma_w(\xi, y) = \gamma_y(\xi - c/2, y)$ (voir Fig. 3.2)

D'un côté, la théorie de profil instationnaire linéarisée considère un sillage 2D du profil depuis son bord de fuite et jusqu'à l'infini aval. Étant donné que le sillage commence au bord de fuite, les intégrales des vitesses induites pour ce cas de figure sont régulières.

D'un autre côté, la théorie de la ligne portante considère un sillage 3D du quart de corde de la pale et jusqu'à l'infini aval. Dans ce deuxième cas, les intégrales sont singulières, puisque le premier panneau est en contact avec le point de calcul.

Il apparaît donc que l'effet de la composante longitudinale de la vorticité γ_y est à la fois prise en compte dans la sillage 2D du profil et dans les panneaux du sillage 3D derrière la section considérée. Pour éviter cela, la prise en compte de cette composante γ_y est omise sur une série de panneaux du sillage 3D, dont le panneau singulier (voir Fig. 3.2). Ainsi, la méthode s'affranchit des intégrales singulières dues à la composante longitudinale de la circulation.

L'équation D.1 peut être réécrite comme:

$$\begin{aligned}\Gamma(y,t) = {} & \pi c(y)\cos\Lambda(y)\left[U_\infty\alpha(y,t) + \dot{h}(y,t) + \frac{c(y)}{2}\dot{\alpha}(y,t)\right] \\ & + \int_0^X \left(\sqrt{1+\frac{c(y)}{\xi}} - 1\right)\gamma_y(\xi,y)d\xi \\ & - \frac{c(y)\cos\Lambda(y)}{4}\int_S \Gamma(P)\overrightarrow{\nabla}_M\left(\frac{\overrightarrow{n_P}.\overrightarrow{PM}}{PM^3}\right)dS_P \\ & + \pi c(y)\cos\Lambda(y)\left[a_1\Gamma(y) + a_2\frac{\partial\Gamma}{\partial y}(y)\right]\end{aligned} \tag{D.5}$$

où:

- La première et la deuxième ligne correspondent au *domaine intérieur* (la théorie de profil mince) : il est composé d'un terme quasi-stationnaire lié au mouvement du profil et d'un terme de sillage proche en formulation profil.
- La troisième ligne correspond au *domaine extérieur* w_O : le sillage est divisé en panneaux et intégré numériquement par la méthode de Gauss-Legendre. Les panneaux du sillage derrière le point de calcul sont calculés sans prendre en compte la composante γ_y.
- La quatrième ligne correspond au *terme complémentaire* (obtenu de la théorie de Guermond et Sellier) : il est dû à la flèche et à la courbure locales de la pale.

D.4 Évaluation de la méthode de ligne portante courbe et instationnaire dans le cas d'hélice simple APIAN

Cette section expose une première évaluation du code HOST pour un cas représentatif d'hélice simple (APIAN) en grandes vitesses et à une certaine incidence. Cette

Table D.1: Effet d'incidence dans le cas grandes-vitesses APIAN.

Test No.	Mach No. [–]	Incidence [°]	RPM [min^{-1}]	J [–]
1145	0.700	0.01	8623.	3.269
1146	0.699	1.00	8632.	3.268
1147	0.700	1.48	8638.	3.272
1148	0.700	2.02	8639.	3.273
1149	0.700	3.00	8639.	3.278

évaluation est faite par comparaison des performances calculées avec des données expérimentales obtenues en soufflerie et des résultats de calculs avec le code *elsA*, un code CFD pour la résolution des équations uRANS. En outre, le modèle pour la prise en compte des effets d'installation et le modèle de profil instationnaire sont aussi évalués.

Dans ce résumé, on montre seulement les résultats de l'effet d'incidence sur les performances, et les forces et moments 1P. Le Tableau D.1 montre les principaux paramètres des cinq points de calcul comparés.

La Fig. D.3 montre la comparaison du coefficient de traction (C_{TH}), du coefficient de puissance (C_{PW}), du coefficient de l'effort 1P (C_{1P}), de la phase de l'effort 1P (Ψ_{1P}), du coefficient du moment 1P (C_{M1P}), et de la phase du moment 1P (Ψ_{M1P}).

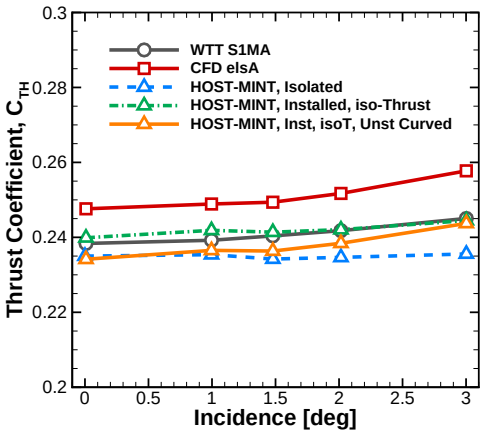
Ces figures montrent, d'un côté, la capacité de HOST-MINT à reproduire avec une précision raisonnable les performances moteur et les efforts 1P, par comparaison aux mesures expérimentales et aux résultats CFD. En outre, les modèles pour prendre en compte les effets d'installation et les effets instationnaires du profil fournissent des meilleures prédictions du module et de la phase des efforts 1P.

D.5 Évaluation de la méthode de ligne portante courbe et instationnaire dans le cas de l'Open Rotor AI-PX7

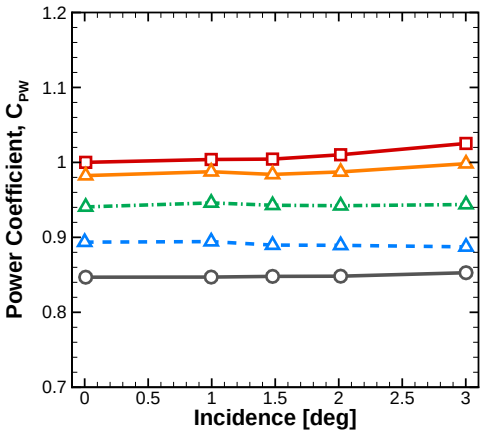
Cette section présente, d'un côté, l'évaluation du code HOST-MINT dans un cas représentatif d'open rotor (AI-PX7) en grande vitesse et en incidence. D'un autre côté, elle présente une méthode, basée sur la décomposition des vitesses induites, pour la quantification de l'impact des mécanismes aérodynamiques sur les performances et les efforts 1P de l'open rotor.

D.5.1 Évaluation de HOST-MINT dans un cas d'open rotor

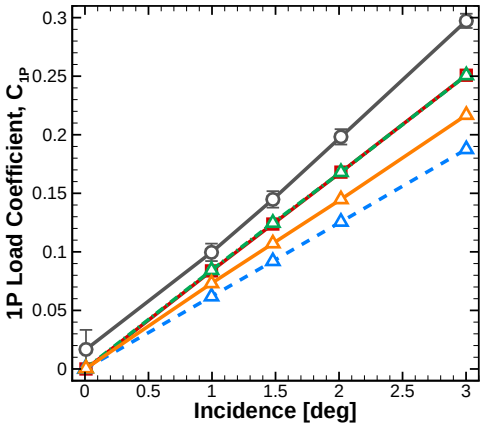
Cette sous-section détaille une comparaison entre le code HOST-MINT et le code CFD *elsA* pour le cas d'un open rotor en grande vitesse ($M = 0.73$) et en incidence



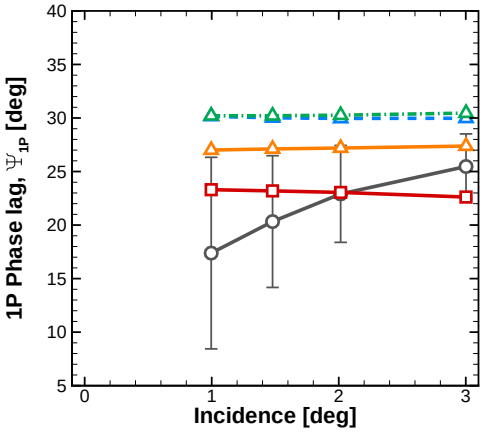
(a) Coefficient de traction, C_{TH}



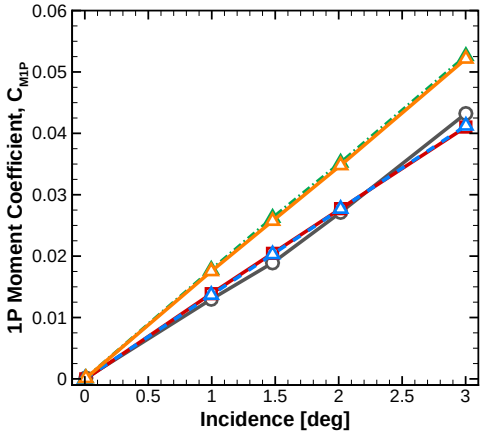
(b) Coefficient de puissance, C_{PW}



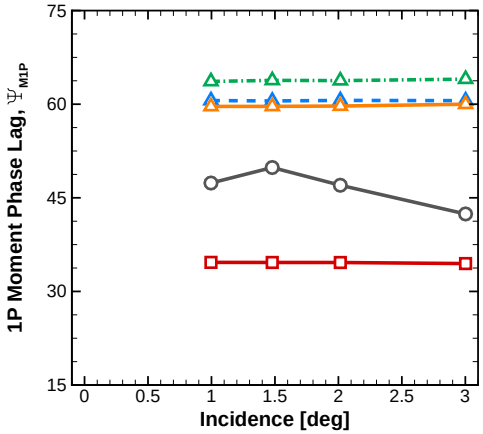
(c) Coefficient de l'effort 1P, $C_{1\mathrm{P}}$



(d) Phase de l'effort 1P, $\Psi_{1\mathrm{P}}$

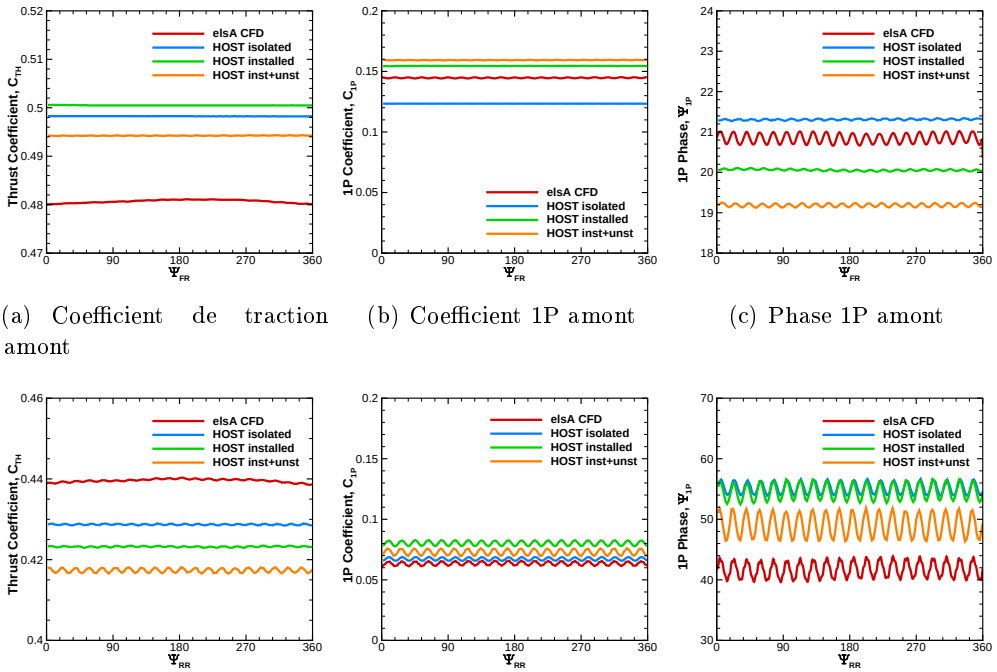


(e) Coefficient du moment 1P, C_{M1P}



(f) Phase du moment 1P, Ψ_{M1P}

Figure D.3: Effet de l'incidence dans le cas APIAN en grandes vitesses. Comparaison entre les mesures expérimentales, les résultats des simulations CFD et les simulations HOST-MINT (cas isolé, cas avec les effets d'installation et cas avec effets d'installation et corrections instationnaires).



(a) Coefficient de traction amont (b) Coefficient 1P amont (c) Phase 1P amont

(d) Coefficient de traction aval (e) Coefficient 1P aval (f) Phase 1P aval

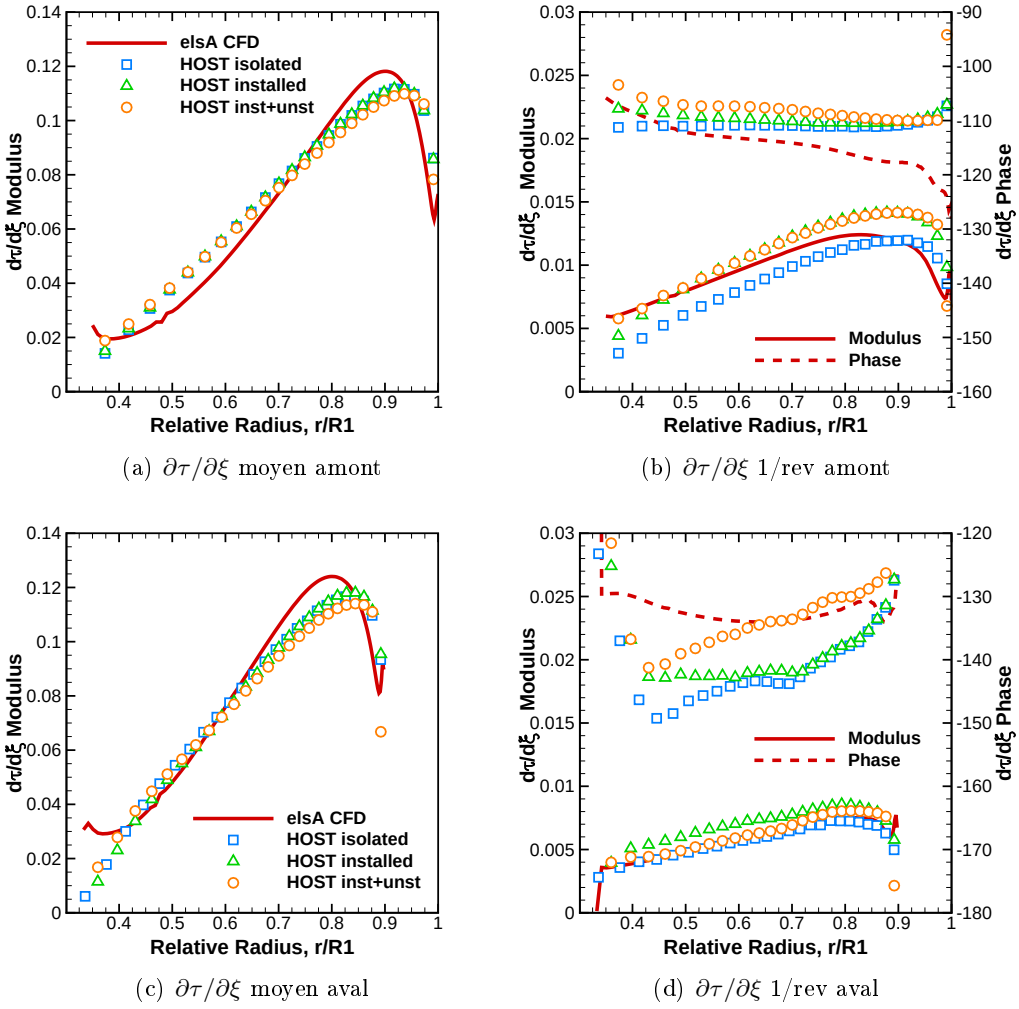
Figure D.4: Comparaison des performances des rotors amont et aval.

($\alpha = 1°$). De manière similaire à ce qui a été fait dans l'évaluation du code HOST-MINT dans la section précédente, trois simulations de ligne portante sont comparées : simulations isolées, simulations avec effets d'installation, et simulations avec effets d'installation et avec le modèle instationnaire.

La Fig. D.4 montre la prédiction du coefficient de traction, du module des efforts 1P et de la phase des efforts 1P pour les quatre simulations : la simulation CFD avec *elsA* et les trois simulations HOST-MINT. Enfin, la comparaison de la distribution de la charge sur pale amène aux résultats de la Fig. D.5. Dans toutes ces comparaisons, on peut remarquer l'amélioration des prédictions grâce aux modèles d'effets d'installation et de profil instationnaire.
Cependant, on peut remarquer également certaines différences qui montrent les limites de la méthode de la ligne portante utilisée dans HOST. D'un côté, l'effet potentiel entre le rotor aval et le rotor amont n'est pas capturé par les simulations HOST-MINT. Cela est dû à la modélisation de la pale par une ligne au quart de corde, négligeant ainsi tous les effets de corde et de volume dans l'interaction entre les rotors.

D.5.2 Un aperçu dans les mécanismes des efforts 1P

Basée sur l'hypothèse de linéarité des méthodes de singularités, une technique pour quantifier l'impact des mécanismes aérodynamiques sur la traction, le module de



(a) $\partial\tau/\partial\xi$ moyen amont

(b) $\partial\tau/\partial\xi$ 1/rev amont

(c) $\partial\tau/\partial\xi$ moyen aval

(d) $\partial\tau/\partial\xi$ 1/rev aval

Figure D.5: Transformée de Fourier discrète du $\partial\tau/\partial\xi$ amont et aval.

l'effort 1P et la phase de l'effort 1P est ici proposée. Tout d'abord, une première simulation "complète" est réalisée dans HOST-MINT. Deuxièmement, les vitesses induites sur chacune des pales des deux rotors sont extraites à chaque instant. En troisième lieu, les vitesses induites sont décomposées en fonction de leur origine : effets d'installation, vitesses auto-induites, vitesses mutuelles, ou encore corrections instationnaires. De plus, les vitesses induites sont décomposées en un terme moyen, un terme en 1/rev et un terme à la fréquence de passage de pale (BPF). Finalement, une simulation est faite pour chacun des huit différents termes identifiés, où à chaque fois leur contribution est enlevée des vitesses induites totales. Ainsi, par comparaison avec la simulation initiale "complète", on peut déterminer la contribution de chacun des huit termes sur les deux rotors. La Fig. D.6 montre la contribution de chacun des termes sur la traction, le module de l'effort 1P et la phase de l'effort 1P.

Cette méthode présente l'avantage de fournir à un coût modéré la sensibilité

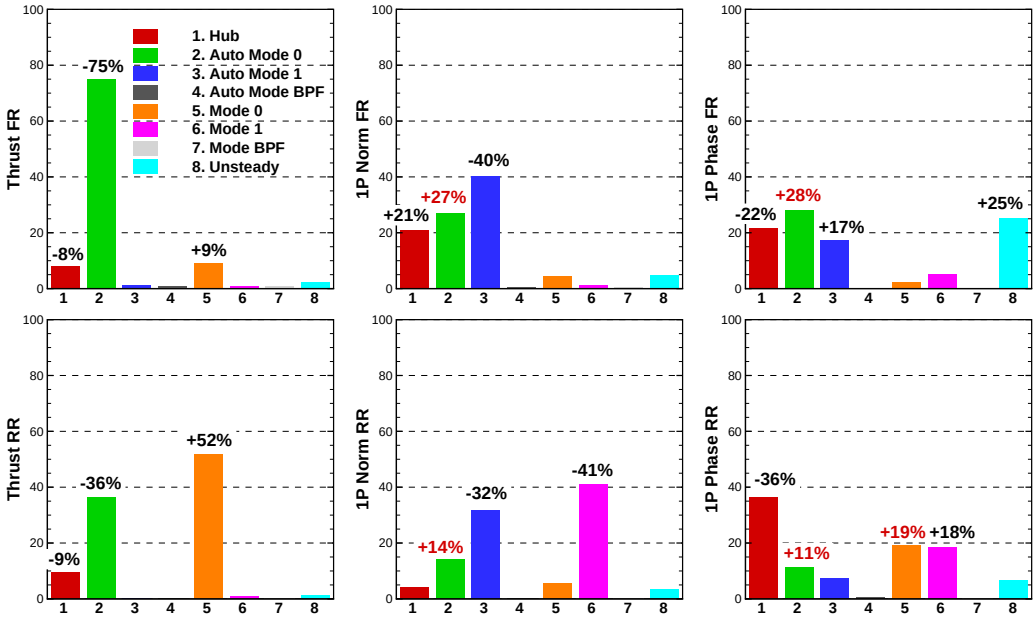


Figure D.6: Contribution des termes de $\vec{v}_{\text{ind}}$ sur la traction, le module de l'effort 1P et la phase de l'effort 1P des rotors amont et aval.

d'une certaine configuration à un paramètre de conception, ou encore de permettre de mieux contrôler l'interaction entre les deux rotors. Ce sont des informations inaccessibles par les méthodes CFD classiques, et très utiles lors de la conception de nouveaux open rotors.

D.6 Développement d'une méthodologie de couplage entre les codes HOST et elsA

La dernière section de la thèse est consacrée au développement d'une méthodologie de couplage entre un code CFD comme *elsA*, pour simuler avec précision l'écoulement proche de la paroi de l'une des pales de chaque rotor, et un code ligne portante comme HOST-MINT, afin de simuler l'effet des autres pales et leurs sillages sur la pale simulée dans *elsA*. La Fig. D.7 montre la stratégie de couplage fort mise en place partiellement pendant ces travaux de thèse. Actuellement, les différentes routines de couplage sont mises en place pour extraire les vitesses induites par les sillages sur un maillage quelconque à chaque instant d'un calcul HOST-MINT. Ces vitesses induites peuvent ensuite être introduites comme conditions limites d'un calcul CFD *elsA* dans un maillage proche-paroi.

La Fig. D.8 montre une comparaison entre un maillage complet et un maillage proche-corps de l'hélice APIAN. Les résultats obtenus avec cette stratégie n'ont pas été satisfaisants et d'autres études doivent être menées pour mieux comprendre l'origine de ces écarts.

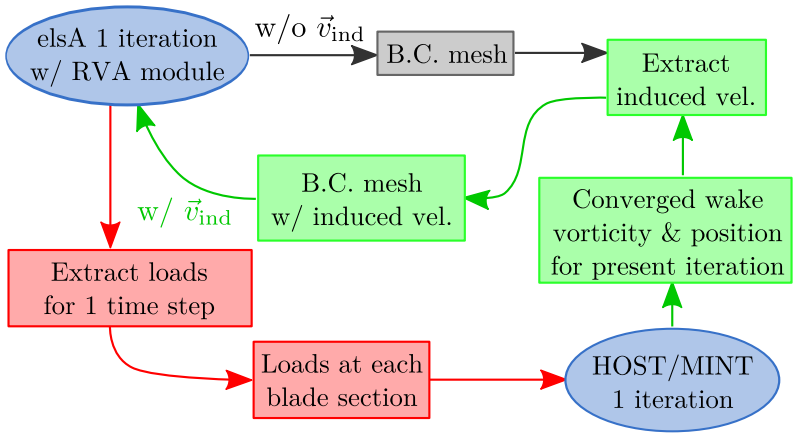
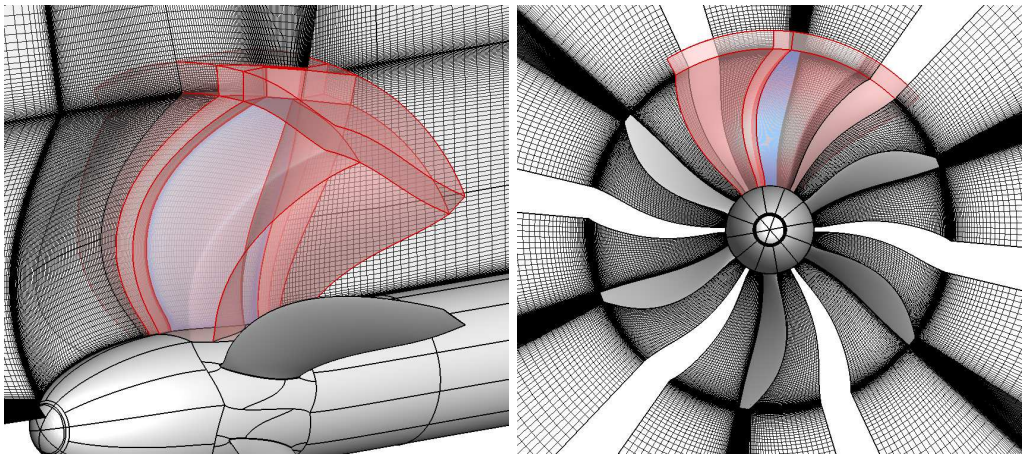


Figure D.7: Stratégie de couplage fort entre les codes HOST-MINT et *elsA*.



(a) Vue latérale. Coupe du maillage dans la direction J.

(b) Vue frontale. Coupe du maillage dans la direction I.

Figure D.8: Coupes du maillage APIAN pour des simulations uRANS dans *elsA*. Le maillage proche-corps (en rouge) utilise la même discrétisation que le maillage complet (en noir).

D.7 Conclusions

Cette thèse a été l'occasion d'approfondir la compréhension des mécanismes à l'origine des efforts dans le plan hélice (efforts 1P), ainsi que l'occasion de développer, tester et valider une méthodologie à coût modéré pour la conception aérodynamique des open rotor.

En outre, cette étude a ouvert un certain nombre de perspectives qui pourront être explorées dans la recherche à venir: (1) Les simulations HOST ont montré des déficiences à l'heure de prédire les charges proche du pied de pale. Il semblerait donc intéressant de développer un modèle de paroi basé sur la méthode des singularités pour améliorer les prédictions dans cette zone de l'écoulement. (2) Le modèle de profil instationnaire implémenté actuellement néglige la singularité des intégrales due à la composante radiale de la circulation sur le sillage. Une régularisation plus rigoureuse du sillage pourrait fournir une approche plus stable dans les simulations HOST-MINT. (3) Afin de réduire le temps de calcul lié principalement à la déformation du sillage, l'Onera étudie les méthodes fast-multipole, promettant des gains importants dans le temps de calcul. (4) Les études futures devraient aussi envisager de finir l'implémentation du couplage entre les codes HOST-MINT et *elsA* pour la simulation des hélices et des open rotors. (5) Étendre l'utilisation de HOST-MINT pour des applications avec une prise en compte de la souplesse de pale ou encore pour des simulations aéro-acoustiques.

Bibliography

[Adamczyk 1986] J. J. Adamczyk, R. A. Mulac, and M. L. Celestina. *A Model for Closing the Inviscid Form of the Average-Passage Equation System.* Journal of Turbomachinery, vol. 108, no. 2, October 1986. (Cited in page 26.)

[Adv 2001] Advisory Council for Aeronautics Research in Europe. *European Aeronautics: A Vision for 2020*, 2001. (Cited in page 10.)

[Adv 2004] Advisory Council for Aeronautics Research in Europe. *Strategic Research Agenda*, October 2004. (Cited in page 10.)

[Ahmadi 1985] A.R. Ahmadi, and S.E. Widnall. *Unsteady Lifting-Line Theory as a Singular Perturbation Problem.* Journal of Fluid Mechanics, vol. 153, 1985. (Cited in page 44.)

[Altmikus 2002] A.R.M. Altmikus, S. Wagner, P. Beaumier, and G. Servera. *A Comparison: Weak versus Strong Modular Coupling for Trimmed Aeroelastic Rotor Simulations.* In AHS 58th Annual Forum, Montreal, Quebec, June 2002. American Helicopter Society. (Cited in pages 29 and 30.)

[Amato 2000] M. Amato, M.A. Averardo, J.A. Eaton, F.J. Boyle, F. de Gregorio, J. Kompenhans, P. Gardarein, J.A. Hernanz Manrique, J.I. Oquillas Teresa, L.G.M. Custers, and A.. Elsenaar. *Wind Tunnel Tests and CFD Predictions of the Flow-Field of a High-Speed Six-Bladed Propeller in Steady and Unsteady Conditions.* In Workshop on EU-Research on Aerodynamic Engine/Aircraft Integration for Transport Aircraft, 2000. (Cited in page 69.)

[Anderson 2001] John D. Anderson. Fundamentals od aerodynamics. McGraw-Hill, 3rd edition, 2001. (Cited in pages 5 and 40.)

[Ashley 1985] Holt Ashley, and Marten Landahl. Aerodynamics of wings and bodies. Dover Publications, 1985. (Cited in page 40.)

[Averardo 2000] Michele A. Averardo. *Numerical / Experimental Aerodynamic Analysis of the APIAN Isolated Propeller Configuration.* Technical Report 65/NT/N361B/00-0015, Alenia Aeronautica, November 2000. (Cited in page 69.)

[Bairstow 1939] Leonard Bairstow. Applied aerodynamics. Longmans, 2nd edition, 1939. (Cited in page 23.)

[Barrie 2007] D. Barrie. *Open Rotor Poses Maturity Dilemma for Next-Gen Narrow Body.* In Aviation Week. Aviation Week, October 21 2007. (Cited in page 13.)

[Barth 2012] Marcus Barth, and Benoît Calmels. *Aerodynamics of Counter-Rotating Open Rotors at High Speed.* In 30th AIAA Applied Aerodynamics Conference, number 2012-2786, June 2012. (Cited in pages 16 and 227.)

[Barton 1986] J.M. Barton, and S.K. Yoon. *Finite Difference Solution of the 3-D Euler Equations using a Multistage Runge-Kutta Method.* Lecture Notes in Physics, vol. 264, 1986. (Cited in page 26.)

[Beaumier 1994] Philippe Beaumier. *A Coupling Procedure Between a Rotor Dynamics Code and a 3D Unsteady Full Potential Code.* In AHS 3rd Decennial Specialists' Conference on Aeromechanics, San Francisco, CA, January 1994. (Cited in page 29.)

[Béchet 2011] S. Béchet, C.A. Negulescu, V. Chapin, and F. Simon. *Integration of CFD Tools for the Aerodynamic Design of Contra-Rotating Propeller Blades.* In 3rd CEAS Air & Space Conference. Airbus Operations S.A.S., 2011. (Cited in page 70.)

[Ben Nasr 2013] N. Ben Nasr, B. Ortun, A. Chelius, and S. Canard-Caruana. *Assessment of Advanced Grid Strategies for CFD on Open-Rotor Applications.* In 49th AIAA/ASME/SAE/ASEE Joint Propulsion Conference, number AIAA-2013-3800, San Jose, CA, USA, July 14-17 2013. American Institute of Aeronautics and Astronautics. (Cited in page 70.)

[Benoit 2000] Bernard Benoit, Konstantin Kampa, André-Michel Dequin, Wolfgang Grunhagen, Pierre-Marie Basset, and Bernard Gimonet. *HOST, a General Helicopter Simulation Tool for Germany and France.* In 56th Annual Forum, Virginia Beach, May 2000. American Helicopter Society. (Cited in page 56.)

[Berkman 1997] Mert E. Berkman, Lakshmi N. Sankar, Charles R. Berezin, and Michael S. Torok. *A Navier-Stokes/Full Potential/Free Wake Method for Advancing Multi-Bladed Rotors.* In American Helicopter Society 53rd Annual Forum, Virginia, May 1997. (Cited in page 29.)

[Betz 1927] Albert Betz, and Ludwig Prandtl. Vier abhandlungen zur hydrodynamik und aerodynamik. Universitätsverlag Göttingen, 1927. (Cited in page 23.)

[Block 1984] Patricia J.W. Block. *The Effects of Installation on Single- and Counter-Rotation Propeller Noise.* In AIAA/NASA 9th Aeroacoustics Conference, number AIAA-84-2263, Williamsbourg, VA, October 1984. NASA Langley Research Center. (Cited in pages 13 and 15.)

[Bober 1983] L. J. Bober, D. S. Chaussee, and P. Kutler. *Prediction of High-Speed Propeller Flow FIelds Using a Three-Dimensional Euler Analysis.* In 21st AIAA Aerospace Science Conference, number 83-0188, Reno, Nevada, January 1983. NASA Lewis Research Center. (NASA TM-83065). (Cited in page 26.)

[Boisard 2012] Ronan Boisard, Fabrice Falissard, and Gregory Delattre. *HPC Capabilities of the elsA CFD Software Applied to a Counter Rotating Open Rotor Test Rig.* In 3AF, editor, 47th Symposium of Applied Aerodynamics, Paris, March 2012. (Cited in pages 15 and 28.)

[Borst 1981] Henry V. Borst. *Propeller Performance and Design as Influenced by the Installation.* In Business Aircraft Meeting & Exposition, number 810602, Wichita, Kansas, April 1981. Society of Automotive Engineers, INC. Introduction: for doing a parallel between states-of-art in 1980's and 2010's Ref 7: McCormick's panel method to model bodies around the propellers. Fig 8: interesting to illustrate the increase in efficiency due to propeller installation. Ref 6: design procedures. (Cited in page 13.)

[Bousman 1999] W.G. Bousman. *Putting the Aero Back into Aeroelasticity.* In 8th ARO Workshop on Aeroelasticity of Rotorcraft Systems, University Park, PA, October 1999. (Cited in page 28.)

[Bousquet 1985] Jean-Marc Bousquet. *Aerodynamic Methods Used in France for Designing Advanced High-Speed Propellers.* La Recherche Aérospatiale, vol. 1, 1985. (Cited in pages 7 and 81.)

[Bousquet 1986] Jean-Marc Bousquet. *Theoretical and Experimental Analysis of Highspeed Propeller Aerodynamics.* In AIAA/SAE/ASME 22nd Joint Propulsion Conference, Hunstville, Alabama, Juin 1986. Onera – The French Aerospace Lab, American Institute of Aeronautics and Astronautics. (Cited in page 7.)

[Bousquet 2000] Jean-Marc Bousquet, and Patrick Gardarein. *Recent improvements in Propeller Aerodynamic Computations.* In 18th AIAA Applied Aerodynamics Conference, number 4124. American Institute of Aeronautics and Astronautics, 2000. (Cited in pages 27 and 69.)

[Bousquet 2003] Jean-Marc Bousquet, and Patrick Gardarein. *Improvements on Computations of High Speed Propeller Unsteady Aerodynamics.* Aerospace Science and Technology, vol. 7, 2003. (Cited in pages 27, 69 and 91.)

[Boyd 2009] David D. Boyd. *HART-II Acoustic Predictions using a Coupled CFD/CSD Method.* In AHS 65th Annual Forum, Grapevine, TX, May 2009. American Helicopter Society. (Cited in page 28.)

[Boyle 1999] F.J. Boyle, M.P.O. Flaherty, and J.A. Eaton. *Validation of Efficient Euler Algorithms for Advanced Propellers Under Transonic and Subsonic Conditions.* In 17th AIAA Applied Aerodynamics Conference, number 99-3228, Norfolk, VA, June-July 1999. Aerospace Research Center, National University of Ireland, American Institute of Aeronautics and Astronautics. (Cited in page 69.)

[Butterworth-Hayes 2010] Philip Butterworth-Hayes. *Open Rotor Research Revs Up.* Aerospace America, vol. 48, no. 3, March 2010. (Cited in page 12.)

[Cambier 2008] Laurent Cambier, and Jean-Pierre Veuillot. *Status of the elsA CFD Software for Flow Simulation and Multidisciplinary Applications.* In 46th AIAA Aerospace Sciences Meeting and Exhibit, number 2008-664, Reno, Nevada, USA, January 2008. (Cited in pages 17 and 78.)

[Caradonna 1978] François-Xavier Caradonna, and Jean-Jacques Philippe. *The flow over a helicopter blade tip in the transonic regime.* Vertica, vol. 2, 1978. (Cited in page 21.)

[Castillon 2012] Lionel Castillon. *Evaluation of a Multiple Frequency Phase Lagged Method for Unsteady Numerical Simulations of Multistage Turbomachinery.* In 28th International Congress of the Aeronautical Sciences, 2012. (Cited in page 53.)

[Celestina 1986] M. L. Celestina, R. A. Mulac, and J. J. Adamczyk. *A Numerical Simulation of the Inviscid Flow Through a Counterrotating Propeller.* In 31st ASME International Gas Turbine Conference and Exhibit, number 86-GT-138, 1986. (Cited in page 26.)

[Chassaing 2000] Patrick Chassaing. Mécanique des fluides : Éléments d'un premier parcours. Institut National Polytechnique de Toulouse, 2000. (Cited in page 38.)

[Chattot 1980] Jean-Jacques Chattot, and Jean-Jacques Philippe. *Pressure distribution computation on a non-lifting symmetrical helicopter blade in forward flight.* La Recherche Aérospatiale, vol. 5, 1980. (Cited in page 21.)

[Cheng 1976] H.K. Cheng. *On Lifting-Line Theory in Unsteady Aerodynamics.* Technical Report 133, USCAE Department of Aeronautical Engineering, 1976. (Cited in page 44.)

[Cheng 1978] H.K. Cheng. *Lifting-Line Theory of Oblique Wings.* AIAA Journal, vol. 16, 1978. (Cited in page 44.)

[Cheng 1984] H.K. Cheng, and L.E. Murillo. *Lunate-Tail Swimming Propulsion as a Problem of Curved Lifting-Line in Unsteady Flow.* Journal of Fluid Mechanics, vol. 143, 1984. (Cited in page 44.)

[Clark 1913] T. W. K. Clark. *Effect of Side Wind on a Propeller.* Reports and Memoranda 80, British A. C. A., 1913. (Cited in page 17.)

[Colin 2012] Yann Colin, Florian Blanc, Bastien Caruelle, Frédéric Barrois, and N. Djordjevic. *Computational Strategy for Predicting CROR Noise at Low-speed, Part II: Investigation of the Noise Sources Computation with the Chorochronic Approach.* In 18th AIAA/CEAS Aeroacoustic Conference, number AIAA Paper 2012-2222, 2012. (Cited in page 70.)

[Collercandy 1984] Ranjit Collercandy. *Etude et Calcul Théorique d'écoulements transsoniques autour d'une hélice propulsive du type Prop-Fan.* PhD thesis, Université Pierre et Marie Curie, Paris, France, July 1984. (Cited in page 26.)

[Conlisk 2001] A.T. Conlisk. *Modern Helicopter Rotor Aerodynamics.* Progress in Aerospace Sciences, vol. 37, 2001. (Cited in page 58.)

[Conway 1995] John T. Conway. *Analytical Solutions for the Actuator Disk with Variable Radial Distribution of Load.* Journal of Fluid Mechanics, vol. 297, 1995. (Cited in page 22.)

[Conway 1998] John T. Conway. *Exact actuator disk solutions for non-uniform heavy loading and slipstream contraction.* Journal of Fluid Mechanics, vol. 365, 1998. (Cited in page 22.)

[Costes 2012] Michel Costes, Thomas Renaud, Benoit Rodriguez, and Gabriel Reboul. *Application of Vorticity Confinement to Rotor Wake Simulations.* International Journal of Engineering Systems Modelling and Simulation, vol. 4, no. 1-2, January 2012. (Cited in page 28.)

[Crozier 1999] P. Crozier. *Test on isolated APIAN propellers at 1/8 scale in S1MA wind tunnel.* Technical Report PV 1/8106 DSMA/Y, Office National d'Etudes et de Recherches Aérospatiales, Châtillon, France, November 1999. (Cited in pages 69 and 70.)

[Crozier 2001] P. Crozier. *APIAN Installed Tests in the ONERA S1MA Wind Tunnel.* In 39th Aerospace Sciences Meeting and Exhibit, number 2001-0580, Reno, NV, January 2001. American Institute of Aeronautics and Astronautics. (Cited in page 69.)

[Custers 1999] L.G.M. Custers, and A. Elsenaar. *Test Report of the APIAN Wind Tunnel Test in the DNW-HST.* Technical Report NLR-CR-98571, National Aerospace Laboratory NLR, Amsterdam, The Netherlands, March 1999. (Cited in page 69.)

[Czech 2013] Michael J. Czech, and Russell H. Thomas. *Open Rotor Aeroacoustic Installation Effects for Conventional and Unconventional Airframes.* In 19th AIAA/CEAS Aeroacoustics Conference, number AIAA-2013-2185, Berlin, Germany, May 2013. The Boeing Company. (Cited in pages 11 and 15.)

[Datta 2004] A. Datta, J. Sitaraman, I. Chopra, and J. Baeder. *Improved Comprehensive Analysis for Prediction of Rotor Vibratory Loads in High-Speed Forward Flight.* In AHS 60th Annual Forum, Baltimore, MD, June 2004. American Helicopter Society. (Cited in page 29.)

[Delamore-Sutcliffe 2006] D. W. Delamore-Sutcliffe, and D. I. Greenwell. *A Model for Fast Prediction of Propeller Stall Flutter.* In 24th AIAA Applied Aerodynamics Conference, number AIAA Paper 2006-3477, 2006. (Cited in page 24.)

[Denton 1979] J.D. Denton, and U. Singh. *Time Marching Methods for Turbomachinery Flow Calculation.* In VKI Lecture Series. Von Karman Institute, 1979. (Cited in page 52.)

[Denton 1980] J.D. Denton. Numerical methods in fluid dynamics. Academic Press, New York, 1980. (Cited in page 26.)

[Devinant 1998] Philippe Devinant. *An Approach for Unsteady Lifting-Line Time-Marching Numerical Computation.* International Journal for Numerical Methods in Fluids, vol. 26, 1998. (Cited in pages 47, 61 and 103.)

[Devinant 1999] Philippe Devinant, Annie Leroy-Chesneau, and Michel Mudry. *Unsteady 3D Nonlinear Kutta-Joukowski Condition for Thin Lifting Surfaces.* Computation Mechanics, vol. 24, 1999. (Cited in pages 47, 101, 124 and 199.)

[Devinant 2002] Philippe. Devinant, and Thierry Gallois. *Swept and curved wings: a numerical approach based on generalized lifting-line theory.* Journal of Computational Mechanics, vol. 1, 2002. (Cited in page 63.)

[Dietz 2007] Markus Dietz, Manuel Kessler, Edwald Krämer, and Siegfried Wagner. *Tip Vortex Conservation on a Helicopter Main Rotor Using Vortex-Adapted Chimera Grids.* AIAA Journal, vol. 45, no. 8, August 2007. (Cited in page 28.)

[Donelson 1988] John E. Donelson, William T. Lewerenz, and Roger T. Durbin. *UHB Technology Validation – The Final Step.* In AIAA/SAE/ASME/ASEE 24th Joint Propulsion Conference, number 88-2807, Boston, MA, 1988. (Cited in page 14.)

[Dron 2008] Sébastien Dron. *Toward ACARE 2020: Innovative Engine Architectures to Achieve the Environmental Goals?* In 26th International Congress of the Aeronautical Sciences, 2008. (Cited in page 12.)

[Dumas 1998] Alain Dumas, and Claude Castan. *Aerodynamic Integration of High Speed Propeller on Aircraft. Recent Investigations in European Wind Tunnels.* In 21st ICAS Congress, number A98-31661, Melbourne, Australia, September 1998. Aerospatiale, Aircraft Business, International Council of Aeronautical Sciences. (Cited in page 69.)

[Egolf 1979] T.A. Egolf, O.L. Anderson, D.E. Edwards, and A.J. Landgrebe. *An Analysis for High Speed Propeller-Nacelle Aerodynamic Performance Prediction Theory and Initial Application.* NASA Contract NAS3-20961, United Technologies Research Center, 1979. (Cited in page 26.)

[Erdos 1977] J.I. Erdos, E. Alzner, and W. McNally. *Numerical Solution of Periodic Transonic Flow through a Fan Stage.* AIAA Journal, vol. 11, no. 11, November 1977. (Cited in page 52.)

[Euvrard 1984] Daniel Euvrard. Résolution numérique des Équations aux dérivées partielles. Jean-Claude Masson, 1984. (Cited in page 60.)

[Falkner 1943] V.M. Falkner. *The Calculation of Aerodynamic Loading on Surfaces of any Shape.* Reports and Memoranda 1910, Aeronautical Research Committee, August 1943. (Cited in page 25.)

[François 2011] Benjamin François, Michel Costes, and Guillaume Dufour. *Comparison of Chimera and Sliding Mesh Techniques for Unsteady Simulations of Counter Rotating Open Rotors.* In 20th ISABE Conference, 2011. (Cited in pages 54 and 70.)

[François 2013a] Benjamin François. *Unsteady Aerodynamic Simulations of Contra-Rotating Open-Rotors: Investigation of Efficient CFD Methods, Prediction and Understanding of In-Plan Loads.* PhD thesis, UniversitéPierre et Marie Curie, 2013. (Cited in page 54.)

[François 2013b] Benjamin François, Martin Laban, Michel Costes, Guillaume Dufour, and Jean-François Boussuge. *In-plane Forces Prediction and Analysis in High-speed Conditions on a Contra-rotating Open Rotor.* Journal of Turbomachinery, 2013. (Article submitted). (Cited in pages 27, 136 and 147.)

[Froude 1878] R. Froude. *On the Elementary Relation between Pitch, Slip and Propulsive Efficiency.* Transactions of the Institute of Naval Architects, vol. 19, 1878. (Cited in page 22.)

[Froude 1889] R. Froude. *On the Part Played in Propulsion by Difference in Fluid Pressure.* Transactions of the Institute of Naval Architects, vol. 30, 1889. (Cited in page 22.)

[Gallois 2003] Thierry Gallois, and Philippe Devinant. *Une Méthode De Calcul pour la Ligne Portante Instationnaire Courbe et en Flèche.* In 16ème Congrès Français de Mécanique, 2003. (Cited in pages 47, 63, 183 and 184.)

[Gardarein 1991] Patrick Gardarein. *Calculs Aérodynamiques des Hélices Rapides Transsoniques.* In 28ème Colloque d'Aérodynamique Appliquée, Saint Louis, France, October 1991. (Cited in page 81.)

[Gear 1966] C. W. Gear. *The Numerical Integration of Ordinary Differential Equations of Various Orders.* Technical Report 7126, Argonne National Laboratory, 1966. (Cited in page 79.)

[Giauque 2012] A. Giauque, B. Ortun, B. Rodriguez, and B. Caruelle. *Numerical Error Analysis with Application to Transonic Propeller Aeroeacoustics.* Journal of Computers & Fluids, vol. 69, 2012. (Cited in page 70.)

[Glauert 1922] H. Glauert. *An Aerodynamic Theory of the Airscrew.* Reports and Memoranda 786, Aeronautical Research Comitee, Great Britain, 1922. (Cited in page 22.)

[Glauert 1935] H. Glauert. Airplane propellers. miscellaneous airscrew problems, volume IV of Aerodynamic Theory. Julius Springer, Berlin, 1935. (Cited in page 23.)

[Goldstein 1929] Sydney Goldstein. *On the Vortex Theory of Screw Propellers.* In Royal Society A, number 123, 1929. (Cited in page 23.)

[Groeneweg 1988] John F. Groeneweg, and Lawrence J. Bober. *NASA Advanced Propeller Research.* Technical Memorandum 101361, NASA Lewis Research Center, Cleveland, Ohio, September 1988. (Cited in page 26.)

[Guermond 1990] Jean-Luc Guermond. *A generalized lifting-line theory for curved and swept wings.* Journal of Fluid Mechanics, vol. 211, 1990. (Cited in pages 45, 103, 122, 185 and 200.)

[Guermond 1991] Jean-Luc Guermond, and Antoine Sellier. *A unified unsteady lifting-line theory.* Journal of Fluid Mechanics, vol. 229, 1991. (Cited in pages 4, 45, 46, 47, 59, 101, 118, 121, 199 and 227.)

[Hadamard 1932] Jacques Hadamard. Le problème de cauchy et les équations aux dérivées partielles linéaires hyperboliques. University of Yale, 1932. (Cited in pages 4, 45 and 184.)

[Hager 1988] Roy D. Hager, and Deborah Vrabel. *Advanced Turboprop Project.* NASA-SP 495, NASA Glenn Research Center, 1988. (Cited in pages 1, 6, 7, 11, 14 and 227.)

[Hall 1987] Kenneth C. Hall. *A Linearized Euler Analysis of Unsteady Flows in Turbomachinery.* PhD thesis, Massachussets Institute of Technology, 1987. (Cited in page 53.)

[Harris 1918] R. G. Harris. *Forces on a Propeller Due to Sideslip.* Reports and Memoranda 427, British A. C. A., 1918. (Cited in page 23.)

[Harris 1987] Robert W. Harris, and R.D. Cuthbertson. *UDF^{TM}/727 Flight Test Program*, 1987. (Cited in page 7.)

[He 1992] L. He. *Method for Simulating Unsteady Turbomachinery Flows with Multiple Perturbations.* AIAA Journal, vol. 30, no. 11, November 1992. (Cited in page 52.)

[Heidelberg 1986] L.J. Heidelberg, and B.J. Clark. *Preliminary Results of Unsteady Blade Surface Pressure Measurements for the SR-3 Propeller.* Technical Report AIAA-86-1893, National Aeronautics and Space Administration, Cleveland, Ohio, 1986. (Cited in page 26.)

[Hendricks 2013] Eric S. Hendricks, Jeffrey J. Berton, William J. Haller, and Michael T. Tong. *Updated Assessment of an Open Rotor Airplane using*

Advanced Blade Designs. In 49th AIAA/ASME/SAE/ASEE Joint Propulsion Conference, number 2013-3628, San Jose, CA, July 2013. NASA Glenn Research Center. (Cited in page 15.)

[Hess 1972] John L. Hess. *Calculation of Potential Flow About Arbitrary Three-Dimensional Lifting Bodies.* Final Technical Report J5679/01, McDonnell Douglas Corporation, Long Beach, CA, October 1972. (Cited in pages 37, 105 and 111.)

[Hess 1990] J.L. Hess. *Panel Methods in Computational Fluid Dynamics.* Annual Review of Fluid Mechanics, vol. 22, no. 1, 1990. (Cited in page 25.)

[Hoffer 2012] P.-A. Hoffer, T. Deconinck, Ch. Hirsch, B. Ortun, S. Canard-Caruana, G. Rahier, S. Pascal, and B. Caruelle. *Aeroacoustic Computations of Contra-Rotating Open Rotors Using the Nonlinear Harmonic Method and a Chorochronic Approach.* In ASME Turbo Expo 2012: Turbine Technical Conference and Exposition, number GT2012-68982, Copenhagen, Denmark, June 11-15 2012. ASME. (Cited in page 54.)

[Iosilevskii 1999] Iosilevskii Ya. A. Iosilevskii G., and A. Rosen. *Asymptotic Aerodynamic Theory of Oscillating Rotary Wings in Axial Flight.* SIAM Journal on Applied Mathematics, vol. 59, no. 4, 1999. (Cited in page 24.)

[James 1975] E.C. James. *Lifting-Line Theory for an Unsteady Wing as a Singular Perturbation Problem.* Journal of Fluid Mechanics, vol. 70, 1975. (Cited in page 44.)

[Jameson 1991] A. Jameson. *Time Dependent Calculations Using Multigrid, with Applications to Unsteady Flows Past Airfoils and Wings.* In AIAA 10th Computational Fluid Dynamics Conference, number 1596, Honolulu, HI, June 1991. Princeton University. (Cited in page 79.)

[Jarrah 1989] Mohammad-Ameen M. Jarrah. *Low-Speed Wind-Tunnel Investigations of Flow About Delta Wings, Oscillating in Pitch to Very High Angle of Attack.* In 27th AIAA Aerospace Sciences Meeting, number AIAA 89-0295, Reno, NV, January 1989. (Cited in pages 19, 20 and 227.)

[Jeracki 1981] R. Jeracki, and G. Mitchell. *Low and High Speed Propellers for General Aviation – Performance Potential and Recent Wind Tunnel Test Results.* Technical Memorandum TM-81745, NASA Lewis Research Center, April 1981. (Cited in pages 6 and 227.)

[Jobard 1996] N. Jobard, M. Costes, and P. Beaumier. *Three-Dimensional BVI Simulation on Aeroelastic Blades Using a New Deforming Grid Approach Coupled to a Free-Wake Analysis.* In AHS 52nd Annual Forum, Washington, June 1996. American Helicopter Society. (Cited in page 29.)

[Johnson 1980] Wayne Johnson. Helicopter theory. Dover Publications, 1980. (Cited in page 58.)

[Johnson 1998] Wayne Johnson. *Rotorcraft Aerodynamics Models for a Comprehensive Analysis.* In 54th AHS Annual Forum. American Helicopter Society, May 1998. (Cited in page 51.)

[Jones 1945] Robert T. Jones. *Wing plan forms for high-speed flight.* Technical Report 863, NASA Langley Research Center, June 1945. (Cited in pages 57, 80 and 187.)

[Jones 1976] W. P. Jones, and J. A. Moore. *Aerodynamic Theory for a Cascade of Oscillating Airfoils in Subsonic Flow.* AIAA Journal, vol. 14, no. 5, May 1976. (Cited in page 24.)

[Jou 1982] W.H. Jou. *Finite Volume Calculation of Three-Dimensional Potential Flow Around a Propeller.* In AIAA Paper, number 82-0957, June 1982. (Cited in page 26.)

[Katz 2001] Joseph Katz, and Allen Plotkin. Low-speed aerodynamics. Cambridge Aerospace Series. Cambridge University Press, U.K., 2nd edition, 2001. (Cited in pages 40 and 117.)

[Khalid 2013] S. Arif Khalid, John P. Wojno, Andy Breeze-Stringfellow, David P. Lurie, Trevor H. Wood, Kishore Ramakrishnan, and Umesh Paliath. *Open Rotor Designs for Low Noise and High Efficiency.* In ASME Turbo Expo 2013: Turbine Technical Conference and Exposition, number GT2013-94736, San Antonio, TX, June 2013. General Electric, ASME. (Cited in page 15.)

[Kida 1978] T. Kida, and Y. Miyai. *An Alternative Treatment of Lifting-Line Theory as a Perturbation Problem.* Journal of Applied Mathematics and Physics, vol. 29, no. 4, 1978. (Cited in page 45.)

[Kim 1991] K.-C. Kim, A. Desopper, and I. Chopra. *Blade Response Calculations Using Three-Dimensional Aerodynamic Modeling.* Journal of the American Helicopter Society, vol. 36, no. 1, January 1991. (Cited in page 29.)

[Kok 2000] J. C. Kok. *Resolving the Dependence on Freestream Values for k-ω turbulence model.* AIAA Journal, vol. 7, no. 38, 2000. (Cited in page 79.)

[Kruppa 2004] Nikolaj Kruppa. Unsteady aerodynamics in an aeroelastic rotorcraft simulation tool. Master's thesis, Department of Mechanical Engineering Technical University of Denmark and Eurocopter SAS, France, 2004. (Cited in page 63.)

[Laban 2010] M. Laban, J. C. Kok, and B. B. Prananta. *Numerical Tools for Contra-Rotating Open-Rotor Performance, Noise and Vibration Assessment.* In 27th International Congress of the Aeronautical Sciences, 2010. (Cited in page 27.)

[Lanchester 1907] Frederic William Lanchester. Aerial flight: Aerodynamics. Constable & Co. Ltd., London, 1907. (Cited in page 41.)

[Lanchester 1917] Frederick William Lanchester. The flying-machine from an engineering standpoint. Kessinger Publishing, London, 1917. (Cited in pages 17 and 23.)

[Le Bouar-Coppens 1999] Gaëlle Le Bouar-Coppens. *Méthode pas à pas en temps pour l'aérodynamique instationnaire des rotors d'hélicoptère.* PhD thesis, Université d'Orléans, October 1999. (Cited in pages 58, 59, 60, 62 and 103.)

[Le Bouar-Coppens 2004] Gaëlle Le Bouar-Coppens, Michel Costes, Annie Leroy-Chesneau, and Philippe Devinant. *Numerical simulations of unsteady aerodynamics of helicopter rotor in manoeuvring flight conditions.* Aerospace Science and Technology, vol. 8, 2004. (Cited in pages 28, 51 and 59.)

[Leishman 1989] J.G. Leishman, and T.S. Beddoes. *A Semi-Empirical Model for Dynamic Stall.* Journal of the American Helicopter Society, vol. 34, no. 3, July 1989. (Cited in page 19.)

[Leishman 2006] J. G. Leishman. Principles of helicopter aerodynamics. Cambridge Aerospace Series. Cambridge University Press, 2nd edition, 2006. (Cited in pages 20 and 227.)

[Lesieutre 1985] D. J. Lesieutre, and J. P. Sullivan. *The Analysis of Counter-Rotating Propeller Systems.* SAE Paper 850869, Society of Automotive Engineers, April 1985. (Cited in page 26.)

[Lock 1945] C. N. H. Lock, R. C. Pankhurst, and J. F. C. Conn. *Strip Theory Method of Calculation for Airscrews on High-Speed Aeroplanes.* Reports and Memoranda 2035, British A. C. A., 1945. (Cited in page 23.)

[Loewy 1957] Robert G. Loewy. *A Two-Dimensional Approximation to the Unsteady Aerodynamics of Rotary Wings.* Journal of the Aeronautical Sciences, vol. 24, no. 2, February 1957. (Cited in page 24.)

[Luu 1984] Thoai-Sum Luu, and Ranjit Collercandy. *Design Concept and Performance Prediction Technique for Potential Flows Around Advanced Propellers.* In AGARD Conference Proceedings. Aerodynamics and Acoustics of Propellers, number AGARD-CP-366, Toronto, Canada, October 1984. LIMSI, Advisory Group for Aerospace Research and Development. (Cited in page 26.)

[Malard 2005] L. Malard, J.M. Bousquet, O. Atinault, J.L. Larcher, and J.F. Sechaud. *High Speed Testing and CFD Investigations for the New Generation Military Transport Aircraft Development.* In 35th AIAA Fluid Dynamics Conference and Exhibit, number AIAA 2005-4744, Toronto, Canada,

June 2005. Airbus Operations S.A.S., American Institute of Aeronautics and Astronautics. (Cited in page 8.)

[Meijer-Drees 1949] J. Meijer-Drees. *A theory of inflow through rotors and its application to some helicopter problems.* Journal of the Helicopter Association of Great Britain, vol. 3, no. 2, September 1949. (Cited in page 57.)

[Michéa 1992a] B. Michéa, A. Desopper, and M. Costes. *Method with Free Rotor Wake for Low Speed Descent Flights.* In 18th European Rotorcraft Forum, number 66, Avignon, September 1992. (Cited in pages 51 and 58.)

[Michéa 1992b] Bertrand Michéa. *Étude des sillages de rotors d'hélicoptère en vol d'avancement et de leur influence sur les performances du rotor. (Intéraction Pale-Tourbillon).* PhD thesis, Université Pierre et Marie Curie (Paris VI), September 1992. (Cited in page 28.)

[Miller 1964] R. H. Miller. *Rotor blades harmonic air loading.* AIAA Journal, vol. 2, no. 7, July 1964. (Cited in page 24.)

[Min 2010] Byung-Young Min, and Lakshmi N. Sankar. *Hybrid Navier-Stokes/Free-Wake Method for Modeling Blade-Vortex Interactions.* Journal of Aircraft, vol. 47, no. 3, May-June 2010. (Cited in page 29.)

[Misztal 1933] Franz Misztal. *The Problem of the Propeller in Yaw with Special Reference to Airplane Stability.* Technical Memorandum 696, National Advisory Comitee for Aeronautics, 1933. (Cited in page 23.)

[Mudry 1982] Michel Mudry. *La théorie générale des nappes et filaments tourbillonaires et ses applications à l'aérodynamique instationnaire.* PhD thesis, Université Pierre et Marie Curie (Paris VI), July 1982. (Cited in page 59.)

[Muller 2007] Sébastien Muller. *Développement d'une méthode de ligne portante courbe et instationnaire pour l'évaluation aéroacoustique des pales d'hélicoptère de forme non conventionnelle.* PhD thesis, Université d'Orléans, May 2007. (Cited in pages 4, 47, 60, 63, 102, 105, 183, 184 and 199.)

[Murayama 2001] Mitsuhiro Murayama, Kazuhiro Nakahashi, Shigeru Obayashi, and Takuma Kato. *Numerical Simulation of Vortical Flows Using Vorticity Confinement Coupled with Unstructured Adaptive Grid Refinement.* Computational Fluid Dynamics Journal, vol. 10, no. 1, 2001. (Cited in page 28.)

[Nallasamy 1991] Groeneweg J. F. Nallasamy M. *Unsteady Blade-Surface Pressures on a Large-Scale Advanced Propeller: Prediction and Data.* Journal of Propulsion, vol. 7, November-December 1991. (Cited in page 66.)

[Nallasamy 1994] M. Nallasamy. *Unsteady Blade Pressures on a Propfan: Predicted and Measured Compressibility Effects.* Journal of Aircraft, vol. 31, no. 3, May-June 1994. (Cited in page 27.)

[Negulescu 2013] Camil Negulescu. *Airbus AI-PX7 CROR Design Features and Aerodynamics.* SAE International Journal of Aerospace, vol. 6, no. 2, December 2013. (Cited in page 70.)

[Nichols 1988] Herbert E. Nichols. *UDF Engine/MD-80 Flight Test Program.* In AIAA/SAE/ASME/ASEE 24th Joint Propulsion Conference, number 88-2805, Boston, MA, 1988. (Cited in page 14.)

[Nicoud 1989] D. Nicoud, J. Brochet, and M. Goutines. *A Methodology Proposal to Design and Analyse Counterrotating High Speed Propellers.* In ASME Paper, number 89-GT-38, 1989. (Cited in page 26.)

[Norris 2007] G. Norris. *Pratt & Whitney's Geared Turbofan Moves Closer to Launch with Mitsubishi RJ Selection.* In Aviation Week. Aviation Week, October 15 2007. (Cited in page 12.)

[Num 2004] Numeca, Brussels, Belgium. *AutoGrid v.5.1 User Manual*, December 2004. (Cited in page 78.)

[Ortun 2012] Biel Ortun, Ronan Boisard, and Ignacio Gonzalez-Martino. *Assessment of Propeller 1P Loads Predictions.* International Journal of Engineering Systems Modelling and Simulation, vol. 4, no. 1-2, 2012. (Cited in pages 19, 27, 70, 79 and 84.)

[Pahlke 2000] K. Pahlke, J. Sidès, and M. Costes. *Towards the CFD Computation of the Complete Helicopter: First Results Obtained by French and German Research Centers.* In Aerospace Science and Technology, Berlin, Germany, June 2000. Second ONERA-DLR Aerospace Symposium. (Cited in page 30.)

[Pahlke 2005] Klausdieter Pahlke. *Chimera Simulations of Multibladed Rotors in High-Speed Forward Flight with Weak Fluid-Structure Coupling.* Aerospace Science and Technology, vol. 9, no. 5, 2005. (Cited in page 30.)

[Peake 2012] Nigel Peake, and Anthony B. Parry. *Modern Challenges Facing Turbomachinery Aeroacoustics.* Annual Review of Fluid Mechanics, vol. 44, 2012. (Cited in page 14.)

[Peters 2010] Andreas Peters. Assessment of propfan propulsion systems for reduced environmental impact. M.sc. in aeronautics and astronautics, Massachusetts Institute of Technology, January 2010. (Cited in page 15.)

[Pistolesi 1928] E. Pistolesi. *Nuove considerasioni sui problema dell'elica in un vento laterale.* L'Aerotecnica, vol. 7, March 1928. (Cited in page 23.)

[Polacsek 2000] C. Polacsek, P. Spiegel, H. Brouwer, R. Nijboer, F. Boyle, and J. Eaton. *Noise Computation of High-Speed Propeller-Driven Aircraft.* In 6th AIAA Aeroacoustics Conference and Exhibit, number A00-31095. American Institute of Aeronautics and Astronautics, June 2000. (Cited in page 69.)

[Pomin 2001] H. Pomin, and S. Wagner. *Aeroelastic Analysis of Helicopter Blades on Deformable Chimera Grids.* In AIAA 40th Aerospace Sciences Meeting and Exhibit, number AIAA Paper 2002-0951, Reno, NV, January 2001. (Cited in page 30.)

[Potsdam 2004] Mark Potsdam, Hyeonsoo Yeo, and Wayne Johnson. *Rotor Airloads Prediction Using Loose Aerodynamic/Structural Coupling.* In American Helicopter Society International, editor, 60th Annual Forum, American Helicopter Society, 2004. (Cited in page 29.)

[Prandtl 1923] Ludwig Prandtl. *Applications of Modern Hydrodynamics to Aeronautics.* Technical Report 116, National Advisory Comitee for Aeronautics, 1923. (Cited in pages 25, 40 and 183.)

[Rankine 1865] W. Rankine. *On the Mechanical Principles of the Action of Propellers.* Transactions of the Institute of Naval Architects, vol. 6, 1865. (Cited in page 22.)

[Reed 1966] Wilmer H. Reed. *Propeller-Rotor Whirl Flutter: A State-of-the-Art Review.* Journal of Sound Vibrations, vol. 4, no. 3, 1966. (Cited in page 24.)

[Renaud 2008] T. Renaud, G. Perez, C. Benoit, and G. Jeanfaivre. *Blade-Vortex Interaction Capture by CFD.* In 34th European Rotorcraft Forum, Liverpool, 2008. (Cited in page 28.)

[Ribner 1945] Herbert S. Ribner. *Propellers in Yaw.* Technical Report NACA-TR-820, National Advisory Comitee for Aeronautics, 1945. (Cited in pages 23 and 24.)

[Rodriguez 2010] Benoit Rodriguez. *Blade Vortex Interaction and Vortex Ring State captured by a fully time marching unsteady wake model coupled with a comprehensive dynamics code.* In Heli Japan, 2010. (Cited in page 55.)

[Rodriguez 2012] Benoit Rodriguez, Ronan Boisard, and J. Mayeur. *Eulerian-Lagrangian Coupling for Helicopter Rotor Aerodynamics.* In European Rotorcraft Forum, 2012. (Cited in pages 30 and 67.)

[Saffman 1992] P.G. Saffman. Vortex dynamics. Cambridge University Press, 1992. (Cited in page 40.)

[Schulten 1996] J. Schulten. *Advanced Propeller Performance Calculation by a Lifting Surface Method.* Journal of Propulsion and Power, vol. 3, May 1996. (Cited in page 25.)

[Sclavounos 1987] P.D. Sclavounos. *An Unsteady Lifting-Line Theory.* Journal of Engineering Mathematics, vol. 21, 1987. (Cited in page 45.)

[Servera 2000] Gaëlle Servera, Philippe Beaumier, and Michel Costes. *A Weak Coupling Method Between the Dynamics Code HOST and the 3D Unsteady Euler Code WAVES*. In 26th European Rotorcraft Forum, The Hague, Netherlands, September 2000. (Cited in page 29.)

[Sicot 2009] Frédéric Sicot. *Simulation Efficace des Écoulements Instationnaires Périodiques en Turbomachines*. PhD thesis, École Centrale de Lyon, 2009. (Cited in page 52.)

[Simpson 1989] M.A. Simpson, P.M. Druez, A.J. Kimbrough, M.P. Brock, P.L. Brugé, G.P. Mathur, M.R. Cannon, and B.N. Tran. *UHB Demonstrator Interior Noise Control Flight Test Analysis*. Contractor Report 181897, National Aeronautical and Space Agency, Long Beach, CA, October 1989. (Cited in page 14.)

[Sitaraman 2003] J. Sitaraman, J. Baeder, and I. Chopra. *Validation of UH-60A Rotor Blade Aerodynamic Characteristics Using CFD*. In AHS 59th Annual Forum, Phoenix, AZ, May 2003. American Helicopter Society. (Cited in page 29.)

[Smith 1985] A. F. Smith. *Analysis and Test Evaluation of the Dynamic Response and Stability of Three Advanced Turboprop Models at Low Forward Speed*. Technical Report NASA CR-175026, National Aeronautics and Space Administration, December 1985. (Cited in page 24.)

[Srivastava 1990] R. Srivastava, N.L. Sankar, T. S. R. Reddy, and D. L. Huff. *Application of an Efficient Hybrid Scheme for Aeroelastic Analysis of Advanced Propellers*. Technical Memorandum 102428, Georgia Institute of Technology, Atlanta, Georgia, January 1990. (Cited in page 21.)

[Strawn 1989] R.C. Strawn, A. Desopper, M. Miller, and A. Jones. *Correlation of PUMA Airloads – Evaluation of CFD Prediction Methods*. In 15th European Rotorcraft Forum, number 14, Amsterdam, Netherlands, September 1989. (Cited in page 29.)

[Strawn 1991] R.C. Strawn, and J.O. Bridgeman. *An Improved Three-Dimensional Aerodynamics Model for Helicopter Airloads Prediction*. In AIAA 29th Aerospace Sciences Meeting and Exhibit, number 91-0767, Reno, NV, January 1991. (Cited in page 29.)

[Stuermer 2008] Arne Stuermer. *Unsteady CFD Simulations of Contra-Rotating Propeller Propulsion Systems*. In 44th AIAA/ASME/SAE/ASEE Joint Propulsion Conference & Exhibit, number 5218, Hartfort, CT, July 2008. (Cited in pages 27 and 70.)

[Stuermer 2009] Arne Stuermer, and J. Yiny. *Low-Speed Aerodynamics and Aeroacoustics of CROR Propulsion Systems*. In 15th AIAA/CEAS Aeroacoustics Conference, number 2009-3134, Miami, FL, May 2009. (Cited in page 15.)

[Stuermer 2011] Arne Stuermer, and Jianping Yin. *Installation Impact on Pusher-CROR Engine Low-Speed Performance and Noise Emission Characteristics.* In 46th Symposium of Applied Aerodynamics. 3AF, 2011. (Cited in page 27.)

[Stuermer 2012] Arne Stuermer, Carlos Marquez-Gutierrez, Eric W. M. Roosenboom, Andreas Schröder, Reinhard Geisler, Dieter Pallek, and Janos Agocs. *Experimental and Numerical Investigation of a Contra Rotating Open-Rotor Flowfield.* Journal of Aircraft, vol. 49, no. 6, November-December 2012. (Cited in page 28.)

[Suder 2012] Kenneth L. Suder. *Overview of the NASA Environmentally Responsible Aviation Project's Propulsion Technology Portfolio.* In 48th AIAA/ASME/SAE/ASEE Joint Propulsion Conference and Exhibit, number AIAA 2012-4038, Atlanta, Georgia, August 2012. NASA Glenn Research Center. (Cited in pages 11 and 15.)

[Sullivan 1977] J.P. Sullivan. *The Effect of Blade Sweep on Propeller Performance.* In AIAA Conference on Fluid and Plasmadynamics, number AIAA-77-716, Albuquerque, NM, June 1977. Purdue University, American Institute of Aeronautics and Astronautics. (Cited in page 5.)

[Theodorsen 1935] Theodore Theodorsen. *General Theory of Aerodynamic Instability and the Mechanism of Flutter.* Technical Report 496, National Advisory Comitee for Aeronautics, 1935. (Cited in pages 24 and 93.)

[Theodorsen 1944] Theodore Theodorsen. *The Theory of Propellers. Determination of the circulation function and the mass coefficient for dual-rotating propellers.* Technical Report 775, National Advisory Commitee for Aeronautics, October 1944. (Cited in page 23.)

[Theodorsen 1945] T. Theodorsen, and A. A. Regier. *Effect of Lift Coefficient on Propeller Flutter.* Technical Report L5F30, National Advisory Committee for Aeronautics, July 1945. (Cited in page 23.)

[Thurber 1965] J.K. Thurber. *An Asymptotic Method for Determining the Lift Distribution of a Swept-Back Wing of Finite Span.* Communication in Pure Applicative Mathematics, vol. 18, 1965. (Cited in page 44.)

[Toulmay 1986] F. Toulmay. *Modèle d'Étude de l'Aérodynamique du Rotor.* Rapport Technique R371.76, Aérospatiale Hélicoptères, Marignane, France, 1986. (Cited in pages 28 and 58.)

[Tung 1984] C. Tung, F.X. Caradonna, and W.R. Johnson. *The Prediction of Transonic Flows on an Advancing Rotor.* In AHS 40th Annual Forum, Arlington, VA, May 1984. American Helicopter Society. (Cited in page 29.)

[Van Dyke 1964] Milton Van Dyke. Perturbation methods in fluid mechanics, volume 8 of *Applied Mathematics and Mechanics*. Academic Press, New York, May 1964. (Cited in pages 42, 101 and 199.)

[Van Holten 1976] Th. Van Holten. *Some Notes on Unsteady Lifting-Line Theory*. Journal of Fluid Mechanics, vol. 77, October 1976. (Cited in page 44.)

[Van Zante 2012] Dale E. Van Zante, and Mark P. Wernet. *Tip Vortex and Wake Characteristics of a Counterrotating Open Rotor*. Technical Memorandum 217713, NASA Glenn Research Center, Cleveland, Ohio, October 2012. (Cited in page 11.)

[Van Zante 2013] Dale E. Van Zante. *The NASA Environmentally Responsible Aviation Project/General Electric Open Rotor Test Campaign*. In 51st AIAA Aerospace Sciences Meeting, number AIAA 2013-0415, Grapevine, TX, 2013. NASA Glenn Research Center. (Cited in page 11.)

[Vernon 1987] D.F. Vernon, and J.P. Hughes. *Aerodynamic Integration of Aft-Mounted UHB Propulsion Systems*. In AIAA/AHS/ASEE Aircraft Design, Systems and Operations Meeting, number 87-2920, St. Louis, MO, September 1987. (Cited in page 14.)

[Vogeley 1951] Arthur W. Vogeley. *Axial-Momentum Theory for Propellers in Compressible Flow*. Technical Note 2164, National Advisory Committee for Aeronautics, Langley Field, VA, July 1951. (Cited in page 22.)

[Von Karman 1938] Th. Von Karman, and W. R. Sears. *Airfoil Theory for Non-Uniform Motion*. Journal of the Aeronautical Sciences, vol. 5, no. 10, August 1938. (Cited in page 62.)

[Wenren 2001] Y. Wenren, M. Fan, W. Dietz, G. Hu, C. Braun, J. Steinhoff, and B. Grossman. *Efficient Eulerian computation of realistic rotorcraft flows using Vorticity Confinement – A survey of recent results*. In Aerospace Sciences Meetings. American Institute of Aeronautics and Astronautics, January 2001. (Cited in page 28.)

[Whitehead 1960] D. S. Whitehead. *Force and Moment Coefficients for Vibrating Airfoils in Cascades*. Reports and Memoranda 3254, Advisory Committee for Aeronautics, February 1960. (Cited in page 24.)

[Whitfield 1987] D. L. Whitfield, T. W. Swafford, R. A. Mulac, D. M. Belk, and J. M. Janus. *Three-dimensional Unsteady Euler Solutions for Propfans and Counter-Rotating Propfans in Transonic Flow*. In 19th AIAA Fluid Dynamics, Plasma Dynamics, and Lasers Conference, 87-1197, Honolulu, HI, June 1987. (Cited in pages 26 and 27.)

[Wong 1988] P. Wong, M. Maina, C. R. Forsey, and A. J. Bocci. *Single and Contra-Rotating High-Speed Propellers: Flow Calculation and Performances Prediction.* In International Counciln of Aeronautical Sciences, number ICAS-88-242, 1988. (Cited in page 26.)

[Yabili 2010] Sacha Yabili. Evaluation of turbomachinery methods for the simulation of counter rotating open rotor. Master's thesis, ISAE-SUPAERO, September 2010. (Cited in page 53.)

[Yamamoto 1986] 0. Yamamoto, J.M. Barton, and L.J. Bober. *Improved Euler Analysis of Advanced Turboprop Flows.* In AIAA Paper, number 86-1521, June 1986. (Cited in page 26.)

[Yoshpe 1996] Rosen A. Yoshpe M., and A. Isser. *The Influence of Unsteady Aerodynamics and Inter-Blade Aerodynamic Coupling on the Blades Responses to Harmonic Variations of Their Pitch Angles.* The Aeronautical Journal, vol. 100, 1996. (Cited in page 24.)

[Zachariadis 2011] A. Zachariadis, and C. A. Hall. *Application of a Navier-stokes Solver to the Study of Open Rotor Aerodynamics.* Journal of Turbomachinery, vol. 133, no. 3, July 2011. (Cited in page 28.)

[Zhao 2012] J. Zhao, and C. He. *Coupled CSD/CFD and Viscous Vortex Particle Method for Rotorcraft Comprehensive Analysis.* In AHS 68th Annual Forum, Fort Worth, TX, 2012. (Cited in pages 28 and 30.)

List of Figures

1 Propeller and open rotor efficiency as estimated by Jeracki [Jeracki 1981] . . . 6
2 Wind tunnel tests during the ATP program [Hager 1988] . . . 7
3 HT3 minimum-body configuration in Onera S1MA transonic wind tunnel facility . . . 8
4 Gemini II full-aircraft model at Onera S1MA transonic wind tunnel facility . . . 9
5 APIAN Full-aircraft model in the low-speed DNW-LLF wind tunnel facility . . . 9
6 Effect of the front rotor induced swirl on rear rotor efficiency . . . 12
7 Longitudinal and lateral stability of an open rotor powered aircraft [Barth 2012] . . . 16
8 Geometrical explanation of 1P loads of a propeller under incidence α 18
9 Blade circulation and in-plane loads along a cycle for a propeller in incidence. *elsA* simulation. . . . 18
10 Comparison of theory and experiment for the lift and pitching moment coefficients in fully attached flow under oscillatory plunge forcing conditions at $M = 0.4$ (in [Leishman 2006]) . . . 20
11 Unsteady lift of a delta wing (in [Jarrah 1989]) . . . 20
12 Vorticity conservation and velocity at point P induced by a vortex segment . . . 32
13 Vortex modeled as the flowfield around a cylindrical core rotating as a rigid body . . . 33
14 The wing and the domain of integration . . . 34
15 Hess equivalence between a surface doublet distribution (right), and a combination of surface vortex distribution and vortex filaments (left). 37
16 The wing and its wake. . . . 38
17 A blade cross-section Σ and its two-dimensional wake Σ_W. . . . 38
18 Different orders in the lifting-line. Constant Γ in each blade section or continuous Γ distribution . . . 41
19 Finite wing problem (left) solved using the Matched Asymptotic Expansions method: infinite-span airfoil (center) and the lifting-line method(right) . . . 43
20 Influence domains in the unified theory [Guermond 1991] . . . 47
21 Different $\vec{v}_{\text{ind}}$ terms in the unified lifting-line theory. . . . 48
22 One channel per row domain with mixing-plane condition in the stage interface. . . . 52
23 Chorochronic or time-space periodicity in two contra-rotating rows . 53
24 Assets and drawbacks of different available simulation tools. . . . 55
25 HOST modules for the simulation of an Open Rotor . . . 57

26 Vortex filament and panel regularization strategies in MINT wake model. . . . 60
27 MINT wake panels, surface vorticity and lifting-line circulation . . . 61
28 HOST-MINT code structure . . . 63
29 Absolute value of the perturbation velocity field for a propeller at high-speed conditions ($M_\infty = 0.7$) and at 3° of incidence . . . 65
30 Two coupled computations: uRANS computation in *elsA* (left) and a lifting-line computation in HOST (right). . . . 67
31 APIAN propeller minimum-body configuration in Onera-S1MA wind tunnel facility . . . 69
32 The generic open rotor configuration AI-PX7 designed by Airbus. . . . 71

1.1 The effect of the number of sections on the blade circulation . . . 74
1.2 The effect of time step on the blade circulation . . . 76
1.3 The effect of wake length on the blade circulation . . . 77
1.4 The effect of wake deformation on the blade circulation . . . 77
1.5 RANS mesh details for *elsA* CFD simulations . . . 79
1.6 Convergence of propeller thrust for the Case No. 1149 . . . 80
1.7 Infinite swept wing theory applied to propeller simulations . . . 81
1.8 Sweep correction effect. Circulation and Mach number spanwise distribution at $\Psi = 120°$ (maximum load). . . . 82
1.9 Hub model as implemented in MINT wake model . . . 82
1.10 Definition of loads and moments . . . 84
1.11 Incidence effect on propeller performance and 1P loads. Comparison between wind tunnel data, CFD uRANS computations and HOST-MINT simulations . . . 85
1.12 Spinner effect scheme (side and front view) . . . 86
1.13 Blade load distribution modes in Case No. 1149. *elsA* computations are compared to three HOST simulations: isolated, with installation effects, and with installation effects and hub model. . . . 87
1.14 RPM effect on propeller performance and 1P loads. Comparison between wind tunnel data, CFD uRANS computations and HOST-MINT simulations . . . 89
1.15 Blade load distribution modes. *elsA* computations are compared to three HOST simulations: isolated, with installation effects, and with installation effects and hub model. . . . 90
1.16 Rigorous wall effect implementation in the case of a propeller . . . 92

2.1 Theodorsen's function, $C(k)$ . . . 94
2.2 Wake convection following the freestream velocity and following the normal to the propeller plane . . . 96
2.3 Number of panels in the wake: 2, 5, 25 and 275 (full wake) . . . 97
2.4 Contribution of each model element to the 1P load phase lag. . . . 98

3.1 The wing and its wake are divided into several calculation domains. . 102
3.2 Different $\vec{v}_{\text{ind}}$ terms in the unsteady curved lifting-line theory. 104
3.3 Strategy for the calculation of a finite-length singular panel. 107
3.4 Detail of the singular vortex geometry. 108
3.5 Hess and Smith equivalence for a singular panel 115
3.6 Wake effect on an airfoil under an incidence step 117

4.1 The unsteady airfoil model as implemented in HOST-MINT code . . 123

5.1 Incidence effect on APIAN High-Speed simulations. Comparison between WTT data, *elsA* CFD computations and HOST-MINT simulations (isolated, with installation effects and with both unsteady corrections) 129
5.2 Local results for APIAN high-speed conditions at 3° of incidence . . 131
5.3 Blade load distribution modes for several HOST simulations: isolated, installed, and with unsteady & curvature corrections 132
5.4 RPM effect on APIAN High-Speed simulations. Comparison between WTT data and HOST-MINT simulations (isolated, with installation effects and with both unsteady corrections) 133
5.5 Blade load distribution modes for several HOST simulations: isolated, installed, and with unsteady & curvature corrections 134

6.1 Load terms definition in AI-PX7 open rotor geometry 136
6.2 Front and Rear Rotor performance comparison 138
6.3 Blade loading along a cycle. *elsA* compared to HOST simulations . . 139
6.4 Discrete Fourier Transform of the front and rear rotors $\partial\tau/\partial\xi$ 140
6.5 Comparison between *elsA* and HOST-MINT results for an x-plane upstream the front rotor 141
6.6 Comparison between *elsA* and HOST-MINT results for an X-slice between rotors 142
6.7 Decomposition of the induced velocities $\vec{v}_{\text{ind}}$ for the front and the rear rotors. 144
6.8 Contribution of the $\vec{v}_{\text{ind}}$ terms on the thrust, the 1P load norm, and the 1P load phase lag of front and rear rotors. 145
6.9 Example of two-dimensional airfoil data and the oscillation of angle of attack due to the incidence along a blade cycle. Comparison between the case with and the case without mean induced velocities. 147
6.10 Angle of attack evolution during a revolution for a rear rotor blade section. Auto-induced and mutually-induced $\Delta\alpha$ are plotted together with the total $\Delta\alpha$ for a given blade section 148

7.1 Loose coupling strategy between HOST/MESIR and *elsA* simulations. 155
7.2 Tight coupling strategy between HOST-MINT and *elsA*. 156

7.3 APIAN mesh slices for uRANS simulations in *elsA*. The near-wall mesh (in red) uses the same discretization than in the full-annulus mesh (in black). 158
7.4 Thrust convergence for near-wall case with $\vec{v}_{\text{ind}}$ from HOST-MINT. . 159
7.5 Axial $\vec{v}_{\text{ind}}$ from MESIR and MINT wake models. 160
7.6 Scheme of the regularization of velocities induced by vortex filaments in MINT. 162
7.7 Potential induced velocities on the outer BC's of a near-wall APIAN mesh. 163
7.8 Scheme of the current and modified $\vec{v}_{\text{ind}}$ regularization by vorticity panels in MINT. 163
7.9 Potential induced velocities on the outer BC's of a near-wall APIAN mesh. 164
7.10 The velocity induced on a point by a finite straight vortex filament of constant circulation Γ. 165
7.11 Potential induced velocities on the outer BC's of a near-wall APIAN mesh. 166
7.12 Two interpolation strategies to capture a vortex passage. $T_\star$ correspond to the physical time steps, whereas $t_\star$ correspond to the interpolation time steps. 167
7.13 The MINT interpolation time step effect on CFD blade loads. Comparison between 5°/it, 2°/it, and 1°/it interpolations. 168
7.14 Blade thrust along a revolution. Comparison between *elsA* 360° mesh, near-wall mesh w/o $\vec{v}_{\text{ind}}$, HOST-MINT simulation, and near-wall mesh w/ $\vec{v}_{\text{ind}}$ from HOST-MINT. 169
7.15 Spanwise distribution of the blade thrust. Comparison between full-annulus CFD simulation, HOST-MINT simulation, near-wall mesh w/o $\vec{v}_{\text{ind}}$, and near-wall mesh w/ MINT $\vec{v}_{\text{ind}}$. 170
7.16 Pressure coefficient on the blade skin. Comparison between CFD results on full-annulus mesh and on near-wall mesh. 172
7.17 Iso-surface 10^6 of Q-criterion on uRANS computations in *elsA*. Comparison between full-annulus mesh and near-wall mesh w/ MINT $\vec{v}_{\text{ind}}$ at azimuth $\Psi = 0°$. 173
7.18 Norm of the in-plane velocity for two uRANS computations in *elsA*. Comparison between full-annulus mesh and near-wall mesh w/ MINT $\vec{v}_{\text{ind}}$ at azimuth $\Psi = 0°$. 174
7.19 Side view of APIAN propeller and two considered X-planes (in red) . 175
7.20 Induced angle of attack on the upstream X-plane. Comparison between *elsA* and HOST. 175
7.21 Induced angle of attack on the downstream X-plane. Comparison between *elsA* and HOST. 176
7.22 Velocity triangles considering or not the induced velocities 176

B.1 Sweep correction hypothesis in the blade-element theory. 187

C.1 Parabolic blade and wake models to calculate finite singular panel $\vec{v}_{\text{ind}}$ 190
C.2 Local reference frame for singular panel $\vec{v}_{\text{ind}}$ calculation 190

D.1 Contribution de chaque élément du modèle à la phase des efforts 1P. 198
D.2 Different $\vec{v}_{\text{ind}}$ terms in the unsteady curved lifting-line theory. 199
D.3 Effet de l'incidence dans le cas APIAN en grandes vitesses. Comparaison entre les mesures expérimentales, les résultats des simulations CFD et les simulations HOST-MINT (cas isolé, cas avec les effets d'installation et cas avec effets d'installation et corrections instationnaires). 203
D.4 Comparaison des performances des rotors amont et aval. 204
D.5 Transformée de Fourier discrète du $\partial\tau/\partial\xi$ amont et aval. 205
D.6 Contribution des termes de $\vec{v}_{\text{ind}}$ sur la traction, le module de l'effort 1P et la phase de l'effort 1P des rotors amont et aval. 206
D.7 Stratégie de couplage fort entre les codes HOST-MINT et *elsA*. . . . 207
D.8 Coupes du maillage APIAN pour des simulations uRANS dans *elsA*. Le maillage proche-corps (en rouge) utilise la même discrétisation que le maillage complet (en noir). 207

List of Tables

1.1 Wind tunnel test conditions for APIAN minimum-body configuration. Wind tunnel case No.1149 74
1.2 Sensitivity of performance and 1P loads to several simulation parameters 75
1.3 Incidence sweep in APIAN experimental high-speed tests 83
1.4 Rotational speed sweep in APIAN experimental high-speed tests . . 88

2.1 Theodorsen's function $C(k)$ estimation for APIAN wind tunnel test conditions. Radius at 75% span $R_{75} = 0.188$m, chord at 75% span $c_{75} = 0.094$m. 95
2.2 Full wake case test vs. Prescribed wakes (normal and V_∞): 97
2.3 Full wake vs. Near wake: 97
2.4 Full wake with or without unsteady aerodynamics: 98

5.1 Incidence effect on APIAN high-speed test cases 128
5.2 Advance ratio effect on APIAN high-speed test cases 131

6.1 AI-PX7 Case Conditions 135
6.2 AI-PX7 Performance. Comparison between *elsA* and HOST-MINT results (isolated, installed and installed+unsteady) 137

7.1 Conditions for APIAN minimum-body configuration. From wind tunnel case No.1149 157
7.2 Wind tunnel test conditions for APIAN minimum-body configuration. Wind tunnel case No.1149 168
7.3 APIAN propeller performance and 1P loads comparison 170

D.1 Effet d'incidence dans le cas grandes-vitesses APIAN. 202

Développement de méthodologies à coût modéré pour la simulation aérodynamique des open rotors

Résumé : Cette étude s'inscrit dans le domaine des moteurs à doublets d'hélices contrarotatives, aussi appelés *open rotors*. Elle a porté sur le développement des méthodologies à coût modéré pour la simulation aérodynamique des *open rotors*. Elle avait pour objectif, d'un côté, la mise en place et la validation de ces méthodologies rapides ; et d'un autre côté, l'approfondissement de la compréhension de l'origine des efforts dans le plan hélice, aussi appelés les *efforts 1P*. Pour le premier des objectifs, le code HOST-MINT, basé sur la méthode de la ligne portante a été adapté et amélioré pour la simulation de l'aérodynamique instationnaire des hélices et des open rotors. Des validations ont été réalisées avec succès par comparaison avec des données expérimentales et des simulations CFD plus avancées. Enfin, les premiers développements et les premiers tests pour le couplage Lagrangien/Eulerien entre HOST-MINT et le code CFD *elsA* ont été aussi réalisés. Cette étude a ainsi ouvert des nombreuses perspectives d'application de ce type de méthodologies rapides dans la conception aérodynamique des futurs *open rotors*. En outre, cette méthode s'est révélée aussi adaptée pour d'autres domaines autour de l'aérodynamique, comme par exemple, pour les problèmes d'aéroélasticité ou pour les prédictions aéroacoustiques préliminaires.

Mots clés : Hélice Contrarotative, Efforts 1P, Ligne Portante, Mécanique des Fluides Numérique, Aérodynamique Instationnaire.

Development of Moderate-Cost Methodologies for the Aerodynamic Simulation of Contra-Rotating Open Rotors

Abstract: This study is devoted to the development of moderate-cost methodologies for the aerodynamic simulation of open rotors. The main goals are, on one side, to develop and validate these rapid methodologies, and, on the other side, to better understand the mechanisms behind propeller in-plane loads, also called the *1P loads*. To reach the first goal, the HOST-MINT code, based on the lifting-line theory, has been adapted and improved for the unsteady simulation of propellers and open rotors. The code has been assessed by comparison with experimental data and more complex and precise CFD simulations. Finally, the first developments and tests of a Lagrangian/Eulerian coupling strategy between HOST-MINT and the *elsA* CFD code have been performed. These studies enable to endeavor a number of applications of this type of rapid methodologies in the aerodynamic design of future open rotors. Moreover, these methodologies may be adapted for other domains linked to aerodynamics, such as aeroelastic problems or preliminary aeroacoustic predictions.

Keywords: Open Rotor, In-Plane Load (1P Load), Lifting Line, Computational Fluid Dynamics, Unsteady Aerodynamics.